TECHNISCHE UNIVERSITÄT MÜNCHEN

Department of Chemistry and Catalysis Research Center
Chair of Technical Electrochemistry

Discharge and Charge Mechanisms of Sulfur Electrodes in Lithium-Sulfur Batteries

Qi He

Vollständiger Abdruck der von der Fakultät für Chemie der
Technischen Universität München zur Erlangung des akademischen Grades eines

Doktors der Naturwissenschaften (Dr. rer. nat.)

genehmigten Dissertation.

Vorsitzender:	Prof. Dr. Tom Nilges
Prüfer der Dissertation:	1. Prof. Dr. Hubert A. Gasteiger
	2. Prof. Dr. Corinna Hess

Diese Dissertation wurde am 11.12.2020 bei der Technischen Universität München eingereicht und durch die Fakultät für Chemie am 21.01.2021 angenommen.

Abstract

One major obstacle in the way of developing an efficient Lithium-Sulfur battery is the poor understanding of its working mechanism. Especially, the many reaction intermediates of a Li-S battery (i.e. seven possible polysulfide species ranging from Li_2S_2 to Li_2S_8) are not only thermodynamically metastable but also are entangled with each other in various equilibria. In addition, these equilibria are susceptible to their (electro)chemical environment in an as yet poorly defined manner, with respect to the type of solvents, cations and anions. Concerning that matter, results of polysulfide speciation from *ex-situ* analysis are especially questionable when they are used to interpret the polysulfide speciation in an operating Li-S battery.

For a deeper insight into the Li-S battery chemistry, it is therefore required 1) to understand the underlying speciation mechanisms of the various polysulfides and 2) to identify the exact polysulfide species in a cycling cell using *operando* techniques.

In the first part of this PhD thesis, a systematic investigation of the electrolyte´s influence on the polysulfide speciation is performed in nine different electrolyte solvents. The classic rotating ring disc electrode technique and UV-Vis spectroscopy are therefore employed to better understand the correlation between the specific solvent properties and the speciation of polysulfides as well as their redox behaviors. In the second part of this thesis, we present a novel *operando* UV-Vis spectroelectrochemical cell design, with which we seek to identify the present polysulfides intermediates in a cycling Li-S battery as a function of potential. In addition, we implement a micro-reference electrode into a Li-S cell to acquire the sulfur-cathode electrochemical impedance spectra *in-situ*, which provides insights into the contributions of different physical/chemical processes to the discharge performance of a Li-S battery in a quantitative manner. In the final part of this thesis, the reaction intermediates during charging of a Li-S battery are characterized by spatially resolved measurements using *operando* X-ray absorption spectroscopy.

Kurzfassung

Ein Haupthindernis bei der Realisierung leistungsfähiger Lithium-Schwefel (Li-S) Batterien ist das fehlende Verständnis der grundlegenden Prozesse während des Ladens/Entladens von Li-S Batterien. Insbesondere sind die vielen dabei auftretenden Zwischenprodukte (Polysulfid-Spezies, von Li_2S_2 bis Li_2S_8) nicht nur thermodynamisch metastabil, sondern gehen auch über mögliche Gleichgewichte ineinander über. Darüber hinaus sind diese Gleichgewichte auf eine bisher unbekannte Art und Weise stark beeinflusst durch ihre chemische Umgebung (z.B. durch die Art der Lösungsmittel, Kationen, Anionen). Dies führt dazu, dass *ex-situ*-Methoden zur Bestimmung der Polysulfid-Spezies nur bedingt Einblicke in die tatsächliche Verteilung der Polysulfid-Spezies in laufenden Li-S Zellen liefern.

Für eine tiefere Einsicht in die (elektro-)chemischen Prozesse in einer Li-S Batterie ist es daher notwendig 1) die zugrunde liegenden Entstehungsmechanismen der verschiedenen Polysulfide zu verstehen und 2) die vorliegenden Polysulfid-Spezies in einer zyklisierenden Li-S Zelle anhand von *operando*-Methoden zu identifizieren.

Im ersten Abschnitt dieser Doktorarbeit wird daher eine systematische Untersuchung des Einflusses des Elektrolyten auf die Polysulfide in neun verschiedenen Lösungsmitteln beschrieben. Hier werden die klassische rotierende Ring-Scheibenelektrode sowie die UV-Vis Spektroskopie eingesetzt, um die Zusammenhänge zwischen den Eigenschaften des Lösungsmittels und der Entstehung unterschiedlicher Polysulfide sowie deren Redoxverhalten zu erfassen. Im zweiten Abschnitt wird ein neues Design für eine elektrochemische Zelle für *operando*-UV-Vis Spektroskopie entwickelt. Hiermit können die Polysulfid-Spezies, die sich während des Zyklierens einer Li-S Batterie bilden, beobachtet und deren Potential-Abhängigkeiten bestimmt werden. Zudem wird eine Mikro-Referenzelektrode in Li-S Batteriezellen integriert, um die elektrochemischen Impedanz Spektren einer Schwefel-Kathode *in-situ* zu bestimmen und somit auch die Beiträge verschiedener physikalischer bzw. chemischer Prozesse im Rahmen des Entladungsvorgangs einer Li-S Batterie in quantitativer Hinsicht zu evaluieren. Abschließend wird die Untersuchung der Zwischenprodukte während des Ladens von Li-S Batterien mittels der in unserer Arbeitsgruppe entwickelten *operando*-Röntgenabsorptionsspektroskopie vorgestellt.

Contents

List of Acronyms

Abbreviation	**Description**
AM	Active material
AN	(Gutmann) Acceptor number
ACN	Acetonitrile
BET	Brunauer-Emmett-Teller
DMA	Dimethylacetamide
DME	1,2-Dimethoxyethane
DMSO	Dimethyl sulfoxid
DN	(Gutmann) Donor number
DOD	Depth-of-discharge
DOL	1,3-Dioxolane
E/S	Electrolyte/Sulfur ratio (in $mL \cdot g^{-1}$)
EDX	Energy-dispersive X-ray spectroscopy
EIS	Electrochemical Impedance Spectroscopy
FT-IR	Fourier-transform infrared spectroscopy
HFE	Hydrofluorinated ether
LiB	Lithium-ion batteries
Li-S	Lithium-Sulfur
LiTFSI	Lithium bis(trifluoromethanesulfonyl)imide
NMC	Lithium nickel manganese cobalt oxide ($LiNi_xMn_yCo_zO_2$)
PS	Polysulfides
SEI	Solid electrolyte interphase
SEM	Scanning electron microscopy
SOC	State-of-charge
TBA	Tetrabutylammonium (ion)
TEGDME	Tetraethylene glycol dimethylether
TEM	Transmission electron microscopy
XAS	X-ray absorption spectroscopy
XPS	X-ray photoelectron spectroscopy
XRD	X-ray diffraction

1 Introduction

Lithium-ion battery (LiB) technology has tremendously shaped the consumers´ daily life since its commercialization by Sony in 1991.[1,2] Combined with the rapid development in semiconductors and microelectronics, LiBs have enabled the rapid mass market penetration of consumer portable electronics, such as video cameras, cellular phones, and laptops.[1,3–5] While the development of semiconductor and microelectronics is blessed by the so-called "Moore´s" law, the development of batteries has been often blamed of being too clumsy.[1] Rolison et al.[5] have described this phenomenon by estimating the annual performance improvement using a factor of $1/2^n$ to empirically describe the device development progress, where n stands for the so-called transport function. As a result of the movement of only electrons in integrated circuits, the transport function in semiconductors is taken as $n = 1$, indicating a doubling of the computing performance every two years. However, the coupled movement of electrons, ions, and molecules in a battery system translates into a transport function with a minimal value of 3, which predicts only a ~10% annual performance improvement for battery systems.[1,5]

In addition, CO_2 emissions are commonly accepted to be the main cause for the greenhouse effect and must be seriously reduced to mitigate the global warming phenomenon.[6,7] According to the Intergovernmental Panel on Climate Change (IPCC),[8] 14% of the CO_2 (~7 Gt) was emitted by the transport sector in 2010, of which 95% comes from petroleum-based fuels (largely gasoline and diesel).[8] On that account, many policymakers strive to replace conventional vehicles (based on internal combustion engine) with electric vehicles, in order to reduce the global CO_2 emissions.[7,8] For instance, the European Union has passed a legislation to regulate the fleet average emissions of 95 g_{CO2}/km by 2020.[7] In order to achieve these ambitious goals set by the governments, a substantial market penetration of electric vehicles is required.[6] However, the consumers´ acceptance of all-electric vehicles is largely influenced by the vehicle driving range and price, which are difficult to satisfy with the current LiB technology.[9,10] According to the estimation by Gröger, Gasteiger and Suchsland,[6] a 300 mile driving range may not be viable for the mid-size car market owning to the excessive battery-system cost even in the best scenario with a price assumption of 125 \$/kWh$_{\text{name-plate}}$.

Despite the fact that LiB technology is still the most mature and pragmatic approach for current and near-future application,[3,6,9] there is still a growing consensus that it cannot meet all of the future requirements and that, eventually, a next generation inexpensive and high energy density battery will likely be required.[9–11]

1.1 Lithium-Sulfur Batteries: Technological Challenges

In the search for a high-performance and cost-effective next generation energy storage system, Lithium-Sulfur (Li-S) battery technology has appealed to many researchers[12–14] and industry partners[15–19] due to the theoretical high specific capacity of the sulfur-cathode (1675 mAh/g_S) and the low cost of elemental sulfur.[12]

Fig. 1.1 schematically depicts the current understanding of the discharging process of Li-S batteries. The reversible conversion (described in equation 1) between elemental sulfur (S_8) and lithium sulfide (Li_2S) is generally associated with a series of intermediates, namely polysulfides (PS or S_x^{2-}, where x is generally believed to be ranging from 2 to 8) that are soluble in commonly used nonaqueous solvents and in the state-of-the-art glyme based electrolyte mixture, 1,2-dimethoxyethane (DME) and 1,3-dioxolane (DOL) in a volumetric ratio of 1:1.[13,20]

$$\mathrm{S_8} + 16\mathrm{e}^- + 16\mathrm{Li}^+ \leftrightarrow \frac{8}{m}\mathrm{Li_2S}_m + a\mathrm{Li}^+ + a\mathrm{e}^- \leftrightarrow \frac{8}{n}\mathrm{Li_2S}_n + b\mathrm{Li}^+ + b\mathrm{e}^- \leftrightarrow 8\mathrm{Li_2S} \qquad (1)$$

where Li_2S_m and Li_2S_n represent long-chain and short-chain polysulfides respectively, i.e. ($m > n$), in which case $a = \frac{16(m-1)}{m}$ and $b = \frac{16(n-1)}{n}$.

The value of m and n are unidentified, since the polysulfides are believed to be thermodynamically metastable[21] and their speciation is strongly dependent on the specific environment, including the type of solvents[22–24] and salts,[25–27] the temperature,[28,29] and the polysulfide concentration,[30] which leads to various disproportionation and comproportionation reactions such as:[20,22,31,32]

$$\mathrm{S_8^{2-}} \leftrightarrow \frac{1}{4}\mathrm{S_8} + \mathrm{S_6^{2-}} \qquad (2)$$

When using Li metal as anode and glyme based electrolytes, the average cell voltage of the S-electrode in current Li-S systems is around 2.1 V. Despite the low cell voltage (about half of the mid-point voltage of current lithium ion battery with an NMC ($LiNi_xMn_yCo_{1-x-y}O_2$) cathode of ~3.8 V[3]), Li-S batteries have a potential to achieve higher energy densities over LiBs owing to its higher theoretical capacity of 1675 mAh/g_S[12,20] compared to that of NMC materials (~270 mAh/g).[9] Another major advantage of using Li-S batteries is the abundance of the active material (sulfur), leading to 1) a negligible price compared to NMC materials;[6,10,33] and 2) less concern about the recycling and the re-use of the active material, which may eventually result in a cost advantage of Li-S batteries. Furthermore, the sulfur-based cathode is also more environmentally benign than the transition metal-based materials used in LiB cathodes.[34] Lastly, Li-S batteries have a relatively good low-temperature performance.[28,35]

But, “there are two sides to every coin”. The abovementioned potentials of Li-S batteries can only be unlocked if the currently observed technological challenges can be resolved. The widely accepted major difficulties with regard to the development and implementation of Li-S batteries are: 1) active material (S_8 and polysulfide) dissolution in the electrolyte; 2) consumption of electrolyte and S-species on the Li anode; 3) the insulating properties of S_8 and Li_2S; and, 4) the needed high electrolyte/sulfur weight ratio (E/S ratio), leading to a high passive weight in practical cells.[6,10,13,14,33]

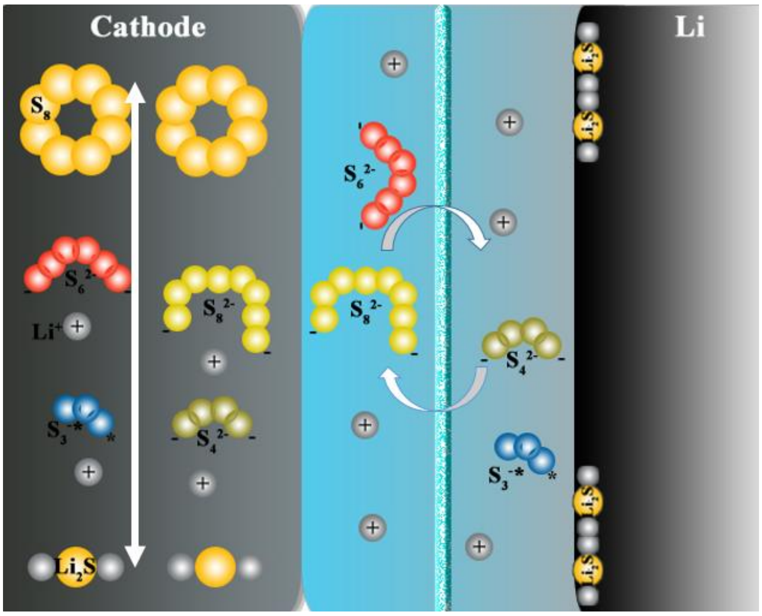

Figure 1.1 Schematic depiction of the current understanding on the chemical processes in non-aqueous liquid electrolyte-based Li-S batteries; illustrating the presence of soluble polysulfides, solid S_8 and Li_2S, and of Li_2S-like species deposited on the surface of the lithium metal anode. The porous carbon in the cathode is omitted for clarity.

One characteristic issue of Li-S batteries is the dissolution of active material (AM), namely S_8 and polysulfides. As Fig. 1.1 demonstrates, the formed long-chain polysulfides (Li_2S_m, $4 < m \leq 8$) are soluble in the electrolyte and can thus diffuse to the anode and get reduced there, resulting either in the formation of short-chain polysulfides (Li_2S_n, $2 \leq n \leq 4$) or solid product (Li_2S) precipitates. On one hand, the dissolution of AM and its chemical reduction at the anode give rise to a self-discharge during discharging the battery or during open circuit conditions, which eventually leads to a reduced discharge capacity. On the other hand, the chemically generated short-chain polysulfides at the anode can in turn diffuse back to the cathode and get electrochemically oxidized again to long-chain polysulfides, especially during the charging process. This repeated cycling of polysulfides between cathode and anode is the so-called polysulfide shuttling phenomenon,[36,3727] which, depending on the magnitude of the shuttling current, can greatly affect the charging efficiency of Li-S batteries. As a result, the coulombic efficiency of a Li-S cell is as of now rather insufficient, without even considering the parasitic reactions of lithium metal with the electrolyte.[27]

The dilemma of using a lithium metal anode is a further critical facet of current Li-S batteries. In order to maximize the usable energy and to pair the high specific capacity of a sulfur-cathode, metallic lithium with a specific capacity of 3860 mAh/g has been commonly adopted in Li-S batteries. Unfortunately, the use of metallic lithium is always accompanied with two major disadvantages, viz. 1) the continuous consumption of the electrolyte and of the S-species, which is partially due to the formation of mossy lithium deposits (with high surface area),[1,4,13,37,38] and 2) the inevitable lithium dendrite formation at high-charging rate, which could lead to internal shorts and thus to safety concerns.[1,6,39] As a result, Li-S pouch cells were in fact reported to fail in long-term cycling, owing to electrolyte depletion and Li metal pulverisation.[37,39,40]

Another difficulty on the way to commercializing Li-S batteries is the required excess of electrolyte.[6,10,33,41] It was recently discovered that the electrochemical performance of Li-S batteries largely hinges on the amount of electrolyte provided to the cell.[41,42] Since this phenomenon has not been found critical in LiBs, little attention had originally paid to this phenomenon in the Li-S research. However, at the time when Hagen et al.[41] calculated the realistic cell density of Li-S batteries, it was realized that all the reported Li-S cells with high cycle-life and good sulfur utilization have either a low sulfur loading or an excess of electrolyte.[41] In order to quantitatively investigate this phenomenon, Zhang et al.[42] and Hagen et al.[41] have introduced the electrolyte/sulfur ratio (E/S in $ml \cdot g^{-1}_{sulfur}$), which allows to better compare the cycling performance and cell energy density between different Li-S cells presented in literature. Quite obviously, that the value of the E/S ratio is influenced by many factors, including the electrolyte composition (e.g., solvents and conducting salts), the electrode design (e.g., composition, structure, porosity, specific surface area) as well as the cell configuration.[42] For instance, as long as the E/S ratio is below 7/1 ml·g^{-1}_{sulfur} in a glyme-based electrolyte,[41] a severe decline in sulfur utilization can already be observed, resulting in a much lower energy density. The so far reported lowest E/S ratio (to our knowledge) is ~4/1 ml·g^{-1} reported by Mikhaylik et al.[27] Recently, Oxis Energy Ltd.[43] has also reported their ultra-light lithium sulfur pouch cells with a specific energy density of > 400 Wh/kg_{cell} and with a cycle life of 60-100, which may be achieved by using a sulfone-based electrolyte and with an optimized E/S ratio in the range of 4 mL g^{-1} or lower.[44] For comparison, the electrolyte to cathode active material ratio in LiBs is near 0.3 ml·g^{-1}.[45]

Apart from the excess of electrolyte, a large amount of conductive porous carbon is also a necessity for Li-S cells, owing to the electrically insulating S_8 and Li_2S, solid products forming upon charge and discharge, respectively.[12] Usually a minimum 20 wt.% of porous carbon are reported in the literature[6,10,12] to increase the electrochemically active surface area for a high sulfur utilization, which in turn increases the passive weight of a Li-S cell and thus lowers the cell energy density.

On top of the above described challenges in developing a high-performance Li-S battery, many other issues also need to be resolved before its commercialization, such as the volume expansion of at the cathode during cycling,[46] the poor cell performance at high temperature,[47] and the gassing issue.[48] Furthermore, better performance models need to be developed for battery management systems (e.g., state of charge and state of health determination),[49] and scalable production must also be devised.[50]

1.2 Recent Progress in the Development of Lithium-Sulfur Batteries

Numerous efforts have been made in the last decades to address the aforementioned issues. In the year 2009, two significant contributions were made by the Nazar group[12] and the Aurbach group[36] which attracted countless attention from both industrial and academic circles, and thus motivated many researchers to start or intensify their Li-S research.[33,50] From then on, the number of publications in Li-S research has increased dramatically. In the following, a brief review of the progress in resolving 1) the polysulfide shuttling issue, 2) the depletion of electrolyte and active material issue, and 3) the low practical energy density issue, will be presented.

Research Addressing the Polysulfide Shuttling Issue

Mainly two strategies have been developed to address the polysulfide shuttling issue, namely, i) encapsulating polysulfides within the cathode electrode using tailored cathode components and architectures;[46,51,52] and ii) minimizing the solubility of polysulfides in the selected electrolytes.[53–55]

The Nazar group[12] has demonstrated the concept of confining polysulfides within the cathode by using a highly ordered nanostructured carbon-sulfur composite. This cathode material provided a mesoporous carbon framework that can constrain the polysulfides to remain within its nanometer-sized porous channels in its channel and that can simultaneously generate the necessary electric contact to the insulating S_8 and Li_2S.[12] The large surface area and the chemical “chambers” created by this structured framework can therefore facilitate a more complete conversion of the redox processes. Inspired by this work, many researchers have proposed various approaches to either chemically and/or physically encapsulate polysulfides in specifically designed cathode architectures.[46,51,52]

Three families in the development of composite sulfur cathodes are often reported in the literature.[56] The first family is the nanostructured carbon as a conductive host material for sulfur, including various porous carbon types (microporous,[57] mesoporous[12]), carbon fibers,[58] carbon nanotubes,[59] graphene,[60] and their hybrids.[61] Despite their good physical entrapment of polysulfides, the conjugate non-polar carbon cannot strongly anchor the polar polysulfides. Hence, doped carbons with tunable polar sites represent a second family of materials, such as graphene oxide[62] or other materials doped with heteroatoms.[63] To further enhance the anchoring effect of the cathode host material with polysulfides, the third family — nanostructured polar inorganic compounds — was proposed lately, such as transition metal oxides (Ti_4O_7[64], TiO_2[65], MnO_2[66,67]) and sulfides (TiS_2[68]). A detailed discussion of this strategy of confining polysulfides is beyond the scope of this work, but a good overview is provided in the reviews by Pang et al.,[46,52]Liang et al.,[66] and Liu et al.[56]

The other approach is to minimize the solubility of polysulfides in electrolytes. For this, one needs to either modify the state-of-the-art DOL:DME-based electrolyte system or completely switch to other electrolyte systems and concepts. This approach of developing an effective electrolyte for Li-S batteries is considered to be not only extremely important but also adventurous and convoluted. This is due to the so far poor knowledge on the influence of solvents on polysulfide speciation, which strongly affect the charge and discharge reaction pathways in Li-S batteries, and thus may result in a totally different electrochemical behavior (e.g., voltage profiles, capacity, coulombic efficiency).[22–24,29,69] At the same time, it has to be considered that the electrolyte has to satisfy other demanding requirements in an electrochemical system,[70] such as a sufficient stability within the relevant operating potential window, chemical stability against radicals (e.g., $S_3^{\bullet -}$), good ionic conductivity, high safety (flammability, toxicity) and low cost. In the case of Li-S batteries a low but finite polysulfide solubility is also required.

Ionic liquids have been considered to be appropriate electrolytes for Li-S batteries, owning to their high electrochemical stability, their non-flammability and non-volatility, as well as the flexibility in designing its cationic and anionic composition.[71–73] For instance, the Watanabe group[71] has shown that ionic liquids with low Gutmann donor number (governed by the selection of anionic component (e.g., amide anions)), are able to suppress polysulfide dissolution. Nevertheless, the rate capability of Li-S batteries employing these ionic liquids is rather poor, owing to their low Li^+ ion diffusion coefficients and Li^+ transference number.[46,73]

A further concept to suppress the polysulfide dissolution are the so-called "solvent-in-salt" electrolytes, which have an exceptionally high concentration of Li salt in the solvent to decrease its ability to solvate lithium polysulfides.[46,53,55,72,74] Suo et al.[55]

have successfully demonstrated that a DOL:DME-based electrolyte system with 7 M LiTFSI is able to suppress the polysulfide dissolution. Ueno et al. [75] have examined the ionic liquid electrolyte for Li-S batteries with a series of equimolar mixtures of Li salts and glyme solvents. In order to reduce the viscosity of such "solvent in salt" electrolytes, Dokko et al.[73] have proposed adding a less viscous and nonsolvating hydrofluorinated ether (HFE) diluent to the electrolyte. Hence, Cuisinier et al.[76] have adopted this approach in their HFE:ACN$_2$-LiTFSI (1:1, *v*:*v*) sparingly (Li_2S_x) solvating electrolyte,[53,74] and demonstrated a reduced viscosity of 8.6 cp and an increased ionic conductivity of 1.57 mS/cm (note that this is still inferior to conventional DOL:DME-based electrolytes with a viscosity of ~1.6 cp and a conductivity of ~10 mS/cm). In addition to the considerably reduced dissolution of polysulfides and their mobility, a distinct electrochemical behavior with only one discharge plateau at 2.2 V_{Li} manifested itself in this sparingly (Li_2S_x) solvating electrolyte system,[53,74] possibly due to a different polysulfide speciation in such electrolyte. Nevertheless, such systems may not be viable for a practical Li-S batteries due to their high density and the high cost of the salts.[46]

Alternatively, a solid electrolyte would be highly efficient in suppressing the polysulfide dissolution and shuttling, exemplified by the P_2S_5-Li_2S lithium-ion-conducting solid electrolyte.[77,78] However, this requires a completely different design of the Li-S battery when compared to that with conventional liquid electrolytes. Challenges such as low sulfur content, low Li-ion conductivity, inferior solid-solid contact, poor processability, unsatisfying long-term cycle-life as well as the little fundamental understanding of the S-redox reactions in solid electrolyte have to be addressed.[79,80]

Research Addressing the Depletion of Electrolytes and Polysulfides on Anodes

While over 60% of the research articles are focusing on the cathode design for Li-S batteries, only a few percent of the research publications have addressed the development of the anode.[39,50] The issues introduced by the anode are often underestimated in the coin-cell-based academic research, owing to the excess of Li metal and electrolyte as well as the low current densities, which are examined.[39] When using cathodes with the high sulfur loadings that are required to get high energy densities, the associated high current densities at even modest C-rates lead to dendritic Li deposition and largely enhanced electrolyte consumption.[39] In addition, the porous and highly resistant layer in the Li metal anode can give rise to a considerable polarization, which can also lead to a short service life of a Li-S battery.[39]

Although polysulfides are reported to help forming a stable solid-electrolyte-interphase (SEI), this process is rather difficult to control in a cycling cell,[39] as only particular polysulfide species within a narrow range of concentration are able to build such an SEI.[81] Hence, additional strategies are required to protect the anode in a Li-S battery.

First, various additives have been investigated to improve the SEI quality of a lithium anode. The most popular additive in glyme-based Li-S batteries is $LiNO_3$, which can react with polysulfides to build a protective film with $Li_2S_xO_y$ and Li_xNO_y species.[36] These species are believed to help mitigating the polysulfide reduction at the lithium anode, resulting in a high coulombic efficiency of ~99%.[36] Unfortunately, the use of $LiNO_3$ is not an ultimate solution for the Li anode metal in Li-S batteries, as it is continuously consumed both at the lithium anode (due to the freshly formed Li surface during each plating process(i.e. charging)),[80] and at the cathode, once its potential is below 1.9 V_{Li} (note that V_{Li} refers to the potential with respect to the Li^+/Li potential).[82] Other additives, such as lithium iodide (LiI) and phosphorous pentasulfide (P_2S_5) have also been proposed for Li-S batteries. For instance, rationalized by the polymerization of DME initiated by the $I^\bullet$ radical,[83] LiI is believed to form a protective coating on both the cathode and the Li metal anode. P_2S_5 was also proposed to be bifunctional in Li-S batteries, as it is thought to be able to chemically activate both electrically connected and isolated Li_2S as well as to passivate the Li surface.[84]

The second approach to protect the anode is the use of an artificial interfacial layer for the Li anode, created either by (electro)chemical preformation of an effective "SEI" on Li metal or by depositing a protective layer onto the Li metal anode. For instance, N_2 has been proposed to react with Li metal and to form a Li_3N layer[85] that has been demonstrated to mitigate the polysulfide consumption on the Li anode. Coincidently, N_2 has been also detected by the Janek Group as one of the main decomposition products of $LiNO_3$ upon charging using online continuous flow differential electrochemical mass spectrometry coupled with infrared spectroscopy.[48] As another option, the company Oxis Energy Ltd. has reported the use of a ceramic lithium sulfide based passivation layer to protect the Li metal anode.[35]

Using alternative anode materials would be the third possibility to address the electrolyte consumption issue. Silicon-based anodes with high theoretical capacity (3580 mAh/g_{Si}) have been suggested.[86] However, owing to the continuously side reactions at the electrode/electrolyte interface caused by the repeated volume expansion and contraction of Si,[87] a stable SEI as observed on graphite has not been achieved in silicon-based electrodes.[88] Simply put, the continuous decomposition of electrolyte on silicon anodes is already inevitable in Li ion batteries. Therefore, a continuous depletion of polysulfides and electrolyte would also be anticipated in a sulfur-silicon battery.

Research Addressing the Low Practical Energy Density of Li-S Batteries

After years of academic research on Li-S batteries, a realistic estimation of energy density on the cell and pack level was required to orient further research activities toward the commercialization of Li-S batteries. Hagen et al.[33] calculated the practical gravimetric and volumetric energy density of Li-S batteries on a cell level, using information on the passive weight distribution obtained from an 18650 "$LiNi_{0.8}Co_{0.15}O_2$-graphite" cell. They discovered a significant gap between the energy density required for a battery system and that projected on the basis of published performance data of current Li-S batteries. To be more specific, they quantitatively analyzed the parameters responsible for this gap, such as sulfur utilization, sulfur loading, and E/S ratio. Eventually, they concluded that Li-S batteries can only outperform current LiB technology with regard to cost and gravimetric energy density if high sulfur loadings ($> 6\ mg_S \cdot cm^{-2}$) and low E/S ratios ($\leq 3\ \mu l \cdot mg_S^{-1}$) can be realized.

In the same year, Eroglu et al.[10] have applied another techno-economic model to calculate the energy density of Li-S batteries on the pack-level, where they even incorporated the reaction kinetics and areal-specific impedance into the model. Their analysis not only indicated that a high sulfur loading ($7\ mg_S \cdot cm^{-2}$) along with a low E/S ratio is required for a competitive battery system, but also suggested that increasing the exchange current density (kinetics) and a deeper mechanistic understanding are in urgent need for the further development of Li-S batteries.

Influenced by these works, more and more effort has been made recently to develop electrodes with high sulfur loadings. With different synthesis approaches and various electrode structures or materials, cathodes with a sulfur loading of 8,[89] 10.1,[90] and up to 20 $mg_S \cdot cm^{-2}$ [91] have been demonstrated. For a detailed overview of the high loading sulfur cathodes developed recently, please refer to Pang et al.[46] and Peng et al.[51]

However, these cells with high-sulfur loading electrodes are still insufficient for a long-term practical application, owing to 1) the severe issue on the lithium anode induced by the large current density (see above), and 2) the unsatisfying energy density on the cell level on account of the still necessary high E/S ratios.[46,89,90]

While there are several strategies to protect the lithium metal (discussed in the previous section), very few studies have been conducted to better define and understand the issues related to the E/S ratio. Hagen et al.[41] were the first ones who have systematically investigated the correlation between sulfur utilization and E/S ratio, and thus have emphasized the necessity of low E/S ratio for practical energy densities. Fan et al.[92] also investigated the correlation between the kinetics of Li_2S electrodeposition and the E/S ratio, observing much slower Li_2S electrodeposition kinetics for cells with low E/S ratio compared to those with high E/S ratio. They have thus proposed using an aluminum-doped zinc oxide coating to improve the kinetics of Li_2S electrodeposition. In addition, Sun et al.[93] have attempted to elucidate the individual impact of S-loading and E/S ratio by separately varying the sulfur loading (3-10 mg_S/cm^2) and the E/S ratio (4-30 µl/mg_S) in Li-S batteries. As a result, they have associated the poor performance of low E/S ratio cells with Li metal corrosion and emphasized that the use of a high concentration of $LiNO_3$ improves the electrochemical performance of high S-loading cells.

Apparently, this issue has bottlenecked further development of Li-S batteries. If Li-S batteries cannot function well with an E/S ratio less than 3 µl/mg_S, high energy density Li-S batteries cannot be realized (> 400 Wh/kg).[10,41,92] This would discourage the momentum of researchers in the further development of Li-S batteries.

In order to advance the progress of research and development of Li-S batteries, effort in better understanding the fundamental working mechanisms of a Li-S battery has to be made, such as 1) understanding how the solvent intrinsically interacts with the reaction intermediates (e.g., polysulfides); and 2) which polysulfide species are present as a function of SOC during the charge/discharge processes of Li-S batteries.

1.3 State-of-the-art Mechanistic Understanding of Lithium-Sulfur Batteries

The exact working mechanism of Lithium-Sulfur batteries is still undisclosed due to the thermodynamically metastable polysulfides,[21] which are notoriously elusive and do not allow for an easy detection and identification. In addition, the potential existence of many reaction intermediates (from Li_2S_2 to Li_2S_8), which are entangled, results in a multitude of possible reaction pathways. Despite all these difficulties, significant progresses in the understanding of Li-S batteries have nevertheless been achieved over the past decade.

In the following, we first introduce our current mechanistic understanding of the discharging and charging processes in Li-S batteries in the conventional glyme-based electrolytes. Afterwards, we discuss the challenges in fundamental research of Li-S batteries with regard to the various analytical techniques applied in literature, and eventually we discuss the desired experimental techniques that need to be developed for Li-S batteries.

Discharging Mechanisms of Li-S Batteries

The typical discharge voltage profile of a Li-S battery in glyme-based electrolyte is presented in Fig. 1.2. During discharge (lithiation) process, the reaction on the negative electrode and cathode are shown in equation 3 and 4, respectively.

$$16\mathrm{Li} \rightarrow 16\mathrm{Li}^{+} + 16\mathrm{e}^{-} \tag{3}$$

$$\mathrm{S}_8 + 16\mathrm{Li}^{+} + 16\mathrm{e}^{-} \rightarrow 8\mathrm{Li}_2\mathrm{S} \tag{4}$$

Two distinct discharge plateaus with voltages of ~2.35 V_{Li} and ~2.1 V_{Li} can be observed in the glyme-based electrolyte. Note that the accurate voltages for Li-S batteries is largely influenced by the selected electrolyte system, for instance, the 2nd discharge plateau in the tetraethylene glycol dimethylether (TEGDME):DOL-based electrolyte is ~2.0 V as shown in Fig. 1.2. This voltage variation in different electrolytes can be explained by two main factors, namely 1) the different solvation ability of the solvent for the ionic species (e.g., Li^+) present in the system,[94,95] and 2) the exact polysulfide species present in different solvents.[13,22,25,31,95] For example, Lu et al.[95] have proposed that dimethyl sulfoxide (DMSO) with much higher donicity than DOL:DME (donor number DN (DMSO) ≈ 29.8 vs. DN (DOL:DME) ≈ 19 (averaged)) can better solvate Li^+, and thus can exert a pronounced influence on the voltage of the lithium stripping/plating process (equation 3), resulting in a ~400 mV higher voltages in Li-S batteries with DMSO-based electrolyte compared to DOL:DME-based electrolytes.

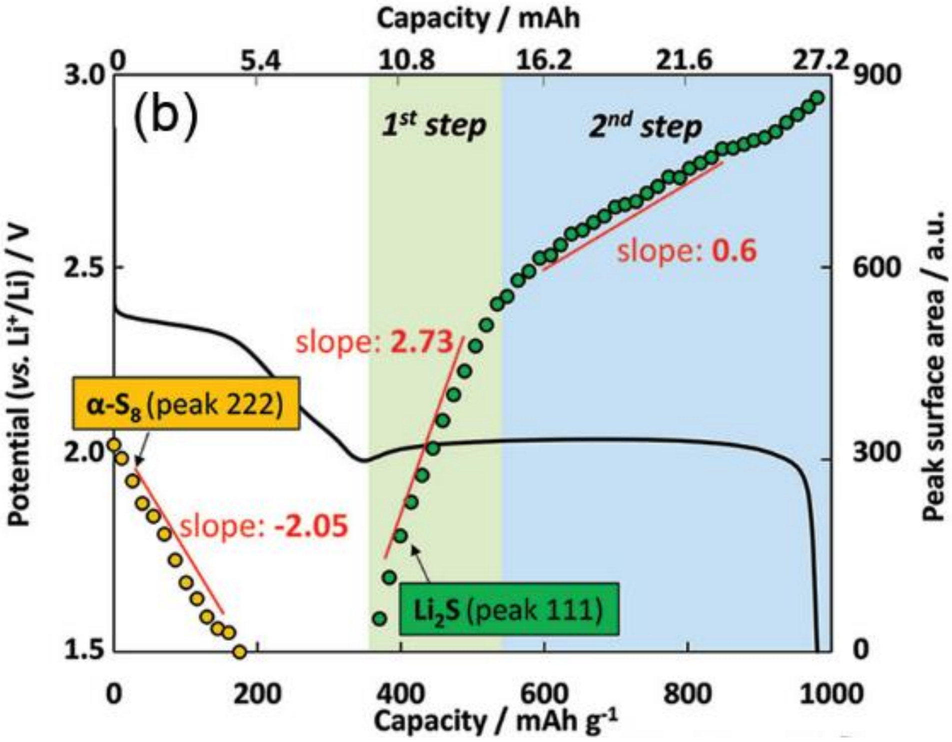

Figure 1.2 Typical discharge voltage profile (solid black line) of a Li-S battery in a glyme-based electrolyte system. A sulfur cathode (~4.3 mg_S/cm^2) is cycled here at C/20 in 1 M lithium bis(trifluoromethane) sulfonimide (LiTFSI) and 0.1 M $LiNO_3$ dissolved in TEGDME:DOL (1:1,v:v). The circles (yellow and green) are the results of (the diffraction peak) surface area from *operando* X-ray diffraction (XRD), where the yellow circles stand for α-S_8 (peak 222) and the green circles represent the Li_2S (peak 111). (Reproduced with permission from ref 96 (Fig. 1b). Copyright 2015 John Wiley & Sons.)

As indicated in Fig. 1.2 (yellow circles), elemental sulfur (S_8) is present in the beginning of discharge and gradually disappears along the first discharge plateau. The first step of S_8 reduction is commonly accepted as:[22,23,95,97,98]

$$S_8 + 2e^- \rightarrow S_8^{2-} \tag{5}$$

While the formed S_8^{2-} could either disproportionate to S_8 and S_6^{2-}/ $S_3^{\bullet -}$ (equation 6 and 7)[22,23,95,97,98] or be further reduced to S_4^{2-} (equation 8).[22,23,95,97,98]

$$S_8^{2-} \leftrightarrow \frac{1}{4}S_8 + S_6^{2-} \tag{6}$$

$$S_6^{2-} \leftrightarrow 2S_3^{\bullet -} \tag{7}$$

$$S_8^{2-} + 2e^- \rightarrow 2S_4^{2-} \tag{8}$$

The formation of the $S_3^{\bullet-}$ radical has been mostly reported in high-dielectric solvents (often with high DN), which was verified by both electron paramagnetic resonance measurements,[20,32,99] X-ray absorption spectroscopy (XAS),[31,69] and UV-Vis spectroscopy (blue color, absorption at ~618 nm).[22,23,25,97,100] Similarly, the formation of S_4^{2-} has also been verified by various groups using UV-Vis spectroscopy[22,23,25,97,100] and the rotating ring disc electrode (RRDE) technique.[95] For instance, it is accepted by most of the literature that S_4^{2-} is only generated in the transition phase between the two discharge plateaus.[20,101–103]

Subsequently, S_4^{2-} is believed to be reduced at the 2nd discharge plateau to shorter chain polysulfides (including the insulating Li_2S, equation 9). Using *operando* XRD approach, Walus et al.[96] in fact have observed the formation of Li_2S already at the beginning of the 2nd discharge plateau, as shown by the green circles in Fig. 1.2.

$$S_4^{2-} + me^- + nLi^+ \rightarrow Li_2S_3/Li_2S_2/Li_2S \tag{9}$$

Independently, it has also been confirmed by *operando* XAS,[31] that the formation of Li_2S already starts at the early stage of the 2nd discharge plateau, rather than at the end of discharge. Therefore, it was concluded that the shorter chain polysulfides (Li_2S_3, Li_2S_2) and Li_2S were generated not necessarily successively but rather concurrently.[13,31]

In contrast to the detection of Li_2S and S_8, the identification of polysulfides upon discharging a Li-S battery has encountered much more challenges both with regard to their experimental detection and the rigorous identification/differentiation between various polysulfide species. While S_8 and Li_2S are thermodynamically stable species,[21] which can be isolated and characterized with various techniques,[96,104] the extraction of single lithium polysulfide from the entangled polysulfide blends (dissolved in solution) is at best elusive, if not impossible. Even though several researchers claimed to have synthesized some lithium polysulfides as solids such as Li_2S_X,[64,105] we believe the synthesized polysulfides would have the tendency to instantaneously disproportionate to other polysulfide species once they are dissolved in solvents. Hence, their characterization in solution phase is still up for discussion.

As one of the most referenced work in this context, Barchasz et al.[20] have applied many analytical techniques to detect and identify the possible polysulfides in

TEGDME:DOL (1:1, v:v)-based electrolyte. After extracting polysulfide samples from Li-S cells at different potentials, they conducted ex-situ analyses on the speciation of the polysulfides, using high-performance liquid chromatography, UV-Vis absorption, and electron paramagnetic resonance. After analyzing the results from these different techniques, they speculated on the presence of many polysulfide species (such as S_7^{2-}, S_6^{2-}, S_5^{2-}, S_4^{2-} and $S_3^{\bullet -}$) in Li-S batteries; the major polysulfide species they detected are depicted in Fig. 1.3. For the exact experimental details and all the proposed (electro)chemical reactions, please directly refer to their work.[20]

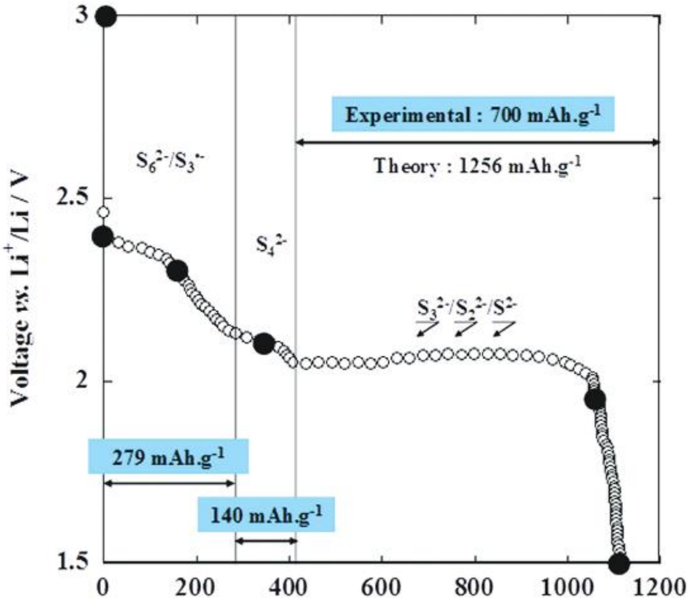

Figure 1.3 The (major) polysulfides that are detected at various potentials, are marked on the voltage profile of a Li-S battery cycled in TEGDME:DOL (1:1, v:v)-based electrolyte. (Reproduced with permission from ref 20 (Fig. 5). Copyright 2015 American Chemical Society.)

Using *operando* transmission UV-Vis spectroscopy, Zou et al.[22] investigated the cyclic voltammetry (CV) of elemental S_8 in DOL:DME-based electrolyte with a gold electrode. They have observed the formation and depletion of S_4^{2-} during a CV scan, but could not identify the stoichiometry of other polysulfide species. As a result, the exact reaction pathway from S_4^{2-} to the final discharge product Li_2S still remains poorly understood. In their work, Zou et al.[22] summarized their current understanding of the discharge process in Li-S batteries with DOL:DME-based electrolytes as follows:

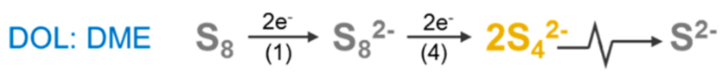

Scheme 1.1 Proposed sulfur-reduction pathway in DOL:DME-based electrolyte. Solid lines represent the electrochemical processes and polygonal line stands for multiple reaction steps (possibly a combination of electrochemical reactions and chemical disproportionation reactions). (Reproduced with permission from ref 22 (Scheme 1). Copyright 2016 American Chemical Society.)

Charging Mechanisms of Li-S Batteries

Fig. 1.4 presents the typical charging voltage profile of Li-S batteries in a glyme-based electrolyte.

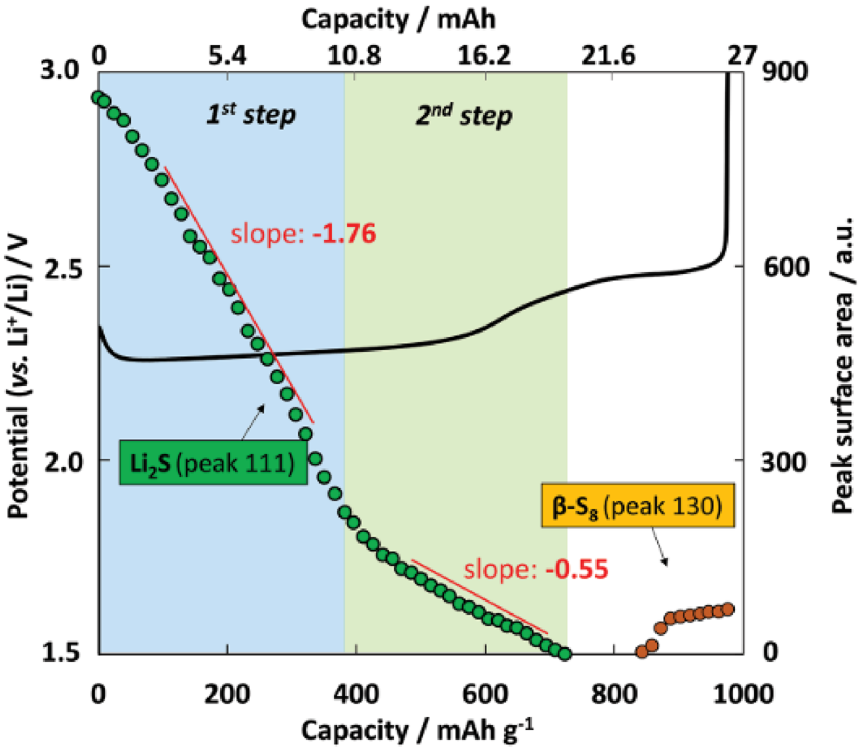

Figure 1.4 Typical charge voltage profile (solid black line) of a Li-S battery in a glyme-based electrolyte system. A sulfur cathode (~4.3 mg_S/cm^2) is cycled here at C/20 in 1 M LiTFSI and 0.1 M $LiNO_3$ dissolved in TEGDME:DOL (1:1,v:v). The circles (green and yellow) are the results of (the diffraction peak) surface area from *operando* X-ray diffraction (XRD), where the green circles represent the Li_2S (peak 111) and the yellow circles stand for β-S_8 (peak 130). (Reproduced with permission from ref 96 (Fig. 2). Copyright 2015 John Wiley & Sons.)

A small kink/spike is often observed at the commencement of the charge curve (Fig. 1.4),[27] which is assigned to the direct oxidation of the Li_2S that had been formed electrochemically in the preceding discharge process.[96] This potential spike is reported to correlate with the capacity delivered by the 2nd discharge plateau of the preceding cycle.[106,107] At a slow discharge rate, more polysulfides are reduced to

Li_2S, leading to a longer 2nd discharge plateau and consequently a higher overpotential in the beginning of subsequent charging.[106,107]

Following that, two plateaus with potentials at ~2.3 V_{Li} and ~2.5 V_{Li} are clearly shown for the Li-S charging curve in Fig. 1.4, where their exact potential values are dependent on the electrolyte system, as described previously. Along with the first charge plateau, a decrease of Li_2S is observed in *operando* XAS studies[31,101] and also by the *operando* XRD results shown in Fig. 1.4 (green circles). Simultaneously, the polysulfides concentration in the electrolyte increases, which is demonstrated by *operando* reflectance UV-Vis spectroscopy[105,108] and *operando* XAS.[101,108] While no more Li_2S can be tracked thereafter, the elemental sulfur (β-S_8) can be clearly detected at the end of the 2nd charging plateau (~2.5 V_{Li} in Fig. 1.4).[86,96,101] If a cell is charged at a slow rate without $LiNO_3$ additive, this voltage plateau appears "endless", which is a consequence of the polysulfide shuttling.[27,106]

Combined with the results from Zou et al.[22] (polysulfide identification upon cyclic voltammetry of sulfur), it is most likely that S_4^{2-} is generated in the charging process. However, this sole solution species cannot explain the shuttling phenomenon, for which a second solution species is required. In closing, a generic understanding of the Li-S charging process is summarized in scheme 1.2.[101,109]

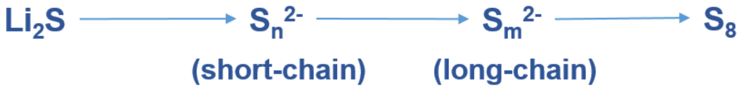

Scheme 1.2 A generic proposed charging mechanism of a Li-S battery. The exact polysulfide speciation and the reaction pathway (chemical and electrochemical processes) still remain unclear.

First charging process with a Li_2S cathode. — It has been widely reported that a much higher overpotential (~1 V) is required in the very first charge for a Li_2S cathode, while the subsequent charging processes operate at a much lower potential.[83,86,109] Several researchers have manipulated/reduced this overpotential by varying the charging rate,[86,109] the electrolyte composition (including additives),[69,83,110] as well as the structure and composition of the cathode.[109,111,112] These studies, however, have not yet been unified to obtain a general understanding of the Li_2S charging process at both high and low potentials. Therefore, more efforts have to be undertaken for a more fundamental understanding of this process to in order to develop an effective strategy to enhance the charging efficiency of Li-S batteries.

Challenges of Fundamental Research in Li-S Batteries

First of all, many techniques applied in analyzing Li-ion batteries cannot be employed for Li-S batteries or extra carefulness has to be assured. According to Conder et al.,[113] several imaging techniques such as conventional scanning electron microscopy (SEM) / energy-dispersive X-ray spectroscopy (EDX) cannot be considered reliable when sulfur containing samples are investigated. Under the high vacuum and the elevated temperature (induced by the beam heating, especially at high magnification), severe consequences of radiation damage would happen to the volatile sulfur, such as sublimation of sulfur, leading to significant sulfur mass loss and a continuous migration/redistribution of sulfur to the sulfur-free areas. This can result in misinterpretations of the SEM/EDX data, particularly when trying to determine the distribution of sulfur within the cathode composite. One monolayer of sulfur atoms per second is estimated to be sublimated under vacuum (e.g., at 8.8×10^{-8} Torr and 18 °C).[114] For a 40 min transmission electron microscopy (TEM) measurement, a micron-size sulfur particle can completely vanish and residues of "super-sublimated" polymeric sulfur (that is relatively stable under high vacuum),[114] would be left behind.

In addition to the imaging techniques, many of the early studies adopted further *ex-situ* approaches to investigate the working mechanisms of a Li-S battery, such as ex-situ X-ray diffraction,[115] UV-Vis[116] as well as Raman and FT-IR spectroscopy,[117,118] high performance liquid chromatography,[20] X-ray absorption spectroscopy,[119] as well as electrochemical impedance spectroscopy (EIS).[120]

However, these *ex-situ* approaches generally have intrinsic issues that need to be seriously considered prior to their application in Li-S batteries.[113,121] When a cell is interrupted at a desired potential or state of charge (SOC), the system is still in a metastable state that may run into a relaxation phase. By the time the characterization is performed, the sample may differs substantially from its original state and may not reflect its state during cycling.[113] In addition, if the sample has to be pre-treated prior to analysis (e.g., washing, drying, applying vacuum, heating, dissolving in other solvents, even diluting with the same solvents), the speciation of the polysulfides in the sample would most likely not remain unchanged. Finally, the influence of the preparation/pre-treatment on the sample may be difficult to control and poorly reproducible. Therefore, the *ex-situ* analysis of Li-S batteries always suffers from the uncertainty as to whether it reflects the actual conditions in an operating battery or whether it is influenced by artefacts introduced by the relaxation process and/or the sample preparation.[113]

For this reason, many *operando* techniques have been developed for Li-S batteries, and meanwhile the characterization of Li_2S, elemental sulfur (S_8) and polysulfides in general have been achieved in operating cells.[31,96] However, the detailed reaction mechanisms in Li-S batteries is still unrevealed owing to the inability of current analysis techniques to differentiate the dissolved polysulfides formed upon cycling. For example, using *operando* XAS, various polysulfides and the $S_3^{\bullet-}$ radical can be detected and their total concentration can be qualitatively conjectured, but the differentiation of the various polysulfide species and their quantification are not possible, owing to the self-absorption effect.[31,122] In addition, the uncertainty of the peak assignments for polysulfides in Raman and FT-IR spectroscopy as well as reflectance UV-Vis spectroscopy has complicated the interpretation of the *operando* results in various studies.[123–125]

For the above given reasons above, *operando* techniques that can either qualitatively identify the polysulfide species or can quantitatively evaluate their electrochemical performance (e.g. kinetics) are highly desired.

2 Experimental Methods

2.1 Electrochemical Techniques Based on Planar Electrodes

2.1.1 Cyclic Voltammetry

Cyclic voltammetry (CV) is a powerful and popular electrochemical technique that is often employed for the initial investigation of a new electrochemical system.[126] It is a basic potential-scan technique that reverses the scan at a selected potential/time, and the current that develops under this condition is continuously recorded.[126,127] The basis of cyclic voltammetry is a linear potential sweep or ramp, as depicted in Fig. 2.1a, where the resulting current response (y-axis) is plotted versus the potential (x-axis).

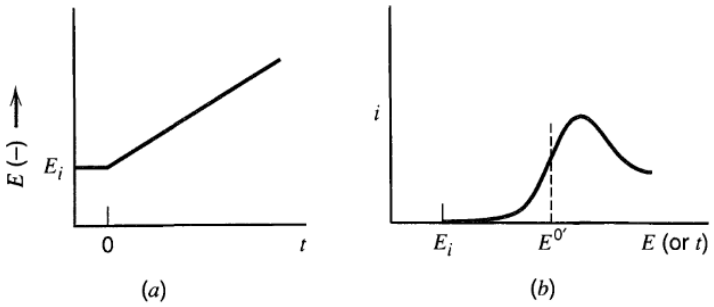

Figure 2.1 (a) Linear potential sweep starting at E_i. (b) Resulting i-E curve (in US convention), where the high to low potential is plotted from left to right, and reduction (oxidation) is above (below) the x-axis. (Reproduced with permission from ref 126 (Fig. 6.1.2). Copyright 2000 John Wiley & Sons.)

As the scan shown in Fig. 2.1b starts at E_i (a potential well positive of the equilibrium potential ($E^{0'}$), where the forward and reverse rate constants have the same value), only capacitive currents flow for a while. Once the electrode potential approaches the vicinity of $E^{0'}$, the reduction (equation 10) commences and faradaic currents starts to flow. As the potential is further ramping to more negative values (i.e., in direction of the x-axis in Fig. 2.1b) , the surface concentration of A drops, resulting in a growing flux of A to the surface and consequently an increasing current. As the potential scans past $E^{0'}$, the surface concentration falls nearly to zero, where the mass transport approaches a maximum rate (current peak in Fig. 2.1b). Afterwards, the mass transport declines due to the depletion of the reactants on account of a growing thickness of the diffusion layer.

$$\mathrm{A} + \mathrm{e}^{-} \rightarrow \mathrm{A}^{\bullet -} \tag{10}$$

When the potential reverses at E_λ, the reduction current keeps declining (see Fig. 2.2b). The accumulated reduced species $A^{\bullet -}$ will only be oxidized once the potential reaches the vicinity of $E^{0'}$and the oxidation current wave has a shape similar to that of the reduction current wave, as depicted in Fig. 2.2.

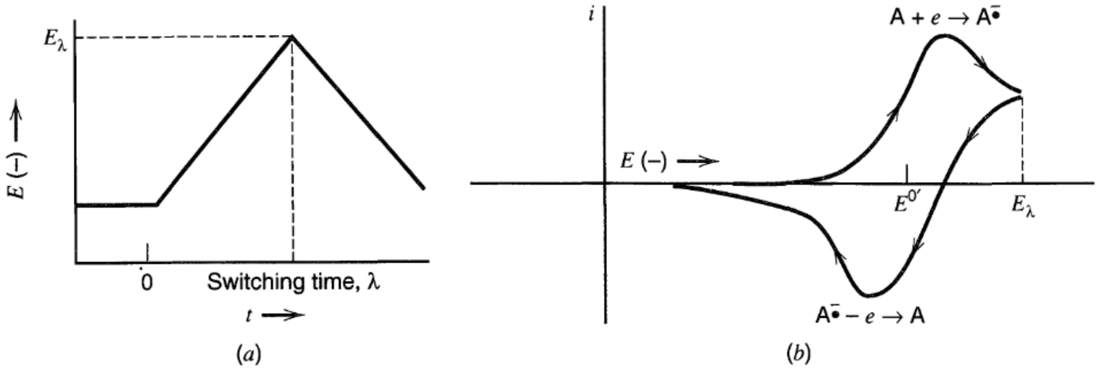

Figure 2.2 (a) Cyclic potential sweep. (b) Resulting cyclic voltammogram (in US convention). (Reproduced with permission from ref 126 (Fig. 6.1.3). Copyright 2000 John Wiley & Sons.)

Considering the entanglement of diffusion of active species (Fick´s second law) and the voltage-controlled kinetics (Butler-Volmer relation), the solution of the current response is sophisticated and can only be resolved numerically.[126] Nevertheless, a simple diagnostic test has been derived from the numerical solution. As demonstrated in Fig. 2.3, the difference between E_{pa} (anodic peak potential) and E_{pc} (cathodic peak potential), often denoted by ΔE_{p}, can be used as a diagnostics for a nernstian process. Even though ΔE_{p} slightly depends on where the potential reverses (E_λ), it always has a value closed to $2.3RT/nF$ or ($59/n$ mV at 25 °C), whereby R stands for the universal gas constant (8.314 J·mol^{-1}·K^{-1}), T for the temperature (K), n for the number of electron number transferred, and F for the Faraday constant (96485 C·mol^{-1}).

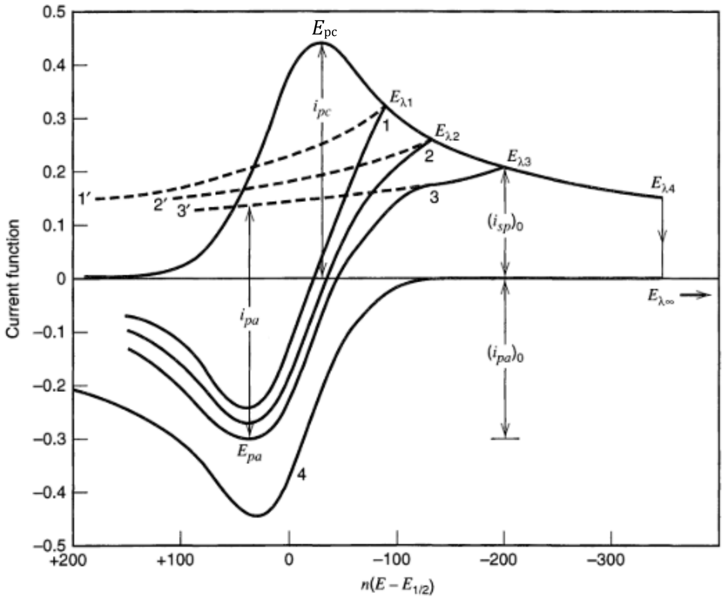

Figure 2.3 Numerically simulated cyclic voltammograms in terms of dimensionless current function, where the values on the potential axis are for 25 °C. Various CVs are shown for different reverse potential ($E_{\lambda 1}, E_{\lambda 2}, E_{\lambda 3}, E_{\lambda 4}$), where $E_{\lambda 4}$ ($E_{\lambda\infty}$) represents the potential with the cathodic current approaching zero. The dash lines mark the baselines for the anodic peak current calculation. (Reproduced with permission from ref 126 (Fig. 6.5.2). Copyright 2000 John Wiley & Sons.)

A further characteristics for a nernstian process is that the ratio of peak currents equals one ($i_{pa}/i_{pc} = 1$), regardless of scan rate and diffusion coefficients (Fig. 2.3). Yet, this approach is rather ambiguous, since the determination of peak currents in a CV is imprecise due to the difficulty in identifying the baseline. Eventually, CV is unable to reliably quantify the crucial properties of an electrochemical system, as these quantifications (e.g., concentration of electroactive species, diffusion coefficients) all require a precise determination of the peak current.

2.1.2 Rotating Disc Electrode (RDE) and Rotating Ring Disc Electrode (RRDE) Techniques

For a more quantitative analysis, the rotating disc electrode (RDE) and rotating ring disc electrode (RRDE) setup are often employed. It is one of the electrode systems with forced convection, whose hydrodynamic equations (yielding the velocity profiles) and convective-diffusion equation have been rigorously solved for the steady-state.[126] Such a hydrodynamic system has the following advantages: 1) a relatively quickly attained steady state, 2) less influence from double layer charging, 3) larger mass transfer rate than for only diffusion-driven transport, leading to a smaller contribution of mass transfer to the kinetics analysis, and 4) although the valuable time variable is "lost" in the steady-state, transient processes can be probed by changing the rotation rate of the electrode.[126]

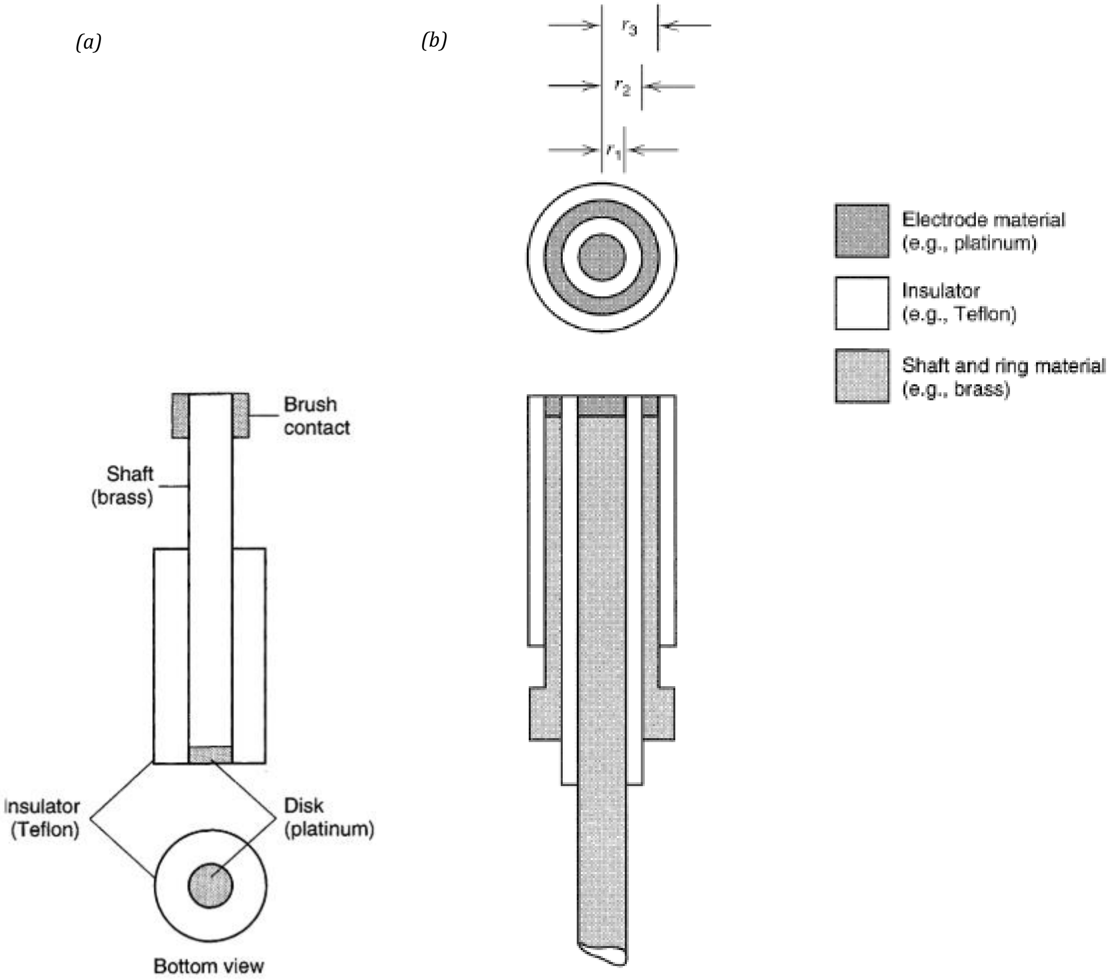

Figure 2.4 Schematic illustration of a rotating disc electrode (a) and rotating ring disc electrode (b), where the disc electrode has a radius of r_1 and the ring has an inner and external radius r_2 and r_3. (Reproduced with permission from ref 126 (Fig. 9.3.1 and Fig. 9.4.1). Copyright 2000 John Wiley & Sons.)

As schematically showed in Fig. 2.4a, an RDE consists of a disc electrode (e.g., platinum, diameter of 2r_1) imbedded in a rod of insulating material (e.g., polytetrafluoroethene, PTFE), which is attached to a motor by a flexible rotating shaft. Through the brush contact, the electrode is electrically contacted with the potentiostat. In addition to that, an RRDE setup requires a further ring electrode imbedded in the rod, which symmetrically surrounds the disc electrode, as demonstrated in Fig. 2.4b.

The rod with the electrode(s) rotates with a frequency of f (revolutions per second) or an angular velocity of ω (s^{-1}), where $\omega = 2\pi f$. A schematic illustration of the fluid velocity profile near a rotating disc is presented in Fig. 2.5

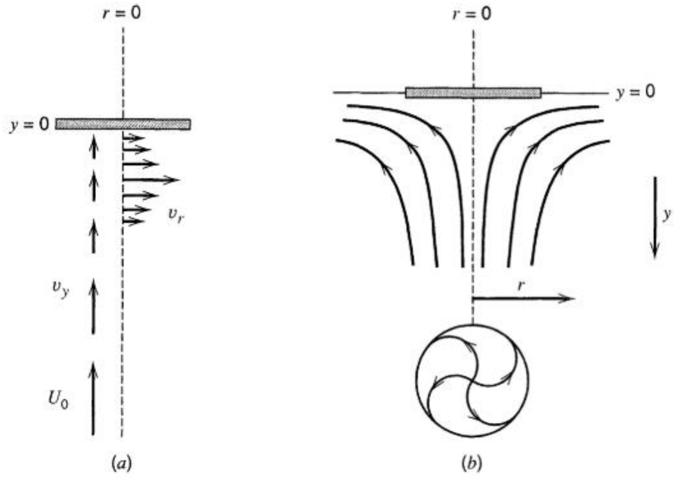

Figure 2.5 (a) Vector representation of fluid velocities (cylindrical coordinates) near a rotating disc. (b) Schematic of the resultant flows. While v_r represents the velocity in r direction, v_y stands for velocity in y direction. U_0 toward the disc is the velocity of the fluid far from the disc, where no flow in the r and ϕ (rotational) directions. (Reproduced with permission from ref 126 (Fig. 9.3.4). Copyright 2000 John Wiley & Sons.)

RRDE in Steady States — Levich Equation

Unlike the transient that appears in a static solution, where the faradaic current decays towards zero after a sufficiently long time (e.g., for potentiostatic step experiment), the faradaic current at an RDE or RRDE approaches a steady-state value. At steady-state, the concentrations near the electrode are time independent ($\frac{\partial C_O}{\partial t} = 0$) and the steady-state convective-diffusion equation can be solved, since the velocities in the three directions (hydrodynamic equations) can be mathematically well described. Therefore the limiting current $i_{l,c}$ can be described by the so-called Levich equation:

$$i_{l,c} = 0.62nFAD_O^{2/3}\omega^{1/2}v^{-1/6}C_O^* \quad (11)$$

where n stands for the number of electrons transferred, F for the Faraday constant (96485 C·mol^{-1}), A for the electrode surface area (cm^2), D_O for the diffusion coefficient of the reacting species (O) , ω for angular velocity (rad·s^{-1}), v for the kinematic viscosity (cm^2/s), and C_O for the concentration of the reacting species (O) (mol·L^{-1}). To note, this equation is valid for the purely *mass-transfer-limited* condition at the RDE.

If one were to apply the diffusion-layer model to the RDE, the diffusion layer thickness δ_O can be determined using equation 12.

$$\delta_O = 1.61D_O^{1/3}\omega^{-1/2}v^{-1/6} \quad (12)$$

Parameter Determination using RRDE — Koutecký-Levich Equation

In addition to the Levich equation (steady-state, limiting-current), the current under non-limiting condition can be analyzed by the Koutecký-Levich equation:

$$\frac{1}{i} = \frac{1}{i_k} + \frac{1}{i_{l,c}} = \frac{1}{i_k} + \frac{1}{0.62nFAD_O^{2/3}\omega^{1/2}v^{-1/6}C_O^*} \quad (13)$$

with i_k being the so-called kinetic current that would be measured in the absence of any mass-transfer effects. For a totally irreversible one-step, one-electron reaction, i_k can be expressed as:

$$i_k = FAk^0e^{\frac{-\alpha F}{RT}\eta}C_O^* \quad (14)$$

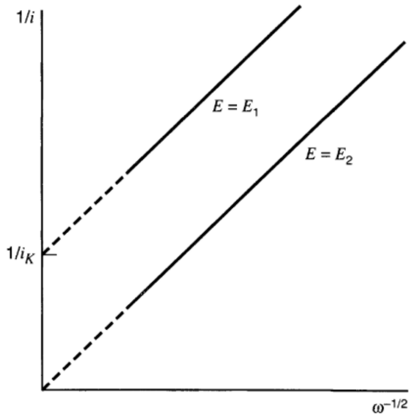

Figure 2.6 Koutecký-Levich plots at a potentials E_1, where the rate of electron transfer is slow, and at a potential E_2, where electron transfer is rapid (i.e. in the limiting-current region). (Reproduced with permission from ref 126 (Fig. 9.3.7). Copyright 2000 John Wiley & Sons.)

By plotting i^{-1} versus ω^{-1} from (R)RDE results, the so-called Koutecký-Levich plot is obtained (Fig. 2.6). One can estimate i_k at different overpotentials by the intersection with y-axis (i^{-1}), while other variables (e.g., the concentration of electroactive species) can also be determined using the slope ($\frac{1}{0.62nFAD_O^{2/3}v^{-1/6}C_O^*}$), if all the other parameters are known. One example is to determine the concentration of O_2 dissolved in the electrolyte for Li-O_2 batteries using Koutecký-Levich plots, since n, D_O, and v can be obtained independently.[128] Similarly, the number of electrons transferred was determined by the Koutecký-Levich plot for the initial S_8-reduction step in Li-S batteries.[95]

Tafel Plots from RRDE Experiments

As mentioned as an advantages of using an (R)RDE, the relative contribution of mass transport to the electron transfer kinetics is often smaller, since the mass transfer rate at the electrode surface is larger than the rates of diffusion alone. The electron transfer kinetics are thus often determined using an (R)RDE.

In the absence of mass-transfer effects, the net kinetic current i_k can be expressed by the Butler-Volmer equation (equation 15).

$$i_k = i_0[e^{\frac{-\alpha nF}{RT}\eta} - e^{\frac{(1-\alpha)nF}{RT}\eta}] \tag{15}$$

$$i_0 = FAk^0 C_O^{*(1-\alpha)} C_R^{*\alpha} \tag{16}$$

with i_0 as the exchange current density (A/m^2), α as the transfer coefficient, η as the overpotential (V), C_O^* and C_R^* as the bulk concentration (mol·m^{-3}) of oxidized (O) and reduced (R) species, respectively.

Although the net current is zero at equilibrium, a balanced faradaic activity is still with the cathodic current being the same as the anodic current but with opposite sign ($i_c = i_a$), expressed as exchange current i_0. The Nernst equation describing the equilibrium potential based on the bulk concentration of the oxidized (O) and reduced species (R) can be expressed as eq.17:

$$E_{eq} = E^{0'} + \frac{RT}{F} ln \frac{C_O^*}{C_R^*} \tag{17}$$

For sluggish reaction kinetics, i.e., at high anodic or cathodic overpotentials, i_0 can be determined using the so-called Tafel-analysis with the kinetic current (i_k) calculated from the (R)RDE data. For instance, if the back reaction contributes less than 1% of the current, e.g., if $e^{\frac{-\alpha nF}{RT}\eta} > 100 * e^{\frac{(1-\alpha)nF}{RT}\eta}$, we obtain equation 18 and 19 from equation 15:

$$i_k = i_0 \cdot e^{\frac{-\alpha nF}{RT}\eta} \tag{18}$$

$$\eta = \frac{RT}{\alpha nF} ln(| \ i_0 \ |) - \frac{RT}{\alpha nF} ln(| \ i_k \ |) \tag{19}$$

where i_k can be calculated from the RDE/RRDE current i using equation 20:

$$i_k = \frac{i_l \cdot i}{i_l - i} \tag{20}$$

Where i_l is the diffusion limited current. By plotting $ln(|i_k|)$ or $log(|i_k|)$ against η from equation 19, we attain a Tafel-slope (Fig. 2.7). The exchange current density i_0 can be estimated from the intersection with the y-axis of $ln(|i_k|)$ or $log(|i_k|)$ and the slope. If we assume the transfer coefficient to be α = 0.5, the number of electrons transferred (n) can also be estimated from the slope, as exemplified by the "Tafel"-plots in Li-O_2 batteries.[128]

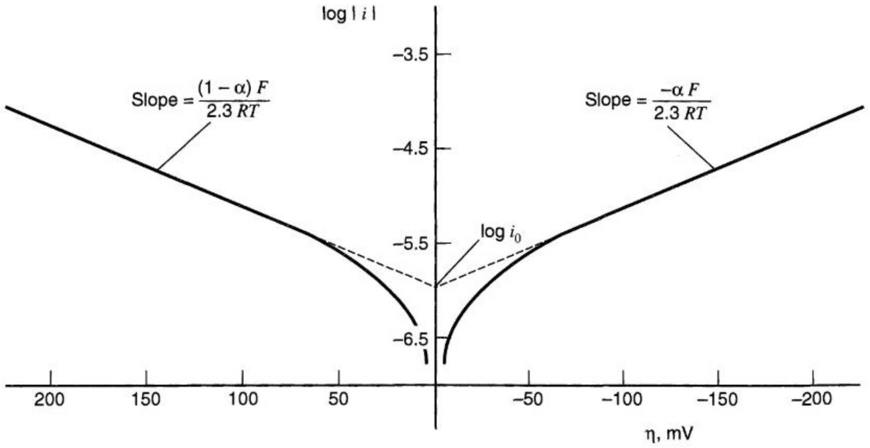

Figure 2.7 Tafel plots for anodic and cathodic branches with α = 0.5, T=298 K, n=1 and i_0 = 10^{-6}A/cm^2. (Reproduced with permission from ref 126 (Fig. 3.4.4). Copyright 2000 John Wiley & Sons.)

Transient at the RRDE Experiments — Diffusion Coefficient Determination

The diffusion coefficient of a dissolved species (reactant or product) can be determined using potential-stepping experiments with rotating ring disc electrode. Taking a simple redox of O + e^- ↔ R as an example, the ring electrode is set to a potential where R is oxidized to O under diffusion-controlled conditions throughout the experiment, and the disc electrode potential is initially set to a value at which no R can be generated (e.g. open circuit potential). Once R is produced at the disc by stepping the disc potential to an appropriate value, it will be transported to the ring and get oxidized there (Fig. 2.8). The required time for R to transit from the disc edge to the inside edge of the ring is the *transient time t´*.

Since 1) the fluid velocity in the r direction is given by the mathematical solution of the hydrodynamic equations for the RRDE, 2) the distance for R to travel is the gap between the disc and the ring electrodes is shown, and 3) the transient time can be experimentally determined, the diffusion coefficient of R (D_R) can thus be estimated using equation 21 or equation of 22 (rearrangement of Eq. 21).

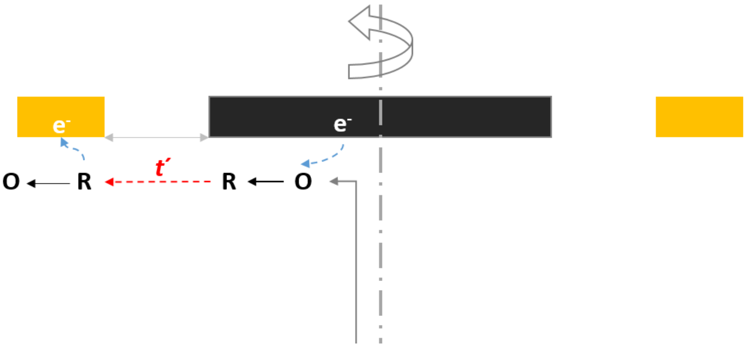

Figure 2.8 Schematic representation of the processes occurring at the RRDE during the potential-stepping experiments, which can be used to determine the diffusion coefficient of species R.

$$\omega t' = 3.58\left(\frac{v}{D}\right)^{1/3}\left[\log\left(\frac{r_2}{r_1}\right)\right]^{2/3} \tag{21}$$

$$D = 45.9v(\omega t')^{-3}\left[\log\left(\frac{r_2}{r_1}\right)\right]^{2} \tag{22}$$

with ω being the angular velocity (rad·s^{-1}), v being the kinematic viscosity (cm^2/s), and r_1, r_2 refer to the radius of the disc and the internal ring radius, respectively. Examples of determining the diffusion coefficients of $O_2^{\bullet-}$ (in a Li-O_2 battery) and S_8 (in a Li-S battery) can be found in the work by Herranz et al.[128] and Lu et al..[95]

2.2 *Operando* Transmission UV-Vis Spectroscopy

Ultraviolet-Visible Spectroscopy

Although ultraviolet (UV) and visible (VIS) radiation occupy only a narrow range of the electromagnetic spectrum, it is of great importance in molecular spectroscopy, since the energy differences within this frequency range correspond to those of the electronic states of atoms and molecules.[129] Therefore, UV-Vis light has enough energy to induce electrons transiting from a lower to a higher energy level. Concurrently, the many transitions (with different energies) caused by the superposition of vibrational and rotational energy levels on the electronic energy level will lead to a broadened UV-Vis absorption band.[129]

Considering that 1) the electron transition is not a unique feature for a specific substance, and 2) that the position of the absorbance maximum is moderately dependent on the molecular environment of the chromophore (e.g., solvent, pH and temperature), UV-Vis spectroscopy is thus not a technique, that allows an absolute identification of an undisclosed species, but generally only allows to identify a substance via the comparison with reference spectra.[129] Therefore, having defined reference spectra is the premise for a reliable UV-Vis spectroscopy analysis.[129]

Transmittance and Absorbance

When light traverses or is reflected from a sample, the transmittance is defined as:[129]

$$T = \frac{I}{I_0} \ or \ \ \% T = \frac{I}{I_0} \times 100 \tag{23}$$

whereby I refers to the transmitted radiation intensity and I_0 to the incident radiation intensity. Besides transmittance, the term “Absorbance” is also widely used in UV-Vis spectroscopy and defined as follows:[129]

$$A = -\log T \tag{24}$$

Here one should note, that 1) absorbance is not a fraction of incident light that is absorbed by the sample but a measure for the transmitted light,[130] and that 2) it is dimensionless.[130]

The Beer-Bouguer-Lambert law is often applied to quantify the absorbance (Eq. 25):

$$A = \varepsilon bc \tag{25}$$

with b being the path length of the sample in cm, c being the concentration of the light-absorbing substances (mol·L^{-1}), and ε being the molar decadic extinction coefficient in (L·mol^{-1}·cm^{-1}), which is a characteristic quantity characteristic of a given substance at a specific wavelength and under a defined condition (e.g., solvent and temperature).[129]

Derivative Spectra

Derivative UV-Vis spectra are often used to analyze multicomponent samples, as they can 1) better visualize the differences among spectra and thus better resolve between overlapping absorption bands and shoulders, and, 2) reduce the interference effects from scattering, the surrounding environment etc.[129]

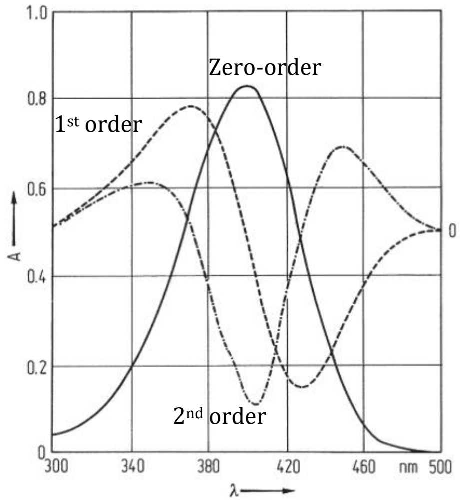

Figure 2.7 Zero-order absorption spectrum (solid line), first-order derivative spectrum (dashed line) and second-order derivative spectrum (dash-dotted line). (Reproduced with permission from ref 129 (Fig. 27). Copyright 1992 Springer-Verlag Berlin Heidelberg.)

Examples are shown in Fig. 2.7, where the zero crossing of the first order spectrum and the minimum of second order spectrum correspond to the absorption maximum in the zero-order spectrum. In addition, the Beer-Lambert law also applies to the derivative spectra, as shown in equation:[129]

$$\frac{d^n A}{d\lambda^n} = bc\frac{d^n \varepsilon}{d\lambda^n} \tag{26}$$

In spite of the many benefits above, extra caution has to be taken when using derivative spectra, since the signal/noise ratio is decreasing with an increasing order of the derivative spectra.

Operando Transmission UV-Vis Spectroelectrochemical Cells

UV-Vis spectroscopy is one of the most frequently applied analytic technique for Li-S batteries, as the reaction intermediates (polysulfides) are soluble in the commonly used non-aqueous electrolytes and have strong and unique absorption characteristics. In order to characterize the generated polysulfides during charging/discharging a Li-S battery, *operando* UV-Vis spectroscopy (in transmission mode) is in principle the most practical technique that needs to be employed and developed.

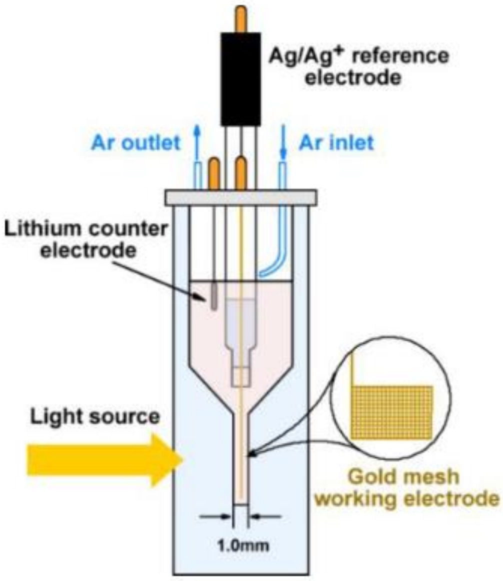

Figure 2.8 Schematic illustration of a three-electrode *operando* UV-Vis spectroelectrochemical cell. (Reproduced with permission from ref 22(Fig. S1). Copyright 2016 American Chemical Society.)

Different designs of (transmission) spectroelectrochemical cell have been proposed for fundamental electrochemical research, for instance, cells based on optically transparent electrode (thin-film semiconductors or metals (e.g., Pt, Au) deposited on glass)[126] or cells connected with an optical fiber.[131] One example is illustrated in Fig. 2.8 — a three-electrode *operando* UV-Vis cell to study the Li-S battery chemistry.[22] This cuvette-based cell (with a relatively short path length of 1 mm) consists of a gold mesh working electrode (WE), a Ag/Ag$^+$ reference electrode, and a Li metal foil counter electrode. The *operando* cell operates under argon atmosphere and all the electrodes are immersed in the catholyte solution, which in this example was 2 mM S_8 in an aprotic electrolyte.

Using this setup, one is able to obtain reliable information of the reaction intermediates at quasi steady-state after a partial charge/discharge experiment (or electrolysis). However, the *operando* results during transient experiments, e.g., during cyclic voltammetry, require a careful interpretation. For instance, Zou et al.[22] have selected a scan rate of 1 mV/s for their experiments, with which it took only ~10 min to scan the potential region of interest (2.4 V_{Li} – 1.8 V_{Li}). During these fast charge in potential, the intermediates will not be distributed equally across the volume element sampled by the beam, resulting in a mixed UV-Vis absorption signal from polysulfides produced over the entire potential range. For instance, it requires about 10 min for polysulfides diffusing from the WE to the edge of the cuvette, considering their diffusion coefficient in DOL:DME-based electrolyte ($\sim 2.6 \cdot 10^{-6}$ cm^2/s) and the diffusion length of 0.5 mm. The long-chain polysulfides (S_x^{2-}, $x > 4$) generated at 2.4 V_{Li} would partially diffuse away from the WE, while short-chain polysulfides will be generated (S_y^{2-}, $y < 4$) at the WE as the potential is being scanned further to a lower potential (e.g., 2.1 V_{Li}). For this reason, the *operando* spectra obtained at 2.1 V_{Li} are rather a mixed signal from short-chain polysulfide (near WE) and the long-chain polysulfides (far from WE). In addition, this cell setup is incapable of galvanostatically cycling a Li-S battery with a sulfur/carbon (S/C) composite electrode (the most common configuration in actual Li-S batteries), and the employed gold mesh electrode may also potentially introduce unknown interaction with polysulfides.

In this dissertation, we have developed a pouch cell based transmission spectroelectrochemical cell, which exhibits a fairly comparable electrochemical performance as that obtained with Swagelok® T-cells, while allowing for a much longer experimental time due to its tight sealing from the ambient, which translates into a better resolution of the intermediates spectra versus potential (9 hours for a potential range between 2.4 V_{Li} and 1.8 V_{Li}).

As sketched in Fig. 2.9, the transmission of the UV-Vis beam is enabled by the two quartz-glass windows sealed into the pouch case as well as by the small slit (1 mm*5 mm) in the electrode assembly (cathode, separator, and anode). The detailed cell design and its spectroscopic and electrochemical performance are presented in section 3.2.1.

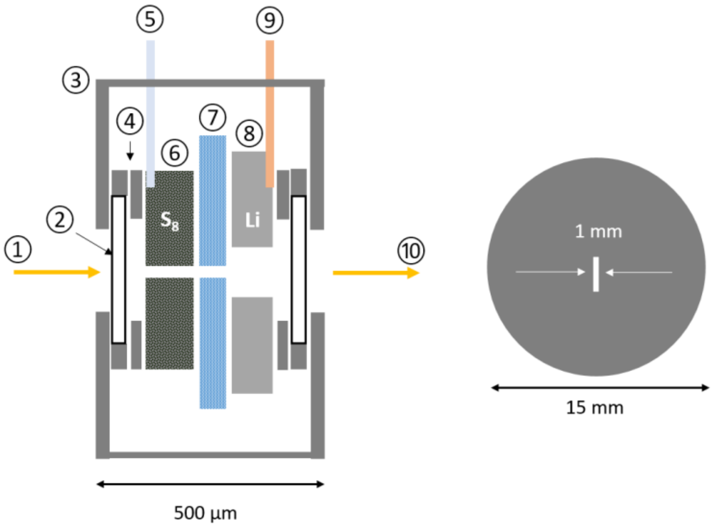

Figure 2.9 Left panel: *operando* UV-Vis spectroelectrochemical cell design. (1) incident UV-Vis beam, (2) quartz-glass (~165 µm), (3) pouch case (115 µm), (4) sealing ring, (5) Al current collector tab (~100 µm), (6) S_8/C cathode (~60 µm), (7) separator (80 µm = 4 layers of Celgard H2013), (8) anode (Li metal or graphite), (9) Ni current collector tab (~100 µm), (10) transmitted beam. Right panel: top view of cathode (⌀ 15 mm) with a slit (1 mm × 5 mm).

2.3 Electrochemical Impedance Spectroscopy

Unlike the electrochemical techniques that drive the electrode to a condition far from equilibrium, in electrochemical impedance spectroscopy (EIS) the electrode reaction is usually perturbed around its steady-state with an alternating signal of a small magnitude.[126] Therefore, it is a noninvasive technique that can be applied to the cell over a long term. In addition, the small amplitude of the applied signal enables a linearization (or simplification) of the current-potential relation when treating the response.[126] Apart from that, EIS also allows to measure the system over a wide range of time scale (or frequencies), e.g., from typically 10^{-3} to 10^{6} Hz.[132]

Basics of Impedance Spectroscopy

The impedance $Z(\omega)$ describes the frequency-dependent complex resistance of an electrical circuit or of an electrochemical system that can be measured upon on AC perturbation of either the current or the voltage at different frequencies (f) or angular frequencies ($\omega = 2\pi f$). If the observed system contains resistive, capacitive and/or inductive elements, the frequency-dependent ratio of the voltage ($\hat{V}(\omega)$) over the current ($\hat{I}(\omega)$) amplitudes is referred to the magnitude of the impedance ($|Z(\omega)|$) and the phase shift between the voltage and the current signal that is described by the phase angle φ. The definition $Z(\omega)$ is given by eq. 27.

$$Z(\omega) = \frac{\hat{V}(\omega)}{\hat{I}(\omega)} e^{j\varphi} = |Z(\omega)|e^{j\varphi} = |Z(\omega)|cos\varphi + j|Z|sin\varphi = Z_{Re} + jZ_{Im} \quad (27)$$

The frequency-dependent impedance is commonly presented either in a Bode plot, where both log $|Z|$ and φ are plotted against log ω, or in a Nyquist plot with Z_{Im} (or Z'') vs. Z_{Re} (or Z') for different frequencies (Note that in electrochemistry, the y-axis is usually -Z_{Im} rather than +Z_{Im}).

In this study, impedance results are only presented in terms of Nyquist plots, as exemplified for a Randles-circuit in Fig. 2.10, which is one of the simplest models describing the processes at an ideal electrode/electrolyte interface, such as a planar electrode. It is described by the resistance in the separator (R_{sep}), by the charge transfer resistance (R_{ct}), by the double layer capacitance at the electrolyte/electrode surface (C_{dl}), and by the Warburg diffusion (Z_{W}) of the active material, as illustrated in Fig. 2.10.

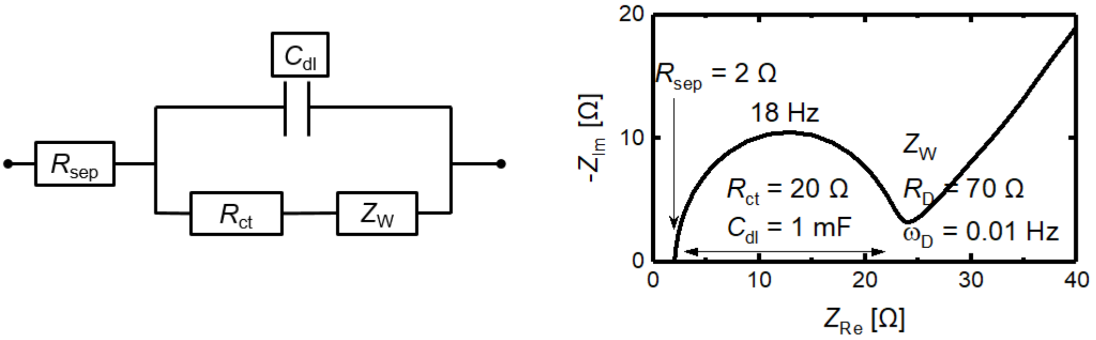

Figure 2.10 A Randles circuit (left) and its impedance response in a Nyquist plot (right), where the values of each component are directly marked in the plot.

Depending on the boundary conditions, the Warburg diffusion element impedance behavior shown in a Nyquist plot can be very different, as demonstrated in Fig. 2.11.

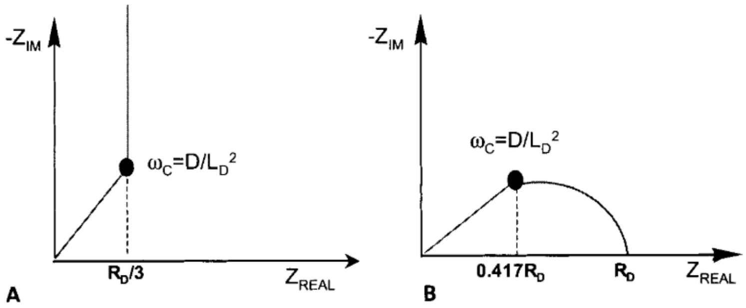

Figure 2.11 Nyquist plot of a Warburg element (an ordinary diffusion in a layer with thickness of L). (A) Reflecting boundary condition and (B) absorbing (transmissive) boundary condition. (Reproduced with permission from ref 132 (Fig. 5-7). Copyright 2012 John Wiley & Sons.)

A 45° line at higher frequencies ($\omega > \omega_C$) is present in both conditions for a homogenous diffusion (Fig. 2.11 A & B), whereas the impedance response at lower frequencies ($\omega < \omega_C$) depends on whether the species are reflected (reflection boundary with $\frac{dc}{dx} = 0$ at $x = L$, showing a vertical 90° line) or extracted (absorbing/transmitting boundary with $c = 0$ at $x = L$, displaying a depressed semicircle).[132]

Application of Electrochemical Impedance Spectroscopy to Batteries

EIS is often applied to batteries to investigate kinetics and transport properties of the active material as well as processes at the electrode/electrolyte interface.[132,133] In order to inspect the processes occurring at an individual electrode in a battery cell, so-called half-cell impedance spectra have to be acquired. However, the experimental acquisition of a reliable half-cell impedance spectrum in a cycling cell is rather problematic, owing to the geometric and electrochemical asymmetry that are commonly encountered when trying to integrate a reference electrode into a battery cell.[134,135]

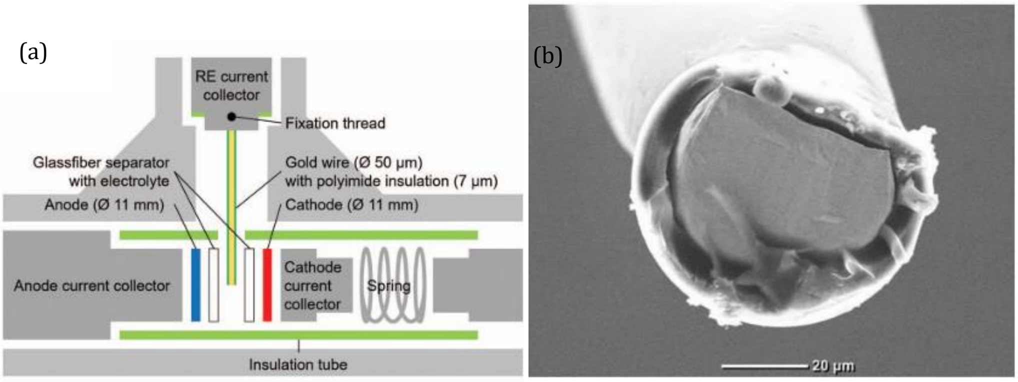

Figure 2.12 a) Modified Swagelok® T-cell design with gold wire reference electrode (GWRE), (b) SEM image of the cut cross-section of the gold wire tip prior to lithiation. (Reproduced with permission from ref 133 (Fig. 1b,c). Copyright 2016 The Electrochemical Society.)

Solchenbach et al.[133] recently introduced a novel micro-reference electrode design for Li-ion batteries, which was shown to provide high-quality half-cell impedance spectra in an operating lab-scale cell based on a Swagelok® T-cell configuration (Fig. 2.12a). It is a gold wire reference electrode (GWRE, ⌀ 50 µm) encapsulated in a polymer insulation (~7µm thickness), with only the wire tip being exposed to the electrolyte (Fig. 2.12b). Prior to its application in a cycling cell, the GWRE has to be pre-lithiated to provide a stable potential over the course of the impedance measurement. The measured impedance in such setup was shown to be rather stable and less error-prone, as the geometric and electrochemical asymmetry will not falsify the measurement results.[133–135]

In this dissertation, the adaptation and the application of a GWRE to Li-S batteries have been accomplished, including 1) pre-lithiation of the GWRE in a Li-S electrolyte, 2) validation of its stability and suitability for measuring EIS in a Li-S environment, and 3) a rigorous interpretation of the obtained real-time EIS results. The experimental details are presented in section 3.2.2.

2.4 Further Experimental Techniques

Apart from the methods described in the preceding sections, a variety of further characterization techniques are employed in this dissertation.

X-ray Absorption Spectroscopy (XAS), in particular X-ray absorption near-edge structure spectroscopy(XANES), has been deployed to investigate the intermediate species present in a cycling Li-S cell. By exciting core-level electrons (K-edge) with X-ray radiation, sulfur atoms with different oxidation states will absorb different energy, resulting in distinct absorption edges.[136] Therefore, this element-specific technique can characterize both amorphous and crystalline Li_2S and S_8, as well as soluble polysulfides.[31,136] However, owing to the self-absorption effect occurring at high-sulfur concentration, the XANES spectra are distorted, so that it is generally not possible to 1) differentiate between various polysulfide species and 2) to quantify the absolute concentration of each of the S-species.[31,137]

Lately, the XANES has been applied to Li-S batteries, such as for the characterization of reaction intermediates during the discharge process.[31,101] Especially, when X-ray fluorescence (XRF) is combined with a novel XAS spectroelectrochemical cell design, a spatially resolved mapping of the produced reaction intermediates in an operating Li-S cell can be achieved.[137] In this dissertation, spatially-resolved XAS measurements have been performed to characterize the reaction intermediates produced both during the initial charging (> 3.5 V_{Li}) and during a subsequent second charging (~2.5 V_{Li})of a Li_2S//Li cell (in DOL:DME-based electrolyte).

The cell design and the schematic illustration of the *operando* XAS cell setup are shown in Fig. 2.13, where a monochromatic X-ray beam penetrates the cell through an aluminized Kapton® window. The spatial resolution was achieved by a defined beam size, which was focused to 20 µm in one direction, and defocused to 400-500 µm in the other direction. The XANES spectra were measured in fluorescence mode at 90° with respect to the incident beam. The detailed experiments are described in section 3.3.

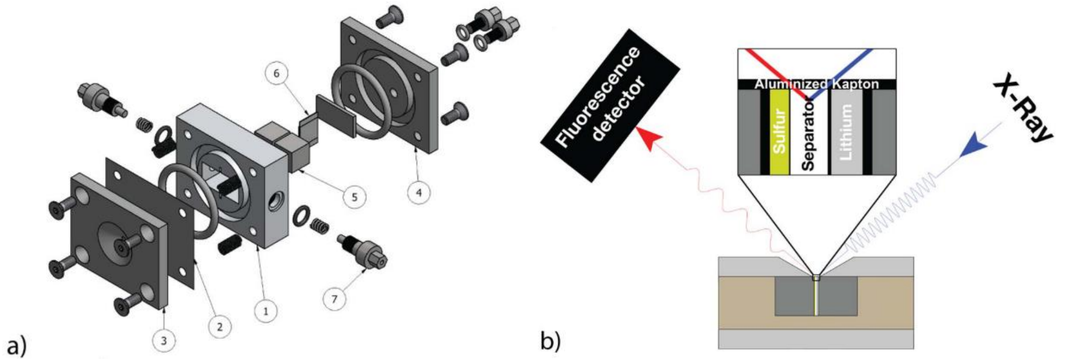

Figure 2.13 a) Cell design of a spectroelectrochemical *operando* XAS cell with its components. 1) cell base; 2) X-ray window (aluminized Kapton); 3) and 4) aluminum front and back plate; 5) stainless steel current collectors; 6) electrode-separator assembly; 7) stainless-steel electric contact pins. b) Schematic illustration of the *operando* XAS setup, that allows for spatial resolution using micro-focused X-ray beam. (Reproduced with permission from ref.31 (Fig. 1). Copyright 2015 The Electrochemical Society.)

In addition, a two-compartment cell design separating the cathode and anode compartments by a lithium ion conducting solid electrolyte was used to investigate the cell performance of Li-S batteries in different electrolytes (section 3.1). On one hand, it can prevent polysulfides from diffusing to the anode and thus can avoid active material loss on the Li anode as well as shuttling current even in the absence of $LiNO_3$. One the other hand, it also enables the cycling of Li-S batteries in Li-metal incompatible electrolytes, such as acetonitrile.

Other techniques such as X-ray photoelectron spectroscopy (XPS) have been used to identify the component that is responsible for the contact resistance occurring at the electrode/current collector interface. More specifically, an Al foil previously immersed in polysulfide or sulfur containing solution was examined by XPS (Kratos Axis Supra Spectrometer). Thermogravimetric analysis (TGA) was performed with a TGA/DSC instrument (Mettler Toledo) and was used to characterize the sulfur content in an S_8/C composite. The S_8/C electrodes prepared from this composite (66.7 wt. %S_8 and 33.3 wt.% vulcan carbon) have been frequently used in section 3.1 and section 3.2.1. The specific area of carbon paper (untreated Toray 030) has been characterized with Krypton gas adsorption using an AutosorbiQ instrument (Quantachrome). The specific surface area of Toray TP030 carbon paper was calculated by the Brunauer-Emmett-Teller (BET) method and determined to be 0.311 m^2/g.

3 Results

This section summarizes three peer-reviewed journal articles and a manuscript prepared for submission to a peer-reviewed journal.

The first focus of this dissertation is to understand the correlation between electrolyte solvent properties and the sulfur redox behavior (section 3.1). Various analytical techniques are applied, such as cyclic voltammetry, rotating ring disc electrode measurements, UV-Vis spectroscopy, and galvanostatic charge/discharge cycling in a two-compartment cell. By seeking to understand the underlying (electro)chemical processes, we hope to gain insights into how one can influence polysulfide speciation.

The emphasis of the second part is placed on the mechanistic understanding of the Li-S discharge process. Section 3.2.1 deals with the real-time polysulfide speciation in the state-of-the-art DOL:DME-based electrolyte. We present in this part a novel battery cell design for *operando* transmission UV-Vis spectroscopy. In combination with a systematic analysis of *ex-situ* UV-Vis references and with rotating ring disc electrode experiments, we attempt to better understand the detailed mechanisms during the discharge of Li-S batteries. Subsequently, a more quantitative approach is imperatively required to identify the contributions of the charge transfer processes that originate from the above identified reaction intermediates. We thus utilize *in-situ* electrochemical impedance spectroscopy to record the impedance response of the sulfur cathode by incorporating a micro-reference electrode into a Li-S battery cell – a so-called gold wire reference electrode (GWRE). The contributions of different chemical/physical processes (e.g., ionic conduction, charge transfer and diffusion process) upon discharging will be presented in section 3.2.2.

In the final part, we pay a closer attention to the mechanistic understanding of the Li-S charging process. The technique used is *operando* X-ray absorption near edge structure spectroscopy (XANES) that can spatially resolve the reaction intermediates present at the cathode and in the electrolyte phase at real-time. The detailed results and the proposed charging mechanism are extensively discussed in section 3.3.

3.1 Dependencies of Polysulfide Speciation on the Electrolyte Solvent Properties

This section presents the article "Unraveling the Correlation between Solvent Properties and Sulfur Redox Behavior in Lithium-Sulfur Batteries",[138] which was published in December 2018 in the Journal of The Electrochemical Society. It is an open access article distributed under the terms of the Creative Commons Attribution 4.0 License. The paper was also presented by Qi He at the 232nd ECS Meeting in National Habour, MD. (October 1-5, 2017), Abstr. 466. The permanent web-link to the article is http://dx.doi.org/10.1149/2.0991816jes.

This study focuses on the understanding of the correlation between solvent properties and the sulfur redox behavior in a variety of solvents. Here, a rather large sample size (i.e., in total nine non-aqueous solvents) is selected to cover a wide range of three main physiochemical properties of solvents, namely the dielectric constant (ε), the Gutmann donor number (DN),[139] and the acceptor number (AN).[140]

First, a three-electrode cell with a planar electrode is deployed, which (1) provides a defined hydrodynamics,[126] i.e., a well-defined mass transport for a quasi 1D electrode geometry (i.e., in contrast to a porous electrode), (2) minimizes the influence from the counter electrode, and (3) provides a homogenous and well-defined system with regards to the concentration of the active material. As a result, we noticed that the sulfur redox behavior (shape of the cyclic voltammogram, its reversibility and the number of transferred electron) is mainly governed by the DN of the solvent, rather than by the dielectric constant,[25,95] that had been proposed previously.

Next, *ex-situ* UV-Vis spectroscopy is exploited to investigate the dependency of polysulfide speciation on the solvent (properties), where the influence of the conducting salt type and concentration are also carefully examined. Again, the DN is found to be the critical solvent property controlling polysulfide speciation.

To further confirm that the DN is the property that most strongly influences the sulfur redox behavior, we performed galvanostatic charge/discharge cycling experiments in a two-compartment cell in three solvents with contracting properties, viz., DOL:DME (low DN, low ε), ACN (low DN, high ε), and DMSO (high

DN, high ε). Consistently, comparable voltage profiles can be observed in the solvents with similar DN, whereas cells with solvents of different DN present distinct voltage profiles, regardless of the dielectric constant.

To understand why the solvent DN would affect polysulfide speciation, we deploy the classic Hard Soft Acid Base (HSAB) theory, where a soft acid (strongly solvated Li^+, e.g., Li^+ in high DN solvents) prefers coordination with a soft base (e.g., long-chain polysulfides) and vice-versa. The softness of polysulfides is found (by several theoretical studies[136,141]) to correlate with the electron density distribution on its sulfur chain, that is, long-chain polysulfides with delocalized electrons are softer compared to short-chain polysulfides. We therefore varied the cation type and concentration in a critical solvent (ACN) that has a low DN but a high dielectric constant in order to validate this hypothesis. We in fact observe that the type (e.g., Li^+(hard acid), TBA^+ (soft acid)) and the concentration of cations in the ACN solvent are able to shift the polysulfide equilibria and thus the polysulfide speciation. Finanlly, we propose a mechanism of how polysulfide speciation is governed by the surrounding electrolyte via the HSAB theory and propose strategies for controlling polysulfide speciation in a Li-S battery.

Author Contributions

Q.H. performed the CV, RRDE and galvanostatic charge/discharge experiments. M.U.M.P. conducted the UV-Vis spectroscopy measurements. Y.G. discussed the CV and RRDE results. H.G. and Y.C.L. developed the concept of the RRDE and the two-compartment Li-S battery cell. Q.H. and Y.C.L. wrote, revised the manuscript. All authors discussed the results and commented on the manuscript.

Journal of The Electrochemical Society, **165** (16) A4027-A4033 (2018) A4027

Unraveling the Correlation between Solvent Properties and Sulfur Redox Behavior in Lithium-Sulfur Batteries

Qi He,[1,z] Yelena Gorlin,[1,a,*] Manu U. M. Patel,[1] Hubert A. Gasteiger,[1,] and Yi-Chun Lu[2,*,z]**

[1] *Chair of Technical Electrochemistry, Department of Chemistry and Catalysis Research Center, Technical University of Munich, Munich, Germany*
[2] *Electrochemical Energy and Interfaces Laboratory, Department of Mechanical and Automation Engineering, The Chinese University of Hong Kong, Hong Kong*

Systematic understanding of how solvent property influences Li-S redox chemistry is required to develop an effective electrolyte for Li-S batteries. In this study, we investigate the correlation between solvent property and Li-S redox chemistry in nine non-aqueous electrolyte solvents that cover a wide range of three main solvent physiochemical properties, namely dielectric constant (ε), Gutmann donor number (DN), and acceptor number (AN). We exploit various analytical techniques including cyclic voltammetry, rotating ring disk electrode technique, UV-Vis spectroscopy and galvanostatic measurement in a two-compartment cell. We show that the potential of S_8-reduction increases with increasing AN and that the polysulfide-reduction/oxidation is strongly influenced by the DN. The common discrepancy in the literature on the role of dielectric constant and donor number is addressed by examining the redox reactions, polysulfide stability, and the effect of salt concentration in acetonitrile - a solvent with high dielectric constant and low DN. We show that the DN is the primary descriptor for polysulfide redox reactions, as it controls the effective charge density of the solvated cation (Li^+), which affects the stability of polysulfides with different charge density via Pearson's Hard Soft Acid Base theory.

[DOI: 10.1149/2.0991816jes]

Manuscript submitted October 8, 2018; revised manuscript received December 10, 2018. Published December 29, 2018.

In the search for high energy density and inexpensive post Li-ion batteries, lithium-sulfur (Li-S) batteries have been intensively researched due to their high theoretical capacity (≈1675 mAh/g_{sulfur}), high natural abundance, and non-toxicity of elemental sulfur.[1–6] The reversible conversion (described in Reaction 1) between elemental sulfur (S_8) and lithium sulfide (Li_2S) in a Li-S battery is normally associated with a series of intermediates, namely polysulfides (Li_2S_n, $2 \leq n \leq 8$), which are believed to be soluble in common organic solvents and in the state-of-the-art glyme-based electrolyte mixture, i.e. 1,2-dimethoxyethane (DME):1,3-dioxolane (DOL) (1:1, v:v).[1]

$$S_8 + 16e^- + 16Li^+ \leftrightarrow \frac{8}{n}Li_2S_n + aLi^+ + ae^- \leftrightarrow \frac{8}{m}Li_2S_m + bLi^+ + be^- \leftrightarrow 8Li_2S \qquad [1]$$

where $a = \frac{16(n-1)}{n}$, $b = \frac{16(m-1)}{m}$, and $2 \leq m < n \leq 8$.

The cycling performance of Li-S batteries suffers from capacity fading and low efficiency, owing to the dissolution of active materials (elemental sulfur, polysulfides) into the electrolyte and diffusion away from the cathode host material, followed by their continuous depletion at the anode.[1,2] In addition, the practical gravimetric energy density of Li-S batteries is limited due to the generally used high electrolyte/sulfur ratio. Therefore, developing an effective electrolyte to control the active material dissolution and to reduce the electrolyte/sulfur ratio has been one of the most critical objectives to improve the performance of Li-S batteries.[2–4,7–9]

The search and development for effective electrolytes require fundamental understanding of how solvent properties affect the Li-S redox chemistry.[5,10,11] The selection of solvent strongly influences the stability of polysulfides which consequently affects the chemical equilibrium between various polysulfides, e.g. chain-breaking reactions (e.g. $S_6{}^{2-} \leftrightarrow 2S_3{}^{\bullet-}$)[12] and/or disproportionation reactions (e.g. $S_8{}^{2-} \leftrightarrow S_6{}^{2-} + \frac{1}{4}S_8$).[5,10–15] However, the primary solvent property that dictates the stability of polysulfides and its role in Li-S battery performance are still under debate. Here, the stability refers to polysulfide's stability against disproportionation instead of side-reactions with solvents. The dielectric constant (ε) of the solvent was suggested to be the primary descriptor governing the stability of polysulfides,[5,8] as evidenced by the clear distinction of polysulfide phases in high-dielectric solvents (blue colored solutions, indicative of the presence of $S_3{}^{\bullet-}$ radical,[12] exemplified by dimethyl sulfoxide (DMSO), dimethylacetamide (DMA), dimethylformamide (DMF), or acetonitrile (ACN)) and in low-dielectric solvents (yellow colored solutions, indicative of $S_4{}^{2-}$, exemplified by tetrahydrofuran (THF), DOL, and DME). Similarly, Bieker et al.[16] employed UV-Vis spectroscopy to examine the chemically prepared "Li_2S_8" and "MgS_8" polysulfides in different solvents (note that the stoichiometry in these cases only represents an overall average value), and concluded that the dielectric constant would be the primary descriptor determining polysulfide stability. They reported that high-dielectric solvents such as DMSO, DMF and ACN are observed to stabilize long-chain polysulfides ($S_8{}^{2-}$ and/or $S_6{}^{2-}$) and the $S_3{}^{\bullet-}$ radical, while short-chain polysulfides ($S_4{}^{2-}$) dominate in low-dielectric solvents such as THF, DME, and tetraethylene glycol dimethyl ether (TEGDME).[16] On the other hand, Cuisinier et al.[17] showed that high EPD (electron pair donor) solvents exhibit significantly different behaviors from low EPD solvents and proposed that high EPD solvents (e.g. DMA) may be beneficial for redox-flow type Li-S batteries, as they can prevent electrode from passivating by Li_2S formation during cycling due to the facile phase transition from Li_2S to polysulfides. In addition, Zou et al.[10] studied the cyclic voltammetry of elemental sulfur in two different solvents using operando UV-Vis spectroscopy, revealing that the dominant sulfur reaction intermediate in the high-DN solvent DMSO is the $S_3{}^{\bullet-}$ radical, while that in the low-DN solvent mixture DOL:DME is the $S_4{}^{2-}$ polysulfide.

These studies are inconclusive in resolving the primary descriptor for polysulfide stability due to the issues (1) that high (low) dielectric solvents in most cases have high (low) donor number, and (2) that the type of salt and its concentration are typically neglected in these discussions. In the present work, we systematically study the Li-S redox chemistry in nine non-aqueous solvents, covering a wide range of three major solvent properties, viz., in dielectric constant (ε), in Gutmann donor number (DN), and in acceptor number (AN) (s. Table 1), representing the polarity/polarizability (e.g. Z, π*), Lewis basicity (β), and Lewis acidity (e.g. $E_T{}^N$) of the solvent, respectively.[18] We exploit a well-defined three-electrode setup to conduct cyclic voltammetry (CV) and rotating ring disk electrode (RRDE) measurements

---

*Electrochemical Society Member.
**Electrochemical Society Fellow.
[a] Present Address: Research and Technology Center, Robert Bosch LLC, California, USA.
[z] E-mail: qi.he@tum.de;yichunlu@mae.cuhk.edu.hk

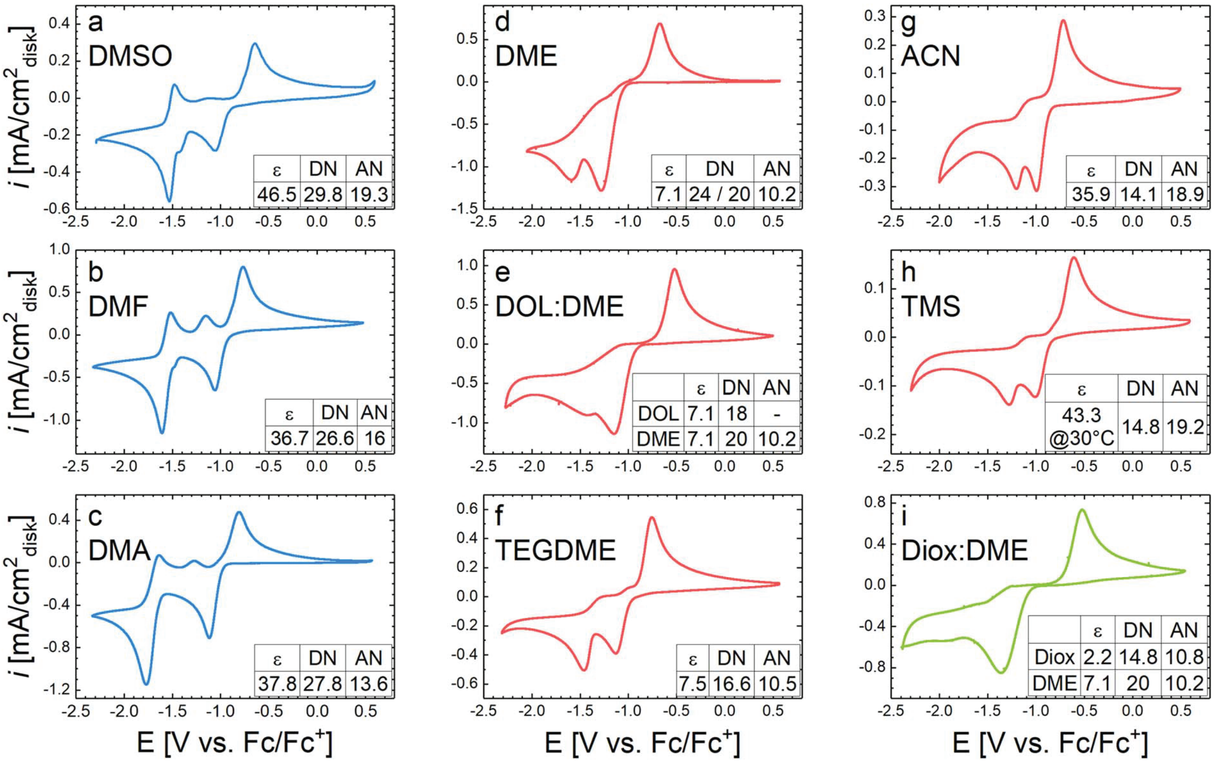

Figure 1. CVs recorded at 50 mV/s on a glassy carbon (GC) electrode under argon atmosphere at room temperature (25±1°C) in various organic solvents with dissolved S_8: (a) 2 mM S_8 in 1 M LiTFSI in DMSO; (b) 3 mM S_8 in 1 M LiTFSI in DMF; (c) ≈4 mM S_8 in 1 M LiTFSI in DMA; (d) 4 mM S_8 in 1 M LiTFSI in DME; (e) 4 mM S_8 in 1 M LiTFSI in DOL:DME (1:1, v:v); (f) 4 mM S_8 in 1 M LiTFSI in TEGDME; (g) 0.5 mM S_8 in 1 M LiTFSI in ACN; (h) 2 mM S_8 in 1 M LiTFSI in TMS; and (i) 4 mM S_8 in 1 M LiTFSI in Diox:DME (1:1, v:v).

in order to study how each solvent property affects the Li-S redox reactions; Furthermore, we employ UV-Vis spectroscopy to examine the primary solvent property that dictates the stability of polysulfides. To better deconvolute the effects of ε and DN which are either both high or both low for most solvents, we further study the effect of the type and concentration of salt on polysulfide stability in ACN, a solvent exhibiting a high ε (35.9) which is similar to DMSO or DMF but demonstrating a low DN (14.1) which is similar to glymes. Thereby, we could decouple the influence of DN from ε and AN on polysulfide stability, which resolved the discrepancy in the literature in determining the primary descriptor for polysulfide stability. Detailed correlations between each solvent property and the Li-S redox behavior as well as the underlying mechanisms affecting the performance of Li-S batteries will be discussed.

Results and Discussion

***Correlation between Li-S redox behavior (CV features) and solvent properties.*—**Figure 1 shows the cyclic voltammograms (CVs) of dissolved S_8 in nine representative solvents (or solvent mixtures), including DMSO, DMA, DMF, DOL, DME, TEGDME, ACN, sulfolane (TMS) and 1,4-dioxane (Diox). We converted the recorded potential to the Fc/Fc^+ scale in order to eliminate solvent's influence on the Li/Li^+ redox potential.[5] As is quite apparent from Fig. 1, three groups of distinct CV patterns were observed which can be categorized based on (i) the number of oxidation and reduction peak, and (ii) the peak separation of the reduction peaks. **Group 1:** CVs recorded in DMSO, DMF, and DMA largely resemble each other and are consistent with the CVs reported in literature (DMSO,[15,19] DMF,[20] DMA),[19] having three oxidation peaks and two reduction peaks with large peak separation ($\Delta E > 500$ mV, see Figs. 1a–1c, CVs in blue). **Group 2:** CVs recorded in DME, DOL:DME (1:1,v:v), TEGDME, ACN, and TMS, showing only one oxidation peak and two reduction peaks with small peak separation ($\Delta E \approx 200$–300 mV, see Figs. 1d–1h, CVs in red). The 2nd reduction peak in DOL:DME is less clear at 50 mV/s but is quite pronounced at a slow scan rate of 5 mV/s (Fig. 2c). **Group 3:** The CV recorded in Diox:DME (1:1, v:v) shows only one oxidation peak and only one reduction peak (see Fig. 1i, CV in green), which is consistent with CV collected at a slow scan rate of 5 mV/s as indicated in Fig. S1.

Several studies have reported similar results for DOL:DME,[5,10] DME[19] and ACN,[19] while to the best of our knowledge CVs on a planar carbon electrode in TEGDME, TMS, and Diox:DME are not available in the literature. Qualitatively, we attribute the Group 1 to high-DN solvents, and Groups 2 and 3 to low-DN solvents. Although the solvents in Group 1 exhibit high values of DN, ε, and AN, we propose that actually DN would be the primary descriptor instead of ε or AN, because ACN which has a high ε and a high AN belongs to Group 2 and thus no trend can be established using ε or AN. We note that, Diox:DME (1:1, v:v) in Group 3 not only has a low DN but also the lowest dielectric constant ε (≈4, roughly estimated based on the work of Hall et al.)[21] among all solvents. It is known that a solvent (mixture) with a dielectric constant approaching one would lead to an incompletely salt (charges) dissociation.[22] Therefore, in group 3, the anion (polysulfide) is believed to strongly associate with cation and consequently, it would have less interaction with solvent molecules. That is, solvent molecules would have less impact on polysulfide stability via dipole-ion interaction (AN, DN) compared to it in a highly dissociated system. In addition to these CV classifications, we will further examine the correlations between each solvent property (ε, AN, DN) and (i) the onset potential of S_8-reduction, and (ii) the reversibility of the 2nd oxidation peak.

The onset potential of S_8-reduction vs. AN of the solvent.—A positive correlation was found between the onset potential of S_8-reduction and the AN of solvents (Fig. 2a), i.e. the higher the AN of the solvent, the higher the onset potential of S_8-reduction. The onset potentials of S_8 reduction were taken from the 1st derivative of the current density

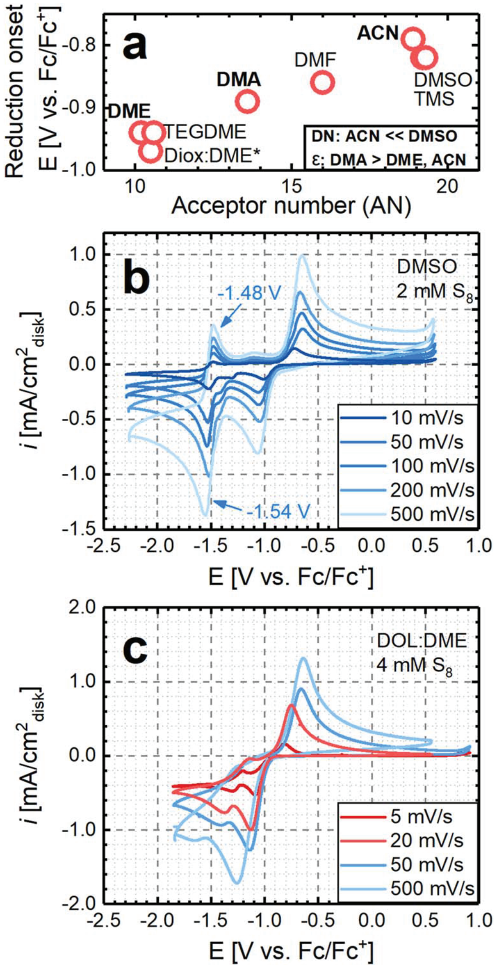

Figure 2. a) Correlation between acceptor number and the onset potential for the reduction of S_8 in different solvents (obtained from the CVs in Fig. 1 using a procedure outlined in Fig. S2), with the inset comparing the DN and the dielectric constant for selected solvents. Only eight solvents are shown in Fig. 2a, as no acceptor number for DOL is available in literature; b) iR-corrected CVs of a GC electrode in 1 M LiTFSI in DMSO with 2 mM S_8 at various scan rates (the peak potentials at 500 mV/s of the 2nd redox pair are marked); c) iR-corrected CVs of a GC electrode in 1 M LiTFSI in DOL:DME (1:1, v:v) with 4 mM S_8 at various scan rates.

(Fig. S2). The acceptor number was introduced by Mayer et al.,[23] seeking to empirically describe the electrophilic property of a solvent. The acceptor number is generally derived from ^{31}P-NMR measurements of triethylphosphine oxide dissolved in the respective solvents and is considered as an indicator for the ability of the solvent to solvate anions. The first step of S_8-reduction is generally agreed to be the reduction of elemental S_8 to S_8^{2-}:[5,10,15,24,25]

$$S_8 + 2e^- \rightarrow S_8^{2-} \tag{2}$$

The solvation energy of the S_8^{2-} anion in high-AN solvents is greater than that in low-AN solvents due to the stronger electrophilic property of the high-AN solvents, which leads to a more positive reduction potential of S_8 to S_8^{2-} in high-AN solvents than in low-AN solvents (see. Equation 3).

$$E \sim f\left(E^\circ + \frac{RT}{nF} lnK\right) \sim f\left(\Delta G^\circ\right) \sim f$$
$$\left(solvation\ energy\ of\ anion\ \left(e.g.\ S_8{}^{2-}\right)\right) \sim f\left(AN\right) \tag{3}$$

Our observation is consistent with Mayer et al.,[23] showing that the AN of the solvent influences the half-wave potential (polargarphic) of the reduction of $[Bu_4N]_3[Fe(CN)_6]$ (tetrabutylammonium hexacyanoferrate), which can also be rationalized using Equation 3.

The reversibility of the 2nd oxidation peak vs. DN of the solvent.—It is clear from Fig. 1 that the second redox pair (at ≈−1.5 V_{Fc}) is more reversible in solvents with high DN (e.g. DMSO, DMA, DMF, see Figs. 1a–1c, blue CVs) and appears irreversible in solvents with low DN (e.g. DME, DOL:DME, TEGDME, TMS, ACN, and Diox:DME). Note that there is no ambiguity between DN and dielectric constant, as this redox pair is irreversible in ACN (low DN, high ε). Due to the limited sample size and the inaccuracy of DN describing the solvation ability of solvent to Li^+, it is not our intention to draw a linear correlation between DN and CV features. One is only able to qualitatively couple CV features such as oxidation peak number and reduction peak separation with the range of DN of the solvent, *rather* than with other properties such as AN and dielectric constant. Taking DMSO (high DN) as an example, the second redox couple exhibits a one-electron reversible process, as evidenced from the scan rate independent peak separation of ≈60 mV (Fig. 2b).[26] The assignment of the 2nd redox pair in DMSO has been extensively discussed in the literature. After the 1st reduction peak, during which S_8 is electrochemically reduced, other polysulfides are generated by disproportionation reactions as described in Equations 4, 5 and 6.[15,25,27,28]

$$S_8 + 2e^- \rightarrow S_8^{2-} \tag{4}$$

$$S_8^{2-} \leftrightarrow S_6^{2-} + \frac{1}{4} S_8 \tag{5}$$

$$S_6^{2-} \leftrightarrow 2S_3^{\bullet -} \tag{6}$$

The 2nd redox pair has been assigned to the electrochemical reduction and oxidation reaction between $S_3{}^{\bullet -}/S_3{}^{2-}$,[28–30] as shown in Equation 7.

$$S_3^{\bullet -} + e^- \rightarrow S_3^{2-} \tag{7}$$

Zou et al.[10] have applied operando UV-Vis spectroscopy to show that the UV-Vis absorbance of $S_3{}^{\bullet -}$ (620 nm) decreases significantly as the electrode potential goes below ∼−1.5 V_{Fc} and increases drastically as soon as the electrode potential reverses, suggesting that the $S_3{}^{\bullet -}/S_3{}^{2-}$ redox process is relatively reversible. This is consistent with our observation of a fast and reversible 2nd redox peak observed in DMSO (Fig. 2b).

In contrast, the oxidation reaction of the 2nd redox pair is much less reversible in low-DN solvents, resulting in a less visible oxidation peak (Figs. 1d–1h). In addition, the potential of the 2nd reduction peak shifts strongly with scan rate in a low-DN solvent like DOL:DME (Fig. 2c), indicating the irreversibility of the 2nd redox process. Interestingly, the related oxidation peak can be clearly observed at the slow scan rate of 5 mV/s (located at −1.15 V_{Fc}, see Fig. 2c), indicating that the oxidation process exhibits sluggish electrode kinetics rather than poor chemical stability. The 2nd redox pair in DOL:DME has been assigned to the reduction of $S_4{}^{2-}$ based on the decreasing UV-Vis absorption at 420 nm ($S_4{}^{2-}$).[10] However, no increase of absorbance at other wavelength was observed in the operando UV-Vis study.[10] This suggests that $S_4{}^{2-}$ is electrochemically reduced to form species that are UV-Vis inactive (e.g. solid), which can be generalized to[10,11,14,31]

$$S_4^{2-} + ne^- + mLi^+ \leftrightarrow Li_2S_2/Li_2S \tag{8}$$

In addition, considering the sluggish kinetics observed in low-DN solvents, we believe that this redox pair involves the formation of solid phases such as Li_2S_2/Li_2S from $S_4{}^{2-}$. Consistent behavior was also observed in other solvents (Fig. S3), showing that the 2nd oxidation peak is much more visible/reversible in high-DN solvents, e.g. DMF (DN = 26.6) and DMA (DN = 27.8), compared to low-DN solvents, e.g. ACN (DN = 14.1).

In addition to the CV analyses, we also exploited the rotating ring disk electrode technique to investigate the kinetics and Li-S reaction

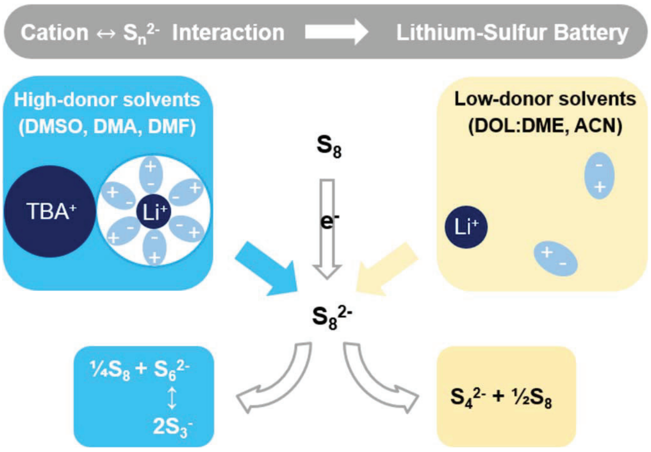

Scheme 1. Summary of how polysulfide stability/speciation is affected by its interaction with cations and solvent molecules.

mechanism in various electrolytes, as we had done previously for DMSO and DOL:DME-based electrolytes.[5] We observed that electrolytes with high-DN solvents and electrolytes with TBA^+ cation (a strongly solvating cation) have always two well-defined reduction plateaus, among which the 1st reduction wave was always accompanied with an electron transfer of ~1.7 e^-/S_8, estimated by applying the Levich-equation (see Fig. S4). This suggests a two-electron reduction of S_8 to S_8^{2-} (Eq. 3), indicating S_8^{2-} is more stabilized in such electrolyte environments, that is, with high-DN solvent and/or with strongly solvating cation (TBA^+).[5,32]

Other CV analyses such as peak current evaluation using the Randle-Sevcik equation are further illustrated in the supporting information (Fig. S5 and S6). The parameters used in the Levich equation for the analysis of the RRDE data, which are also useful for numerical modeling of Li-S batteries (e.g. the diffusion coefficient of dissolved S_8 in various electrolytes) are presented in the supporting information (Table S2). In short, two clear correlations between solvent properties and CV features were identified: 1) the onset potential of the first S_8-reduction peak increases with increasing AN, and 2) the reversibility of the second oxidation peak increases with increasing DN, owing to the formation of soluble polysulfides, rather than solid phase polysulfides, in high-DN solvents.

Why the donor number is the primary descriptor for polysulfide redox chemistry?—Here we employ UV-Vis spectroscopy to examine the polysulfide stability in different solvents and we show that the stability of various polysulfides (S_n^{2-}) is mainly dictated by the solvated cations, which can be manipulated by solvent donor number (DN), cation concentration, and the cation type (Li^+, TBA^+), as illustrated in Scheme 1.

Effect of solvent donor number.—Fig. 3a shows the UV-Vis spectra of a 5 mM concentration of polysulfides with a nominal stoichiometry of "Li_2S_8" in nine different solvents with 1 M LiTFSI. Clearly, high-DN solvents (blue lines labeled g-i) all have a strong absorption at 620 nm (corresponding to $S_3^{\bullet -}$), 475 nm (S_6^{2-}), 492 nm (S_8^{2-}), and 350 nm (S_6^{2-}),[10,13,15,16,25] while low-DN solvents (red lines labeled a-f) all have similarly pronounced absorption maxima at 420 nm (S_4^{2-}) without any absorption at 620 nm ($S_3^{\bullet -}$). We note that TEGDME with lower DN of 16.6 has a higher absorption at 620 nm compared to DME (DN ≈ 20 or 24), which can be explained by 1) the chelate effect, the known cage structure formed by TEGDME that can better solvate Li^+ cation[33,34] and 2) that donor number, an empirical parameter derived from the solvation of $SbCl_5$, cannot fully represent the solvation of Li^+.[35] The distinct speciation of polysulfides in different solvents are consistent with the literature and can be well explained by the Pearson´s Hard Soft Acid Base (HSAB) theory.[36] The Li ions solvated in high-DN solvents (strongly solvated Li^+, soft acid) preferentially stabilize polysulfides with lower charge density (softer base, e.g. S_8^{2-}, S_6^{2-}, $S_3^{\bullet -}$), whereas the Li ions solvated in low-DN solvents (poorly solvated Li^+, hard acid) preferentially stabilize polysulfides with higher charge density (harder base, e.g. S_4^{2-}). Here, we compare the hardness/softness (i.e. charge density) of different polysulfides based on reported theoretical studies. Both Steudel et al.[37] and Pascal et al.[38] have calculated the charge density of terminal and in-chain sulfur atoms in different polysulfides (summarized in Fig. S7). Although Steudel et al.[37] have focused their work on sodium-sulfur system at elevated temperature (600 K), their calculations were also conducted at 298 K to address the structure and atomic charges of isolated polysulfide dianions and anion radicals at 298 K. It was reported that regardless of the assumed nature of the continuum medium (e.g. vacuum or polarizable continuum model with dielectric constants 8 and 78), the negative charge density of terminal sulfur atoms in S_x^{2-}-chains decreases in the following order

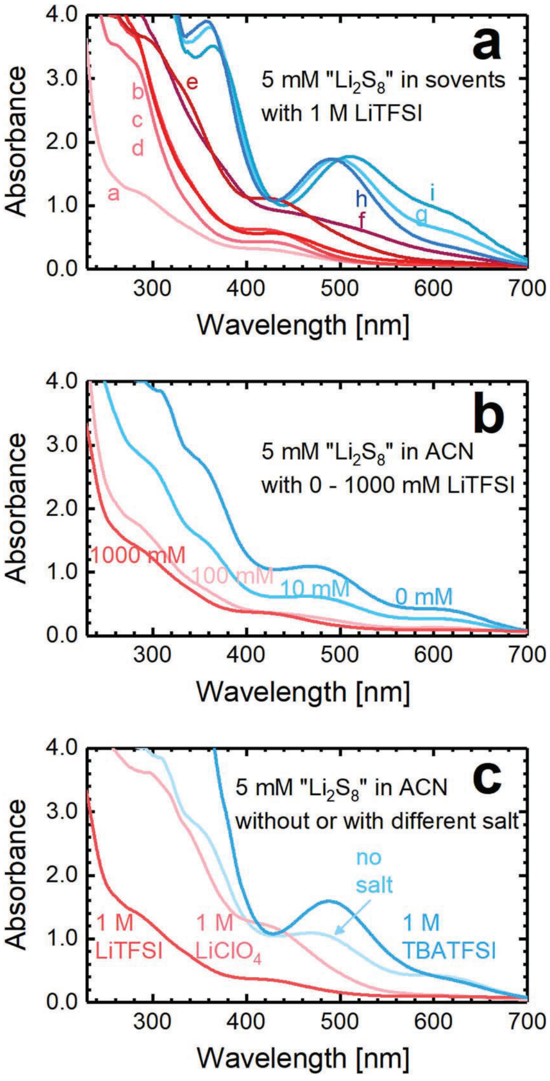

Figure 3. Ex-situ UV-Vis spectra of various electrolytes with a 5 mM concentration of polysulfides with a nominal stoichiometry of "Li_2S_8" with different conductive salts and salt concentrations. a) UV-Vis spectra in the presence of 1 M LiTFSI in nine different solvents: six low-DN solvents, namely (a) ACN (incompletely dissolved "Li_2S_8"), (b) DME, (c) DOL:DME (1:1, v:v), (d) Diox:DME (1:1, v:v), (e) TMS, (f) TEGDME, as well as three high-DN solvents, namely (h) DMSO, (i) DMA, and (g) DMF. b) UV-Vis spectra in ACN with different concentration of LiTFSI or without LiTFSI: 0 mM (blue), 10 mM (light blue), 100 mM (light red), and 1000 mM (red). c) UV-Vis spectra in ACN without added salt or with different salts: 1 M TBATFSI (blue), no added salt (light blue), 1 M $LiClO_4$ (light red), and 1 M LiTFSI (red).

$S_2^{2-} > S_3^{2-} > S_4^{2-} > S_5^{2-} > S_6^{2-} > S_7^{2-} > S_8^{2-}$; in addition, it was calculated that that the negative charge density of $S_3^{\bullet-}$ would be even lower than that reported for S_8^{2-} (see comment to Fig. S7 in the SI).[37,38] Similar trend was also reported by Pascal et al.,[38] who calculated the average valence electron populations for the internal and terminal sulfur atom of Li_2S_x in a 12 TEGDME molecule environment (see Fig. S7). Although the absolute value of the negative charge density is different in different studies and also depends on the assumed surrounding continuum (see Fig. S7), the overall trend is still the same in all studies, namely that short-chain polysulfides (e.g. S_4^{2-}) have a higher negative charge density on the terminal sulfur atoms than that in long-chain polysulfides (e.g. S_8^{2-}) and in the $S_3^{\bullet-}$ radical. In other words, the negative charge is more strongly delocalized on long-chain polysulfides (S_8^{2-}) and on $S_3^{\bullet-}$ radicals compared to that on short-chain polysulfides (S_4^{2-}), which in turn implies that the softness of polysulfides decreases in the following order: $S_3^{\bullet-} > S_8^{2-} > S_6^{2-} > S_4^{2-} > S_3^{2-} > S_2^{2-}$. Therefore, the S_4^{2-} polysulfide (harder base) is better stabilized by weakly solvated Li^+ (hard acid) prevalent in low-DN solvents, whereas $S_3^{\bullet-}$, S_8^{2-}, and S_6^{2-} (softer base) are better stabilized by strongly solvated Li^+ (soft acid) prevalent in high-DN solvents.

To confirm that the polysulfide stability is mainly affected by donor number rather than by the dielectric constant (ε)[5,16] or the acceptor number (AN), we further investigated the polysulfide speciation in a rather unique solvent (ACN) which has a low donor number (DN = 14.1, similar as TEGDME) but high dielectric constant (ε = 36) and acceptor number (AN = 18.9) which are close to those of DMSO (which, however, has also a very high DN; see Table S1). In Fig. 3a, we show that the speciation of polysulfides in ACN resembles that in the low-DN system (TEGDME) despite ACN has a completely different ε and AN compared to TEGDME. This clearly suggests that dielectric constant and acceptor number are not the critical parameters governing polysulfide stability/speciation in the presence of a high concentration of Li^+ cations.

Effect of Li^+ concentration.—In contrary to our results, Bieker et al.[16] reported that the UV-Vis spectrum of a nominal "Li_2S_8" stoichiometry in ACN resembles that of "Li_2S_8" in DMSO, and it was thus concluded that ε is the primary descriptor for polysulfide stability/speciation rather than DN. After careful analysis, we believe this discrepancy is related to a difference in the Li^+ concentration. In our work, 1 M LiTFSI was added to the 5 mM "Li_2S_8" dissolved in ACN to mimic the practical Li-S battery environment, whereas no additional salt was used for the preparation of the 1 and 10 mM "Li_2S_8" containing ACN solution in the work by Bieker et al.[16] To resolve this question, we evaluated UV-Vis spectra of 5 mM "Li_2S_8" in ACN with different concentrations of LiTFSI and without added LiTFSI (Fig. 3b). The sample of "Li_2S_8" in ACN without added LiTFSI salt (light blue) indeed shows a similar spectrum as "Li_2S_8" in DMSO (line h in Fig. 3a), with a high absorption at 620, 475, and 350 nm, quite analogous to what was reported by Bieker et al.[16] On the other hand, the solution of "Li_2S_8" in ACN with 1 M LiTFSI presents a similar absorption spectrum as "Li_2S_8" in low-DN TEGDME and DOL:DME, with a pronounced absorption maximum at 420 nm. This experiment confirms our hypothesis that the Li^+ concentration is responsible for the apparent discrepancy between our data and those by Bieker et al.[16] We believe that when no additional "naked" Li^+ is present, soft polysulfides (e.g. $S_3^{\bullet-}$) can be stabilized by the surrounding ACN molecules owing to the high charge accepting ability of ACN (high AN of 18.9). That is, at extremely low cation concentrations, the stability of polysulfides is governed by the solvent molecules via dipole-anion interaction (solvent – S_n^{2-}), instead of the cation-anion interaction ($Li^+(\text{solvents})_n$ – S_n^{2-}). However, with increasing Li^+ concentration, the number of "naked" Li^+ (hard acid) increases and the influence of the cation on polysulfide stability becomes significant, which shifts the equilibrium to stabilize hard polysulfides (e.g. S_4^{2-}). As shown in Fig. 3b, with increasing Li^+ concentration (0 M → 1 M), the absorption at 620 nm ($S_3^{\bullet-}$) and at 475 nm (S_6^{2-})/492 nm (S_8^{2-}) decreases gradually, while the absorption at 420 nm (S_4^{2-}) increases. This experiment confirms our hypothesis and resolves the apparent discrepancy in the literature with regards to the speciation of polysulfides in ACN solvent.

Recently, several research groups have proposed a sparingly solubilizing electrolyte system for Li-S batteries,[4,39,40] aiming to limit the concentration of polysulfides on the order of 1 mM or less by occupying most of the solvent molecules with supporting salt, leaving none left to coordinate to polysulfide molecules.[4] In addition, a high concentration of Li-salts are required to achieve sparingly solubilizing electrolyte such as $ACN_2LiTFSI$-TTE[39] and ACN_2-LiTFSI–HFE.[40] We have learned from Fig. 3b that more "naked" Li^+ in the system will shift the polysulfides equilibrium to the one with higher charge density, namely shorter chain polysulfides (e.g. S_4^{2-}). Although the solvation state of polysulfides are likely different in sparingly solubilizing electrolytes, the impact of Li^+ cation on the polysulfide stability/speciation may still apply, that shorter chain polysulfides are preferably promoted by the cation-anion interaction in a highly concentrated electrolyte.

Effect of cation type.—To further show that cations can very strongly affect polysulfide speciation, we replaced the 1 M Li^+ cations (a hard acid) with 1 M TBA^+ cations (a soft acid regardless of solvent)[41] in the solution of "Li_2S_8" in ACN. As shown in Fig. 3c, the spectrum of "Li_2S_8"in ACN-TBATFSI resembles that in DMSO with 1 M LiTFSI (line h in Fig. 3a) where long-chain polysulfides are clearly dominating (e.g. 620 nm ($S_3^{\bullet-}$), 475 nm (S_6^{2-}), 492 nm (S_8^{2-})). This further confirms that large concentrations of cations and their type will affect the speciation of polysulfides.

Li-S cell charge/discharge behavior in two-compartment cells.—To further distinguish the impact of donor number, dielectric constant, and acceptor number on the charge/discharge behavior of Li-S cells, we employ a two-compartment cell with a lithium metal anode and a cathode either based on a dissolved S_8 containing catholyte or based on a solid S_8/C composite cathode. The two-compartment cell is a closed system that confines polysulfides in the cathode and allows full reactions (long reaction time in hours), whereas CV and RRDE were conducted in an open system where polysulfides are freely to diffuse in a large amount of electrolyte (short reaction time in seconds). With this, we evaluate the Li-S cell behavior in ACN (DN = 14.1, ε = 35.95, AN = 18.9) and compare it first to that in DMSO (DN = 29.8, ε = 46.5, AN = 19.3) and then to that in commonly used electrolyte DOL (DN = 18, ε = 7.13):DME (DN = 24, ε = 7.1, AN = 10.2).

Figs. 4a and 4b show the voltage profiles of the catholyte (0.5 mM S_8) two-compartment cell in ACN (green) and DMSO (blue) at 0.5C and 2.9C (based on 1672 $mAh/g_s \equiv 1C$). Despite the fact that ACN and DMSO exhibit very similar dielectric constant and acceptor number, the catholyte two-compartment cell voltage profiles and discharge/charge potentials in ACN are significantly different from that in DMSO. The voltage plateau separation in the two-compartment cell is found to be well-correlated to the separation of the reduction peaks in cyclic voltammograms (Fig. 1). The significantly different voltage profiles observed in DMSO and ACN cannot be explained by their almost identical dielectric constant and acceptor number, but can be correlated to their differences in DN (ACN (14.1) vs DMSO (29.8)) as already discussed above. Consistently, DMSO-alike voltage profiles were also reported for other high-DN solvents, such as DMA (DN = 27.8)[11] and DMF (DN = 26.6).[10]

In contrast, the cell voltage profiles with ACN based electrolyte is very similar to that in the low-DN solvent DOL:DME (average DN ~20). Even using conventional S_8/C composite cathodes (albeit with relatively low loadings of 0.25–0.6 mg_s/cm^2), the voltage profiles obtained in ACN and DOL:DME based electrolytes are still very similar (Fig. 4c; note that the larger hysteresis for high-loaded sulfur electrodes is due to the higher current densities in this case, as the C-rate is kept constant). Therefore, we conclude that the donor number – governing the effective charge density of the solvated cation (Li^+) – is the primary descriptor determining the voltage profile (reaction potentials and peak separations) of Li-S batteries via dictating the speciation of polysulfides in different electrolytes. Similar findings were also reported by Schneider et al.,[42] who observed distinctly different cell voltages in different solvents and attributed this to the considerably stronger solvation effect for small and hard lithium ions

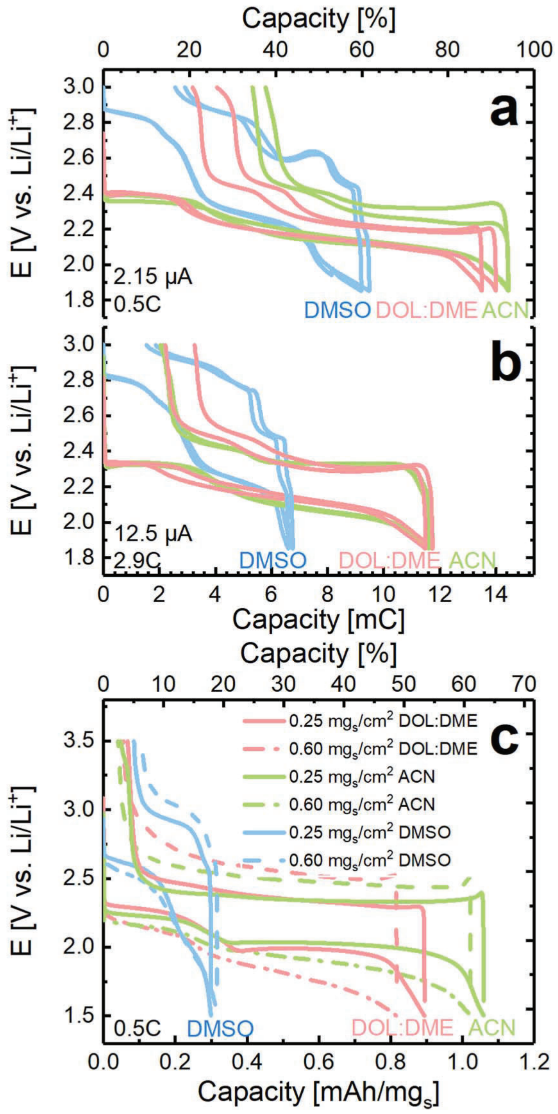

Figure 4. Galvanostatic discharge/charge profiles of sulfur cathodes either based on dissolved sulfur or based on an S_8/C composite, recorded in a two-compartment cell where anode (metallic lithium) and cathode are separated by a lithium ion conducting glass membrane. a) Charge/discharge at 2.15 μA (≡ 0.5C) and b) at 12.5 μA (≡ 2.9C) of a Li−S catholyte cell with a cathode based on a carbon fiber paper filled with 20 μL of 0.5 mM S_8 (corresponding to a theoretical capacity of 15.4 mC) and 0.6 M LiTFSI with various solvents: DOL:DME (1:1, v:v) in red, ACN in green, and DMSO in blue (anolyte in all cases: 0.6 M LiTFSI in DOL:DME (1:1, v:v)). c) Galvanostatic discharge/charge profiles of S_8/C composites (sulfur loadings are given in the figure) at 0.5C with 1.5 M LiTFSI containing catholytes: DOL:DME (1:1, v:v) in red, ACN in green, and DMSO in blue (anolyte in all cases: 1.5 M LiTFSI in DOL:DME (1:1, v:v)).

(indicated by the DN) compared to that for the polysulfide anions (indicated by AN).

Lastly, the discharge capacity achieved in ACN is similar to that of DOL:DME, which is higher than it is in DMSO. However, the discharge capacity of Li-S cells in DMSO is also much lower compared to that in other high-DN solvents such as DMF[10] and DMA[11] measured under comparable conditions. Therefore, we believe that the limited discharge capacity in DMSO is related to its high viscosity (1.99 cp)[18] compared to that of other solvents DMF (0.79 cp),[18] DMA (0.93 cp),[18] ACN (0.34 cp),[18] and DOL:DME (average ∼0.5 cp),[18] which significantly reduces the mobility of Li^+ cations and soluble polysulfides and thus limits the growth of solid lithium sulfide in the electrode. Based on our observations, solvent viscosity show limited effect on polysulfide stability/speciation and the electrochemical redox behavior. Despite TMS (∼10.07 cp)[18] has a much higher viscosity than ACN (∼0.34 cp),[18] they both have shown similarity in redox behavior i.e. CV features (Figs. 1g, 1h, oxidation/reduction peak numbers, reduction peak separation, reduction onset potential and the reversibility of 2nd oxidation peak) and polysulfide stability/speciation represented by UV-Vis spectra (Fig. 3a). We believe that viscosity mainly affects the transport behavior of polysulfide, which has great importance to the cell performance, such as rate capability (shown in Fig. 4) and ohmic resistance affecting energy efficiency. On the other hand, the polysulfide stability/speciation is determined by the cation-anion interaction and the dipole-anion interaction. In the nine solvents investigated, we observed that the cation-anion interaction has a stronger impact on the polysulfide stability over dipole-anion interaction. Therefore, we propose donicity would be the primary descriptor (but not the only one) determining the redox behavior of polysulfides in a well dissociated electrolyte system (reasonable dielectric constant required), and acceptor number can also regulate the redox pair, as exemplified by its influence on reduction onset potential (Fig. 2a).

In addition to solvent and the concentration of salt, the type of anions has been shown to influence the sulfur redox pair, as anions with different donicity may also contribute to the coordination of Li^+.[43–45] For instance, Watanabe and co-workers[43] have shown a strong anionic effects on polysulfide solubility in solvate ionic liquid electrolytes, which is directly related to polysulfide shuttling. Furthermore, a strong influence of anions on the reaction intermediates were reported in the $Li\text{-}O_2$ system where NO_3^- with higher donicity is believed to assist the solvation of Li^+, resulting in an increased capacity and toroid formation.[46] Efforts in understanding anion effect in Li-S redox chemistry and cell behavior are on-going and will be reported in future work.

Conclusions

In summary, we study the correlation between solvent property and Li-S redox chemistry in nine nonaqueous electrolyte solvents that cover a wide range of dielectric constant (ε), donor number (DN) and acceptor number (AN). We reveal that the potential of the S_8/S_8^{2-} redox process increases with increasing AN of the solvent, which could be attributed to a higher solvation energy of S_8^{2-} in high-AN solvents. We show that the donicity of the solvent (expressed in donor number, DN) is the primary solvent property controlling polysulfide redox reactions, as it dictates the effective charge density of the solvated cation (Li^+), which affects the stability and thus the speciation of the various polysulfides via Pearson's Hard Soft Acid Base theory. The commonly encountered discrepancy in the literature on the role of dielectric constant and donor number is addressed by examining the redox reactions and the polysulfide speciation as function of salt concentration and type in acetonitrile, a solvent with high dielectric constant and low donor number. Our study shows that the interaction between the cation-complex with the polysulfide anions is the most critical factor controlling the sulfur/polysulfide redox reactions and the polysulfide speciation (Scheme 1), which can be tailored via the donicity of the solvent (DN) as well as via the concentration and the type of cations in the sulfur-based rechargeable batteries.

Acknowledgments

The German Federal Ministry for Economic Affairs and Energy is acknowledged for funding under the auspices of the "LiMo" project (funding number 03ET6045D). Y. Gorlin gratefully acknowledges the support of the Alexander von Humboldt Postdoctoral fellowship and Carl Friedrich von Siemens Fellowship Supplement.

ORCID

Yelena Gorlin https://orcid.org/0000-0002-9242-8914
Yi-Chun Lu https://orcid.org/0000-0003-1607-1615

References

1. M. Barghamadi, A. S. Best, A. I. Bhatt, A. F. Hollenkamp, M. Musameh, R. J. Rees, and T. Rüther, *Energy Environ. Sci.*, **7**, 3902 (2014).
2. S. Zhang, K. Ueno, K. Dokko, and M. Watanabe, *Adv. Energy Mater.*, **5**, 1500117 (2015).
3. D. Eroglu, K. R. Zavadil, and K. G. Gallagher, *J. Electrochem. Soc.*, **162**, 982 (2015).
4. L. Cheng, L. A. Curtiss, K. R. Zavadil, A. A. Gewirth, Y. Shao, and K. G. Gallagher, *ACS Energy Lett.*, **1**, 503 (2016).
5. Y.-C. Lu, Q. He, and H. A. Gasteiger, *J. Phys. Chem. C*, **118**, 5733 (2014).
6. D. Zheng, G. Wang, D. Liu, J. Si, T. Ding, D. Qu, X. Yang, and D. Qu, *Adv. Mater. Technol.*, **3** (2018).
7. Y. Chen, H. Zhang, W. Xu, X. Yang, Y. Yu, X. Li, and H. Zhang, *Adv. Funct. Mater.*, **28**, 1 (2018).
8. G. Zhang, H.-J. Peng, C.-Z. Zhao, X. Chen, L.-D. Zhao, P. Li, J.-Q. Huang, and Q. Zhang, *Angew. Chemie Int. Ed.*, 1 (2018).
9. Z. Li, Y. Zhou, Y. Wang, and Y. C. Lu, *Adv. Energy Mater.*, **1802207** (2018).
10. Q. Zou and Y.-C. Lu, *J. Phys. Chem. Lett.*, **7**, 1518 (2016).
11. Y. Gorlin, A. Siebel, M. Piana, T. Huthwelker, H. Jha, G. Monsch, F. Kraus, H. A. Gasteiger, and M. Tromp, *J. Electrochem. Soc.*, **162**, A1146 (2015).
12. T. Chivers and P. J. W. Elder, *Chem. Soc. Rev.*, **42**, 5996 (2013).
13. C. Barchasz, F. Molton, C. Duboc, J. C. Leprêtre, S. Patoux, and F. Alloin, *Anal. Chem.*, **84**, 3973 (2012).
14. M. Cuisinier, P.-E. Cabelguen, S. Evers, G. He, M. Kolbeck, A. Garsuch, T. Bolin, M. Balasubramanian, and L. F. Nazar, *J. Phys. Chem. Lett.*, **4**, 3227 (2013).
15. R. P. Martin, W. H. Doub, J. L. Roberts, and D. T. Sawyer, *Inorg. Chem.*, **12**, 1921 (1973).
16. G. Bieker, J. Wellmann, M. Kolek, K. Jalkanen, M. Winter, and P. M. Bieker, *Phys. Chem. Chem. Phys.*, **19**, 11152 (2017).
17. M. Cuisinier, C. Hart, M. Balasubramanian, A. Garsuch, and L. F. Nazar, *Adv. Energy Mater.*, **5**, 1401801 (2015).
18. D. Aurbach, *Nonaqueous Electrochemistry*, Marcel Dekker, Inc., New York, NY, (1999).
19. Y. Jung, S. Kim, B.-S. Kim, D.-H. Han, S.-M. Park, and J. Kwak, *Int. J. Electrochem. Sci.*, **3**, 566 (2008).
20. F. Gaillard, E. Levillain, and J. P. Lelieur, *J. Electroanal. Chem.*, **432**, 129 (1997).
21. D. S. Hall, J. Self, and J. R. Dahn, *J. Phys. Chem. C*, **119**, 22322 (2015).
22. A. Abbott, *Chem. Soc. Rev.*, **22**, 435 (1993).
23. U. Mayer, V. Gutmann, and W. Gerger, *Monatshefte fuer Chemie*, **106**, 1235 (1975).
24. P. Leghi, J. Lelieur, and E. Levillain, *Electrochem. commun.*, **4**, 406 (2002).
25. R. Bonnaterre and G. Cauquis, *J. Chem. Soc. Chem. Commun.*, **0**, 293 (1972).
26. A. J. Bard and L. R. Faulkner, *Electrochemical Methods Fundamentals and Applications*, 2nd ed., John Wiley & Sons, INC, New York, NY, (2000).
27. T. Fujinaga, T. Kuwamoto, S. Okazaki, and M. Hojo, *Bull. Chem. Soc. Jpn.*, **53**, 2851 (1980).
28. M. Cuisinier, C. Hart, M. Balasubramanian, A. Garsuch, and L. F. Nazar, *Adv. Energy Mater.*, **5**, 1401801 (2015).
29. B.-S. Kim and S.-M. Park, *J. Electrochem. Soc.*, **140**, 115 (1993).
30. J. Paris and V. Plichon, *Electrochim. Acta*, **26**, 1823 (1981).
31. S. Waluś, C. Barchasz, R. Bouchet, J.-C. Leprêtre, J.-F. Colin, J.-F. Martin, E. Elkaïm, C. Baehtz, and F. Alloin, *Adv. Energy Mater.*, **5**, 1500165 (2015).
32. Q. Zou, Z. Liang, G. Du, C. Liu, E. Y. Li, Y. Lu, Q. Zou, Z. Liang, G. Du, C. Liu, E. Y. Li, and Y. Lu, *J. Am. Chem. Soc.*, **140**, 10740 (2018).
33. C. Zhang, A. Yamazaki, J. Murai, J. Park, T. Mandai, K. Ueno, K. Dokko, and M. Watanabe, *J. Phys. Chem. C*, **118**, 17362 (2014).
34. I. Gunasekara, S. Mukerjee, E. J. Plichta, M. A. Hendrickson, and K. M. Abraham, *J. Electrochem. Soc.*, **162**, A1055 (2015).
35. V. Gutmann, *Electrochim. Acta*, **21**, 661 (1976).
36. T.-L. Ho, *Chem. Rev.*, **75**, 1 (1975).
37. R. Steudel and Y. Steudel, *Chem. -A Eur. J.*, **19**, 3162 (2013).
38. T. A. Pascal, K. H. Wujcik, J. Velasco-Velez, C. Wu, A. A. Teran, M. Kapilashrami, J. Cabana, J. Guo, M. Salmeron, N. Balsara, and D. Prendergast, *J. Phys. Chem. Lett.*, **5**, 1547 (2014).
39. C. Lee, Q. Pang, S. Ha, L. Cheng, S. Han, K. R. Zavadil, K. G. Gallagher, L. F. Nazar, and M. Balasubramanian, *ACS Cent. Sci.*, **3**, 605 (2017).
40. M. Cuisinier, P.-E. Cabelguen, B. D. Adams, A. Garsuch, M. Balasubramanian, and L. F. Nazar, *Energy Environ. Sci.*, **7**, 2697 (2014).
41. C. O. Laoire, S. Mukerjee, K. M. Abraham, E. J. Plichta, and M. A. Hendrickson, *J. Phys. Chem. C*, **114**, 9178 (2010).
42. H. Schneider, C. Gollub, T. Weiss, J. Kulisch, K. Leitner, R. Schmidt, M. M. Safont-Sempere, Y. Mikhaylik, T. Kelley, C. Scordilis-Kelley, M. Laramie, and H. Du, *J. Electrochem. Soc.*, **161**, A1399 (2014).
43. K. Ueno, J.-W. Park, A. Yamazaki, T. Mandai, N. Tachikawa, K. Dokko, and M. Watanabe, *J. Phys. Chem. C*, **117**, 20509 (2013).
44. H. Chen and Y. C. Lu, *Adv. Energy Mater.*, **6**, 1 (2016).
45. H. J. Peng, J. Q. Huang, X. Y. Liu, X. B. Cheng, W. T. Xu, C. Z. Zhao, F. Wei, and Q. Zhang, *J. Am. Chem. Soc.*, **139**, 8458 (2017).
46. C. M. Burke, V. Pande, A. Khetan, V. Viswanathan, and B. D. McCloskey, *Proc. Natl. Acad. Sci.*, **112**, 9293 (2015).

Supplementary Information

Unraveling the correlation between solvent properties and sulfur redox behavior in lithium-sulfur batteries

Qi He,[†#] Yelena Gorlin,[†a] Manu U. M. Patel,[†] Hubert A. Gasteiger,[†] and Yi-Chun Lu[††*]

[†]Chair of Technical Electrochemistry, Department of Chemistry and Catalysis Research Center, Technical University of Munich, Munich, Germany

[††]Electrochemical Energy and Interfaces Laboratory, Department of Mechanical and Automation Engineering, The Chinese University of Hong Kong, Hong Kong SAR, China

[a] Present Address: Research and Technology Center, Robert Bosch LLC, California, USA

Email: [#]qi.he@tum.de; [*]yichunlu@mae.cuhk.edu.hk;

Experimental Section

Chemicals

Anhydrous dimethyl sulfoxide (DMSO, Sigma Aldrich, 99.7%), dimethylacetamide (DMA, Sigma Aldrich, 99.8%), dimethylformamide (DMF, Sigma Aldrich, ≥ 99.9%), acetonitrile (CAN, Sigma Aldrich, 99.8%), sulfolane (TMS, Sigma Aldrich, 99%), tetraethylene glycol dimethyl ether (TEGDME, Sigma Aldrich, ≥ 99%), 1,3-dioxolane (DOL, Sigma Aldrich, 99.8%), 1,2-dimethoxyethane (DME, Sigma Aldrich, 99.9%), 1,4-dioxane (Sigma Aldrich, 99.8%), and diethyl ether (DEE, Sigma Aldrich, ≥ 99.7%) were dried over Sylobead MS 564C zeolites (3 Å, Grace Division) for a minimum of 72 h. Lithium bis(trifluoromethane)sulfonamide (LiTFSI) was dried under dynamic vacuum in a glass oven (Büchi, Flawil, Switzerland) at 110 °C over 72 h. Elemental sulfur (Sigma Aldrich, 99.98%) was dried under ambient conditions at 75 °C for overnight.

Cyclic voltammetry and rotating ring disk electrode measurement setup/procedures

The nonaqueous CV and RRDE cell configuration used in this study was adopted from that reported by Lu et al. and Herranz et al.[1,2] This RRDE cell consists of a working electrode, a counter electrode, a reference electrode, and a gas bubbler. The working electrode is a 5.0 mm diameter glassy carbon (GC) disk surrounded by a gold ring electrode with an internal diameter of 6.5 mm and an external diameter of 7.5 mm, where both glassy carbon disk and gold ring electrode are imbedded in PTFE (Pine Research Instrumentation, Durham, NC, USA). Prior to its use, the ring disk electrode was polished with a 0.05 µm alumina suspension (Buehler, Düsseldorf, Germany), cleaned by sonication in ultrapure water, assembled onto a PEEK shaft that was fed through a stopper equipped with a ceramic ball-bearing seal (Pine Research Instrumentation, Durham, NC, USA), and then dried for 1 h in an oven at 70 °C. The counter electrode is a platinum wire (99.99 + %, Advent, Oxford, England) sealed with a glass fitting where on one side it sits in a glass tube which is partially filled with electrolyte that is contacted by the Pt wire; the glass tube is terminated by a medium-porosity frit that prevents the diffusion of the species evolved at the Pt counter electrode into the electrolyte in the working electrode compartment.

The reference electrode is a silver wire extending into a glass tube (sealed by a plastic cap), where it contacts a solution of 0.1 M $AgNO_3$ (99.9999% metal basis, Sigma Aldrich) in acetonitrile; towards the working electrode compartment, the solution in the glass tube is sealed with a Vycor 7930 frit (Advanced Glass & Ceramics, Holden, MA). The reference electrode was assembled in the glovebox before putting together the rest of the electrochemical cell and was first partially immersed into a beaker containing the electrolyte of interest, along with a piece of lithium foil (99.9%, Rockwood Lithium, USA) connected to a Ni wire (99.98%, Advent, Oxford, England). The potential difference between both electrodes was subsequently measured for a minimum of 60 min to assure that a stable potential was reached, corresponding to the potential difference of the Ag reference electrode vs. Li/Li$^+$ in the respective electrolyte (referred to furtheron as “V vs Li/Li$^+$” or V_{Li}).

0.5-4 mM of S_8 were dissolved in the electrolytes of interest and stirred overnight. The RRDE working electrode, the platinum wire counter electrode, the reference electrode, and a glass bubbler which allowed direct flow of gas into the solution or blanketing atop of the electrolyte were all assembled inside the glovebox. Once assembled, the electrochemical cell was taken outside of the glovebox, the working electrode rod was mounted onto the rotator, and the bubbler was connected to a gas line constantly fed with argon (6.0 quality, Westfalen-AG, Münster, Germany). This allowed for a constant overpressure inside the cell and prevented contamination from the atmosphere. All subsequent electrochemical measurements were performed using an AFCBP1 bipotentiostat (Pine Research Instrumentation, Durham, NC, USA) controlled with Aftermath software. Prior to the RRDE measurements, ac impedance measurements to determine the ohmic drop between working and reference electrodes were recorded with a potentiostat (BioLogic SP200, Grenoble, France), applying a 10 mV voltage perturbation (1 MHz to 100 mHz) at open circuit. In the resulting Nyquist plots, the high-frequency intersection with the real axis was taken as the uncompensated solution resistance.

Determination of diffusion coefficient using RRDE

The diffusion coefficients of S_8 in different electrolytes were determined using a method established previously for oxygen and oxygen radicals.[2] Briefly, the diffusion coefficient of S_8 were determined by fitting a relation between the inverse of the rotation speed and the transient time in potential-stepping experiments described below. Note that in all potential-stepping experiments, the disk potential was stepped from a defined potential that is close to OCV (no reaction happening) into a potential region where the reduction of S_8 occurs at a significant rate.

For example, the diffusion coefficient of 4 mM S_8 in DOL:DME (1:1, v:v) with 1 M LiTFSI was measured at a constant ring voltage where S_8 was consumed on the ring (for instance at -1.2 V_{Fc}) and stepping the disk voltage from OCV (≈0.8 V_{Fc}) to a potential where S_8 is being reduced on the disk (i.e., -1.2 V_{Fc}). Upon applying the disk potential step, the ring current will sense a sudden drop of S_8 concentration due to the removal of S_8 from the solution caused by the S_8-reduction at the disk. The relationship between the rotation speed (ω) and the transient time (T_s) can be described as $T_s = K\cdot(\upsilon/D)^{1/3}\cdot\omega^{-1}$, where υ is the electrolyte viscosity, ω is the rotation rate, and K is a proportionality constant depending on the RRDE´s geometry: $K = 43.1\cdot[\log(r_2/r_1)]^{2/3}$ (for T_s reported in seconds and ω in rpm).[2] For the RRDE used here, with r_1 = 2.5 mm and r_2 = 3.25 mm, the theoretical value of K is 10.1 rpm·s. We used optical microscopy to measure the actual ring radii, from which K is determined to be 10.34 rpm·s (r_1 = 2.485 mm, r_2 = 3.257 mm). From the measured transient times, the S_8 diffusion coefficients can be calculated (for further details see also Ref. 1)).

UV-Vis spectroscopy measurement

Polysulfide samples with the nominal composition "Li_2S_8" were prepared following the method developed by Rauh. et al.[3] Briefly, lithium sulfide (Sigma Aldrich, 99.98 %, stored in an Ar-glovebox) and sulfur were mixed in an Ar-filled glovebox with magnetic stirring (over 24 h) in various solvents, reacting according to the following nominal reaction equation

$$Li_2S + \frac{7}{8}S_8 \leftrightarrow \ Li_2S_8 \tag{1}$$

Considering the possible water contamination in solvents/salts (ca. 10 ppm, corresponding to a concentration of 0.5 mM), the concentration of the polysulfide samples was chosen to be an order of magnitude higher (5 mM) in order to minimize the possible effect of water impurities. The longer stirring time (> 24 h) is to ensure a complete dissolution of the educts and their reaction to polysulfides, as well as to reach a stable equilibrium for the various polysulfides through chemical disproportionation reactions.

0.35 mL of the prepared polysulfide solution with a nominal composition corresponding to Li_2S_8 were filled into a quartz cuvette with a sealed screw cap (1/ST/C/Q/1 mm, Starna, USA), and UV-Vis spectra were recorded with a UV-Vis spectrometer (Lambda35, Perkin Elmer, USA). The spectra were background corrected by subtracting the spectra of the respective polysulfide free solvents or solvent mixtures.

Two-compartment cell with catholyte electrode

A two-compartment cell was employed to avoid the strong chemical reaction between ACN and lithium metal anode and to prevent any cross-talk between lithium-sulfur catholyte compartment with the lithium anode. This custom-made two-compartment cell uses a lithium ion conducting Ohara glass membrane (LICGC™, 1 inch diameter, 150 µm thick).[4] To completely prevent any cross-talk between anode and cathode, the LICGC™ was laminated by polypropylene und aluminum foils cut to an annulus, as described by Metzger et al.[5] The cells, furtheron also referred to as Li-S catholyte two-compartment cells were assembled in an Ar-filled glovebox in the following order: (1) placing Li metal onto a stainless steel current collector in the cell; (2) adding 120 µL of 0.6 M LiTFSI in DOL:DME (1:1, v:v) onto a glass-fiber separator (Glass microfiber filter 691, VWR, Germany, 21 mm diameter); (3) placing one piece of laminated LICGC™ on top of this separator; (4) adding 20 µL of 0.5 mM S_8 and 0.6 M LiTFSI dissolved in different solvents onto one piece of carbon paper (Toray Paper TGPH030, 15 mm diameter) as cathode on top of the LICGC™ membrane.

The use of the two-compartment cell with a lithium ion conducting but electrolyte-impermeable membrane (LICGC™) eliminates complicating factor when studying the cathode reactions in Li-S batteries, such as the above mentioned reaction of lithium metal with some of the solvents under investigation as well as the diffusion of $LiNO_3$ and polysulfides to the lithium anode, where they can undergo decomposition reactions. In our experiments, we varied only the electrolyte in the cathode compartment, while keeping the same electrolyte (DOL:DME (1:1, v:v) with 0.6 M LiTFSI in the anode compartment (lithium metal) to avoid changes of the lithium potential at the anode.[1] AC impedance spectroscopy was also performed before and after cycling for each measurement in order to quantify the high-frequency resistance of the cell; however, the ohmic potential drop can be neglected in Fig. 4 (amounting to ≈ 1.3 mV at the highest applied current).

Two-compartment cell with a solid sulfur electrode

S_8/C composite preparation: First, a wet impregnation of 1.5 g Vulcan carbon (XC-72, Tanaka Kikinzoku Kogyo) with 120 ml of a 1 M solution of sodium thiosulfate ($Na_2S_2O_3$ $5H_2O$, 99.5%, Sigma-Aldrich) for 10 min was conducted as described in the literature.[6] Afterwards, a 20 min ultrasonic treatment was followed until a well-dispersed, homogeneous suspension was obtained. An excess of 250 ml of 1 M HNO_3 (ACS reagent, Sigma-Aldrich) was added into the suspension, followed by a sonication for 20 min. Subsequently, the supernatant was decanted, washed three times with ultrapure water, and filtered to obtain the sulfur/carbon composite. The obtained composite was dried over silica gel in a Büchi oven at 75 °C for 72 h; the final sulfur content of the S_8/C composite was 67 wt.%, as determined by thermogravimetric analysis.

Electrode preparation: Electrodes consist of 90 wt.% S_8/C composite and 10 wt.% PVDF (polyvinylidene difluoride, HSV900, Kynar). First, PVDF was dissolved in N-Methyl-pyrrolidinone (NMP, 99.5%, anhydrous, Sigma-Aldrich) and then the S_8/C composite was added into this PVDF-NMP solution. After a sequential mixing of the suspension in a planetary centrifugal mixer (Thinky Mixer, Japan), the resulting ink was spread onto a current collector (17 µm thick aluminum foil) using a Mayer rod with different thickness to achieve the desired sulfur loadings of 0.25 mg_{sulfur}/cm^2 and 0.6 mg_{sulfur}/cm^2. The coatings were dried overnight at room temperature and electrodes were punched out with a diameter of 15 mm. Finally, these electrodes were dried under static vacuum at 60 °C for 6 hours.

Two-compartment cell assembly with a solid sulfur electrode and cell testing procedure: Cells were assembled in an Ar-filled glovebox in the following order: (1) placing Li metal onto a stainless steel current collector in the cell; (2) adding 120 µL of 1.5 M LiTFSI in DOL:DME (1:1, v:v) onto a glassfiber separator (21 mm diameter); (3) placing one piece of laminated LICGC™ on top of this separator; (4) placing another piece of a glassfiber separator with a diameter of 16 mm onto the LICGC™ and adding 80 µL of 1.5 M LiTFSI in different solvents onto the separator; (5) placing the S_8/C cathode onto the wetted glass-fiber separator.

In this experiment, we chose a larger potential window (1.5-3.5 V_{Li}) to avoid incomplete discharging/charging behavior caused by the larger potential hysteresis with these relatively high sulfur loadings. Also, we used 1.5 M LiTFSI as supporting electrolytes instead of the conventional salt concentrations of 1 M LiTFSI and 0.5 M $LiNO_{3,}$[7] in order to (1) avoid any additional influence from $LiNO_3$ on the polysulfide stability and (2) exclude the discharge capacity contributed from $LiNO_3$ reduction (below 1.9 V_{Li}),[8] while at the same time keeping the same ionic strength as with conventional electrolytes. The LICGC™ membrane in the two-compartment cell configuration served to prevent S_8/polysulfide depletion on the lithium anode, which would be substantial in the absence of $LiNO_3$.

Solvent properties

The following table lists the dielectric constant, the donor number, and the acceptor number for the various solvents employed in this study.

Table S1: Dielectric constant (ε), Gutmann donor number (DN), and acceptor number (AN) of the solvents used in this study.

Solvent	**Dielectric constant**	**Donor number**	**Acceptor number**
DMSO (Dimethyl sulfoxid)	**46.5**[a]	**29.8**[a]	**19.3**[a]
DMA (N,N-Dimethylacetamide)	**37.8**[a]	**27.8**[a]	**13.6**[e]
DMF (N,N-dimethylformamide)	**36.7**[a]	**26.6** [a]	**16.0**[c]
ACN (Acetonitrile)	**35.9**[a]	**14.1**[e]	**18.9**[a]
TMS (Sulfolane)	**43.3 @30°C**[a]	**14.8**[a]	**19.2**[a]
TEGDME (Tetraglyme)	**7.5**[a]	**16.6**[d] **12±4**[e]	**10.5**[a]
DOL (1,3-dioxolane)	**7.1**[a]	**18.0**[b]	**-**
DME (1,2-dimethoxyethane)	**7.1**[a]	**24.0**[a] **20.0**[f] **19±1**[e]	**10.2**[a]
Diox (1,4-dioxane)	**2.2**[a]	**14.8**[a]	**10.8**[a]
DEE (Diethyl ether)	**4.3**[a]	**19.2**[a]	**3.9**[a]

[a] Aurbach, D. *Nonaqueous Electrochemistry* (CRC Press, 1999).
[b] Jin, Z., Xie, K. and Hong, X., *J. Mater. Chem. A* **1,** 342 (2013).
[c] Izutrsu, K. *Electrochemistry in Nonaqueous solutions* (Wiley-VCH Verlag, 2009).
[d] Laoire, C. O. et al., *J. Electrochem. Soc.* **158,** A302 (2011).
[e] Lutz L. et al., *J. Phys. Chem. C*, **120**, 20068-20076 (2016).
[f] Reichardt, C. *Solvents and solvent effects in organic chemistry* (Wiley-VCH Verlag, 2003).

CV with a slow scan rate (5 mV/s) in Diox:DME (1:1, v:v)

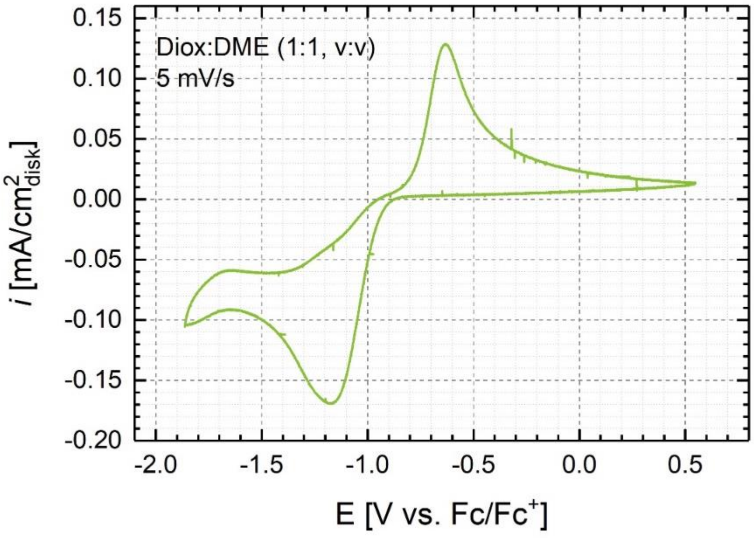

Fig. S1: iR-corrected CV of a GC electrode in 1.5 M LiTFSI in Diox:DME (1:1, v:v) with 4 mM S_8 at scan rate of 5 mV/s.

Determination of the onset potential for S_8 reduction

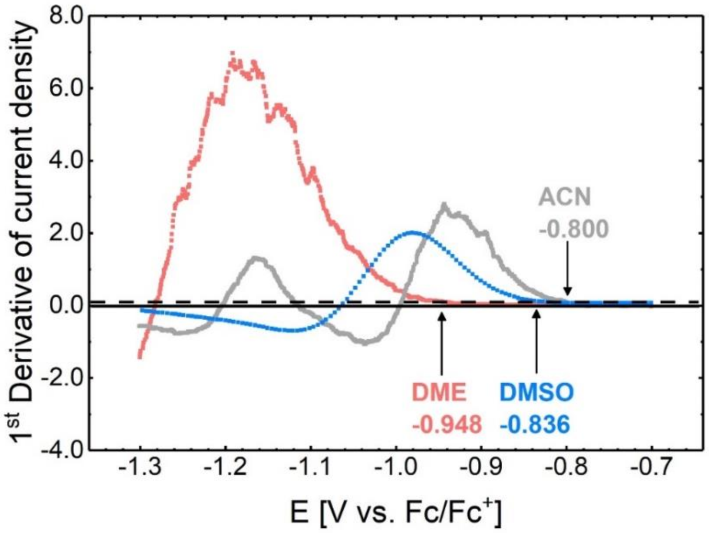

Figure S2: Determination of the onset potential for S_8 reduction in cyclic voltammetry using the 1st derivate of the CVs, shown exemplarily for selected solvents (DMSO, DME, and ACN) for clarity.

As discussed in the main text, the onset potential for S8 reduction in the CVs shown in Fig. 1 was determined by an analysis of the 1st derivative of the first reduction wave.The data used to obtain first derivative $\frac{dy}{dx}$ are from Fig 1, where y (current) has a unit of mA/cm2disk against x (voltage) with a unit of Volt. The value for onset potential were read when the 1st derivate cross the line of y = 0.1 (marked as dash line), where the derivate starts upwards bending, as illustrated by Fig. S2.

CV features vs. scan rate for various additional solvents

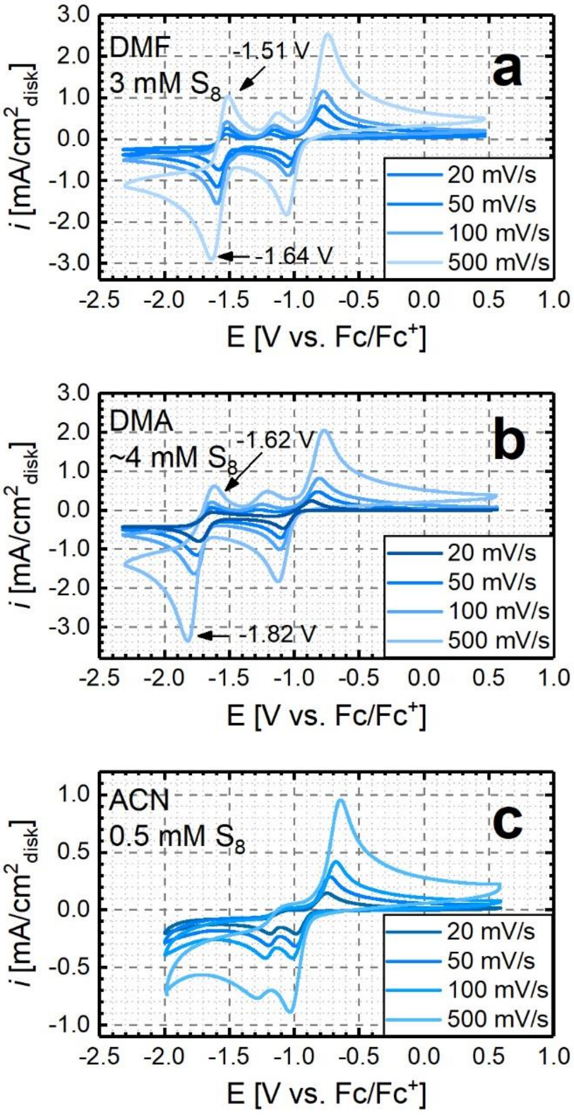

Figure S3: iR-corrected CVs at various scan rates of a GC electrode **a)** in 1 M LiTFSI in DMF with 3 mM S_8, **b)** in 1 M LiTFSI in DMA with ≈4 mM S_8, and **c)** in 1 M LiTFSI in ACN with 0.5 mM S_8. The peak potential at 500 mV/s of the 2nd redox peaks are marked for DMF and DMA based electrolytes.

The same trends for the scan rate dependence in DMSO and DOL:DME (shown in Fig. 2), are also observed in other solvents. In contrast to the CVs in DMF and DMA, the potential of 2nd reduction peak in ACN (Fig.S2c) is much less separated from the 1st reduction peak and it shifts from -1.17 V_{Fc} at scan rate of 20 mV/s to -1.27 V_{Fc} at scan rate of 500 mV/s. In addition, the corresponding oxidation peak for the 2nd redox pair in ACN is less visible (less reversible) as it in DMSO, DMA, or DMF, thus closely resembling the behavior observed in low-DN solvents (e.g. DOL:DME).

RDE analysis of the 1st reduction wave

The following figure shows the number of electrons per S_8 transferred during the first reduction wave, determined by RDE experiments as outlined by Lu et al.[1] The number of electron transferred is estimated from the limiting current (i_{lim}) by applying the Levich-equation, using the parameters listed in Table S2.

$$i_{lim} = 0.62 \cdot n \cdot F \cdot D_{S_8}^{2/3} \cdot A \cdot \upsilon^{-1/6} \cdot c$$

where n is the number of electron exchanged in the electrochemical reaction, F is Faraday´s constant (96485 A·s·mol^{-1}), A is the electrode area (cm^2), c is the dissolved S_8 concentration (mol·L^{-1}), υ is the electrolyte viscosity (cm^2·s^{-1}), and D_{S_8} is the diffusion coefficient of S_8 (cm^2·s^{-1}, obtained using potential-stepping experiments, as described in experimental part).

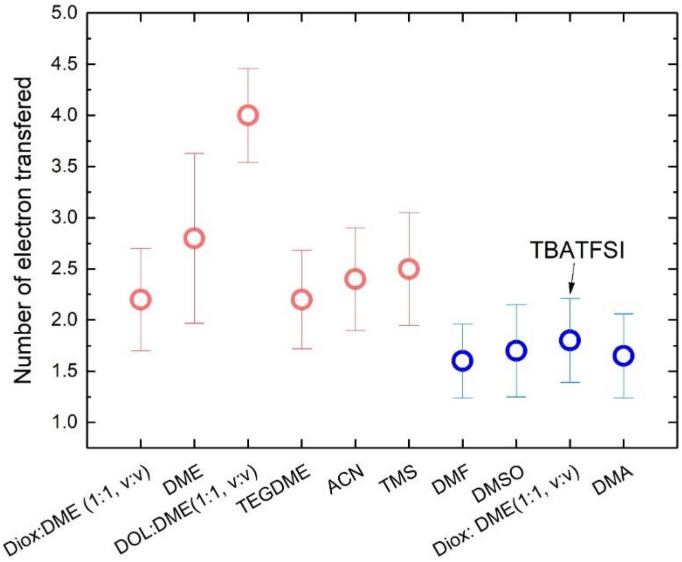

Figure S4: Estimated number of electrons transferred in the 1st reduction plateau in various electrolyte system, obtained from RDE experiments analogous to those conducted by Lu et al.[1] 1 M conducting salt (LiTFSI or TBATFSI) were used, where not specifically indicated, LiTFSI was used.

In order to ensure the high number of electron transferred observed in in DOL:DME(1:1, v:v) is not an artefact of concentration, we repeated the RRDE experiment in DOL:DME with different concentration of dissolved S_8 (2 and 4 mM). Both repeated experiments have shown consistently a higher value of electron transferred in DOL:DME (1:1, v:v) (3.7–3.9 e^-/S_8).

Considering that DOL:DME is a mixture of two solvents, DOL and DME, and that DME exhibits a lower number of electron transfer (2.7 e^-/S_8), we believe that the difference is originated from DOL. To understand the behavior in pure DOL, we conducted a CV/RRDE experiment of 4 mM S_8 in pure DOL with 1 M LiTFSI. Unfortunately, DOL underwent polymerization during the RRDE experiment in the CE (Pt wire) compartment. In addition, after disassembling the RRDE cell, we observed DOL polymerization on the GC WE disk. The polymerization of DOL is consistent with that reported in the literature.[9] Future work on understating how DOL (polymerization) affect polysulfide redox chemistry will provide insight into the high number of electron transferred observed in in DOL:DME(1:1, v:v).

Table S2: Solvent properties, calculated diffusion-limiting current, and calculated number of electrons transferred per S_8 based on a Levich-equation analysis of the limiting current and based on the determined Koutecky-Levich slopes.

							Number of electrons per S_8						
							Levich-equation (limiting current) @400,1600rpm				Koutecky-levich equation		
		Dynamic viscosity (mPa·s)	Kinematic viscosity (cm^2·s^{-1})	S_8 diffusion coefficient (cm^2·s^{-1})	Density (g·cm^{-3})	Conc. (mM)	1st reduction peak		2nd reduction peak		1st	2nd	e# error
							400	1600	400	1600			
ACN	1M LiTFSI	0.95	0.010	1.67E-05	0.95	0.5	1.8 (100 rpm)	2.5	3.3 (100 rpm)	vanished	2.4	vanished	0.5
TMS	1M LiTFSI	31.7	0.232	5.37E-07	1.37	2	2.5	2.8	3.2	vanished	2.5	vanished	0.55
TEGDME	1M LiTFSI	11.4	0.097	1.37E-06	1.17	4	2.0	1.8	3.0	3.0	2.2	3.2	0.48
DioxDME	1M LiTFSI	2	0.018	7.40E-06	1.08	4	2.1	2.1	-	-	2.2	-	0.5
Diox:DME	1M TBATFSI	2.4	0.024	7.14E-06	1.02	4	1.8	1.7	3.0	2.9	1.8	3.2	0.41
DOL:DME (Lu at al.)	1M LiTFSI	1.4	0.013	2.60E-06	1.10	4	4.2	4.3	-	-	4.5	-	0.46
DOL:DME	1M LiTFSI	1.6	0.0146	4.17 E-06	1.09	4	3.7	3.3	-	-	4	-	
DOL:DME	1M LiTFSI	1.6	0.015	3.74E-06	1.08	2	3.9	3.5	-	-	4.5-5.7	-	
DME	1M LiTFSI	1.5	0.014	8.16E-06	1.07	4	2.7	2.4	3.2	vanished	2.8	3.7	0.83
DMSO (Lu et al.)	0.2M LiClO4	2.2	0.020	6.50E-06	1.10	4	1.7	1.6	3.0	2.7	1.7	3.6	0.45
DMF	1M LiTFSI	2	0.018	7.09E-06	1.106	3	1.5	1.5	2.9	2.6	1.6	3.2	0.36
DMA	1M LiTFSI	2.1	0.019	6.95E-06	1.11	4	1.6	1.6	2.9	2.6	1.7	3.3	0.39

CV analysis of the 1st reduction and the last oxidation wave

Yamin et al.[10] have shown, that plotting the logarithm of the peak current density versus the logarithm of the scan rate can reveal more quantitative information from cyclic voltammetry. This is based on the Randles-Sevcik equation, stating $\log_{10}(i_p) = A + \frac{1}{2}\log_{10}(\text{scan rate})$. It implies that a slope of 0.5 represents a diffusion controlled reaction, while a slope different from 0.5 may indicate a slow chemical reaction preceding the charge-transfer step.

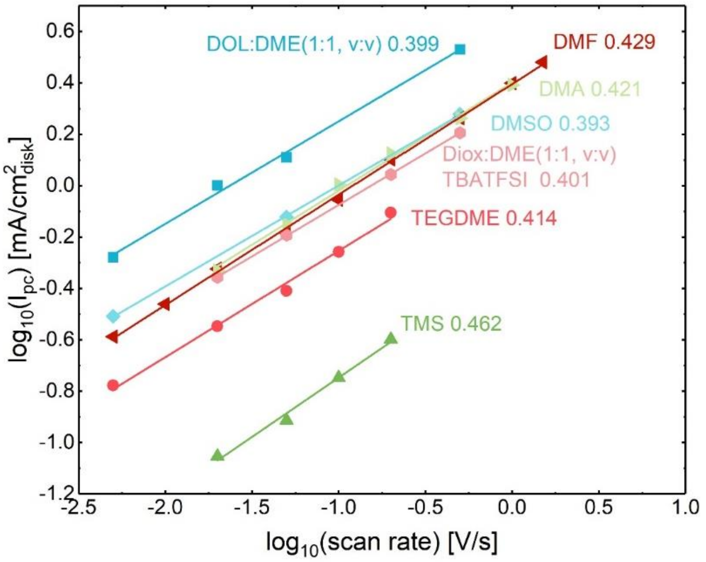

Figure S5: Logarithm of the 1st reduction peak current density in cyclic voltammograms versus the logarithm of the scan rate. Slopes are marked for each electrolyte. 1 M conducting salt (LiTFSI or TBATFSI) were used, where not specifically indicated, LiTFSI was used.

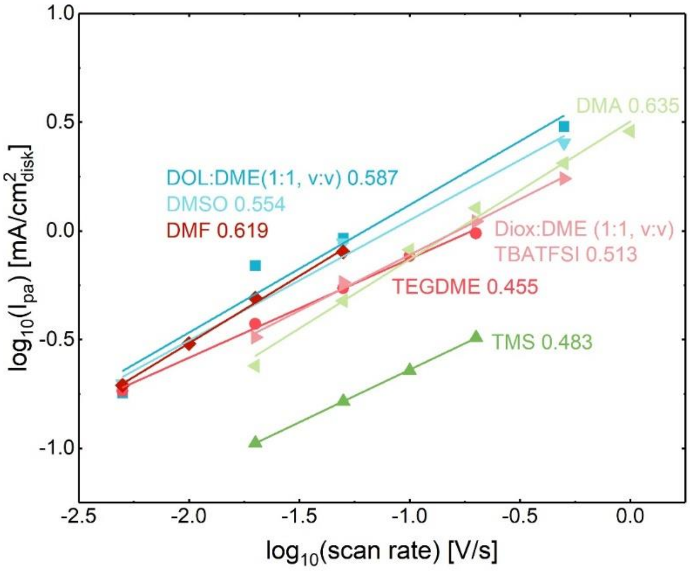

Figure S6: Logarithm of the last oxidation peak current density in cyclic voltammograms versus the logarithm of the scan rate. Slopes are marked for each electrolyte; 1 M conducting salt (LiTFSI or TBATFSI) were used, where not specifically indicated, LiTFSI was used.

This analysis was only conducted for the 1st reduction peak (Fig. S5) and last oxidation peak (Fig. S6), as the peak current of the other CV peaks were difficult to determine due to the undefined current baseline. Unlike the results shown by Yamin et al.,10 it was not possible to draw any firm conclusions from this analysis approach from our data presented here.

Reported theory-based terminal sulfur charge of polysulfides

Based on theoretical calculations, various predictions have been made with regards to the charge on the terminal sulfur atoms on polysulfides (S_x^{2-}), which are summarized in Fig. S7. The charge density of terminal sulfur at the $S_3^{\bullet -}$ radical on the other hand was predicted to be around -0.5, namely -0.53 (in vacuum, Steudel et al.[11]), -0.55 (in polarizable continuum model 8 and 78, Steudel et al.[11]), and -0.45 (in vacuum, Pascal et al.[12]).

Based on the calculation of Steude et al.,[11] the structure and the atomic charges of large polysulfides dianions and anion radicals (Li_2S_x, x > 3, not surrounded by Na^+) are pretty similar in both polarizable continuum model 8 and 78. Here, we therefore plotted the atomic charges of terminal sulfur atom in both cases with one redline in Fig. S6. Similarly, same trend can be summarized by the work of Pascal et al.,[13] where they have calculated the average valence electron populations for the internal and terminal sulfur atom of Li_2S_x in a 12 TEGDME molecule environment (marked as blue line in Fig. S7).

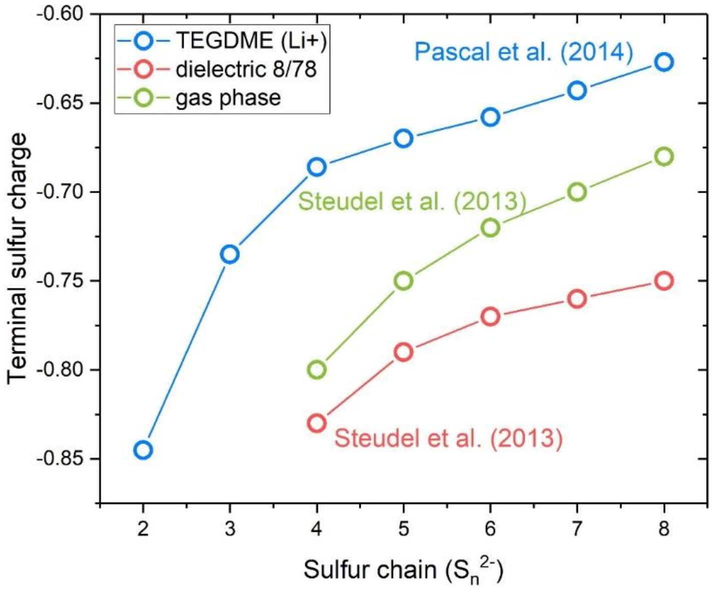

Figure S7: calculated terminal sulfur charge adapted from Pascal et al.[13] in blue as well as from Steudel et al.[11] in green and red, where the red line represents both polarizable continuum model 8 and 78.

Literature

1. Y.-C. Lu, Q. He, and H. A. Gasteiger, *J. Phys. Chem. C*, **118**, 5733–5741 (2014).

2. J. Herranz, A. Garsuch, and H. A. Gasteiger, *J. Phys. Chem. C*, **116**, 19084–19094 (2012).

3. R. D. Rauh, F. S. Shuker, J. M. Marston, and S. B. Brummer, *J. Inorg. Nucl. Chem.*, **39**, 1761–1766 (1977).

4. R. Bernhard, S. Meini, and H. A. Gasteiger, *J. Electrochem. Soc.*, **161**, A497–A505 (2014).

5. M. Metzger, B. Strehle, S. Solchenbach, and H. A. Gasteiger, *J. Electrochem. Soc.*, **163**, A798–A809 (2016).

6. H. Jha and H. Gasteiger, DE Patent No. 102013005082 A1. Munich, Germany: Deutsches Patent- und Markenamt (2014).

7. H. Jha, I. Buchberger, X. Cui, S. Meini, and H. A. Gasteiger, *J. Electrochem. Soc.*, **162**, A1829–A1835 (2015).

8. A. Rosenman, R. Elazari, G. Salitra, E. Markevich, D. Aurbach, and A. Garsuch, *J. Electrochem. Soc.*, **162**, A470–A473 (2015).

9. S. S. Zhang, *J. Power Sources*, **231**, 153–162 (2013).

10. H. Yamin, A. Gorenshtein, J. Penciner, Y. Sternberg, and E. Peled, *J. Electrochem. Soc.*, **135**, 1045–1048 (1988).

11. R. Steudel and Y. Steudel, *Chem. -A Eur. J.*, **19**, 3162–3176 (2013).

12. T. A. Pascal, C. D. Pemmaraju, and D. Prendergast, *Phys. Chem. Chem. Phys.*, **17**, 7743–7753 (2015).

13. T. A. Pascal, K. H. Wujcik, J. Velasco-velez, C. Wu, A. A. Teran, M. Kapilashrami, J. Cabana, J. Guo, M. Salmeron, and N. Balsara, *J. Phys. Chem. Lett.*, **5**, 1547–1551 (2014).

3.2 Mechanistic Understanding of the Discharge Process in a Li-S Battery

This section is separated into two parts to elucidate the discharge process by (1) qualitatively identifying the reaction intermediates produced in an operating Li-S cell using *operando* UV-Vis spectroscopy; (2) quantitatively evaluating the contributions of the important processes at the S-Cathode during discharge of a Li-S cell by means of *in-situ* impedance spectroscopy.

3.2.1 Real-time Monitoring Polysulfides Using *Operando* Transmission UV-Vis Spectroscopy

This section presents the article "*Operando* Identification of Liquid Intermediates in Lithium–Sulfur Batteries via Transmission UV-Vis Spectroscopy", which was published in April 2020 in the Journal of The Electrochemical Society. It is an open access article distributed under the terms of the Creative Commons Attribution Non-commercial No Derivative 4.0 License. This study was presented by Qi He at the 6th "Lithium-Sulfur-Batteries" workshop in Dresden, Germany (Nov 6-7, 2017). The permanent web-link to the article is http://dx.doi.org/10.1149/1945-7111/ab8645.

While the previous section focused on the speciation of polysulfides in various electrolytes, this section concentrates on the polysulfides speciation in the state-of-the-art DOL:DME-based electrolyte. More specifically, this part focuses on the determination of the specific polysulfides produced at each stage of a cycling Li-S cell (with sufficiently potential resolution). We first present a novel design of an *operando* transmission UV-Vis spectroelectrochemical cell that exhibits a reasonably similar electrochemical performance as a conventional Swagelok® T-cell. Simultaneously, it provides a rather high potential resolution, for instance, ~50 spectra over a total of ~10 hours were recorded for the whole discharge process from 2.4 V_{Li} to 1.9 V_{Li}.

Special attention is placed on the *ex-situ* reference UV-Vis spectra, since the identification of a substance in UV-Vis spectroscopy is merely based on the comparison with reference spectra. We therefore establish a series of polysulfide reference spectra to ensure a clear peak assignment for the stable polysulfides in DOL:DME, which has not yet been reported so far.

Unexpectedly, we observed an unidentified UV-Vis absorption feature that appears during the discharge process. Three different cycling procedures are therefore designed 1) to verify that it originates from a polysulfide species, and 2) to identify the exact nature of this polysulfide species (S_3^{2-}). Using the rotating ring disc electrode technique, we also independently validated the existence of this polysulfide species that so far had not been reported to occur in DOL:DME electrolyte.

This study eventually generates three important insights into Li-S batteries: (i) The liquid reaction intermediates upon discharge of a Li-S battery are revealed, as well as their potential-dependency. (ii) A systematic absorption assignment for polysulfides in DOL:DME is presented as well as the absorption of newly identified species (S_3^{2-}). (iii) A discharge reaction pathways based on the observation from this *operando* UV-Vis spectroscopy study in conjunction with other data reported in the literature (e.g., from *operando* XAS), is proposed.

Author Contributions

Q.H. and M.U.M.P. developed the *operando* UV-Vis cell setup. A.F. prepared the graphite anodes. S.Q. prepared the reference samples and performed the reference UV-Vis spectra measurements. Q.H. conducted the *operando* UV-Vis and the RRDE measurements. Q.H. and A.F. discussed and analyzed the *operando* UV-Vis results. Q.H. wrote the manuscript, and A.F. and H.G. revised it. All authors discussed the results and commented on the manuscript.

Journal of The Electrochemical Society, 2020 **167** 080508

Operando Identification of Liquid Intermediates in Lithium–Sulfur Batteries via Transmission UV–vis Spectroscopy

Qi He,[a,z] Anna T. S. Freiberg,[*] Manu U. M. Patel,[b] Simon Qian,[*] and Hubert A. Gasteiger[**]

Chair of Technical Electrochemistry, Department of Chemistry and Catalysis Research Center, Technical University of Munich, D-85748 Garching, Germany

Lithium-sulfur (Li-S) batteries are facing various challenges with regards to performance and durability, and further improvements require a better understanding of the fundamental working mechanisms, including an identification of the reaction intermediates in an operating Li-S battery. In this study, we present an *operando* transmission UV–vis spectro-electrochemical cell design that employs a conventional sulfur/carbon composite electrode, propose a comprehensive peak assignment for polysulfides in DOL: DME-based electrolyte, and finally identify the liquid intermediates in the discharging process of an operating Li-S cell. Here, we propose for the first time a meta-stable polysulfide species (S_3^{2-}) that is present at substantial concentrations during the 2nd discharge plateau in a Li-S battery. We identify the S_3^{2-} species that are the reduction product of S_4^{2-}, as deducted from the analysis of the obtained *operando* UV–vis spectra along with the transferred charge, and confirmed by rotating ring disk electrode measurements for the reduction of a solution with a nominal Li_2S_4 stoichiometry. Furthermore, our *operando* results provide insight into the potential-dependent stability of different S-species and the rate-limiting (electro)chemical steps during discharging. Finally, we propose a viable reaction pathway of how S_8 is electrochemically reduced to Li_2S_2/Li_2S based on our *operando* results as well as that reported in the literature.

[DOI: 10.1149/1945-7111/ab8645]

Manuscript submitted December 31, 2019; revised manuscript received March 8, 2020. Published April 21, 2020.

Supplementary material for this article is available online

As one of the most important strategies to move the world's energy landscape toward clean, renewable energy, lithium-ion batteries (Li-ion, based on intercalation electrochemistry) have been intensively developed and widely commercialized. Despite the significant improvement in increasing the energy density over the years, there is a growing consensus that current Li-ion batteries might be unable to satisfy the requirements of future technologies.[1] In the search for high energy density and inexpensive post Li-ion batteries, the lithium-sulfur battery system (Li-S, based on conversion electrochemistry) has attracted tremendous attention worldwide due to its high theoretical specific capacity (1675 mAh/g_{sulfur}) as well as due to the high natural abundance and non-toxicity of elemental sulfur.[1–8]

The reversible conversion (Eq. 1) between elemental sulfur (S_8) and lithium sulfide (Li_2S) is believed to be accompanied by a series of soluble reaction intermediates, namely polysulfides (Li_2S_x; x referring to the total possible range of S atoms), in liquid electrolyte Li-S batteries. It is general believed that reduction of S_8 first generates long-chain polysulfides (Li_2S_n, here defined to be $5 \leqslant n \leqslant 8$), that can be further reduced to short-chain polysulfides (Li_2S_m, here defined to be $2 \leqslant m \leqslant 4$), and eventually the solid product Li_2S is formed[1,6,7,9–12]:

$$S_8 + 16e^- + 16Li^+ \leftrightarrow \frac{8}{n}Li_2S_n + aLi^+ + ae^- \leftrightarrow \frac{8}{m}Li_2S_m + bLi^+ + be^- \leftrightarrow 8Li_2S \qquad [1]$$

where $a = \frac{16(n-1)}{n}$, and $b = \frac{16(m-1)}{m}$.

One of the major hindrances to develop a high-performance Li-S battery is the uncontrolled dissolution of elemental sulfur (S_8) and polysulfides, which leads to 1) the loss of active material and, 2) poor cycling efficiency caused by the so-called polysulfide shuttling.[1,3,6,7,9,10,13–15] Despite the great progress that has been made in cathode material development to contain the soluble species within the sulfur cathode electrode, the practical performance of current Li-S batteries is still far from satisfying. To further improve and optimize Li-S battery performance, the fundamental processes during charge and discharge need to be better understood, particularly with regards to the dominant polysulfide species in the different charge/discharge regimes.

To address this particular issue, many analytical techniques have been applied.[1,6,7,9,13,15–19] In one of the most referenced studies in the literature, Barchasz et al.[9] have investigated the Li-S system in a TEGDME-based (tetraethylene glycol dimethyl ether) electrolyte using *ex situ* liquid chromatography, UV–vis absorption spectroscopy, and electron spin resonance spectroscopy. In their study, $S_6^{2-}/S_3^{\cdot -}$ species are proposed to be formed at the 1st discharge plateau, which subsequently get reduced to S_4^{2-} in the transition region to the 2nd plateau, at which S_4^{2-} in turn is reduced to $S_3^{2-}/S_2^{2-}/S_1^{2-}$ (note that S_1^{2-} here corresponds to the final Li_2S product).[9] Although much insights have been gained by this study, these *ex situ* results do not necessarily represent the real-time cell chemistry in an operating Li-S battery. Furthermore, this study does not provide insights into the cell chemistry in state-of-the-art electrolytes, i.e., with solvent mixtures of 1,3-dioxolane (DOL) and 1,2-dimethoxyethane (DME), as the stability of polysulfide (or radical) intermediates is largely influenced by the electrolyte solvents[6,7,9,10,17,20–24] (e.g., $S_3^{\cdot -}$ is better stabilized in TEGDME than in DME[10,25]). Moreover, the chemical equilibria in which polysulfides are involved, i.e., chain-breaking (e.g., $S_6^{2-} \leftrightarrow 2S_3^{\cdot -}$)[26] and disproportionation reactions (e.g., $S_8^{2-} \leftrightarrow S_6^{2-} + ¼S_8$),[6,7,9,10,13,21,26] can be easily shifted by the environmental change imposed by *ex situ* analysis (i.e., by either removing the electrolyte or by changing the solvent, the type and concentration of the conducting salt, and/or the temperature).[6,17,27,28]

Hence, various *operando*techniques have recently been developed to investigate the Li-S battery system,[1,7,8,12,13,18,29–32] e.g., *operando* X-ray diffraction (XRD)[31,32] and X-ray absorption near-edge spectroscopy (XANES).[7,8,18] Especially when using spatially

---

[*] Electrochemical Society Student Member.

[**] Electrochemical Society Fellow.

[a] Present Address: Business unit Battery Cell, Volkswagen Group Components, Salzgitter, Germany.

[b] Present Address: Hollingsworth and Vose Advanced Materials, Mysore-571311, India.

[z] E-mail: qi.he@tum.de

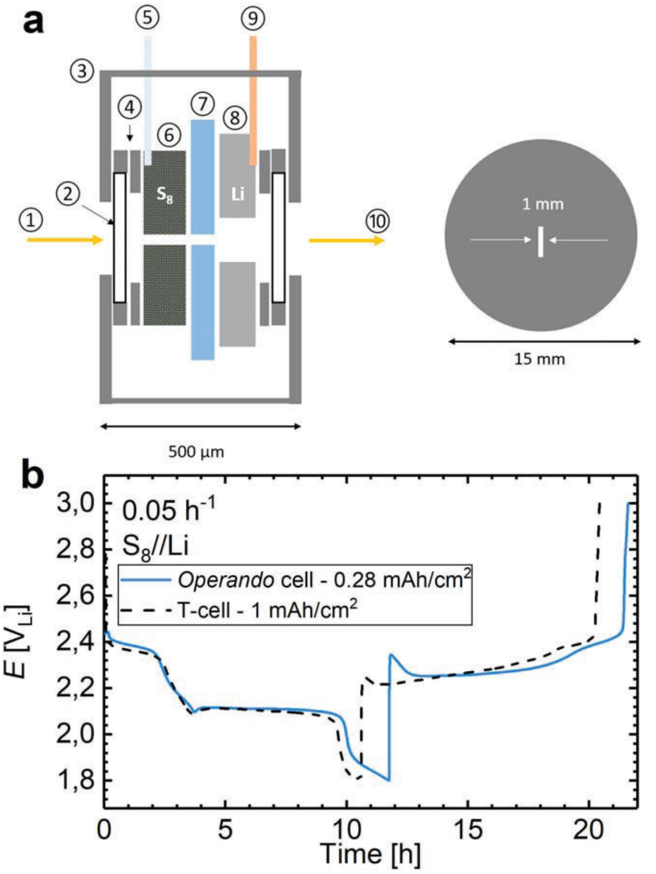

Figure 1. (a) Design and components of the UV–vis spectro-electrochemical cell (transmission mode). Left panel: (1) incident UV–vis beam, (2) quartz-glass (∼165 *µ*m thickness), (3) pouch foil (115 *µ*m thickness), (4) pouch foil based sealing ring, (5) Al current collector tab (∼100 *µ*m thickness), (6) S_8/C composite based cathode coated onto an 18 *µ*m thick Al foil (∼60 *µ*m total thickness), (7) separator (4 layers of Celgard H2013 with a total thickness of 80 *µ*m), (8) anode electrode of either metallic lithium (∼70 *µ*m thickness) or pre-lithiated graphite coated onto an 11 *µ*m thick Cu foil (total thickness of 60 *µ*m), (9) Ni current collector tab (∼100 *µ*m thickness), (10) path of the transmitted beam. Right panel: top view of the cathode electrode with a slit (1 mm × 5 mm). (b) Galvanostatic cycling at a C-rate of 0.05 h^{-1} of the *operando* UV–vis spectroelectrochemical cell (blue line) with an S_8/C composite cathode (0.28 mAh cm^{-2}, with a slit), an Li-anode, and 200 *µ*l electrolyte, benchmarked against a Swagelok® type T-cell (dashed line) with an S_8/C cathode (1 mAh cm^{-2}, without slit), an Li-anode, and 40 *µ*l electrolyte. Electrolyte: DOL:DME (1:1, v:v) with 1 M LiTFSI and 0.5 M $LiNO_3$.

resolved *operando* XANES, both amorphous and crystalline S_8 and Li_2S as well as dissolved polysulfides (S_x^{2-}) and $S_3^{\cdot -}$ can be monitored during cell cycling in both the cathode electrode and in the separator.[7,8] This approach facilitated our comprehension of the evolution of species during the charge and discharge of an operating Li-S battery cell. Nevertheless, the exact reaction pathway of S_8 to Li_2S (or vice versa) still remains unclear, due to the large self-absorption effect in X-ray absorption spectroscopy, which allows neither differentiation of the various polysulfides nor a spectral deconvolution of the S_8 and polysulfide signals. The most practical technique to differentiate between various polysulfides is UV–vis spectroscopy that has been widely employed.[9,10,17,21,24,33–36] For instance, Patel et al.[24] have developed an *operando* UV–vis spectroscopy approach in reflectance mode, by which they were able to confirm that long-chain polysulfides are first formed after the initial S_8 reduction during discharge and that short-chain polysulfides are generated in the subsequent discharge process. However, the absorption shift in reflectance UV–vis spectra is difficult to interpret, since it is greatly influenced by both the type of polysulfide species and their concentration. Hence, the identification of polysulfides in an operating Li-S battery using *reflectance* UV–vis spectroscopy is rather challenging.

On the other hand, the absorption shift in *transmission* UV–vis spectroscopy is only dependent on the chromophoric species themselves (i.e., on the specific polysulfide species), where the concentration of a given chromophore influences nothing but the absorption intensity. Therefore, *operando* UV–vis spectroscopy in transmission mode has been developed over the last two decades, mostly to investigate the cyclic voltammetric response of the various S-redox reactions in different electrolytes.[10,34,37–39] For example, it was observed that S_8^{2-} and $S_3^{\cdot -}$ are predominant in high donor number (high-DN) solvents such as dimethyl sulfoxid (DMSO) and N,N-dimethylformamide (DMF),[21,23,34,36,37,40] whereas S_4^{2-} is one of the most abundant species in low donor number (low-DN) solvents, for example in DOL:DME (1:1, v:v).[10,25] Unfortunately, the classic three-electrode cell design as well as the platinum or gold electrode used in these studies are inappropriate to investigate the conventional galvanostatic cycling of Li-S batteries. Specifically, the typical Li-S galvanostatic voltage profile is difficult to achieve in this open system, owing to the large diffusion distances of soluble S-species in such cells, which result in charge/discharge characteristics very different from conventional thin-layer configurations (e.g., pouch or coin cells). Thus, the inspection of the evolution of the intermediates during galvanostatic cycling of a Li-S cell with a conventional S_8/C composite cathode material is required to attain a deeper knowledge of Li-S reaction mechanism in an actual Li-S battery.

In this study, we present an *operando* transmission UV–vis cell design, benchmark its electrochemical performance, and apply it to identify the soluble reaction intermediates during the discharge of a Li-S battery with an S_8/C composite based cathode. In order to properly evaluate the obtained *operando* UV–vis spectra, we systematically analyze the reference spectra of different polysulfide solutions with a nominal stoichiometry ranging from "Li_2S_2" to "Li_2S_{16}" in DOL:DME-based electrolyte, based on which we propose a peak assignment for the various polysulfides. Thereupon, we obtain real-time *operando* UV–vis spectra during the discharge of a Li-S battery and propose for the first time a meta-stable polysulfide species (S_3^{2-}) that is present at substantial concentrations during the 2nd discharge plateau. We confirm the formation of this meta-stable S_3^{2-} in DOL:DME-based electrolyte by determining the number of electrons transferred for the reduction of "Li_2S_4" using the rotating ring disk electrode (RRDE) technique. To further investigate the electrochemical and chemical behavior of polysulfides of interest (S_4^{2-}, S_3^{2-}), we modify the galvanostatic cycling procedure by introducing constant voltage (CV) and open circuit voltage (OCV) phases during the operation of the *operando* UV–vis cell. Finally, we propose a discharge mechanism for Li-S batteries in DOL:DME-based electrolyte that incorporates both the findings from our *operando* UV–vis results and those from other *operando* studies in the literature, such as XANES[7,13] and XRD.[31]

Experimental

Operando *UV–vis cell design.*—The *operando* cell design is presented in Fig. 1a. It is a pouch cell based design, where two quartz glass windows (∼165 *µ*m thickness, with internal transmittance from 180 nm to 2000 nm greater than 0.99) are sealed into the front and back pouch foil (consisting of a multilayer of Nylon, aluminum and polypropylene), so that the UV–vis incident beam can pass through the *operando* cell onto the detector. The transmission of the incident beam is accomplished through a slit (1.0 mm × 5.0 mm) in both working electrode and separator as well as through a larger slit (2.5 mm × 8.0 mm) in the counter electrode to facilitate alignment, so that the soluble intermediates (S_n^{2-} and S_8) can freely diffuse into the slit and thus absorb UV–vis light of their characteristic wavelength. The slit size of 1.0 mm × 5.0 mm in the working electrode is chosen to be large enough to enable a sufficiently large UV–vis beam to pass through the sample and small enough to reduce the time required for reaction intermediates to diffuse from the slit edge to the slit center. The estimated diffusion time is about 10 min, assuming the diffusivity of dissolved polysulfides to be ~$2.6 \cdot 10^{-6}$ cm^2 s^{-1} in DOL:DME-based electrolyte.[6] This estimation is confirmed by the *operando* data showing that dissolved chromophores can be detected already after at the 1st spectra (~12 min) taken during the charge of an Li_2S-Li cell (data not shown in this study).

Electrode preparation and electrochemical measurements.— *Cathode preparation.*—The preparation of the S_8/C composite (with 66.7wt% S_8 and 33.3wt% vulcan carbon (XC-72, Tanaka Kikinzoku Kogyo)) is described elsewhere in a detailed manner.[17,41] The as-prepared S_8/C composite was added to a dispersion of polyvinylidene difluoride (PVDF, HSV900, Kynar) in N-methyl-pyrrolidinone (NMP, 99.5%, anhydrous, Sigma-Aldrich), and the resulting suspension/ink was mixed in a plenary mixer (Thinky, Japan). It was then coated onto an 18 μm thick aluminum foil (MTI, USA) using a Mayer rod with different gaps to achieve the desired loading (from ~0.15 mg_s cm^{-2} (~0.25 mAh cm^{-2}) to ~0.6 mg_s cm^{-2} (~1.0 mAh cm^{-2})). The final cathode composition is 60wt% S_8, 30wt% vulcan carbon and 10wt% PVDF. The coating was initially dried at room temperature overnight, then electrodes were punched out as disks with a diameter of either 11 mm (for Swagelok®-type T-cells) or 15 mm (for coin cells and for *operando* UV–vis cells, whereby the punching tool for latter also cut out the above specified slit), and finally dried for another 12 h under static vacuum at 60 °C in a sealed glass oven (Büchi, Switzerland).

Graphite anode preparation.—Graphite (SLP30, Timcal, Japan) was mixed with PVDF in NMP to achieve an ink solids composition of 90wt% graphite and 10wt% PVDF. The resulting ink was mixed in a planetary mixer for 20 min and coated onto an 11 μm thick copper foil (99.99%, MTI, USA) using a Mayer rod with different gaps to achieve the desired loadings ranging from 1.3–2.2 mg_{C6} cm^{-2} (~0.45 to ~0.8 mAh cm^{-2}). The coating was initially dried at 50 °C overnight, then electrodes were punched out as disks with a diameter of 14 mm (for coin cells and for *operando* UV–vis cells, whereby the latter were also cut to contain the above specified slit), and finally dried for another 12 h under dynamic vacuum at 120 °C in a glass oven (Büchi, Switzerland). A smaller anode diameter (14 mm) and larger separator diameter (18 mm, Celgard H2013) were chosen to avoid short circuit during the slit alignment while assembling the *operando* cell; since all experiments with graphite anodes were conducted with pre-lithiated graphite electrodes and since only the first discharge of the sulfur working electrode was considered, artefacts from lithium plating which would be expected to occur on an undersized anode must not be considered.

The pre-lithiation of graphite electrodes was accomplished in a C_6//Li coin cell with an electrolyte consisting of 1 M lithium perchlorate ($LiClO_4$, battery grade, 99.99% trace metal basis, Sigma-Aldrich), 0.1 M $LiNO_3$ and 0.5 M vinylene carbonate (BASF SE, Germany) in DOL:DME (1:1, v:v). One formation cycle at 0.1 C followed by a galvanostatic lithiation to 50% SOC were performed in a climate chamber (Binder, Germany) at 25 °C. Afterwards, the pre-formed and partially pre-lithiated graphite electrodes were harvested and washed three times with DOL:DME (1:1, v:v) solution. The areal delithiation capacity of these pre-lithiated graphite electrodes consequently ranges from ~0.2 to ~0.4 mAh cm^{-2}.

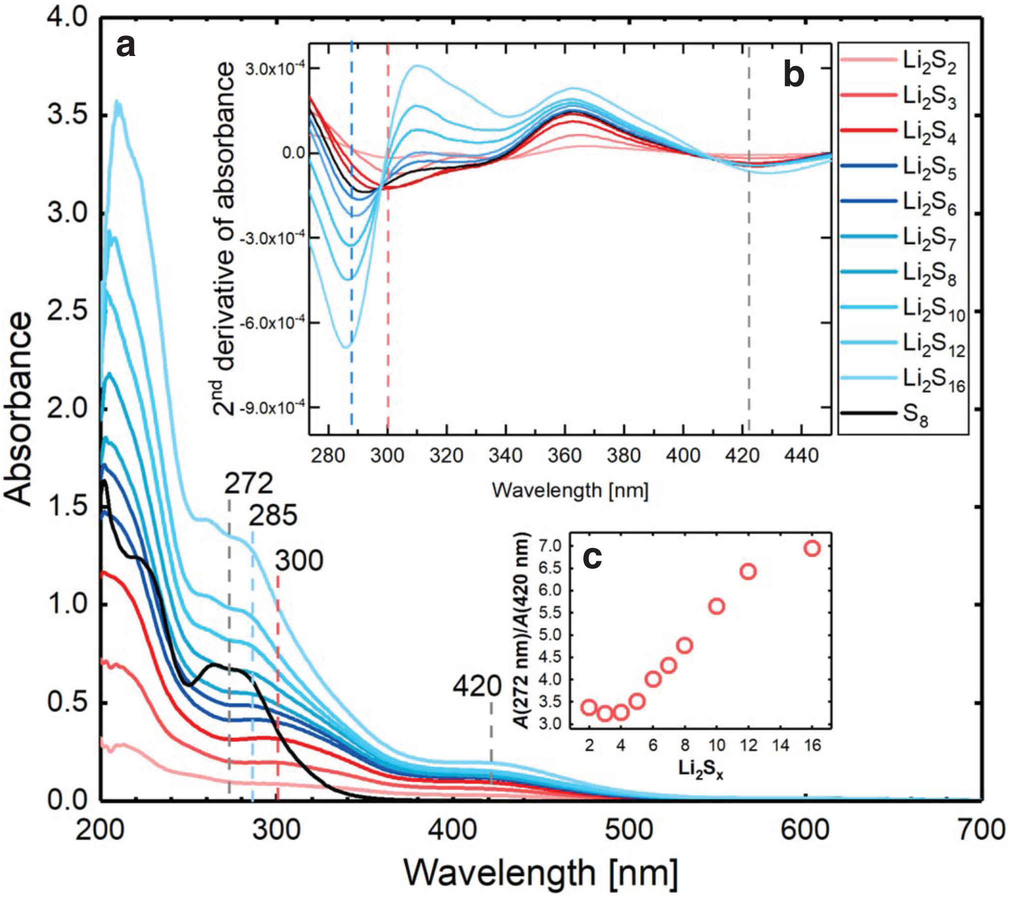

Figure 2. (a) UV–vis spectra of 1 mM "Li_2S_x" and 1 mM S_8 in DOL:DME (1:1, v:v) with 1 M LiTFSI, measured in an air-tight 1 mm thick cuvette at room temperature (25 ± 1 °C). (b) The inset shows the 2nd derivative of the obtained UV–vis spectra. (c) Ratio between the absorption at 272 nm (expressed as A (272 nm)) and at 420 nm (expressed as A(420 nm)) extracted from the spectra for all polysulfide samples.

Cell assembly and electrochemical measurements.—Electrochemical measurements were performed using Swagelok®-type T-cells, coin-cells (CR2031, Hohsen, Japan), and *operando* UV–vis pouch cells (see Fig. 1a). S_8/C composite cathodes were either paired with a lithium metal anode (99.9% purity with 70 or 450 μm thickness, Rockwood lithium, USA) or a pre-lithiated graphite electrode ($\sim$60 μm thickness). All cells were assembled in an Ar-filled glove box (<0.1 ppm O_2 and H_2O, Mbraun, Germany) and were connected either to a multi-channel potentiostat (VMP3, BioLogic, France) in a climate chamber (Binder, Germany) at 25 °C (±0.5 °C) or to a single-channel potentiostat (SP-200, BioLogic, France) in an air-conditioned room (25 ± 1 °C). Four layers of Celgard H2013 were used as separator, and the electrolyte used in this study consisted of a 1:1 (v:v) mixture of 1,3-dioxolane (DOL, anhydrous, 99.8%, Sigma-Aldrich) and 1,2-dimethoxyethane (DME, anhydrous, 99.8%, Sigma-Aldrich) with 1 M lithium bis (trifluoromethane) sulfonamide (LiTFSI, 99.95% trace metal basis, Sigma Aldrich; dried under dynamic vacuum at 120 °C for 3 d in a sealed glass oven) and 0.5 M (for benchmarking) or 0.1 M (for *operando* experiments) lithium nitrate ($LiNO_3$, 99.99% trace metal basis, Sigma-Aldrich; dried under dynamic vacuum at 110 °C for 3 d in a glass oven).

For the T-cells, 40 μl of electrolyte were used, while an excess of electrolyte (200 μl) is required for the *operando* UV–vis cell in order to wet the electrode separator assembly in such a way that the slits in the electrodes and the separator are filled completely with electrolyte, so that reaction intermediates can freely diffuse into the detection region (slit). Another limitation of the *operando* UV–vis Li-S battery cell is that it can only be operated with low-loaded S_8/C composite electrodes ($\sim$0.15 $mg_s\ cm^{-2}$, corresponding to $\sim$0.25 $mAh\ cm^{-2}$), as dissolved S_8 and polysulfides have rather high molar absorptivity (e.g., the molar absorptivity of S_8 at $\sim$270 nm in DOL:DME (1:1, v:v) is $\sim$7000 $L{\cdot}mol^{-1}{\cdot}cm^{-1}$, see black line in Fig. 2a), so that a maximum concentration of $\sim$10 mM S_8 (dissolved) or $\sim$20 mM S_4^{2-} can be resolved in our *operando* UV–vis cell (estimated with an effective path length of $\sim$0.5 mm, an absorbance of 4 as the detection limit and without considering any co-existence of different polysulfides and/or S_8).

Acquisition of reference UV–vis spectra and* operando *UV–vis spectra.—We prepared polysulfides with nominal compositions corresponding to 1 mM "Li_2S_x" ($2 \leqslant x \leqslant 16$) by stoichiometrically mixing elemental sulfur (99.998%, trace metal basis, Sigma-Aldrich) and Li_2S (99.98% trace metal basis, Sigma-Aldrich),[42] and analyzed their absorption behavior systematically after stirring the solution for at least 12 h in an Ar-filled Glovebox (<0.1 ppm O_2 and H_2O, Mbraun, Germany). These reference spectra were taken using an air-tight cuvette with a 1 mm path length (1/ST/C/Q/1, Starna Scientific GmbH) at 25 °C (±1 °C).

The *ex situ* and the *operando* UV–vis measurements were carried out employing a Lambda 35 UV–vis spectrometer (Perkin Elmer, USA), which was switched on at least 30 min prior to any measurements. A scan rate of 60 nm min^{-1} was chosen to increase the signal/noise ratio, and therefore $\sim$8 min were needed to scan the wavelength region from 230 nm to 700 nm with a step-size of 4 nm. Spectra were recorded every 12 min according to the estimated diffusion time of polysulfides into the probing slit ($\sim$10 min, see above). We thus carried out the galvanostatic cycling with a C-rate of 0.05 h^{-1} (referenced to a theoretical discharge capacity of 1675 $mAh\ g_S{}^{-1}$) to collect UV–vis spectra with a sufficiently high capacity resolution throughout the discharge process (ca. Δ17 $mAh\ g_S{}^{-1}$ per spectrum), so that for a typically 9 h long discharge roughly 45 UV–vis spectra can be recorded.

RRDE measurement.—The setup for RRDE measurements in non-aqueous electrolytes was adopted from that reported by Lu et al.[6] and Herranz et al.[43] It is a classic three-electrode cell, employing a working electrode consisting of a PTFE embedded glassy carbon disk working electrode with a diameter of 5.0 mm, and a gold ring electrode with an internal diameter of 6.5 mm and an external diameter of 7.5 mm (Pine Research Instrumentation, USA). The working electrode compartment was filled with 4 mM nominally prepared "Li_2S_4" in DOL:DME (1:1, v:v) with 1 M LiTFSI. A Pt wire was employed as counter electrode in a separated compartment filled with same electrolyte and connected with the working electrode compartment by a glass frit. Ag/$AgNO_3$ (0.1 M) in acetonitrile (ACN) was used as reference electrode, which was separated with a Vycor frit from the working electrode compartment. The RRDE cell was flushed with Ar for 30 min prior to the measurement and blanketed with an Ar flow during the experiment. AC impedance measurements were taken by applying a voltage perturbation of 10 mV (1 MHz to 100 mHz) before the RRDE measurements, and the ohmic drop between reference electrode and working electrode was thereby determined to be $\sim$80 Ω and was used to determine the iR-free voltage. The potentials measured by the Ag^+/Ag reference electrode was finally converted to the ferrocenium/ferrocene (Fc^+/Fc) reference potential scale (0 V vs $Ag^+/Ag \equiv +0.043$ V vs Fc^+/Fc), as reported previously.[6,17]

Results and Discussion

Electrochemical benchmarking of the* operando *UV–vis cell.—The electrochemical performance of our *operando* UV–vis cell were first benchmarked against a Swagelok®-type T-cell with a standard electrolyte (1 M LiTFSI and 0.5 M $LiNO_3$ dissolved in DOL:DME (1:1, v:v)), using an S_8/C composite as working electrode, metallic lithium as counter electrode, and 4 layers of the H2013 separator. The cell voltage vs time for the first discharge and the first charge at a C-rate of 0.05 h^{-1} between 1.8 and 3.0 V_{Li} is shown in Fig. 1b. The T-cell with a sulfur loading of 0.6 $mg_S\ cm^{-2}$ (corresponding to a theoretical capacity of 1 $mAh\ cm^{-2}$) and with a ratio of electrolyte volume to sulfur mass (E/S) of $\sim$71 $\mu l\ mg_S{}^{-1}$ (black dashed line) reaches approximately 50% of its theoretical capacity and closely resembles that reported in the literature.[7,11,44–46] Here it should be noted, that an additional decreasing slope below 1.9 V is observed for the *operando* UV–vis cell, but not for Swagelok®-type T-cell. This phenomenon can be rationalized by the continuous electrochemical reduction of $LiNO_3$ below 1.9 V,[47] especially in the case of cycling at a small discharge current.

While for the above outlined reasons the sulfur loading of the *operando* UV–vis cell is much lower (0.17 $mg_S\ cm^{-2}$, corresponding to a theoretical capacity of 0.28 $mAh\ cm^{-2}$) and while the E/S ratio is much larger ($\sim$700 $\mu l\ mg_S{}^{-1}$), its first discharge with two-plateaus around 2.35 V and 2.1 V separated with a supersaturation point (blue line) is quite comparable with the voltage profiles of Li-S cells with a practical E/S ratio of 8 $\mu l\ mg_S{}^{-1}$ that were reported by Hagen et al.[48] Therefore, we believe that the reaction pathway deduced from our *operando* UV–vis analysis, namely the reduction of S_8 to Li_2S_2/Li_2S is likely to also be operative in actual Li-S batteries despite their substantially lower E/S ratio.

UV–vis Peak assignment for polysulfides in DOL:DME-based electrolyte.—While the UV–vis peak assignment of various polysulfides have already been proposed in different electrolytes, such as in DME,[49] TEGDME,[9,33] DMSO,[21,35,36] DMF,[40,50] DMA,[23] ionic liquid,[51] a comprehensive peak assignment of polysulfides in DOL: DME-based electrolyte is, to the best of our knowledge, not available in the literature. Although the polysulfide speciation is similar in the solvents with comparable donor number,[17] their UV–vis peak position, intensity and the shape of the absorption spectra may still vary in those solvents, owing to the solvatochromism phenomenon.[52] In other words, the surrounding medium of a chromophore (e.g., solvent) may alternate the solvation of the ground and first-excited state of the chromophore,[52] which would result in a hypsochromic or bathochromic shift. Therefore, in order to unambiguously identify the reaction intermediates in a Li-S cell operating in the DOL:DME-based electrolyte, a comprehensive peak assignment of polysulfides, specifically in the same DOL:DME-based electrolyte, is required.

The UV–vis spectra of 1 mM polysulfide samples of the nominal composition "Li_2S_x" ($2 \leqslant x \leqslant 16$) in DOL:DME (1:1, v:v) with 1 M LiTFSI are presented in Fig. 2a. The UV–vis spectra of the same polysulfide compositions in the same electrolyte with additional 0.1 M $LiNO_3$ are shown in Fig. S1 (available online at stacks.iop.org/JES/167/080508/mmedia) in order to confirm that the presence of 0.1 M $LiNO_3$ has no significant influence on the polysulfide composition (discussed in supplementary information section 2.1) and that it only adds a spectral feature at ~285 nm with a very small absorbance. All prepared polysulfides "Li_2S_x" ($2 \leqslant x \leqslant 16$) have three absorption regions, viz., around 400 nm, 300 nm, and 200 nm. We focus the peak assignment mainly on the regions of 400 nm and 300 nm, since the deconvolution of the UV–vis spectra below 250 nm is not possible in the presence of $LiNO_3$ (owing to its high absorbance in this region, see. Fig. S1), that will be required as additive for stable cycling in the *operando* UV–vis experiments.

Spectral features of long and short-chain polysulfides.—Two groups of polysulfides are observed in Fig. 2, viz., short-chain polysulfides ("Li_2S_2"–"Li_2S_4," red lines) and long-chain polysulfides ("Li_2S_5"–"Li_2S_{16}," blue lines). Although both short-chain and long-chain polysulfides have a common absorption shoulder at ~420 nm, their absorption behavior in the region around 300 nm is distinct from each other. Specifically, the long-chain polysulfides (e.g., "Li_2S_{16}," "Li_2S_{12}") show a clear shoulder at 285 nm, while short-chain polysulfides exhibit a shoulder at ~300 nm. This difference in absorption behavior around 300 nm is well resolved in the 2nd derivative of the absorption spectra (Fig. 2b), a commonly used rather sensitive method to analyze shoulders and overlapping absorption bands.[53] It is well established that the minima in the 2nd derivatives of the absorption spectra correspond to the appropriate absorption maxima in the absorption spectra.[53] In Fig. 2b, short-chain polysulfides ("Li_2S_2"–"Li_2S_4," red lines) clearly show a minimum around ~300 nm, while long-chain polysulfides ("Li_2S_5"–"Li_2S_{16}") exhibit no minimum at ~300 nm but at ~285 nm.

We also observe that polysulfides within the each of the two polysulfide sub-groups, represented by the nominal compositions "Li_2S_5"–"Li_2S_{16}" (blue lines) and "Li_2S_2"–"Li_2S_4" (red lines), absorb at the same wavelength with different intensities, albeit their different nominal compositions. Considering the hypothesis that not every "Li_2S_x" can be stabilized in DOL:DME solution, we suggest that polysulfides absorbing at the same wavelength (e.g., "Li_2S_5"–"Li_2S_{16}") go through disproportionation reactions and thereby generate the same species but in different concentrations. In order to keep the charge conserved, the polysulfides involved in disproportionation reactions would have to have different oxidation states (as shown in Eq. 2, with specific examples given by Eqs. 3 and 4). To note, elemental sulfur (S_8) is considered to be a reasonable disproportionation product as shown[6,7,9,10,13,21,26] in Eq. 3.[9,54]

$$S^{2-}_{x} \leftrightarrow S^{2-}_{m}(m < x, \ \text{reduced}) + S^{2-}_{n}(n > x, \ \text{oxidized}) \qquad [2]$$

$$S^{2-}_{8} \leftrightarrow S^{2-}_{6}(\text{reduced}) + \frac{1}{4}S_8(\text{oxidized}) \qquad [3]$$

$$S^{2-}_{6} \leftrightarrow \frac{1}{2}S^{2-}_{4}(\text{reduced}) + \frac{1}{2}S^{2-}_{8}(\text{oxidized}) \qquad [4]$$

In summary, we hypothesize that short-chain polysulfides and long-chain polysulfides go through disproportionation reactions to generate a few short-chain and long-chain polysulfides or dissolved sulfur which are most stable in the electrolyte. As for now, the specific composition of the polysulfide(s) formed by these disproportionation reactions cannot be specified, so that Eqs. 5 and 6 as well as the below listed Eqs. 7–10 are written as simplified non-stoichiometric reactions.

$$S^{2-}_{2-4} \leftrightarrow S^{2-}_{m}(\text{reduced}, \ m \leqslant 2) + S^{2-}_{n}(\text{oxidized}, \ n \geqslant 4) \qquad [5]$$

$$S^{2-}_{5-16} \leftrightarrow S^{2-}_{\text{x}}(\text{reduced}, \ x \leqslant 5) + S^{2-}_{y}(\text{oxidized}, \ y \geqslant 16 \text{ or } S_8) \qquad [6]$$

In preparing the "Li_2S_2" and "Li_2S_3" solutions, we noticed the presence of a white precipitate after 3 d heating (50 °C) and stirring, suggesting the formation of a thermodynamically stable insoluble sulfur-containing species. On the other hand, the "Li_2S_4" solution (as well as solutions with a nominally higher "polysulfide" composition) shows little/no precipitate. Even though Li_2S_2 is hypothesized to be solid,[55,56] it has never been experimentally isolated from a Li-S cell. We thus believe that the here observed white precipitate in "Li_2S_2" and "Li_2S_3" solutions is more likely Li_2S rather than Li_2S_2, whereby Li_2S is known to be insoluble in the DOL:DME-based electrolyte.[31,57] Thus, Li_2S (represented as S_1^{2-}) is a very likely candidate for the reduced S-species (S_{m}^{2-}) in Eq. 5, which can be re-written as:

$$S^{2-}_{2-4} \leftrightarrow S^{2-}_{1} + S^{2-}_{n}(\text{oxidized}, \ n \geqslant 4) \qquad [7]$$

In addition, we note from Fig. 2 that long-chain polysulfides such as "Li_2S_{16}" and "Li_2S_{12}" show a clear absorbance in the 260–285 nm region as well as a clear shoulder at 285 nm, which resembles the characteristics of dissolved elemental S_8 that is marked in black in Fig. 2. Hence, we believe that dissolved S_8 (thermodynamically stable at ambient conditions[57]) is likely present in long-chain polysulfides solutions and can be considered as the oxidized S-species in Eq. 6, which can be re-written as:

$$S^{2-}_{5-16} \leftrightarrow S^{2-}_{x}(\text{reduced}, \ x \leqslant 5) + S_8 \qquad [8]$$

The analysis that suggests that S_{16}^{2-} or higher order polysulfides are not the oxidized species in Eq. 6 is discussed in the supplementary information (section 2.2 in the SI). Furthermore, it is clear that both short-chain polysulfides and long-chain polysulfides have a common absorption at ~420 nm, suggesting that all polysulfides may share a common species, viz., S_n^{2-}(Eq. 7) ≡ S_x^{2} (Eq. 8). Consequently, Eqs. 7 and 8 can be re-written as:

$$S^{2-}_{2-4} \leftrightarrow S^{2-}_{1} + S^{2-}_{x} \qquad [9]$$

$$S^{2-}_{5-16} \leftrightarrow S_8 + S^{2-}_{x} \qquad [10]$$

Determination of the S_x^{2-} species.—Here we show that the ratio of the absorption at 272 nm (highest absorption characteristic of S_8) and 420 nm (assignment to S_x^{2-}), i.e., $\frac{A(272\ nm)}{A(420\ nm)}$ for all polysulfide samples are consistent with the predictions of Eqs. 9 and 10, and also provide a simple assessment of the common species (S_x^{2-}) that exists both in long-chain and short-chain polysulfide groups.

According to Eq. 9 (non-stoichiometric expression) or Eq. 11 (stoichiometric expression), the spectra of short-chain polysulfides would only have spectral characteristic features of S_x^{2-} (~420 nm and ~300 nm), as Li_2S (solid) would be UV–vis inactive in transmission mode. Therefore, the ratio $\frac{A(272\ nm)}{A(420\ nm)}$ would always be the same for short-chain polysulfides.

$$1Li_2S_m \leftrightarrow \frac{x-m}{x-1}Li_2S(\text{solid}) + \frac{m-1}{x-1}Li_2S_x \qquad [11]$$

However, the ratio $\frac{A(272\ nm)}{A(420\ nm)}$ of long-chain polysulfides would increase linearly when the polysulfide chain length increases, since the disproportionation to S_8 would lead to a linear increase of *A* (272 nm) on account of the growing S_8 concentration, whereas the polysulfide concentration represented by *A*(420 nm) remains

Table I. Summary of the absorption characteristics assigned (in this work) to the chromophores dissolved in the DOL:DME-based electrolyte.

Chromophore	Absorption characteristics λ (nm)
S_8	~265–285
$LiNO_3$	~285
$S_4{}^{2-}$	300, 420
$S_3{}^{2-}$	~266

constant, as shown by the stoichiometric expression in Eq. 12.

$$1Li_2S_n \leftrightarrow \frac{n-x}{8}S_8 + 1Li_2S_x \qquad [12]$$

Since S_8 bears only a characteristic absorption at ~272 nm but none at ~420 nm (shown in black in Fig. 2a), the ratio $\frac{A(272\ nm)}{A(420\ nm)}$ of long-chain polysulfides based on Eq. 12 can be written as:

$$\frac{A(272\text{ nm})}{A(420\text{ nm})} = \frac{A(S_8@272\text{ nm}) + A(Li_2S_x@272\text{ nm})}{A(Li_2S_x@420\text{ nm})} = \frac{A(S_8@272\text{ nm})}{A(Li_2S_x@420\text{ nm})} + a \qquad [13]$$

where a is a constant that represents the fixed ratio of $\frac{A(Li_2S_x\ @\ 272\text{ nm})}{A(Li_2S_x\ @\ 420\text{ nm})}$. A correlation between the ratio $\frac{A(272\text{ nm})}{A(420\text{ nm})}$ and the nominal polysulfide chain length is shown in Fig. 2c, in which a horizontal line for short-chain polysulfides ("Li_2S_x," $x \leqslant 4$) and a line with a positive slope for long-chain polysulfides ("Li_2S_x," $x \geqslant 5$) are observed. In theory, the intersection of both lines should indicate the common species Li_2S_x, which could be "Li_2S_4" (likely) or "Li_2S_5" (still possible) in this case. Considering the $S_4{}^{2-}$ assignment in DMSO (420 nm,[21] 435 nm[36]) and in TEGDME (420 nm[9]), we here also assign the spectral features at ~420 nm and at ~300 nm to $S_4{}^{2-}$ in DOL:DME-based electrolyte. The absorption ratios of this two absorption characteristics of $S_4{}^{2-}$ $\left(\frac{A(300\text{ nm})}{A(420\text{ nm})}\right)$ in nominally prepared "Li_2S_2" "Li_2S_3" "Li_2S_4" are presented in Fig. S2 (section 2.3 in the SI). A summary of the peak assignment for the chromophores dissolved in DOL:DME-based electrolyte is shown in the Table I.

Operando ***identification of reaction intermediates in DOL:DME-based electrolyte.***—Here we employ our *operando* UV–vis cell to identify the reaction intermediates during the first discharge of Li-S batteries in DOL:DME-based electrolyte. We apply three different first discharge procedures to better understand the discharge process of Li-S batteries: 1) the conventionally used constant current (CC) discharge (referred to as "CC," as shown in Fig. 3a; 2) a CC discharge with constant voltage (CV) hold at the end of the 1st discharge plateau (CC-CV), followed by a constant current discharge to the end of the 2nd discharge plateau, and a final CV hold (referred to as "2(CC-CV)," shown in Fig. 4a; and, 3) a CC-CV discharge for the 1st plateau (as in 2), followed by a CC discharge into the onset of the 2nd discharge plateau, and a final open circuit voltage (OCV) phase (referred to as "CC-CV-CC-OCV," shown in Fig. 6a). As anode in these *operando* UV–vis cell experiments, we use pre-lithiated graphite rather than lithium metal, as the latter was shown to introduce changes in the spectroscopic background during cell cycling owing to the chemical reactions between lithium metal and electrolyte salt and/or solvent, which is further discussed in the section 3.1 of SI. Representative electrochemistry when employing pre-lithiated and pre-formed graphite instead of lithium metal in lithium-sulfur batteries has been shown in our previous study.[18] No background correction (subtraction of pure electrolyte in the *operando* cell configuration) is performed for the UV–vis analysis in order to prevent any overcorrection due to cell-to-cell variations in terms of slit alignment (on separator/electrodes) and beam alignment. Thus, the obtained *operando* UV–vis spectra in this study are only adjusted to have the same baseline (at 700 nm).

Analysis of the polysulfide species formed during the 1st discharge plateau.—Figure 3a shows the voltage profile for a conventional constant current (CC) discharge in our *operando* UV–vis cell at a C-rate of 0.05 h^{-1}. Two well-defined discharge plateaus and a clear transition region between the 1st and the 2nd discharge plateau can be seen, and a reasonable discharge capacity (~45% of the theoretical capacity) is achieved, despite the high electrolyte volume to sulfur mass (E/S) ratio and the slit in the separator. Figures 3b–3d show the evolution of the *operando* UV–vis spectra during the first constant current discharge.

The very first UV–vis spectrum (lightest blue) in Fig. 3b is taken during the initial OCV phase prior to the first discharge (~30 min after cell assembly). An absorption at 265–285 nm in this spectrum is assigned to S_8, evident from the comparison with the reference spectrum obtained from the electrolyte with 1 mM S_8 (acquired in a cuvette; red line), and therefore indicating the dissolution of elemental S_8 from the S_8/C cathode upon exposure to the electrolyte. At the start of discharge, the S_8 features (265–285 nm) gradually weaken and two additional shoulders appear in the spectra, namely at ~300 nm and at ~420 nm, which have been attributed to $S_4{}^{2-}$ in the peak assignment analysis of our *ex situ* data with reference solutions (Fig. 2). At the end of the first discharge plateau (at ~1.4 h), the UV–vis spectrum is dominated by $S_4{}^{2-}$ features, suggesting that by the end of the first discharge plateau, most S_8 has been reduced to $S_4{}^{2-}$, consistent with the hypothesis reported by Waluś et al.[31] using *operando* XRD. This might seem surprising, as the first step of S_8-reduction is generally considered to be the reduction of elemental S_8 to $S_8{}^{2-}$[6,21,34,36,37,39,58]:

$$S_8 + 2e^- \rightarrow S_8^{2-} \qquad [14]$$

However, no significant additional absorption features other than those of S_8 (265–285 nm) and $S_4{}^{2-}$ (~300 nm, ~420 nm) are visible in Fig. 3b, consistent with the observation reported by Zou and Lu[10] in DOL:DME (1:1, v:v) electrolyte with 1 M LiTFSI. This absence of additional absorption characteristics can be rationalized by the instability of $S_8{}^{2-}$ in DOL:DME-based electrolyte, i.e., any $S_8{}^{2-}$ intermediate either undergoes a fast subsequent electrochemical reduction (Eq. 15) or/and a chemical disproportionation (Eq. 16) before it can diffuse to the detection region (i.e., to the slit through which the UV–vis beam is passing), which is estimated to occur within ~12 min. This fast conversion of S_8 to $S_4{}^{2-}$ in DOL:DME (1:1, v:v) electrolyte with 1 M LiTFSI has also been reported in our previous work,[6] where we have shown a direct electron transfer process with >4 e^-/S_8 for S_8 reduction within the time scale of an RRDE experiment (seconds to[6,21,28,34,58] minutes).[9,54]

$$S_8^{2-} + 2e^- \rightarrow 2S_4^{2-}, \qquad [15]$$

$$S_8^{2-} \leftrightarrow \frac{1}{2}S_8 + S_4^{2-}, \qquad [16]$$

Based on the Beer–Lambert law, one can estimate the observed maximum $S_4{}^{2-}$ concentration in the *operando* cell from its characteristic adsorption at 420 nm that, as shown in Fig. 3b, reaches a maximum of ~1.1 absorbance units over a background of ~0.44 absorbance units, i.e., a net absorbance of ~0.66:

$$c(S_4^{2-}) = \frac{A_{net}(420\text{ nm})}{b^*\varepsilon(420\text{ nm})} = \frac{0.66}{0.04\text{ cm}^*1033\ \text{l}^*\text{mol}^{-1}\text{cm}^{-1}} \approx 16\text{ mM} \qquad [17]$$

where $\varepsilon(420\ nm)$ is the molar absorptivity of $S_4{}^{2-}$ at 420 nm, determined by *ex situ* samples, as shown in Fig. S4, and b is the

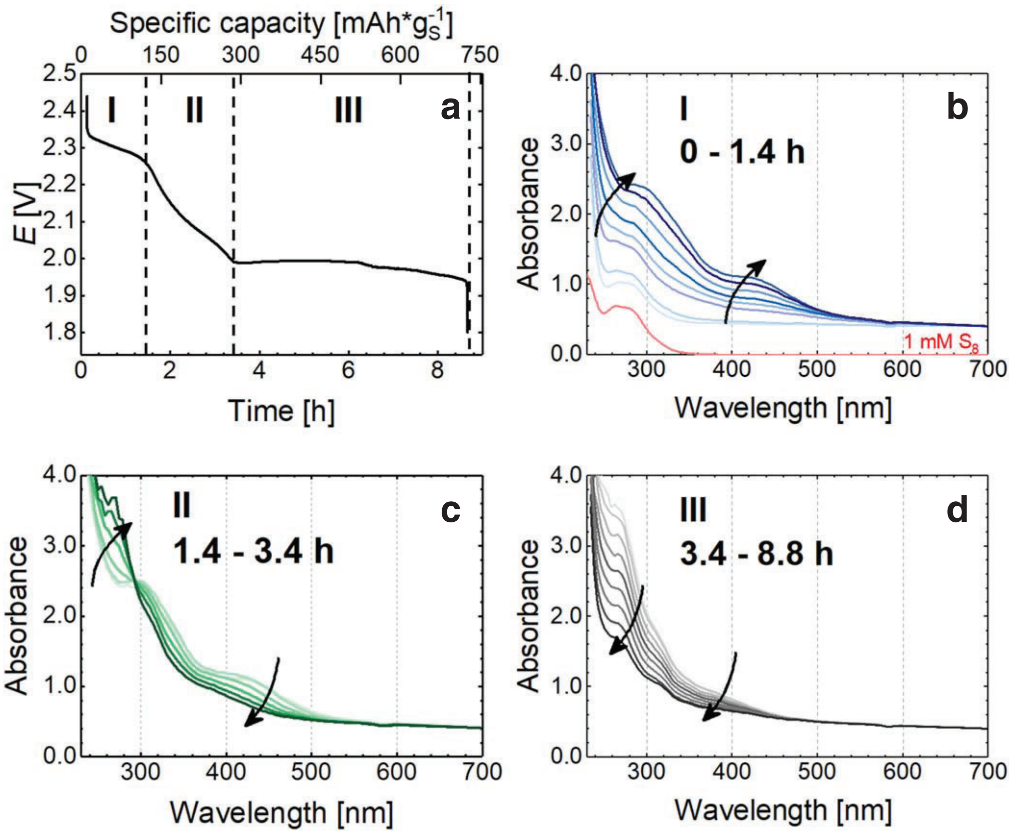

Figure 3. *Operando* UV–vis spectra for a conventional constant current (CC) discharge at a C-rate of 0.05 h^{-1} (referred to as "CC"). (a) Discharge voltage vs time of the *operando* UV–vis cell with an S$_8$/C cathode (0.17 mAh cm^{-2}), a graphite anode pre-lithiated to 50% SOC (referred to as LiC$_6$ (50% SOC), with ~0.22 mAh cm^{-2} delithiation capacity), four separators (Celgard H2013), and 200 μl of DOL:DME (1:1, v:v) with 1 M LiTFSI and 0.1 M LiNO$_3$. The *operando* UV–vis spectra are shown for three different voltage regions (see panel (a)): (b) for the 1st discharge plateau (I), showing one spectrum every ~0.2 h; (c) for the transition between the 1st and the 2nd discharge plateau (II), showing one spectrum every ~0.4 h; and, (d) for the 2nd discharge plateau, showing one spectrum every ~0.6 h.

beam path length through the *operando* UV–vis cell (~0.04 cm). Alternatively, we can also estimate the maximum average S_4^{2-} concentration in the cell specified in Fig. 3, based on the total amount of sulfur in the cell (0.17 mg) and the total amount of electrolyte (200 μl), resulting in ~6.8 mM S_4^{2-}. This higher value calculated from the Beer–Lambert law can be explained by the necessarily inhomogeneous distribution of polysulfides over this rather short time scale (~1.4 h), since a significant fraction of the electrolyte will be outside the active area (i.e., outside the 15 mm electrode diameter) so that homogenous mixing would be expected to be very long.

In the transition region between the 1st and 2nd plateau, the absorption at ~420 nm and ~300 nm drops quickly (Fig. 3c), while another so far unidentified absorption feature at ~266 nm increases rapidly until the end of this transition region. This unidentified absorption feature becomes a dominate feature at the 2nddischarge plateau and decreases slowly until the end of discharge with a small residual signal remaining at the end of discharge (see Fig. 3d). Here is should be noted that the small shoulder at ~326 nm in Fig. 3d originates from the lamp switch (from Vis-lamp to UV-lamp) of the UV–vis spectrometer.

Analysis of the S_x^{2-} species formed after 1st discharge plateau.— To validate that the observed strong absorption at ~266 nm that appears in the transition from the 1st to the 2nd discharge plateau is not an artefact and to achieve a higher time resolution, we modified the cycling procedure to include a constant voltage (CV) phase (labeled as region II in Fig. 4a) at the end of the 1stdischarge plateau (labeled as region I in Fig. 4a), at a point just prior to the appearance of this feature at ~266 nm. This was followed by another CC discharge, for which we noted two spectroscopically distinct regimes, one until the onset of the 2nd discharge plateau (transition region between 1st and 2nd discharge plateau, region III) and one until the end of the 2nd discharge plateau (region IV). This was followed by another CV phase at the final potential of 1.85 V (region V) and the entire procedure will be referred to as "2(CC-CV)" discharge. Analagous to what was shown in Fig. 3b, elemental S$_8$ (~265–285 nm) is reduced to S_4^{2-} (~300 and ~420 nm) during the 1st discharge plateau (see Fig. 4b). Throughout the subsequent CV phase (at ~2.2 V, see Fig. 4c) marked as region II, the absorption of S_4^{2-} (at ~300 and 420 nm) keeps increasing gradually, which confirms that S_4^{2-} is stable at 2.2 V, contrary to S$_8$. The minor but still noticeable increase of the absorbances A(~420 nm) and A (~300 nm) of S_4^{2-} in the CV phase in region II can be rationalized by the continuous reduction of residual S$_8$ that is dissolved in the electrolyte, in regions of the *operando* cell that are not in close proximity to the working electrode. The last two spectra in Fig. 4c are essentially identical, suggesting that the polysulfides formed in the *operando* cell are in equilibrium and that the S_4^{2-} concentration has reached its maximum. Next, the *operando* cell is discharged further at constant current through the transition region between the 1st and the 2nd discharge plateau (region III in Fig. 4a). Consistent with the spectra shown in Fig. 3c (labeled there as region II), we also observe for the transition region in Fig. 4d that the absorption at ~300 and ~420 nm drops significantly while the absorption at ~266 nm increases strongly over the ~1.5 h duration of the transition region. Once the 2nd discharge plateau is reached (region IV in Fig. 4a), the absorption at ~266 nm starts to decrease continuously (purple colored lines in Fig. 4e). This trend continues over the 3 h CV phase at ~1.85 V (region V in Fig. 4a) that is

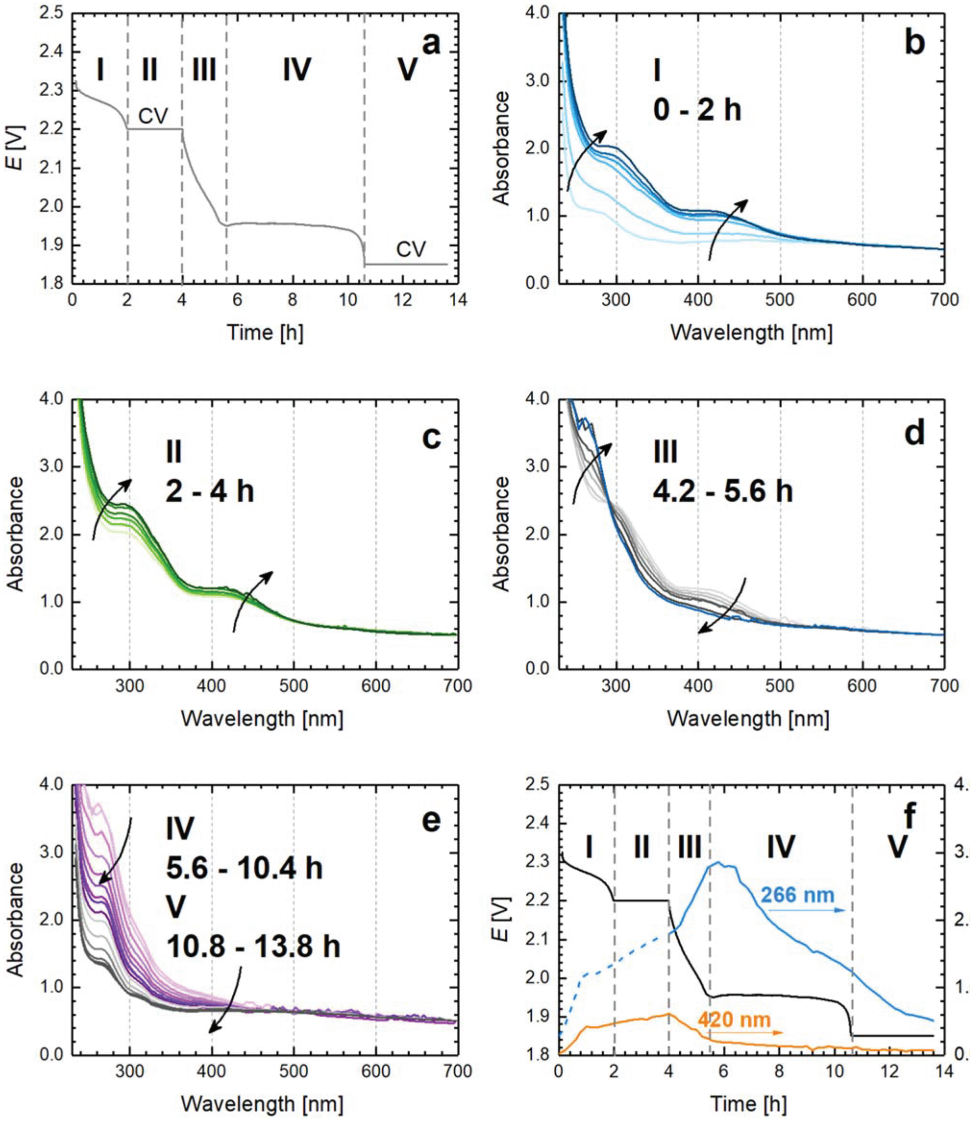

Figure 4. *Operando* UV–vis spectra for a CC discharge at 0.05 h^{-1} C-rate with a 2 h CV hold at the end of the 1st discharge plateau (regions I & II), followed by a CC discharge at 0.05 h^{-1} to the end of the 2nd discharge plateau (regions III & IV), and a final CV hold (region V) (referred to as "2(CC-CV)"). (a) Discharge voltage vs time of the *operando* UV–vis cell with an S_8/C cathode (0.24 mAh cm^{-2}), a graphite anode pre-lithiated to 50% SOC (~0.4 mAh cm^{-2} delithiation capacity), four separators (Celgard H2013), and 200 μl of DOL:DME (1:1, v:v) with 1 M LiTFSI and 0.1 M $LiNO_3$. The *operando* UV–vis spectra are shown for five different voltage regions: (b) for the 1st discharge plateau (I; one spectrum every ~0.4 h); (c) for the CV hold at the end of the 1st discharge plateau (II; one spectrum every ~0.4 h); (d) for the CC discharge during the transition from the 1st to the 2nd discharge plateau (III; one spectrum every ~0.2 h); and, (e) for the CC discharge during the 2nd discharge plateau (IV; one spectrum every ~0.6 h; purple lines), and for the final CV hold (V; one spectrum every ~0.6 h; gray/black lines). (f) Evolution of the baseline corrected absorbance at 266 nm (blue) and 420 nm (yellow) in the *operando* cell along with the voltage profile (black). Since several chromophores strongly absorb at 266 nm (e.g., S_8, S_4^{2-}, and S_x^{2-}), we separated its evolution into two regions, viz., one before (dash blue line) and one after the S_x^{2-} formation (solid blue line), which demonstrates that different processes contribute to the absorbance at 266 nm.

applied at the end of the second discharge plateau (see gray/black lines in Fig. 4e).

With the here described modified "2(CC-CV)" discharge procedure, we thus confirmed that the absorption at ~266 nm is not an artefact but an actual absorption from an as yet unidentified chromophore in the *operando* UV–vis cell. Considering the possible chromophore (S_8, S_x^{2-}, electrolyte consisting of DOL:DME (1:1, v:v), LiTFSI, $LiNO_3$) and comparing the already established UV–vis spectra of S_8 (Fig. 3b, red line) and of the electrolyte (Fig. S3c in section 3.1 of the SI), we propose that these unidentified species with absorption ~266 nm correspond to an as yet uncharacterized polysulfide species S_x^{2-}. In contrast to the here shown results, this absorption at ~266 nm was not observed by Zou and Lu[10] in DOL:DME-based electrolyte, who exploited a spectroelectrochemical cell (cuvette-based design by employing a gold working electrode placed into a 1 mm thick cuvette) to investigate the cyclic voltammogram of the sulfur electrode in a Li-S cell. After careful analysis, we believe that this discrepancy is related to differences in the potential and time resolution over the discharge process. While our "CC" and "2(CC-CV)" discharge procedures require ~9 and ~14 h, respectively, over the ~500 mV discharge potential range (from 2.35 V to 1.85 V), during which spectra are taken every ~10 min, the entire discharge process over a range of 700 mV (from 2.4 V to 1.7 V vs a lithium metal anode) is completed within ~12 min in the study by Zou and Lu.[10] The unidirectional diffusion across the 1 mm thick cuvette in their case may not fulfill the thin-layer (diffusion) condition,[59] which might complicate the deconvolution of the overlapping spectra of unreacted S_8 and the various formed polysulfides, especially in the region below 300 nm.

Figure 4f shows the evolution of two of the major absorption features over the course of discharge, namely that at ~266 nm and that at ~420 nm. While the ~420 nm feature is an exclusive characteristic of S_4^{2-}, the absorption at ∼266 nm is shared by S_8, S_4^{2-}, and the as yet unidentified S_x^{2-} species, so that a careful interpretation of the evolution of the absorption feature at ∼266 nm is required. Clearly, the drastic increase of the absorption at ∼266 nm in the transition region (region III in Fig. 4f) is accompanied by a strong decrease of the absorption at ∼420 nm, suggesting a conversion of S_4^{2-} species (marked by the ∼420 nm absorption) to species with a characteristic absorption at ∼266 nm. Considering that this process only happens after the 1st discharge plateau, where dissolved S_8 is no longer present, and considering that the concentration of S_4^{2-} is clearly decreasing (orange line in Fig. 4f), we assign this increase of the adsorption at ∼266 nm to the unidentified S_x^{2-} species, which must be a soluble reduction product of S_4^{2-}, i.e., either S_3^{2-}or S_2^{2-}.

We also observe that the absorption at ∼266 nm is the dominant absorption feature in the *operando* cell after the transition region between the 1st and the 2nd discharge plateau, which suggests that the conversion of these S_x^{2-} species to Li_2S must be the main process that occurs during the 2nd discharge plateau. In this case, the conversion of the S_x^{2-} species to Li_2S could in principle contribute ∼50% ($x = 2$) or ∼67% ($x = 3$) of the total theoretical capacity of a Li-S battery. Bearing in mind that the decrease in capacity with increasing C-rate is generally accompanied by a loss of capacity in the 2nd discharge plateau,[6,11] the conversion of the S_x^{2-} species to Li_2S is likely the rate limiting process in Li-S batteries. Therefore, it would be desirable to identify S_x^{2-} ($x = 3$, 2) and its possible reaction pathways during the 2nddischarge plateau in order to develop a better understanding of the Li-S chemistry in DOL:DME-based electrolytes.

S_3^{2-} was reported several times as a hypothetic species in Li-S chemistry, mostly as the reduction product of the $S_3^{\cdot-}$ radical[10,20,23,34,35]:

$$S_3^{\bullet-} + e^- \rightarrow S_3^{2-} \qquad [18]$$

S_3^{2-} was proposed to be a soluble species in DMSO[10,34,35] and in DMA,[20,23] with an UV–vis absorption at ∼270 nm in DMSO.[35] However, there are no experimental data that would prove the existence of S_3^{2-} in DOL:DME-based electrolyte (consisting of low donor number solvents) or even its possible UV–vis characteristics. Similarly, Li_2S_2 was suspected to be present as a solid in Li-S batteries, yet no actual experimental evidence was provided.[55] In the following, we will first assume that both Li_2S_2 and Li_2S_3 could be present as dissolved species in DOL:DME-based electrolyte and that they could be UV–vis active.

Identification of the S_x^{2-} species via comparison of transferred charges.—Based on the above discussion, the reduction pathway from S_4^{2-} present at the end of the 1st discharge plateau to Li_2S (here referred to as S_1^{2-}) present at the end of the 2nd discharge plateau (Eq. 19) would presumably go through an intermediate reduction step involving S_x^{2-}, as described generally in Eqs. 20 and 21 which sum up to Eq. 19:

$$S_4^{2-} + 6e^- \rightarrow 4S_1^{2-} \qquad [19]$$

$$S_x{}^{2-}\text{ formation:} \quad S_4^{2-} + \frac{8-2x}{x}e^- \rightarrow \frac{4}{x}S_x^{2-} \qquad [20]$$

$$S_x{}^{2-}\text{ consumption:} \quad \frac{4}{x}S_x^{2-} + \frac{8(x-1)}{x}e^- \rightarrow 4S_1^{2-} \qquad [21]$$

Evidence for an intermediate species in the transition region between 1st and 2nd discharge plateau, i.e., for the above suggested S_x^{2-} species can also be seen in the dQ/dV plot for the galvanostatic charge/discharge of an S_8/C//Li cell, with a discharge peak potential of ∼2.2 V vs Li^+/Li, which corresponds to ∼2.1 V vs the graphite anode pre-lithiated to 50% SOC (see Fig. S6 in section 3.4 of the SI). As discussed above, we believe that the S_x^{2-} species in Eqs. 19 and 20 are either S_2^{2-} or S_3^{2-}. In the case of S_2^{2-}, Eqs. 20 and 21 can be written as follows:

$$S_2{}^{2-}\text{ formation:} \quad 1S_4^{2-} + 2e^- \rightarrow 2S_2^{2-} \qquad [22]$$

$$S_2{}^{2-}\text{ consumption:} \quad 2S_2^{2-} + 4e^- \rightarrow 4S_1^{2-} \qquad [23]$$

On the other hand, if the S_x^{2-} species were to correspond to S_3^{2-}, Eqs. 20 and 21 would transform into:

$$S_3{}^{2-}\text{ formation:} \quad 1S_4^{2-} + \frac{2}{3}e^- \rightarrow \frac{4}{3}S_3^{2-} \qquad [24]$$

$$S_3{}^{2-}\text{ consumption:} \quad \frac{4}{3}S_3^{2-} + \frac{16}{3}e^- \rightarrow 4S_1^{2-} \qquad [25]$$

In the following, we present two different analysis approaches that suggest that the S_x^{2-} species do not correspond to S_2^{2-}, and instead indicates that they correspond to S_3^{2-}. We first compare the actually measured electrons/charges transferred in the experiment shown in Fig. 4a with that predicted by each set of the two intermediate reaction steps (Eqs. 22 and 23 for S_2^{2-} or Eqs. 24 and 25 for S_3^{2-}). Furthermore, we utilize the rotating ring disk electrode (RRDE) technique to directly determine the electrons transferred for the reduction step represented by $S_4^{2-} \rightarrow S_x^{2-}$. Both analysis approaches reveal consistent results and are presented in the following.

One way to differentiate the two reaction pathways is to compare the electrons transferred in the two intermediate reaction steps (Eqs. 22 and 23 for S_2^{2-} or Eqs. 24 and 25 for S_3^{2-}). For example, if the intermediate species were to be S_2^{2-}, Eq. 22 would imply that 2 S_2^{2-} would be generated from 1 S_4^{2-} with the transfer of 2 e^-. In this case, a maximum of another 4 e^- can be transferred to form 4 S_1^{2-} (based on Eq. 23, assuming 100% conversion). Therefore, the ratio of electrons transferred in the Eq. 23 (S_2^{2-} consumption) over that in the Eq. 22 (S_2^{2-} formation) would be $\frac{\#\,\text{e in eq. 23}}{\#\,\text{e in eq. 22}} \leqslant 2$, whereby a value of 2 would be expected for a 100% conversion of S_2^{2-} to S_1^{2-}. Similarly, if S_3^{2-} would be the intermediate, the ratio of electrons transferred in the Eq. 25 (S_3^{2-} consumption) over that in the Eq. 24 (S_3^{2-} formation) would be $\frac{\#\,\text{e in eq. 25}}{\#\,\text{e in eq. 24}} \leqslant 8$.

In the following, we will correlate this analysis of transferred electrons to the voltage profile shown in Fig. 4a, which is replotted in Fig. 5a (there, region V is omitted for clarity). More specifically, we will assign the region III and IV in the voltage profile (Fig. 5a) to the intermediate step of S_x^{2-} formation (Eqs. 20) and of S_x^{2-} consumption (Eqs. 21), respectively. In order to do so, this assignment requires that at the end of the first plateau and after the CV hold (i.e., at the end of region II in Fig. 4a) S_4^{2-} species are predominant and have reached their maximum concentration, corresponding to an essentially complete conversion of S_8 to S_4^{2-}. This is suggested by the last two spectra in Fig. 4c and also by the spectral analysis discussed in section 3.3 of the SI. It also requires that the generated S_4^{2-} is largely consumed during the transition region (region III), as is indeed suggested by the UV–vis data in Fig. 4f (see orange line based on the absorbance at 420 nm) and by the rather facile reduction of S_4^{2-} based on the rapid decrease of A (420 nm) in this region. Finally, for the here proposed sequential reactions (either Eqs. 22/23 or Eqs. 24/25), one would expect that the formed intermediate S_x^{2-} species would reach their maximum concentration at the end of the transition region, as indeed is indicated by the maximum absorbance at ∼266 nm at the end of region III, albeit the consumption of S_4^{2-} and the absence of S_8 (see blue line in Fig. 4f). Based on these considerations, it is reasonable to assume that the process in region III follows Eqs. 22 or 24 (formation of S_x^{2-}) and that the process in region IV follows Eqs. 23 or 25 (consumption of S_x^{2-}), as was hypothesized above.

An evaluation of the charges transferred in the 2nd discharge plateau (region IV) and in the transition region (region III) from the

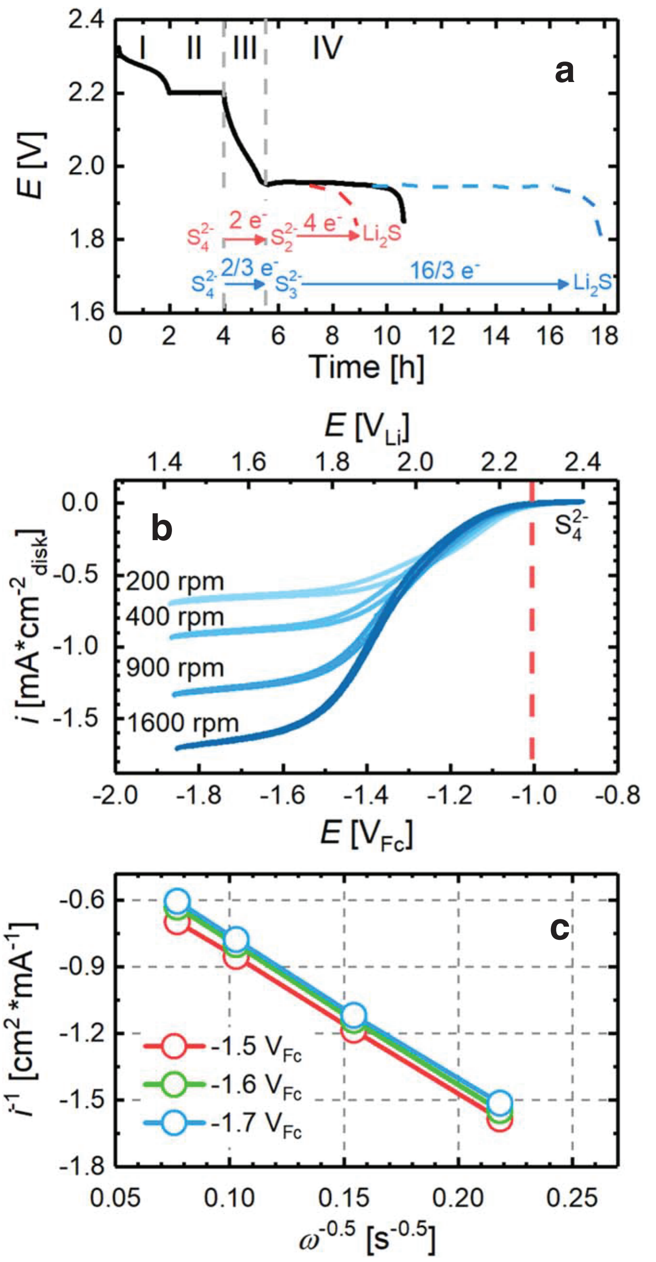

Figure 5. (a) Voltage profile of *operando* UV–vis cell replotted from Fig. 4 (the final CV phase is omitted here for clarity); the red printed reaction sequence corresponds to Eqs. 22 and 23 and the dashed red line sketches of the expected final discharge capacity for this reaction sequence, while the blue printed reaction sequence corresponds to Eqs. 24 and 25 and the dashed blue line sketches of the expected final discharge capacity for this reaction sequence. (b) Rotating ring disk electrode experiment: capacitively and ohmically corrected disk currents recorded vs the Li^+/Li or the Fc^+/Fc potential (note that that the Li^+/Li potential is ∼0.1 V negative of the pre-lithiated graphite electrode) plotted at 50 mV s^{-1} in Ar-saturated solution of 4 mM "Li_2S_4" with 1 M LiTFSI DOL:DME (1:1, v:v). (c) Koutecky-Levich plot of 1/i vs $1/\omega^{-0.5}$ (with ω in rad s^{-1}) at different potentials.

operando UV–vis data in Fig. 4a (replotted in Fig. 5a) yields a charge ratio value of $\frac{Q(region\ IV)}{Q(region\ III)} = 3.3$, which is greater than the maximum value of $\leqslant 2$ that would be expected for an S_2^{2-} intermediate, but smaller than the value of $\leqslant 8$ that would be expected for an S_3^{2-} intermediate (also illustrated by the red and blue colored reaction sequences in Fig. 5a). Consistent with our results, it is often reported that in DOL:DME-based Li-S batteries the capacity delivered by the 2nd discharge plateau is at least twice as large as the capacity delivered in the transition region.[1,6,7,11,13,15,18,27,47,48] In cells where the polysulfide redox shuttle is prevented by using an Li^+ conducting glass ceramic (LiCGC) in which ∼100% discharge capacity was achieved at C/17, this ratio is as large as ∼5.[6] The fact that the here found charge ratio is larger than that of $\leqslant 2$ expected for S_2^{2-} intermediates, suggests that the intermediates are more likely S_3^{2-} rather than S_2^{2-} species.

Identification of the meta-stable S_x^{2-} species via rotating ring disk electrode measurements.—Another approach to resolve the nature of the S_x^{2-} species is to determine the number of electrons involved in the S_4^{2-} reduction process. Here, we employ the rotating ring disk electrode (RRDE) technique to quantify the electrons transferred during S_4^{2-} reduction by means of a Koutecky-Levich analysis in order to determine the product of the S_4^{2-} reduction. For this, we prepared 4 mM nominal "Li_2S_4" solution in DOL:DME (1:1, v:v) with 1 M LiTFSI by mixing the appropriate amounts of Li_2S and elemental S_8. To ensure that S_4^{2-} is sufficiently stable in DOL:DME-based electrolyte within the time scale of an RRDE experiment (hours), we examined the stability of S_4^{2-} using UV–vis spectroscopy and observed no significant spectroscopic changes over a period of ∼24 h (see section 3.5 in the SI, Fig. S7).

In the RRDE measurements, the potential was negatively scanned until 1.4 V_{Li} (corresponding to $-1.9\ V_{Fc}$) in order to reduce S_4^{2-} and scanned positively only up to 2.4 V_{Li} ($-0.85\ V_{Fc}$) to prevent the oxidation of S_4^{2-} to S_8, which would interfere in subsequent measurements. At the lowest rotation rate of 200 rpm a single diffusion limited current density plateau is obtained; at higher rotation rates, the limiting current density plateau is not reached, but there is clearly no transition to a different number of exchanged electrones observed (see Fig. 5b). From this, the number of electrons (n) transferred in the electrochemical reaction can be determined using a Levich-Koutecky plot of $\frac{1}{i}$ vs ω^{-1} (ω being the RRDE rotation rate in units of rad s^{-1}), as shown in Eq. 26 and Fig. 5c.

$$\frac{1}{i} = \left(\frac{1}{i_k}\right) + \left(\frac{1}{0.62 \cdot n \cdot F \cdot D^{2/3} \cdot \upsilon^{-1/6} \cdot c}\right) \cdot \omega^{-1/2} \qquad [26]$$

Here, n is the number of exchanged electrons, F is Faraday′s constant (96485 A·s·mol^{-1}), c is the "S_4^{2-}" concentration, v is the electrolyte kinematic viscosity, D is the diffusion coefficient of "S_4^{2-}," i is the measured current density, and i_k is the kinetic current density. For known viscosity and diffusion coefficient, the number of exchanged electrons can be quantified. The viscosity was measured with a rheometer (0.014 cm^2 s^{-1}) and the diffusion coefficient D (7.0×10^{-6} cm^2 s^{-1}) was obtained through disk-potential stepping experiments. The experiment details and the comparison of D obtained in this study with the literature are discussed in section of 1.2 of the SI. Based on the Levich-Koutecky correlation (Eq. 26, Fig. 5c), the number of electrons passed during S_4^{2-} reduction is determined to be ∼0.9 ± 0.25 e^-/S_4^{2-}, which is reasonably close to the expected 0.67 e^-/S_4^{2-} when S_3^{2-} would be the reduction product (see Eq. 24) and quite different from the 2 e^-/S_4^{2-} when S_2^{2-} would be the reduction product (Eq. 22).

Both Levich-Koutecky analysis and coulomb ratio analysis of $\frac{Q(region\ IV)}{Q(region\ III)}$ suggest that S_3^{2-}, rather than S_2^{2-}, is likely the product of S_4^{2-} reduction. We therefore assign the unknown absorption at ∼266 nm in UV–vis spectrum in DOL:DME-basedelectrolyte to S_3^{2-}.

Zou and Lu[10] as well as Kim and Park[35] have proposed S_3^{2-} to be the reduction product of $S_3^{-\cdot}$ in DMSO (a high donor number solvent), and ascribed the UV–vis absorption feature at ∼270 nm to S_3^{2-}, which closely coincides with our assignment of the absorption at ∼266 nm to S_3^{2-} in DOL:DME-based electrolyte (both low donor number solvents). Moreover, Assary et al.[54] have computed the energetics of disproportionation and association reactions of polysulfide molecular clusters as well as their likely intermediates, based on which they suggested that S_3^{2-} would be the most abundant intermediate after the complete reductive consumption of S_8^{2-} in solvents such as water, DMSO, ACN, and acetone.[54] Therefore, our hypothesis that S_3^{2-} (~266 nm) is the major liquid intermediate at the 2nd discharge plateau in DOL:DME-based electrolytes seems consistent with our analysis and the above discussed literature.

Probing the reaction pathways of S_3^{2-} formation and depletion.—In the following, we want to probe the formation and depletion reactions of S_3^{2-} in order to better understand the discharge mechanism of Li-S batteries in DOL:DME-based electrolytes.

Formation of S_3^{2-}: The formation of S_3^{2-} in high donor number solvents has so far always been proposed to originate from $S_3^{\cdot -}$ reduction (see. Eq. 17).[10,20,23,35] Yet, in our *operando* UV–vis experiments with DOL:DME (see Figs. 3 and 4) we observed no detectable concentration of $S_3^{\cdot -}$ at/near its absorption at ~618 nm reported for DMSO. Based on the molar absorptivity of $S_3^{\cdot -}$ at ~618 nm in DMSO (~4500 l·mol^{-1}·cm^{-1})[21] and assuming that an absorbance of 0.02 is the detection limit for our *operando* UV–vis cell experiments, the maximum concentration of S_3^{2-} in our experiments must be <0.1 mM. Therefore, the rapid increase of the absorption at ~266 nm in the transition region (see region III in Fig. 4f) which we ascribe to the formation of S_3^{2-} cannot be caused by the reduction of $S_3^{\cdot -}$. Furthermore, our *ex situ* UV–vis analysis of "Li_2S_4" dissolved in DOL:DME-based electrolyte demonstrates the long-term stability of S_4^{2-} in this electrolyte (see Fig. S7 in section

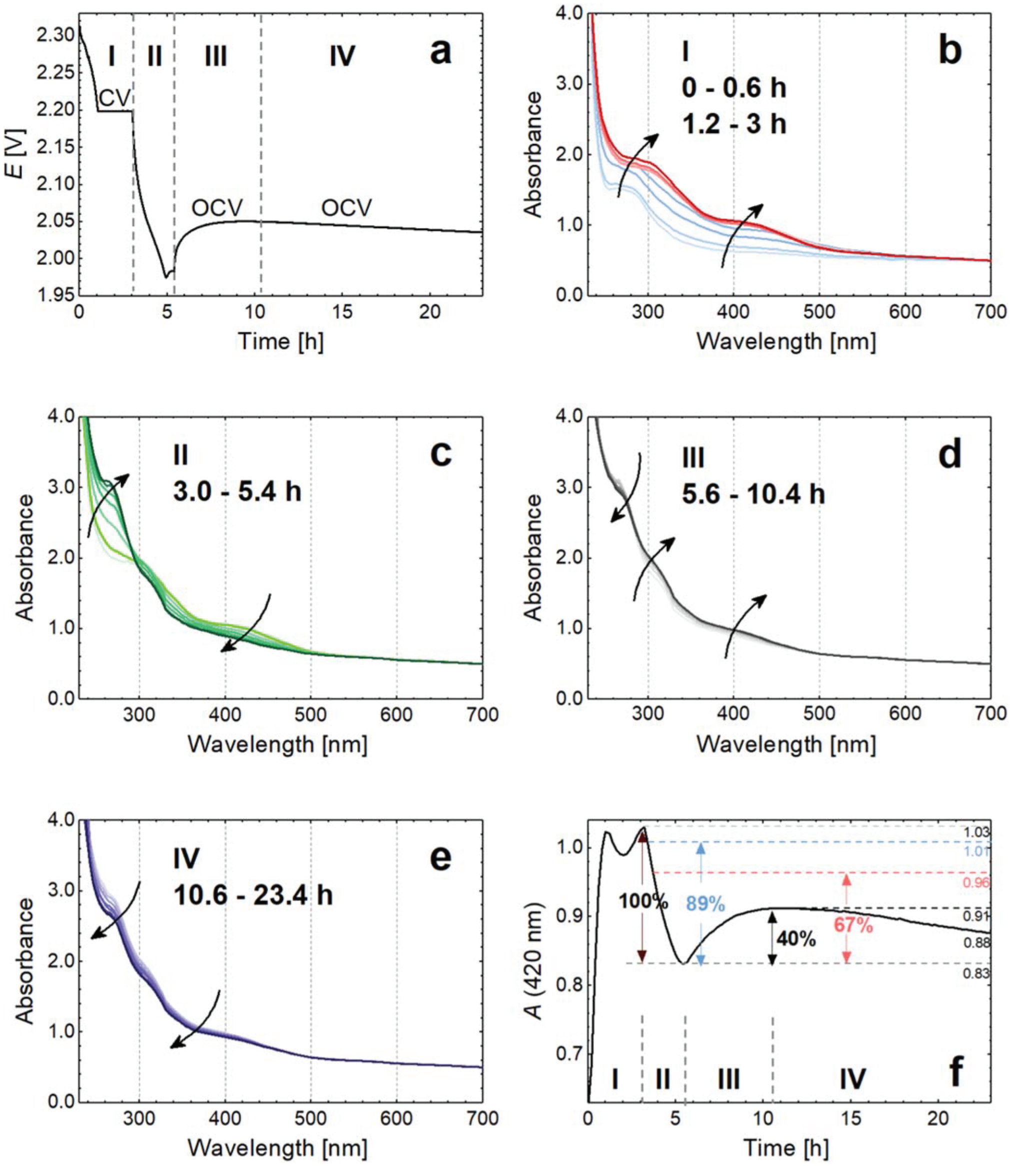

Figure 6. *Operando* UV–vis spectra for a CC discharge at 0.05 h^{-1} C-rate with a 2 h CV hold at the end of the 1st discharge plateau (region I), followed by a CC discharge at 0.05 h^{-1} into the onset of the 2nd discharge plateau (region II), and a final open circuit voltage (OCV) phase at the end of the transition region into the 2nd discharge plateau (regions III & IV) (referred to as "CC-CV-CC-OCV"). (a) Discharge voltage vs time of the *operando* UV–vis cell with an S_8/C cathode (0.16 mAh cm^{-2}), a graphite anode pre-lithiated to 50% SOC (~0.22 mAh cm^{-2} delithiation capacity), four separators (Celgard H2013), and 200 μl of DOL: DME (1:1, v:v) with 1 M LiTFSI and 0.1 M $LiNO_3$. The *operando* UV–vis spectra are shown for four different voltage regions: (b) for the 1st discharge plateau and the subsequent CV hold (I; first four spectra were taken every~0.2 h (in blue color) and subsequent spectra every ~0.6 h (in red color)); (c) for the CC discharge during the transition from the 1st to the 2nd discharge plateau (II; one spectrum every ~0.4 h); (d) during the initial OCV phase at the onset of the 2nd discharge plateau (III; one spectrum every ~0.8 h); and, (e) at later stages of the OCV phase (IV; one spectrum every ~2 h). (f) Evolution of the baseline corrected absorption at 420 nm for the voltage profile shown in panel (a); the numbers in percent represent the change of A(420 nm) referenced to the initial decrease of A(420 nm) in region II, where the 67% (blue dashed line) and 89% (pink dashed line) mark the guidelines for A(420 nm) change, when S_2^{2-} or S_1^{2-} would be the product of S_3^{2-} disproportionation reaction, respectively.

of 3.5 of the SI), suggesting that S_3^{2-} cannot either be produced from the self-disproportionation of S_4^{2-} (acc. to Eq. 5). Therefore, we believe that S_3^{2-} is mainly produced by the electrochemical reduction of S_4^{2-}(Eq. 24).

Depletion of S_3^{2-}: In principle, two possible reaction pathways can be postulated for S_3^{2-} depletion, viz., by its electrochemical reduction or by a chemical disproportionation reaction. Since Li_2S was reported to be detected already at the beginning of 2nd discharge plateau through *operando* XRD[31] and XANES,[7] a direct reduction of S_3^{2-} to Li_2S (Eq. 27) would be a reasonable assumption.

$$S_3^{2-} + 4e^- \rightarrow 3S_1^{2-} \qquad [27]$$

However, an analysis of the absorbance at ∼266 nm suggests that Eq. 27 is unlikely the only pathway for S_3^{2-} reduction to the final S_1^{2-} product (see section 3.6 of the SI). Apart from its direct electrochemical reduction to S_1^{2-} (Eq. 27), S_3^{2-} could also first be reduced electrochemically to S_2^{2-} (Eq. 28),

$$S_3^{2-} + 1e^- \rightarrow \frac{3}{2}S_2^{2-} \qquad [28]$$

followed either by a subsequent electrochemical reduction reaction (Eq. 29)

$$\frac{3}{2}S_2^{2-} + 3e^- \rightarrow 3S_1^{2-} \qquad [29]$$

or by a disproportionation reaction (Eq. 30)

$$\frac{3}{2}S_2^{2-} \leftrightarrow \frac{3(x-2)}{2(x-1)}S_1^{2-} + \frac{3}{2(x-1)}S_x^{2-},\ (x > 2) \qquad [30]$$

Unfortunately, a more detailed discussion of Eqs. 28–30 is beyond the scope of this study, as S_2^{2-} cannot be detected by UV–vis spectroscopy and as there is insufficient information about S_2^{2-} in the literature.

To investigate whether S_3^{2-} can be depleted through chemical disproportionation reactions, we examined its stability over time using UV–vis spectroscopy. Here, we electrochemically produce S_3^{2-} in situ in the *operando* cell and monitor it over a subsequent extended OCV period by UV–vis spectroscopy. In order to do so, we adopted the cycling procedure from Fig. 4a until the beginning of the second discharge plateau to achieve a maximal concentration of S_3^{2-} (i.e., progressing through regions I-III in Fig. 4a) and then kept the cell at OCV for about 18 h, as is shown in Fig. 6a (furtheron referred to as CC-CV-CC-OCV procedure). As expected, the absorption at ∼266 nm (predominantly from S_3^{2-}, as both S_8 and S_4^{2-} are negligible at the beginning of the 2nd discharge plateau, see Fig. 4f) reaches its maximum at the beginning of the 2nd discharge plateau (see end of region II in Fig. 6c), while the absorption at ∼420 nm (from S_4^{2-}) drops to very low values. In the subsequent OCV phase, we observe an increase of A(420 nm) and A(300 nm) in the first 5 h (region III, Fig. 6d), followed by a gradual decrease of A (266 nm), A(300 nm) and A(420 nm) in the 13 h following this initial OCV period (region IV, Fig. 6e). The evolution of A(420 nm) is plotted in Fig. 6f: referenced to the initial decrease of A(420 nm) in region II, its increase in region III would correspond to ∼40%, as shown in Fig. 6f. Here is to note that the increase of S_4^{2-} within 5 h is unlikely originated from the residual S_4^{2-} outside of the electrode diffusing back into the slit, as the diffusion time is estimated to be ∼10 h based on the shortest diffusion path 5 mm (from electrode perimeter to the edge (in the direction of length) of inner slit) and the measured diffusion coefficient of 7.0×10^{-6} cm^2 s^{-1}.

This 40% increase in the initial ∼5 h OCV phase at the onset of the 2nd discharge plateau (region III in Fig. 6) is quite significant and that suggests that S_4^{2-} is gradually regenerated from S_3^{2-} during the OCV phase by chemical disproportionation reactions (see Eqs. 31 and 32).

$$\frac{4}{3}S_3^{2-} \leftrightarrow \frac{2}{3}S_2^{2-}(\text{reduced}) + \frac{2}{3}S_4^{2-}(\text{oxidized}) \qquad [31]$$

$$\frac{4}{3}S_3^{2-} \leftrightarrow \frac{4}{9}S_1^{2-}(\text{reduced}) + \frac{8}{9}S_4^{2-}(\text{oxidized}) \qquad [32]$$

It should be noted here, that no significant decrease of A(∼266 nm) is observed in region III (s. Fig. 3d) where S_3^{2-} would be consumed by its disproportionation to S_4^{2-} (Eqs. 30 and 31)). This can be rationalized by the regeneration of S_4^{2-}, which in turn, can compensate the decreased absorption at ∼266 nm. (see Fig. 2a or Fig. S7).

This disproportionation reaction verifies the thermodynamic instability of S_3^{2-} in DOL:DME-based electrolytes, which is also in good agreement with the fact that S_3^{2-} (∼266 nm) is not observed in the reference spectra (Fig. 2a) and that it is likely not possible to detect S_3^{2-} in the commonly conducted *ex situ* experiments reported in the literature.[9]

To gain a deeper insight into the reaction product of S_3^{2-} reduction, especially, to address whether Li_2S_2 (Eq. 31) or Li_2S (Eq. 32) can be excluded as the product of S_3^{2-}reduction, a semi-quantitative estimation can be performed. Assuming complete conversion of S_4^{2-} via a first electrochemical reduction step (Eq. 24) and a subsequent disproportionation reaction (Eqs. 31 and 32), a maximum of ∼67% (Eq. 31) or ∼89% (Eq. 32) of S_4^{2-} can be regenerated back from the assumed initial 100% S_4^{2-} conversion (Eq. 23) in the transition region. If the possible regeneration of S_4^{2-} through S_3^{2-} disproportionation were higher than ∼67%, it would then suggest S_1^{2-}, rather than S_2^{2-}, is the reduction product. Therefore we try to estimate the maximal amount of S_4^{2-} that can be regenerated from the S_3^{2-} disproportionation.

At the same time, we also observe a very slow but noticeable decrease of the absorption between 250 and ∼500 nm over the last 13 h of the OCV period (region IV, Fig. 6e). This can be rationalized by 1) the existing polysulfides diffusing out of the electrode over this extend OCV period and 2) a continuous depletion of polysulfide species on the graphite anode on account of an imperfect SEI.

We assume this slow consumption of polysulfides in region IV would also occur in region III, so that this needs to be included in the estimate of the maximal regeneration of the S_4^{2-} concentration in region III. For a rough estimate, the decrease of A(420 nm) between 13–23 h in Fig. 6f can be linearized, yielding a constant A(420 nm) signal loss rate:

$$c = \frac{\Delta A}{\Delta t} = \frac{A_{13h}(420\ \text{nm}) - A_{23h}(420\ \text{nm})}{10\ \text{h}} = 0.003\ h^{-1} \qquad [33]$$

With this estimated A(420 nm) signal loss rate, we can now project the loss of the A(420 nm) signal over the course of the initial OCV period (region III) that is caused by the loss of dissolved polysulfides through its diffusion and the slow but continuous reaction with the lithiated graphite counter electrode:

$$\Delta A_{5.6-10.4\,\text{h}}(420\ \text{nm}) = c^{*}\Delta t = 0.003\ \text{h}^{-1*}\ 4.8\ \text{h} = 0.014 \qquad [34]$$

Adding this value to the (local) maximum of the A(420 nm) signal at 10.4 h (see Fig. 6f), we obtain a maximum A(420 nm) value in the initial OCV period of ∼0.92 (from 0.014 + 0.91), which is about 47% of the decrease of the A(420 nm) signal in region II that is caused by the electrochemical reduction of S_4^{2-} to S_3^{2-} in the transition region.

The estimated increase of ∼47% is lower than both maximum value of ∼67% and of ∼89%, so that we can exclude neither Li_2S_2 (Eq. 31) nor Li_2S (Eq. 32) as the reduced species upon disproportionation of S_3^{2-}.

Proposed discharge mechanism of Li-S batteries in DOL:DME-based electrolyte.—Figure 7 summarizes the reaction intermediates

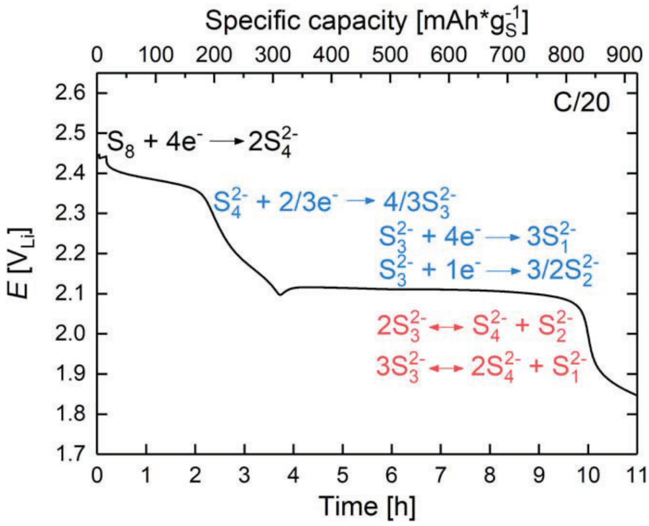

Figure 7. Proposed discharge mechanism of Li-S batteries in DOL:DME-based electrolyte. The relevant electrochemical steps deduced in this study are presented in blue and the disproportionation reactions are presented in red. The exemplary voltage profile (black solid line) is taken from Fig. 1b (blue line).

deduced from our above presented *operando* transmission UV–vis spectroscopy experiments. Based on the proposed discharge reaction pathways, the ratio of coulombic charge delivered at different regions during the discharge would be expected to be as follows:

$$Q(1^{\text{st}}\text{ plateau}){:}\ Q(\text{transition region}){:}\ Q(2^{\text{nd}}\text{ plateau}) \\ = 4e^-{:}\ \frac{4}{3}e^-{:}\ \frac{32}{3}e^- = 3{:}\ 1{:}\ 8 \qquad [35]$$

However, the ratio of Q(2nd plateau):Q(transition region) would always be smaller than = 8:1, since i) the formed S_3^{2-} in the transition region can relatively fast disproportionate to S_4^{2-}, contributing to Q(transition region), and ii) the conversion of S_3^{2-} to Li_2S seems to be limiting (<100% conversion), which would shorten the 2nd discharge plateau.

Like many other research works investigating the Li-S chemistry with transmission UV–vis spectroscopy (e.g., 2 mM S_8 in DOL: DME-based electrolyte,[10] 1.2 mM S_8,[36] and 3 mM S_8,[35] in DMSO-based electrolyte, 2.5 mM S_8 in DMF-based-electrolyte[37]), these low concentrations of sulfur and of the resulting polysulfides are required for UV–vis studies due to the high molar absorptivities of these species. While the relative abundance of the various polysulfides observed in previous studies and in our present study conducted at high E/S ratios may not be in quantitative agreement with that in practical Li-S cells, we do believe that they provide relevant insights into the general speciation in Li-S cells. The mechanistic insights gained in *operando* UV–vis cells restricted to operate at high E/S ratios should still provide further understanding about possible reaction steps and species in the S-redox reactions. Especially, the *operando* UV–vis cell in this study may even present a quite viable, if not the major, reaction pathway of how S_8 is electrochemically discharged to Li_2S_2/Li_2S, as demonstrated by its reasonable discharge voltage profile and discharge capacity, which fairly well resembles those obtained with conventional Li-S cells with high sulfur loadings and low E/S ratios.[11,48]

Conclusions

In this study, we introduce an *operando* transmission UV–vis spectro-electrochemical cell design that is suitable for mechanistic studies of cell chemistries involving soluble chromophoric intermediates, e.g., polysulfides in Li-S batteries.

We accomplish a systematic UV–vis spectroscopic peak assignment for polysulfides in DOL:DME-based electrolyte and, for the first time, we are able to identify and distinguish the liquid intermediates (S_8 and different polysulfides) during the first discharge of a Li-S battery. We show that elemental S_8 is converted to S_4^{2-} during the 1st discharge plateau where other polysulfides are barely detected. The formed S_4^{2-} gets reduced to a meta-stable polysulfide species in the transition region between the two discharge plateaus that dominates the UV–vis spectra over the course of the 2nd discharge plateau. We identify this meta-stable polysulfide as S_3^{2-} via an analysis of the transferred charges and the formed species in the *operando* cell as well as via the number of electrons transferred for S_4^{2-} reduction using the rotating ring disk electrode technique. We show that S_3^{2-} is a meta-stable species that rather quickly disproportionates to S_4^{2-} and Li_2S_2/Li_2S, so that it is difficult to detect in *ex situ* samples/experiments. Our study suggests that the conversion of S_8 to S_4^{2-} and then to S_3^{2-} are fast processes, while the capacity extraction from S_3^{2-} to form Li_2S is limiting the discharge rate in DOL:DME-based Li-S batteries.

Acknowledgments

We would like to acknowledge the funding from the German Federal Ministry for Economic Affairs and Energy (BMWi) under the auspices of the “LiMo” project (funding number 03ET6045D), from the German Federal Ministry of Education and Research (BMBF) under the auspices of the “ExZellTUM II” project (funding number 03XP0081), and from the Deutsche Forschungsgemeinschaft (DFG, German Research Foundation) under Germany’s Excellence Strategy —ECX 2089/1-390776260.

ORCID

Qi He https://orcid.org/0000-0002-2174-8187

References

1. J. Conder, R. Bouchet, S. Trabesinger, C. Marino, L. Gubler, and C. Villevieille, *Nat. Energy*, **2**, 17069 (2017).
2. M. Barghamadi, A. S. Best, A. I. Bhatt, A. F. Hollenkamp, M. Musameh, R. J. Rees, and T. Rüther, *Energy Environ. Sci.*, **7**, 3902 (2014).
3. S. Zhang, K. Ueno, K. Dokko, and M. Watanabe, *Adv. Energy Mater.*, **5**, 1500117 (2015).
4. D. Eroglu, K. R. Zavadil, and K. G. Gallagher, *J. Electrochem. Soc.*, **162**, A982 (2015).
5. L. Cheng, L. A. Curtiss, K. R. Zavadil, A. A. Gewirth, Y. Shao, and K. G. Gallagher, *ACS Energy Lett.*, **1**, 503 (2016).
6. Y.-C. Lu, Q. He, and H. A. Gasteiger, *J. Phys. Chem. C*, **118**, 5733 (2014).
7. Y. Gorlin, A. Siebel, M. Piana, T. Huthwelker, H. Jha, G. Monsch, F. Kraus, H. A. Gasteiger, and M. Tromp, *J. Electrochem. Soc.*, **162**, A1146 (2015).
8. Y. Gorlin, M. U. M. Patel, A. Freiberg, Q. He, M. Piana, M. Tromp, and H. A. Gasteiger, *J. Electrochem. Soc.*, **163**, A930 (2016).
9. C. Barchasz, F. Molton, C. Duboc, J. C. Leprêtre, S. Patoux, and F. Alloin, *Anal. Chem.*, **84**, 3973 (2012).
10. Q. Zou and Y.-C. Lu, *J. Phys. Chem. Lett.*, **7**, 1518 (2016).
11. T. Poux, P. Novák, and S. Trabesinger, *J. Electrochem. Soc.*, **163**, A1139 (2016).
12. H. Wang, N. Sa, M. He, X. Liang, L. F. Nazar, M. Balasubramanian, K. G. Gallagher, and B. Key, *J. Phys. Chem. C*, **121**, 6011 (2017).
13. M. Cuisinier, P.-E. Cabelguen, S. Evers, G. He, M. Kolbeck, A. Garsuch, T. Bolin, M. Balasubramanian, and L. F. Nazar, *J. Phys. Chem. Lett.*, **4**, 3227 (2013).
14. A. Manthiram, Y. Fu, S. Chung, C. Zu, and Y. Su, *Chem. Rev.*, **114**, 11751 (2014).
15. Y. V. Mikhaylik and J. R. Akridge, *J. Electrochem. Soc.*, **151**, A1969 (2004).
16. M. Wild, L. O’Neill, T. Zhang, R. Purkayastha, G. Minton, M. Marinescu, and G. J. Offer, *Energy Environ. Sci.*, **8**, 3477 (2015).
17. Q. He, Y. Gorlin, M. U. M. Patel, H. A. Gasteiger, and Y.-C. Lu, *J. Electrochem. Soc.*, **165**, A4027 (2018).
18. A. T. S. Freiberg, A. Siebel, A. Berger, S. M. Webb, Y. Gorlin, M. Tromp, and H. A. Gasteiger, *J. Phys. Chem. C*, **122**, 5303 (2018).
19. S. D. Talian, J. Moskon, R. Dominko, M. Gaberscek, S. D. Talian, J. Moškon, R. Dominko, and M. Gaberšček, *Appl. Mater. Interfaces*, **9**, 29760 (2017).
20. M. Cuisinier, C. Hart, M. Balasubramanian, A. Garsuch, and L. F. Nazar, *Adv. Energy Mater.*, **5**, 1401801 (2015).
21. R. P. Martin, W. H. Doub, J. L. Roberts, and D. T. Sawyer, *Inorg. Chem.*, **12**, 1921 (1973).
22. H. Yamin, A. Gorenshtein, J. Penciner, Y. Sternberg, and E. Peled, *J. Electrochem. Soc.*, **135**, 1045 (1988).
23. J. Paris and V. Plichon, *Electrochim. Acta*, **26**, 1823 (1981).
24. M. U. M. Patel and R. Dominko, *ChemSusChem*, **7**, 2167 (2014).

25. G. Bieker, J. Wellmann, M. Kolek, K. Jalkanen, M. Winter, and P. M. Bieker, *Phys. Chem. Chem. Phys.*, **19**, 11152 (2017).
26. T. Chivers and P. J. W. Elder, *Chem. Soc. Rev.*, **42**, 5996 (2013).
27. Y. V. Mikhaylik and J. R. Akridge, *J. Electrochem. Soc.*, **150**, A306 (2003).
28. A. Evans, M. I. Montenegro, and D. Pletcher, *Electrochem. Commun.*, **3**, 514 (2001).
29. J. D. Mcbrayer, T. E. Beechem, B. R. Perdue, C. A. Apblett, and F. H. Garzon, *J. Electrochem. Soc.*, **165**, A876 (2018).
30. N. Saqib, G. M. Ohlhausen, and J. M. Porter, *J. Power Sources*, **364**, 266 (2017).
31. S. Waluś, C. Barchasz, R. Bouchet, J.-C. Leprêtre, J.-F. Colin, J.-F. Martin, E. Elkaïm, C. Baehtz, and F. Alloin, *Adv. Energy Mater.*, **5**, 1500165 (2015).
32. H. Jha, I. Buchberger, X. Cui, S. Meini, and H. A. Gasteiger, *J. Electrochem. Soc.*, **162**, A1829 (2015).
33. N. A. Cañas, D. N. Fronczek, N. Wagner, A. Latz, and K. A. Friedrich, *J. Phys. Chem. C*, **118**, 12106 (2014).
34. D.-H. Han, B.-S. Kim, S.-J. Choi, Y. Jung, J. Kwak, and S.-M. Park, *J. Electrochem. Soc.*, **151**, E283 (2004).
35. B.-S. Kim and S.-M. Park, *J. Electrochem. Soc.*, **140**, 115 (1993).
36. R. Bonnaterre and G. Cauquis, *J. Chem. Soc., Chem. Commun.*, **0**, 293 (1972).
37. F. Gaillard and E. Levillain, *J. Electroanal. Chem.*, **398**, 77 (1995).
38. F. Gaillard, E. Levillain, and J. P. Lelieur, *J. Electroanal. Chem.*, **432**, 129 (1997).
39. P. Leghié, J. Lelieur, and E. Levillain, *Electrochem. Commun.*, **4**, 628 (2002).
40. E. Levillain, F. Gaillard, P. Leghie, A. Demortier, and J. P. Lelieur, *J. Electroanal. Chem.*, **420**, 167 (1997).
41. H. Jha and H. A. Gasteiger, *DE Pat. No. 102013005082 A1. Munich, Germany*, Deutsches Patent- und Markenamt (2014).
42. R. D. Rauh, F. S. Shuker, J. M. Marston, and S. B. Brummer, *J. Inorg. Nucl. Chem.*, **39**, 1761 (1977).
43. J. Herranz, A. Garsuch, and H. A. Gasteiger, *J. Phys. Chem. C*, **116**, 19084 (2012).
44. F. Y. Fan and Y. Chiang, *J. Electrochem. Soc.*, **164**, A917 (2017).
45. M. Hagen, D. Hanselmann, K. Ahlbrecht, R. Maça, D. Gerber, and J. Tübke, *Adv. Energy Mater.*, **5**, 1401986 (2015).
46. S.-H. Chung and A. Manthiram, *ACS Energy Lett.*, **2**, 1056 (2017).
47. A. Rosenman, R. Elazari, G. Salitra, E. Markevich, D. Aurbach, and A. Garsuch, *J. Electrochem. Soc.*, **162**, A470 (2015).
48. M. Hagen, P. Fanz, and J. Tübke, *J. Power Sources*, **264**, 30 (2014).
49. A. Kawase, S. Shirai, Y. Yamoto, R. Arakawa, and T. Takata, *Phys. Chem. Chem. Phys.*, **16**, 9344 (2014).
50. P. Leghi, J. Lelieur, and E. Levillain, *Electrochem. Commun.*, **4**, 406 (2002).
51. N. S. A. Manan, L. Aldous, Y. Alias, P. Murray, L. J. Yellowlees, M. C. Lagunas, and C. Hardacre, *J. Phys. Chem. B*, **115**, 13873 (2011).
52. C. Reichardt, *Chem. Rev.*, **94**, 2319 (1994).
53. H.-H. Perkampus, *UV-VIS Spectroscopy and its Applications* (Springer, Berlin Heidelberg) (1992).
54. R. S. Assary, L. A. Curtiss, and J. S. Moore, *J. Phys. Chem. C*, **118**, 11545 (2014).
55. Z. Feng, C. Kim, A. Vijh, M. Armand, K. H. Bevan, and K. Zaghib, *J. Power Sources*, **272**, 518 (2014).
56. M. Helen, M. A. Reddy, T. Diemant, U. Golla-Schindler, R. J. Behm, U. Kaiser, and M. Fichtner, *Sci. Rep.*, **5**, 12146 (2015).
57. T. A. Pascal, K. H. Wujcik, R. Wang, P. Balsara, and D. Prendergast, *Phys. Chem. Chem. Phys.*, **19**, 1441 (2017).
58. T. Fujinaga, T. Kuwamoto, S. Okazaki, and M. Hojo, *Bull. Chem. Soc. Jpn.*, **53**, 2851 (1980).
59. A. J. Bard and L. R. Faulkner, *Electrochemical Methods Fundamentals and Applications* (John Wiley & Sons, INC, New York, NY) 2nd ed. (2000).

Supplementary Information

Operando Identification of Liquid Intermediates in Lithium – Sulfur Batteries via Transmission UV-vis Spectroscopy

Qi He,[a,z] Anna T. S. Freiberg, Manu U. M. Patel,[b] Simon Qian and Hubert A. Gasteiger

Chair of Technical Electrochemistry, Department of Chemistry and Catalysis Research Center, Technical University of Munich, Lichtenbergstr. 4, D-85748, Garching, Germany

[z]Email: qi.he@tum.de

[a]Present Address:Business unit Battery Cell, Volkswagen Group Components, Salzgitter, Germany

[b]Present Address: Hollingsworth and Vose advanced materials, Survey number 38, Mysore-Ooty road, K N Hundi, Kadakola post. Mysore-571311, India

Content

1. Experimental details

1.1. Preparation of polysulfides

The polysulfide samples with an overall nominal stoichiometry were prepared as described by Rauh et al.[1] (eq. S1) by elemental S_8 (99.998% trace metal basis, Sigma-Aldrich) and Li_2S (99.98% trace metal basis, Sigma-Aldrich) in a solution of 1 M LiTFSI in DOL:DME (1:1, v:v) with or without 0.1 M $LiNO_3$ as shown in equation S1. The powder mixtures were prepared in an Ar-filled glovebox (<0.1 ppm O_2 and H_2O, Mbraun, Germany) and stirred at room temperature (25 ± 1 °C) for at least 24 h.

$$\frac{n-1}{8}\mathrm{S_8} + \mathrm{Li_2S} \leftrightarrow \mathrm{Li_2S}_n \tag{S1}$$

1.2. Determination of the parameters used in the RRDE analysis

The diffusion coefficient of S_4^{2-} ($D_{S_4^{2-}}$) was determined by a rotating ring disk (RRDE) experiment by stepping the disk potential from a potential which is positive of the S_4^{2-} reduction wave (i.e., from -0.9 V_{Fc}, see Fig. 5b) into the S_4^{2-} reduction potential (-1.8 V_{Fc}), while at the same time holding the ring electrode at a negative potential (-1.8 V_{Fc}) where S_4^{2-} is being reduced at a diffusion limited rate. From the time delay (T_s) between stepping the disk potential and observing a change in the ring current (caused by a reduced S_4^{2-} flux to the ring electrode as S_4^{2-} is being consumed at the disk), the diffusion coefficient of S_4^{2-} can be obtained via $T_s = K(v/D)^{1/3}\omega^{-1}$, where K is a geometric factor of the RRDE (K = 10.1 rpm·s [2,3]) and ω is the rotation rate in units of rad/s.

The thus obtained $D_{S_4^{2-}}$ value of (7.0 ± 2.1)×10^{-6} cm^2/s in DOL:DME (1:1, v:v) with 1 M LiTFSI and lies in-between the literature values of (12 ± 2)×10^{-6} cm^2/s ($D_{S_x^{2-},(6 \le x \le 12)}$) obtained by Yamin et al.[4] in THF with 0.8 M $LiClO_4$ and 4 mM "Li_2S_x" ($6 \le x \le 12$), and of (0.86)×10^{-6} cm^2/s ($D_{"S_8^{4-}"}$) obtained in our previous work[2] in DOL:DME (1:1, v:v) with 1 M LiTFSI and 4 mM S_8. This much lower diffusion coefficient can be rationalized by the different experiment setup. More specifically, S_8 was the initial reactant in our previous setup and the diffusion coefficient of "S_8^{4-}" was measured with a stepping disk voltage that generating "S_8^{4-}" (i.e., -1.8 V_{Fc}) and holding a constant ring voltage that oxidizes "S_8^{4-}" (i.e., 0.6 V_{Fc}). As soon as the stepping disk voltage is applied, the ring will oxidize the "S_8^{4-}" released from the disk, and from the time delay (T_s) between stepping the disk potential and observing an oxidative ring current, the diffusion coefficient of "S_8^{4-}" was obtained. However, the undefined reactions in this experiment may complicate the interpretation of the time delay (T_s), and thus of the diffusion coefficient. Since chemical disproportionation reactions are likely involved in this stepping experiment, evident by the unidentified >4 e^-/S_8 transfer reduction processes and the irreversible S-redox chemistry with only one oxidation peak but two reduction peaks in the cyclic voltammogram, the measured time delay may not represent the pure diffusion process. On the other hand, S_4^{2-} is the initial reactant in our current system and we stepped the disk potential from a potential (positive of the S_4^{2-} reduction wave) into the S_4^{2-} reduction potential, while holding the ring electrode at a negative potential (-1.8 V_{Fc}) during which S_4^{2-} is being reduced continuously. From the time delay (T_s) between stepping the disk potential and observing a change in the ring current (caused by a reduced S_4^{2-} flux to the ring electrode as S_4^{2-} is being consumed at the disk), the diffusion coefficient of S_4^{2-} can be rather accurately obtained in this experiment regardless of any other electro(chemical) reactions.

The dynamic viscosity v was measured using a rotational rheometer at ambient conditions (MCR 302, Anton Paar, Austria). An electrolyte sample was filled in the measurement gap between the two parallel plates (PP50) with a diameter of 5 cm and a gap dimension of 0.5 mm. It was measured by means of the controlled shear rate (CSR) test mode with a shear rate (γ) range from 0.1 s^{-1} to 1000 s^{-1} at 25 °C. The viscosity value was taken at shear rate of $\gamma = 100\ s^{-1}$.

Table S1: Numerical values and parameters required to perform the Koutecky-Levich analysis, as determined in this work for a solution of 4 mM “Li_2S_4” and 1 M LiTFSI in DOL:DME (1:1, v:v) at 25 °C.

Dynamic viscosity η (cps)	Diffusivity D (cm^2/s)	Density ρ (g/cm^3)	Viscosity ν (cm^2/s)	Concentration c (mol/cm^3)
1.59	$(7.0 \pm 2.1)\times10^{-6}$	1.12	0.014	0.004

2.1. UV-vis reference spectra of polysulfides in the presence of 0.1 M $LiNO_3$

In Fig. 2 of the main text, $LiNO_3$ is not included in the reference solution, as its absorption at ~285 nm (see green line in Fig. S1) overlaps exactly with the absorption of "Li_2S_n" and S_8 at the region of ~260–285 nm (see Fig. 2), which complicates the sulfur and polysulfide peak assignment in the presence of $LiNO_3$. However, $LiNO_3$ was still used in the *operando* UV-vis cell cycling in order to mitigate polysulfide shutting, but the concentration of $LiNO_3$ was reduced from 0.5 M to 0.1 M (absorbance at ~285 nm is ~0.2, as marked by the green line in Fig. S1) in order to minimize the absorption of $LiNO_3$ in this region. In addition, Fig. S1 shows that the presence of 0.1 M $LiNO_3$ has no significant influence on the polysulfide composition, as the absorption behavior of polysulfides with 0.1 M $LiNO_3$ is similar as that without $LiNO_3$ (compare to Fig. 2 of the main text).

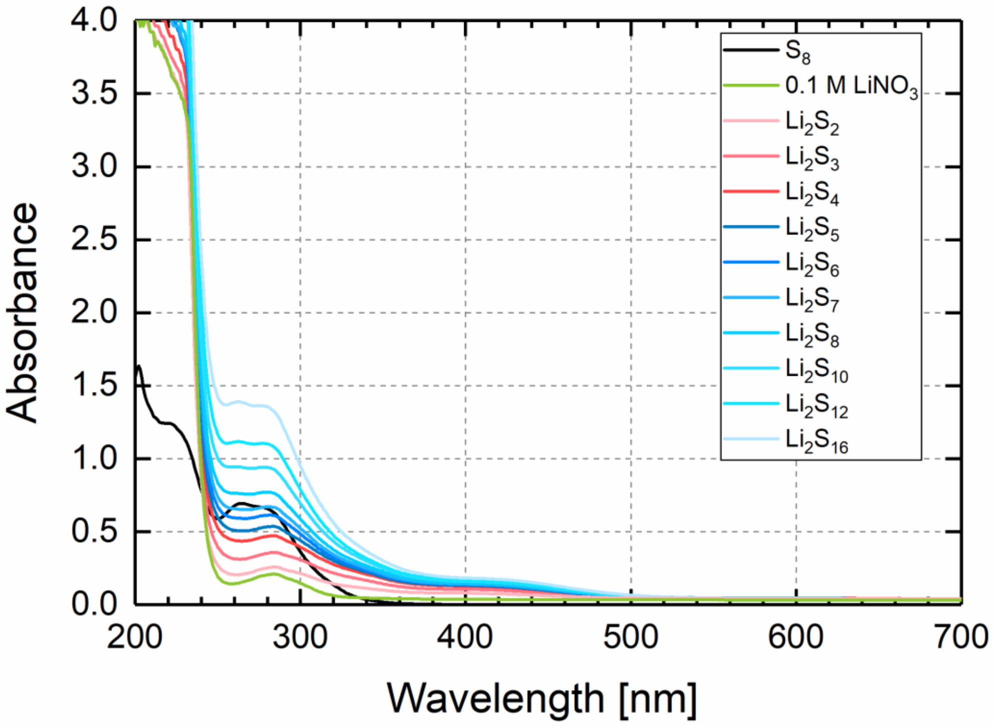

Figure S1: UV-vis spectra of 1 mM "Li_2S_x" and 1 mM S_8 in DOL:DME(1:1, v:v) with 1 M LiTFSI and with 0.1 M $LiNO_3$, measured in an air-tight 1 mm thick cuvette at room temperature (25 ± 1 °C).

2.2. Identifying the oxidized species involved in the disproportionation reaction of long-chain polysulfides

We believe that the long-chain polysulfides, that absorb at the same wavelength in Fig. 2 (main text), all disproportionate to the same species, as shown in eq. S2.

$$\mathrm{S}^{2-}_{5-16} \leftrightarrow \mathrm{S}^{2-}_{x}(\mathrm{reduced}, x \leq 5) + \mathrm{S}^{2-}_{y}(\mathrm{oxidized}, y \geq 16\ or\ \mathrm{S}_8) \qquad \text{(S2)}$$

To determine the oxidized species in eq. S2, we first assume Li_2S_4 to be the reduced species to simplify the following analysis. Thereupon, two scenarios can be considered depending on the oxidation product.

Scenario I: Li_2S_{16} as oxidized product.

$$\mathrm{Li_2S_{12}} \leftrightarrow \frac{2}{3}\mathrm{Li_2S_{16}} + \frac{1}{3}\mathrm{Li_2S_4} \qquad \text{(S3)}$$

$$\mathrm{Li_2S_{10}} \leftrightarrow \frac{1}{2}\mathrm{Li_2S_{16}} + \frac{1}{2}\mathrm{Li_2S_4} \qquad \text{(S4)}$$

$$\mathrm{Li_2S_8} \leftrightarrow \frac{1}{3}\mathrm{Li_2S_{16}} + \frac{2}{3}\mathrm{Li_2S_4} \qquad \text{(S5)}$$

While decreasing the length of the "Li_2S_x" chain, less Li_2S_{16} but more Li_2S_4 would be formed, according to eq. S3–S5. Consequently, the characteristic absorption of Li_2S_{16} would decrease, whereas the absorption of Li_2S_4 would increase (based on the Beer-Lambert law). However, this trend is not observed in Fig. 2a (main text), i.e., no isosbestic point is observed when the polysulfide chain decreases.

Scenario II: S_8 as oxidized product.

$$\mathrm{Li_2S_{12}} \leftrightarrow 1\mathrm{Li_2S_4} + 1\mathrm{S_8} \qquad \text{(S5)}$$

$$\mathrm{Li_2S_{10}} \leftrightarrow 1\mathrm{Li_2S_4} + \frac{3}{4}\mathrm{S_8} \qquad \text{(S6)}$$

$$\mathrm{Li_2S_8} \leftrightarrow 1\mathrm{Li_2S_4} + \frac{1}{2}\mathrm{S_8} \qquad \text{(S7)}$$

In this case, while the "Li_2S_x" chain is decreasing, the Li_2S_4 amount would remain constant, but the amount of S_8 would drop. This trend indeed can be observed in Fig.2a, as the absorption at ~420 nm (Li_2S_4) does not change significantly, whereas the absorption at 260–285 nm (S_8) falls down rapidly.

Combined with the above analysis and the S_8 characteristics shown in long-chain polysulfides, we believe that S_8 rather than Li_2S_x ($x \geq 16$) is the oxidized product in eq. S2.

2.3. Absorption ratio $A(300\ \text{nm})/A(420\ \text{nm})$ for short-chain polysulfides

The absorption ratios $\frac{A(300\ \text{nm})}{A(420\ \text{nm})}$ of nominally prepared “Li_2S_2” and “Li_2S_3” solutions are expected to be the same as those of “Li_2S_4”, based on the hypothesis that lower polysulfides disproportionate to solid Li_2S (white precipitate) and “Li_2S_4” (shown in eq. S8) and that only S_4^{2-} is UV-vis transmission active.

$$1\text{Li}_2\text{S}_m(m = 2, 3) \leftrightarrow \frac{4-m}{3}\text{Li}_2\text{S(solid)} + \frac{m-1}{3}\text{Li}_2\text{S}_4 \tag{S8}$$

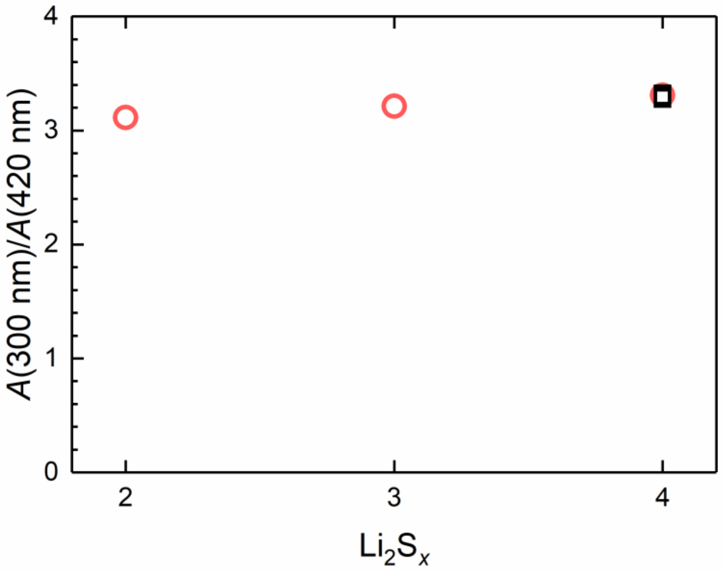

Figure S2: Absorption ratio between *A*(420 nm) and *A*(300 nm) for nominal short-chain polysulfide solutions. Red circle: data obtained from UV-vis spectra of 1 mM “Li_2S_x” in DOL:DME(1:1, v:v) with 1 M LiTFSI; Black square: data obtained from another set of experiments with different concentration of “Li_2S_4” (1 mM – 5 mM) in 1 M LiTFSI DOL:DME (1:1, v:v) solution.

3.1. Influence of the anode selection on the UV-vis spectroscopic background change

Here we examine the effect of metallic lithium on the spectroscopic background change in the *operando* UV-vis cell in the absence of sulfur species, comparing its behavior to a graphite electrode pre-lithiated to 50% state of charge (SOC). The observed spectroscopic background change in the presence of metallic lithium in the cell (see Figure S3a and S3b) could potentially lead to a misinterpretation of the UV-vis spectra in the *operando* UV-vis cell experiments in the presence of sulfur and polysulfides. Therefore we examined the spectroscopic background change over time.

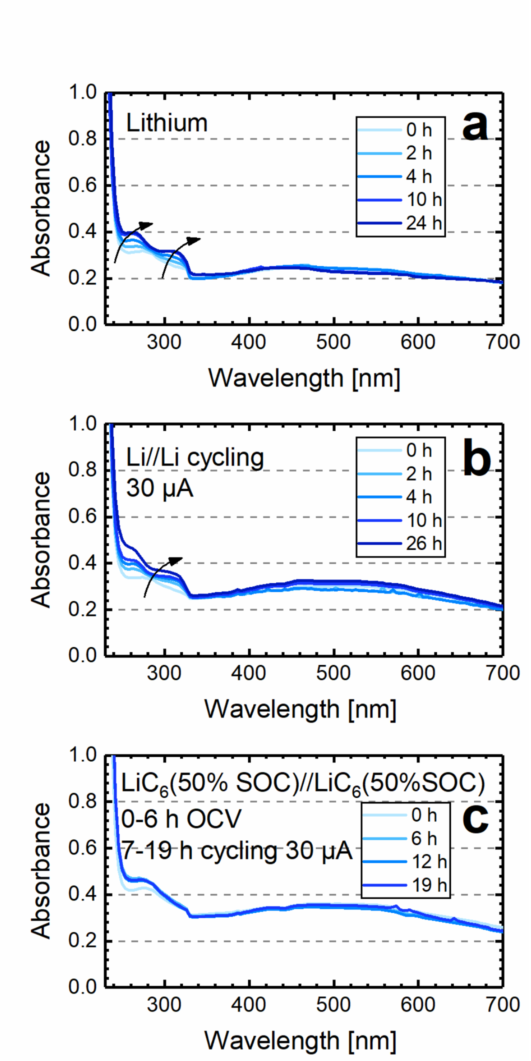

Figure S3: Spectroscopic background change over time in the *operando* UV-vis cell with different electrode combinations. **(a)** The lithium metal symmetric cell was kept at OCV in the *operando* UV-vis cell over the course of 24 hours, where 0 h refers to 15 min after cell assembly. **(b)** A symmetric Li//Li cell (in the *operando* UV-vis cell) was subjected to a lithium plating/stripping experiment, where cycles of a constant current of +30 µA for 1 h followed by a constant current of -30 µA for 1 h were applied repeatedly. **(c)** A symmetric cell with graphite electrodes pre-lithiated to 50% SOC (referred to as LiC$_6$ (50% SOC)//LiC$_6$ (50% SOC)) that is first held at OCV for 6 h, followed by the same lithium plating/stripping experiment as it in (b). Electrolyte: 1 M LiTFSI in DOL:DME (1:1, v:v) with additional 0.1 M LiNO$_3$.

When lithium metal is simply held at open circuit conditions (OCV) in the *operando* UV-vis cell (see Figure S3a), a spectroscopic background change already appears within the initial 4 hours, indicated by two absorption peaks at ~320 nm and ~270 nm, where S_8, $LiNO_3$, S_4^{2-}, and S_3^{2-} (~266 nm) all have an absorption feature. A similar phenomenon is also observed for the Li//Li symmetric cell that was cycled with a constant current of 30 µA to mimic the cycling condition of an *operando* S_8//LiC_6 cell (Fig. S3b). On the other hand, the use of a pre-lithiated and pre-formed graphite anode essentially eliminates the spectroscopic background change (see Fig. S3c).

In a recent work, Freiberg et al.[5] have demonstrated that Li-S cells, either cycled with Li metal or preformed graphite, showed comparable electrochemical behavior at least for the first 20 cycles, e.g. similar voltage profiles and capacities delivered both in discharge and charge processes. While a reasonable cycling behavior was achieved in the work of Freiberg et al.,[5] the charging process of polysulfides or Li_2S in our study is more strongly affected by polysulfide shuttling effects. This phenomenon can be attributed to the much larger surface area of the pre-lithiated graphite electrode compared to a lithium metal electrode, and is particularly pronounced for the low sulfur loadings that have to be used in the *operando* UV-vis cell. Nonetheless, since our study focuses on the first discharge process that is much less affected by polysulfide shuttling, a reasonably good discharge performance can still be obtained with a pre-lithiated graphite electrode (see Fig. 3a).

3.2. Molar absorptivity of S_4^{2-} at 420 nm in DOL:DME-based electrolyte

The molar absorptivity (ε) at 420 nm was determined for nominal “Li_2S_4” solutions at various concentrations (c) in the DOL:DME (1:1, v:v) electrolyte with 1 M LiTFSI using an air-tight cuvette with 1 mm path length (b). For this, the measured absorbance (A(420 nm)) was analyzed using the Beer-Lambert law (eq. S9), resulting in $\varepsilon(420\ nm) = 1033\ \mathrm{L\ mol^{-1}\ cm^{-1}}$.

$$A = \varepsilon * b * c \tag{S9}$$

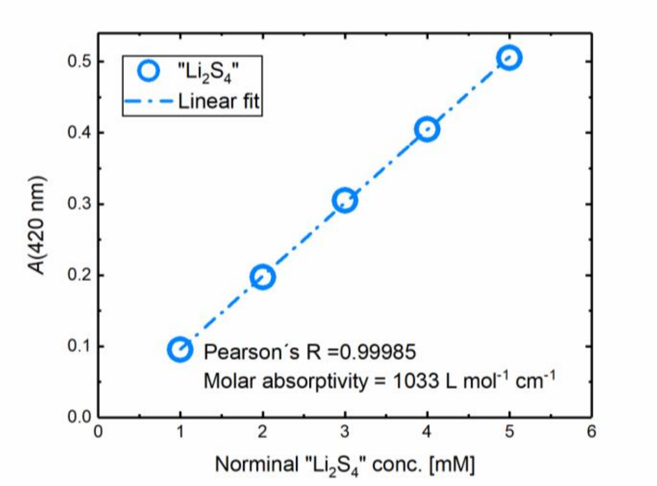

Figure S4: Calibration curve for the “Li_2S_4” concentration vs. the UV-vis absorption at 420 nm. The spectra were recorded in DOL:DME (1:1, v:v) with 1 M LiTFSI in an air-tight 1 mm thick cuvette at room temperature.

3.3. Resolving the dominant liquid intermediates at the 1st discharge plateau in Fig. 4

From the analysis of Fig. 4b is quite clear that S_4^{2-} is formed during the 1st discharge plateau (at ≥2.2 V). However, considering the fact that other sulfur species (e.g., S_8 and the intermediate S_x^{2-} species with $x < 4$) also have an absorption at ~266 nm, so that they could potentially be hiden behind the absorption of S_4^{2-} at ~266 nm, we plotted the ratio $\frac{A(266\ \mathrm{nm})}{A(420\ \mathrm{nm})}$ recorded in Fig. 4 over the course of discharge (s. Fig. S5). It is apparent that the $\frac{A(266\ \mathrm{nm})}{A(420\ \mathrm{nm})}$ ratio recorded in the *operando* UV-vis cell remains constant at ~3.2 in region I and II (see blue line in Fig. S5), at a value which is very close to the $\frac{A(266\ \mathrm{nm})}{A(420\ \mathrm{nm})}$ ratio of the "Li_2S_4" reference spectra (marked by the red dashed line in Fig. S5), which indicates that the species formed in the first discharge plateau and in the subsequent CV hold at 2.2 V is predominantly S_4^{2-}. Here we should note that the initially higher ratio of $\frac{A(266\ \mathrm{nm})}{A(420\ \mathrm{nm})}$ during the first hour of discharge originates mainly from the strong absorption of dissolved S_8 at ~265–280 nm. Finally, the much higher $\frac{A(266\ \mathrm{nm})}{A(420\ \mathrm{nm})}$ ratio in region III, IV, and V arises from the fact that S_x^{2-} ($x < 4$) is generated by the reduction of S_4^{2-} and becomes the dominant species, which has high absorption at ~266 nm but little absorption at ~420 nm.

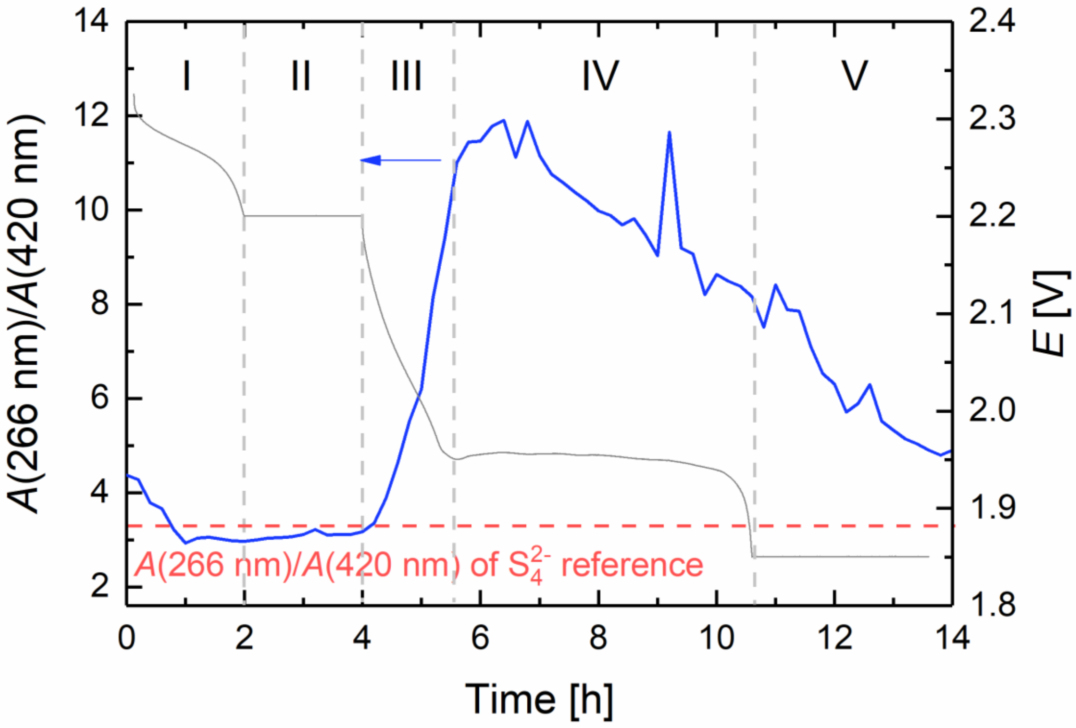

Figure S5: Absorption ratio $\frac{A(266\ nm)}{A(420\ nm)}$ over the course of discharge (blue) recorded in the *operando* UV-vis cell derived from Fig. 4 in main text. The voltage profile is shown in gray and the red dashed line marks the $\frac{A(266\ nm)}{A(420\ nm)}$ ratio of the "Li_2S_4" reference obtained from Fig. 2 or Fig. S7.

3.4. Confirmation of an electrochemical reduction process at the transition phase between the 1st and 2nd discharge plateau

Evidence for an intermediate species between the 1st and the 2nd discharge plateau can be observed in a dQ/dV analysis of the galvanostatic charge/discharge of an S_8/C//Li cell (s. Fig. S6a). The dQ/dV plot (s. Fig. S6b) shows a clear electrochemical reduction process at ~2.2 V vs. Li^+/Li, which corresponds to ~2.1 V vs. the graphite anode pre-lithiated to 50% SOC (i.e., the LiC_6 (50% SOC) anode used in the main text). This reduction feature is located between the dQ/dV peak of the 1st discharge plateau (~2.4 V_{Li} or ~2.3 V vs. LiC_6 (50% SOC)) and that of the 2nd discharge plateau (~2.1 V_{Li} or ~2.0 V vs. LiC_6 (50% SOC)). Its existence in several cycles demonstrates this reduction step is not an exclusive characteristic only for the first discharge process. We believe that the here observed intermediate reduction process originates form the reduction of S_4^{2-} to S_x^{2-}.

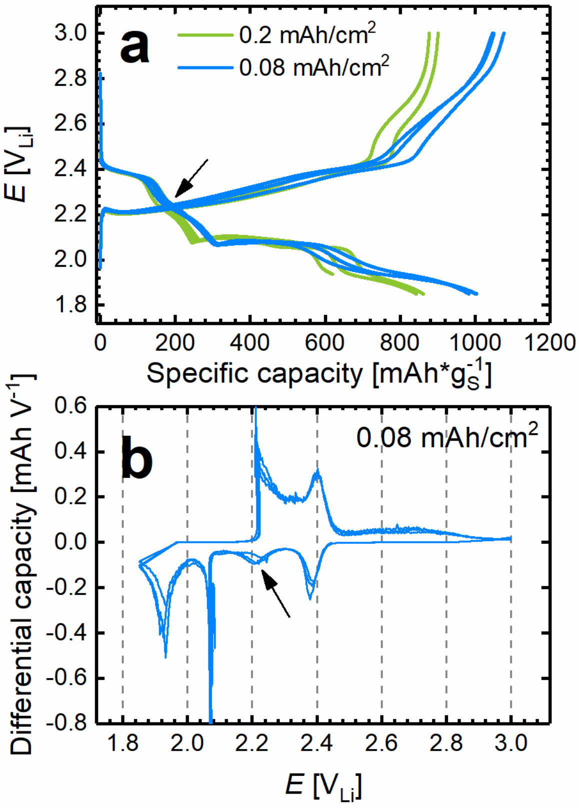

Figure S6: (a) Representative voltage profiles during the constant current cycling with a C-rate of 0.05 h^{-1} of an S_8/C//Li coin cell at two different theoretical areal capacities (0.08 and 0.2 mAh/cm^2), using 1 M LiTFSI and 0.1 M $LiNO_3$ in DOL:DME (1:1, v:v). Voltage profiles of two to three cycles are shown here. **(b)** The corresponding dQ/dV plot of the cell with 0.08 mAh/cm^2 to better resolve the reduction peak in the transition phase at ~2.2 V_{Li}. Note that the potential referenced to Li^+/Li is approximately 0.1 V higher than that referenced to the partially lithiated graphite anode used in the main text (i.e., the LiC_6 (50% SOC) anode).

3.5. Examining the stability of “Li_2S_4” in DOL:DME-based electrolyte

Fig. S7 shows “Li_2S_4” is relatively stable in DOL:DME-based electrolyte, since no significant spectroscopic change is observed for 24 hours. We therefore believe “Li_2S_4” should be stable at least for the rotating ring disk measurement time frame (hours).

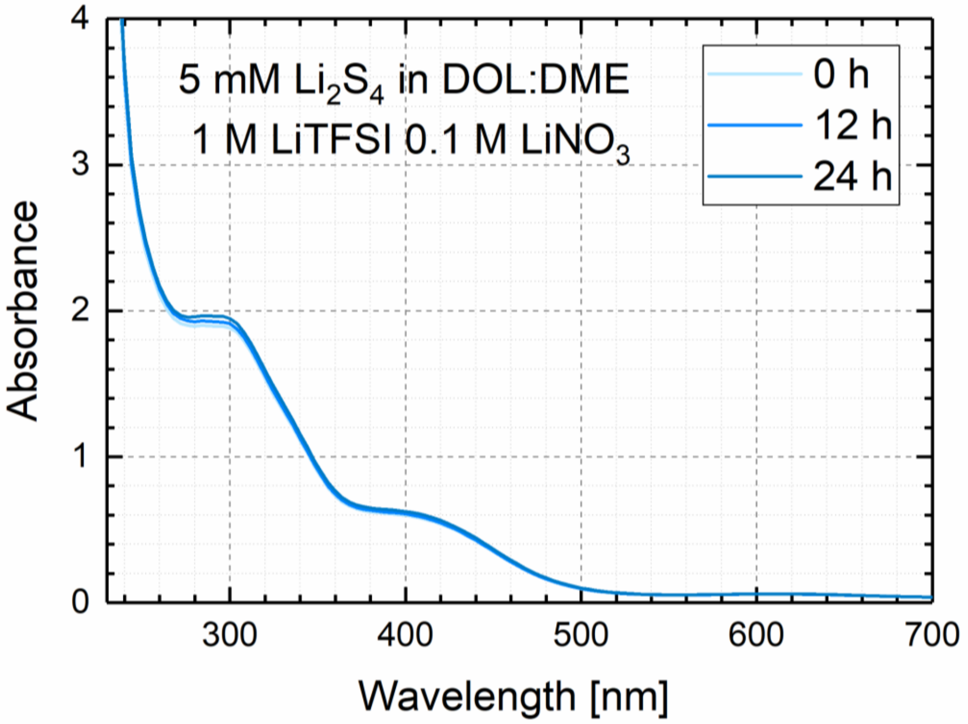

Figure S7: Time dependence of the UV-vis spectra of 5 mM “Li_2S_4” in DOL:DME(1:1, v:v) with 1 M LiTFSI and 0.1 M $LiNO_3$. These measurements were conducted in an air-tight 1mm thick cuvette at room temperature over 24 h.

3.6. Correlation between the transferred charges and *A*(266 nm) in region IV and V of Fig. 4

In the following, we will estimate the dependence of the S_3^{2-} contribution to the absorption at ~266 nm (A_{S32-}(266 nm)) during the discharge in region IV (CC phase in the 2nd discharge plateau) and region V (subsequent CV phase) in Fig. 4 on the coulombic charge delivered in these regions. For this, it must be considered that the absorption at ~266 nm in principle contains contributions from S_4^{2-}, S_3^{2-} , and S_8, whereby the S_8 concentration in the potential region of the second discharge plateau is considered to be negligible. The contribution of S_4^{2-} to the total absorption at ~266 nm (A_{total}(266 nm), see blue symbols in Fig. S8) can be estimated from its absorption at ~420 nm and by multiplying it by the fixed ratio of A(266 nm)/A(420 nm) that was obtained for "Li_2S_4" solutions in (see red line in Fig. S5). Subtracting the thus obtained value from the total absorption at ~266 nm provides an estimate for the absorption at ~266 nm which is contributed by S_3^{2-} (A_{S32-}(266 nm), see red symbols in Fig. S8).

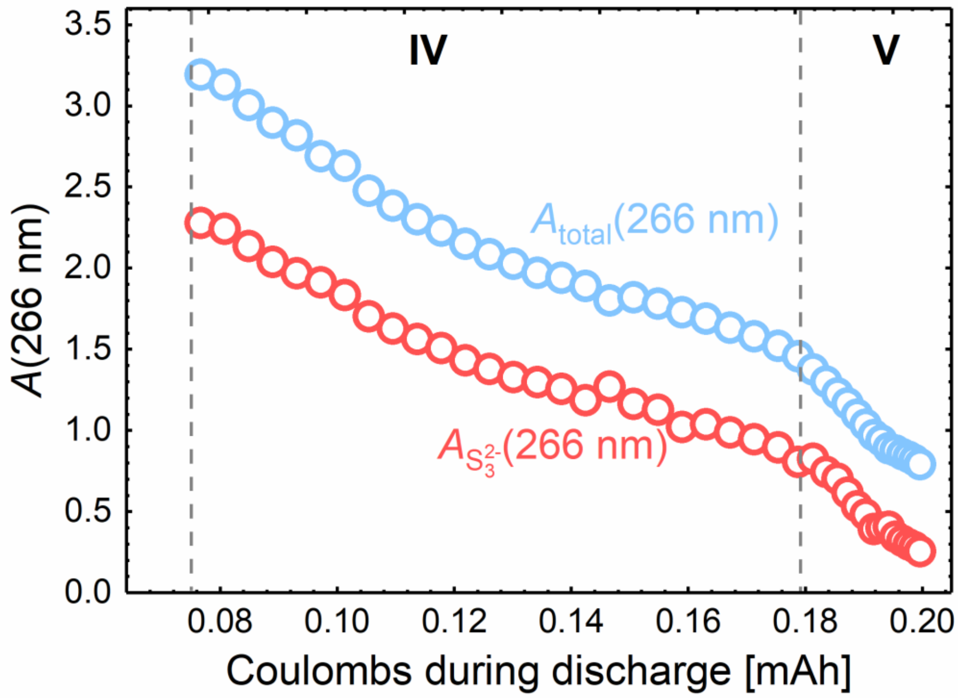

Figure S8: Correlation of *A*(266 nm) with the coulombic charge delivered in region IV (constant current) and V (constant voltage) extracted from the *operando* UV-vis cell shown in Fig. 4. The blue symbols represent the total absorption at ~266 nm, while the red symbols represent the estimated absorption at ~266 nm that is contributed only by S_3^{2-}. The latter is obtained by subtracting the *A*(266 nm) of S_4^{2-} from the total absorption (this estimation is based on the fixed ratio of *A*(266 nm)/*A*(420 nm) for "Li_2S_4" as shown in Fig. S5, and assuming the complete absence of S_8).

If the 2nd discharge plateau were governed by only one electrochemical step, for instance by the electrochemical reduction of S_3^{2-} (eq. S10), a linear correlation between the decrease of its contribution to A_{S32-}(266 nm) (red symbols in Fig. S8) and the delivered coulombic charge would be expected.

$$S_3^{2-} + 4e^- \rightarrow 3S_1^{2-} \tag{S10}$$

As displayed in Fig. S8, it is difficult to conclude whether there is a linear correlation between the decrease of $A_{\mathrm{S32-}}$(266 nm) and the delivered coulombic charge. While it might be considered linear for each of the two regions with, albeit, different slopes, this analysis suggests that several processes (electrochemical and/or chemical disproportionation reactions) occur in parallel, when the potential drops below ~2.0 V (i.e., in the 2nd discharge plateau or beyond).

Literature

1. R. D. Rauh, F. S. Shuker, J. M. Marston, and S. B. Brummer, *J. Inorg. Nucl. Chem.*, **39**, 1761–1766 (1977).

2. Y.-C. Lu, Q. He, and H. A. Gasteiger, *J. Phys. Chem. C*, **118**, 5733–5741 (2014).

3. J. Herranz, A. Garsuch, and H. A. Gasteiger, *J. Phys. Chem. C*, **116**, 19084–19094 (2012).

4. H. Yamin, A. Gorenshtein, J. Penciner, Y. Sternberg, and E. Peled, *J. Electrochem. Soc.*, **135**, 1045–1048 (1988).

5. A. T. S. Freiberg, A. Siebel, A. Berger, S. M. Webb, Y. Gorlin, M. Tromp, and H. A. Gasteiger, *J. Phys. Chem. C*, **122**, 5303–5316 (2018).

3.2.2 Quantification of the Important Processes at the S-Cathode during Discharge via *in-situ* Electrochemical Impedance Spectroscopy

This section presents the recently prepared manuscript "*In-situ* Impedance Measurements for a Sulfur Cathode – an Application of Gold Micro-Reference Electrode in Li-S Batteries". At the time of submission of this PhD thesis, this manuscript has not yet been submitted for publication. This study was presented by Qi He at the 7th "Lithium-Sulfur-Batteries" workshop in Dresden, Germany (Nov 12-13, 2018).

While the specific reaction intermediates have been identified using *operando* UV-Vis spectroscopy, a more quantitative insight would be beneficial in identifying the limiting reaction steps upon discharge. Emphasis here is placed on the specific question whether the practical application of Li-S batteries is limited by the slow charge transfer processes originated from the intermediates identified by UV-Vis spectroscopy. To address this question, electrochemical impedance spectroscopy (EIS) is adapted, as it can quantitatively provide a wealth of information on various physical/chemical processes, such as electric/ionic conduction, charge transfer, and diffusion. The challenge here is to experimentally acquire reliable impedance spectra of the sulfur electrode in a cycling Li-S battery, which requires the use of a reference electrode.

In this work, the gold wire micro-reference electrode (GWRE)[133,173,174] that was developed for use in Lithium-ion batteries is adopted for measurements in Li-S batteries to enable a quantification of the S-cathode impedance. In order to do so, special care is taken to assure the stability of the GWRE in the polysulfide containing electrolyte and its suitability for separating the S-cathode impedance from the cell impedance response. As the interpretation of impedance spectra is usually not straightforward, we first establish a series of "reference" impedance spectra using the so-called symmetric cell setup (i.e., a cell that is assembled with two identical electrodes are assembled).[133,175] By examining their impedance response at various experiment conditions, we are able to identify and quantify the contributions from the various physical/chemical processes in a Li-S system that occur at different frequency ranges.

This study helps to better understand Li-S batteries in three aspects: (i) The aluminum current collector is corroded in the presence of polysulfides, forming a contact resistance at the electrode/current collector interface. (ii) The charge transfer resistance is at least 10 times larger than for the conventional Li-ion battery materials, e.g., LFP[176] or graphite.[177] Therefore, we propose that developing an inexpensive high-surface catalyst can greatly contribute to the further improvement of Li-S batteries. (iii) This work also shows that the use and analysis of the impedance response of symmetric cells allows to quickly examine the catalyst activity (by analyzing R_{ct}) and to estimate the diffusion coefficients of polysulfides (by analyzing Warburg element), when a new electrolyte system is being examined.

Author Contributions

Q.H. and B.K.S. developed the concept of *in-situ* impedance for Li-S batteries. Q.H. and B.K.S. developed the design of symmetric cell setup. R.B. and Q.H. performed the *in-situ* impedance measurements. Q.H. conducted symmetric cell measurements. A.F. D.P., and S.S. discussed the GWRE experimental setup in Li-S batteries and *in-situ* impedance results. D.P. designed the temperature-dependence measurements. A.F. performed the XPS measurements and data treatment. Q.H., B.K.S., A.F., and D.P discussed the symmetric cell results. Q.H. and B.K.S. wrote the manuscript. All authors discussed the results and commented on the manuscript.

Manuscript

In-situ Impedance Measurements for a Sulfur Cathode — an Application of Gold Micro-Reference Electrode in Li-S Batteries

Qi He[#], Rafael Berk, Anna T.S. Freiberg, Daniel Pritzl, Sophie Solchenbach and Bharatkumar Suthar[*]

Technical University of Munich, Chair of Technical Electrochemistry, Lichtenbergstr. 4, D-85748, Garching, Germany

Email: [#]qi.he@tum.de; *bharat.k.suthar@iitb.ac.in;

Abstract

The development of Lithium-Sulfur (Li-S) batteries requires a deeper understanding of its working mechanism. In order to quantify the contributions of various ongoing processes upon discharging, we adopt the approach of *in-situ* electrochemical impedance spectroscopy (EIS) for Li-S batteries. The (already-established) gold wire reference electrode (GWRE) is accommodated in order to real-time acquire impedance spectra of a sulfur cathode. Prior to its application in Li-S batteries, special attention was paid to the stability of GWRE in an S-species containing environment (e.g. polysulfides (radical)) and its suitability of obtaining reliable half-cell (e.g. S-cathode) EIS from the full cell EIS. Since the interpretation of EIS is often fallible, we establish a series of “reference” impedance spectra for Li-S chemistry using the so-called symmetric cell approach. We delicately examine their impedance response by varying different experimental conditions such as temperature, active material concentration, electrochemical active surface area, electrode substrate and the diffusion length. Eventually we are able to assign various physical/chemical processes to the corresponding impedance response, such as contact resistance at the electrode/current collector interface, charge transfer and Warburg diffusion processes. In this way, we are able to analyze the obtained *in-situ* impedance spectra and can thus identify the ongoing processes upon discharge. The quantitative evaluation of those processes such as S-redox kinetics as well as transport properties will be further presented. In addition, we also present here a convenient approach of using symmetric cell impedance 1) to quickly evaluate the exchange current density of S-redox on the developing cathode substrate/catalyst and 2) to estimate the diffusion coefficients of soluble polysulfides when a new electrolyte system is developed.

Introduction

Electrochemical impedance spectroscopy (EIS) is a noninvasive technique that is often employed to investigate both interfacial processes (such as kinetics of redox reaction, adsorption and eletrosorption), and transport processes (for instance, mass transfer in porous electrode and solution phase resistance) of a electrochemical system.[1]

Despite its various application in Li-ion batteries (LiB), for instance in characterizing electrodes (tortuosity determination,[2,3] binder distribution,[4] on-line analysis of contact resistance along with charge transfer resistance[5–7]), its implementation in Li-S batteries has encountered manifold challenges that relate to the soluble active material (S_8, polysulfides Li_2S_x, $2 \leq x \leq 8$). For example, the interface in Li-S batteries is under constant fluctuation due to the perpetual dissolution and precipitation of the non-conducting species (S_8 and Li_2S). On top of that, the versatile and sensitive equilibria among the reaction intermediates (e.g. $Li_2S_8 \leftrightarrow Li_2S_6 + \frac{1}{4}S_8$[8–11]) also allows no ex-situ analysis that involves any cell disassembly process.

Deng et al[12] and Canas et al.[13] pioneered to apply impedance spectroscopy in a Li//S cell to obtain SOC-dependent EIS and monitored the evolution of impedance upon cycling. While Deng et al.[12] concluded that the increasing charge transfer resistance (R_{ct}) is a relevant factor responsible for the capacity fading, Canas et al[13] observed an opposite trend that R_{ct} at cathode decreases ~70% over the course of 50 cycles. The discrepancy in concluding how charge transfer resistance evolves upon cycling and how it contributes to the cell degradation, clearly demonstrates the challenges of implementing EIS in a Li-S system. The impedance obtained in the abovementioned studies are so-called full-cell EIS, which involve all kinds of physical and chemical processes present in both cathode and anode (as well as in the separator). Consequently, the interpretation of a full-cell EIS is extremely challenging since the impedance of different processes often superimpose with each other. Hence, a reasonable interpretation of impedance spectrum requires in the first place an experimental deconvolution of cathode and anode EIS.

A symmetric cell approach is commonly used in LiBs, where two cathodes or anodes from nominally identical cells are resembled.[14,15] Conder et al.[16] and Adamic et al.[17] adopted symmetric cells with Li//Li as electrodes immersed in S-catholyte solution to understand the sulfur-involved anode impedance. Yet, the EIS of a Li//Li symmetric cell often leads to an unreliable interpretation due to the undefined electrochemical redox reaction especially when S-species are present, as well as dynamic and unspecified electrolyte/electrode interface caused by complex parasitic reactions of Li metal with solvent/salt/S-species.

In order to utilize symmetric cell setup in Li-S batteries, a careful design of experiment is essential. The selection of electrode material and its surface area, redox pair and separator thickness all have a significant influence on the shape and magnitude of obtained Nyquist plots, such as whether a phase angle plateau at 45° of Warburg diffusion would appear.[1] The selection of Sinusoidal Perturbation Amplitude and frequency range will also impact the quality of the obtained impedance spectra. For instance, the combination of large amplitude and extreme low frequency (i.e. long polarization time) can cause the non-linearity at low frequencies and the stability of the system is consequently not guaranteed.[18] Talian et al.[19] and Raccichini et al.[3] have cautiously conducted symmetric cell experiments with either freshly-prepared S-electrodes to obtain static information such as tortuosity and MacMullin number of pristine electrodes[3] or with carbon electrodes (e.g. glassy carbon) immersed in catholyte solution to gain insight into the polysulfide properties (e.g. kinetic and transport parameters).[19] Unfortunately, the purpose of using symmetric cells to acquire real-time half-cell impedance by re-assembling two nominally identical cycled electrodes, cannot be fulfilled in Li-S batteries, since the polysulfide equilibrium is highly sensitive to any environmental change upon cell disassembly and re-assembly.

A three-electrode setup employing a reference electrode is therefore superior in investigating the real-time impedance of a cycling Li-S battery owning to its capability of collecting the half-cell impedance without cell disassembly. However, the realization of such experimental setup can be challenging and often give rise to measurements error.[20]

A conventional Swagelok® T-cell with point-like reference electrode is in principle able to serve this purpose, but practically, it is not suitable for faultless impedance measurement[20,21] Two fundamental effects were found to cause distortions and artefacts in its half-cell impedance: 1) the geometric asymmetry, which arises from the different size of cathode and anode or any position shift of electrode to each other; 2) the electrochemical asymmetry (in a non-symmetric setup), that originates from an inhomogeneous current density in the electrolyte at the location of the reference electrode, especially when separator soaked with electrolyte is larger than electrodes.[20,21]

In order to achieve a reliable and reproducible half-cell impedance spectra, three-electrode setups with mesh reference electrode and wire electrode have been proposed, e.g. an isolated thin wire reference electrode with only the tip exposed and sitting in between two electrodes.[20–22] In such experimental setup, the EIS distortions caused by the aforementioned geometric and electrochemical asymmetry will not falsify the measurement results, as long as appropriate reference electrode geometry is chosen,

Except for the careful design of the experimental setup, another challenge of implementing impedance spectroscopy in the Li-S system is the rational interpretation of the obtained EIS and the establishment of a direct relationship with physical and chemical processes. For example, many researchers have proposed various equivalent circuits to understand the EIS in Li-S batteries,[16,17,19] but a validation of the physical-chemical meaning of each component in their equivalent circuits has hardly been accomplished.

The goal of this work is to experimentally deconvolute the S-cathode impedance from the full-cell impedance by adapting a gold wire reference electrode (GWRE)[5,6,22] into Li-S batteries. Therefore, we first inspect the suitability of GWRE in Li-S batteries – a system that is under dynamic and aggressive condition (owning to the high (electro)chemical activity of polysulfides (radical)[23]). More specifically, we examine the potential-stability of GWRE and its capability of collecting proper impedance spectra in a Li-S system. In order to rationally comprehend the EIS in the Li-S system, we additionally design a well-defined symmetric cell setup that enables us to conscientiously validate the physical-chemical meaning of each component in the Nyquist plot by varying various measurement parameters such as temperature, concentration of redox pair, separator thickness, and surface area of carbon substrate.

As a result, we identify the impedance near high frequency range (kHz range) as Z_1 resulting from contact resistance (R_{cont}) at the current collector/cathode interface; impedance around middle frequency (~Hz range) as Z_2 resulting from charge transfer resistance (R_{ct}) and impedance near low frequency (mHz range) as Warburg impedance resulting from diffusion processes in separator (W).Thereby, we are able to provide an estimate of the exchange current density and diffusion coefficient of the redox pair used in this study. Eventually, we apply the three electrode set-up with GWRE in a $Li_2S//LiC_6$ battery to investigate the S-cathode impedance upon cycling. Taking the discharge process as an example, we observe the evolution of high frequency (kHz) and middle frequency (Hz) semicircles in the Nyquist plot, which we assign to contact resistance and charge transfer resistance. We investigate the SOC dependence of R_{cont} and R_{ct} and semi-quantify them using a rather simple Randles-like equivalent circuit, considering the entanglement of the multiple processes in a cycling cell, such as various redox and disproportionation reactions, dynamic precipitating of Li_2S and S_8, as well as the complex diffusion behavior.

The magnitude of R_{ct} implies the necessity of using high surface area conducting carbon to reduce the charge transfer resistance in the cell. Further comparison of R_{ct} and R_{cont} in Li-S batteries with that in Li ion batteries as well as analysis of the evolution of R_{cont} with long-term cycling is discussed.

Experimental

Electrode preparation

Li_2S/C electrodes consist of commercially available Li_2S powder (99.98% trace metal basis, Sigma-Aldrich), Vulcan carbon (XC-72, Tanaka Kikinzoku Kogyo, with a BET of ~240 m^2/g), polyvinylidene fluoride (PVDF, HSV900, Kynar), all of which were stored in an argon-filled glovebox (Mbraun, <1 ppm H_2O and < 1 ppm O_2). The weighted Li_2S and Vulcan carbon (VC) were transferred into an air-tight container and mixed thoroughly using a planetary centrifugal vacuum mixer (Thinky, Japan) outside of the glovebox. The obtained solid mixture was dispersed inside the glovebox in a suspension of PVDF and N-Methyl-2-pyrrolidone (NMP, anhydrous, 99.5%, Sigma-Aldrich). The mixing and dispersion processes were repeated three times. The obtained ink (Li_2S, VC and PVDF dispersed in NMP) was coated onto an 18 µm thick aluminum foil using a 250 µm gap Mayer rod. The coating was initially dried at room temperature inside glovebox for 24 h and electrodes were punched out as a disk with a diameter of 10.95 mm, which were dried additionally under dynamic vacuum (Büchi, Switzerland) at 120 °C overnight. The obtained electrodes have a composition of Li_2S, Vulcan carbon and PVDF in a ratio of 60:30:10 wt. %, where the loadings of the electrode are given in the corresponding result section.

Graphite electrodes consist of graphite (SLP30, Timcal, Japan, 90 wt. %) and PVDF binder in a ratio of 96.2 and 3.8 wt. %, and were prepared as following. Weighted graphite and PVDF were direct dispersed in NMP solution and mixed in the planetary centrifugal vacuum mixer in two steps. The obtained ink was coated onto an 11 µm thick copper foil (99.99%, MTI, USA) using a doctor blade coater. The coating was initially dried at 50 °C overnight and electrodes were punched out as disks with a diameter of 10.95 mm and dried for another 12 hours under dynamic vacuum at 120 °C in a glass oven.

VC electrodes are composed of commercially available Vulcan carbon and PVDF in a ratio of 75:25 wt. % in order to keep the same ratio as VC and PVDF in a Li_2S/C electrode. The weighted Vulcan carbon were dispersed in a suspension of PVDF and NMP, which were mixed in the planetary centrifugal vacuum mixer. The dispersing and mixing steps were repeated three times and the obtained ink were coated an 18 µm thick aluminum foil with a doctor blade coater. The coating was initially dried at 50 °C overnight and electrodes were punched out as disks with a diameter of 10.95 mm or 15 mm and dried for another 12 hours under dynamic vacuum at 120 °C in a glass oven.

Carbon paper disc electrode were direct punched from a carbon paper sheet (Toray, TP030, 110 µm thick) with a diameter of 15 mm and dried for 12 hours under dynamic vacuum at 120 °C in a glass oven.

Preparation of electrolyte and catholyte solutions

If not specifically indicated, the electrolyte used in this study consists of 1,3-dioxolane (DOL, anhydrous, 99.8%, Sigma-Aldrich):1,2-dimethoxyethane (DME, anhydrous, 99.8%, Sigma-Aldrich) (1:1, v:v) with 1 M lithium bis(trifluoromethane) sulfonamide (LiTFSI, 99.95 % trace metal basis, Sigma Aldrich, dried under dynamic vacuum at 120 °C for 3 days in a glass oven) and 0.1 M lithium nitrate ($LiNO_3$, 99.99% trace metal basis, Sigma-Aldrich, dried under dynamic vacuum at 110 °C for 3 days in a glass oven).

The catholyte solution compromises 5 mM S_8 and 10 mM "Li_2S_4" (nominally equivalent to 10 mM "Li_2S_8") dissolved in the aforementioned electrolyte solution. The polysulfide samples were prepared as described in literature.[24] by nominally mixing of elemental S_8 (99.998% trace metal basis, Sigma-Aldrich) and Li_2S in the electrolyte as shown in equation 1. The powder mixtures were prepared in Ar-filled glovebox (<0.1 ppm O_2 and H_2O) and stirred in the electrolyte at room temperature at least for 24 h.

$$\frac{n-1}{8}\mathrm{S_8} + \mathrm{Li_2S} \leftrightarrow \mathrm{Li_2S}_n \qquad (1)$$

Cell assembly and electrochemical measurement procedures

Three electrode Swagelok® T-cell with a gold wire reference electrode (GWRE) — The SEM image of GWRE (~50 µm diameter, coated with a 7 µm polyimide insulation, Goodfellow Cambridge Ltd., United Kingdom) and detailed cell configuration are described in our previous study.[22] The cell was assembled in an argon-filled glovebox (both H_2O and O_2 < 0.1 ppm) by sandwiching two electrodes (either two VC electrodes or $Li_2S//LiC_6$ electrodes) separated by two glass fiber separators (ø 11 mm, 200 µm thickness, glass microfiber #691, VWR, Germany) soaked with 60 µl catholyte solution or electrolyte.

Symmetric coin cells — They were assembled in a coin cell (CR2032 Hohsen, Japan) in an argon-filled glovebox (both H_2O and O_2 < 0.1 ppm), where two identical electrodes (either VC electrodes (ø 15 mm) or carbon paper electrodes (ø 15 mm)) with one layer glass fiber separator (ø 16 mm) were centrally sandwiched. A sufficient amount of catholyte (150 µL) was added into the coin cells to ensure both VC (~5 µm thickness) and carbon paper (110 µm thickness) electrodes were fully soaked with catholyte solution.

Pre-formation and partially pre-lithiation of graphite electrodes — The implementation of graphite electrodes in the DOL:DME-based electrolyte is accomplished only if the graphite are pre-formed with a relative stable SEI.[25] The graphite electrode (C_6) was assembled into a coin cell with lithium metal (99.9% purity, Rockwood lithium, USA) as counter electrode. 80 µL electrolyte consisting of 1 M lithium perchlorate ($LiClO_4$, battery grade, 99.99% trace metal basis, Sigma-Aldrich), 0.1 M $LiNO_3$ and 0.5 M vinylene carbonate (BASF SE, Germany) in DOL:DME (1:1, v:v) were added to the cell. One formation cycle at 0.1C followed by a galvanostatic lithiation to 10% SOC were performed in a climate chamber (Binder, Germany) at 25 °C. Afterwards, the pre-formed and partially pre-lithiated graphite electrodes were harvested and washed three times with DOL:DME(1:1, v:v) solution.

Lithiation of GWRE in Swagelok® T-cells — Direct after cell assembly, the GWRE was first lithiated galvanostatically with a current of 150 nA for 1 h using the partially lithiated graphite or lithium metal (anode) as lithium source. Note that the lithiation capacity of 0.15 μAh is negligible compared to the cathode capacity of ≈1 mAh. A successful lithiation of GWRE in DOL:DME-based electrolyte can only be achieved in the absent of soluble S_8 or polysulfides, i.e. the GWRE cannot be lithiated when S_8/C electrode is present in the cell, since the reduction of S_8/polysulfides would rather take place instead of GWRE lithiation. S_8/C electrode can only be used if the GWRE is elsewhere lithiated. For instance, one can lithiate the GWRE in a S_8/polysulfides-free electrolyte, which will be harvested and re-assembled to a cell that uses S_8/C as cathode.

Electrochemical impedance spectroscopy in symmetric cells — Potentiostatic impedance spectroscopy were carried out for symmetric cells. Various perturbation (3 mV- 20 mV) were tested to examine the linearity of the measured Li-S system. A frequency range from 200 kHz to 1 mHz was chosen to capture impedance of all the relevant processes, including the Warburg diffusion. The impedance measurements were repeated 20 times (acquisition time for each measurement ~2.5 h) to examine the stability of the measured system. If not specifically indicated, all the impedance measurements were conducted in a climate chamber with a temperature of 25 ± 0.5 °C.

Cycling protocols for the SOC-resolved EIS measurement (Fig. 8) — Each charge and discharge process of a $Li_2S//LiC_6$ cell with GWRE consisted of 20 times repeated 30 min galvanostatic cycling at 0.1C followed by a 20 min open circuit voltage (OCV) phase and an impedance measurement (~20 min). The voltage cut-off is chosen to be 4.0 V_{Li} for the 1st charging and 1.9--3.0 V_{Li} for the subsequent discharging/charging cycles. The impedance spectra were recorded potentiostatically between 100 kHz and 0.01 Hz with a perturbation of 20 mV at 25 °C.

Cycling protocol for the long-term cycling EIS measurement (Fig. 9). – The $Li_2S//LiC_6$ cells with GWRE cycled galvanostatically at 0.2C with a voltage cut-off of 4.0 V_{Li} for the 1st charging but 1.9-3.0 V_{Li} for the subsequent discharging/charging cycles. The potentiostatic impedance measurement were performed at the end of charge/discharge with a perturbation of 20 mV between 100 kHz and 0.01 Hz.

UV-Vis spectroscopy

The UV-Vis spectra were obtained using a Lambda 35 UV-Vis spectrometer (Perkin Elmer, USA), which was switched on at least 30 min prior to measurements. The samples were filled in an air-tight quartz-glass cuvette with a thickness of 1 mm and measured at room temperature (25 ± 1 °C) with a scan rate 240 nm/min and a step size of 1 nm in the wavelength window from 700 nm to 200 nm.

Results and discussion

Ender et al.[20] have inspected the suitability of a wire reference electrode for EIS measurement using FEM simulation. Especially, when the wire reference electrode is insulated with only the tip of the wire is active, the practically inevitable geometric and electrochemical asymmetry do not falsify the measurement results.

Whilst the stability and suitability of GWRE have already been examined in LiBs,[22] its application in Li-S batteries is still dubious owning to the (electro)chemically reactive soluble polysulfides (radical).

Potential-stability of gold wire reference electrode in the Li-S system (Fig. 1)

Here, we examine the potential stability of GWRE in a Li_2S//Li cell, which is cycled between 1.9–4.0 V_{Li} for 130 h in the DOL:DME-based electrolyte. The voltage profile of the Li_2S//Li cell is displayed in Fig. 1a, which is comparable with it in other Li_2S//Li cells reported in literature.[26] In other words, the presence of gold wire reference electrode has little/no impact on the Li-S electrochemical performance.

The potential of lithium anode referenced to GWRE is plotted in Fig. 1b. A potential oscillation ($\pm$10 mV) around -0.313 V_{Li} is observed upon cycling, which matches rather well to the 0.311 V_{Li} of the lithiated GWRE potential in Li ion batteries.[22]

Since potential drift of reference electrode can possibly introduce significant impedance distortion, it is necessary to consider whether this potential oscillation originates from the gold wire reference electrode or lithium anode. We therefore galvanostatically cycled a Li//Li cell with a Li metal reference electrode in the same electrolyte to examine if the potential oscillation is still present upon cycling.

The current is selected to be 125 μA/cm^2 to mimic the cycling condition as it in the Li_2S//Li cell in Fig 1b. The working electrode (Li) potential is referenced to the reference electrode (Li) and plotted in the Fig. 1c. Clearly, the working electrode potential still experiences an oscillation behavior of $\pm$10 mV in the absence of a gold wire reference electrode. Under this cycling condition, the potential oscillation can merely be ascribed to the overpotential of lithium plating and stripping, as investigated intensively by Bieker et al.[27] To note, the complicated oscillation behavior in Fig. 1b (e.g. several potential spikes during oxidation) may relate to the presence of different polysulfides during cycling. Moreover, if the GWRE were de-lithiated upon cycling in Fig. 1b, the potential of GWRE would drift rather unidirectionally than oscillating periodically. Hence, we believe the potential of lithiated gold wire (0.313 V_{Li}) is stable enough that can be employed for impedance measurement in Li-S batteries.

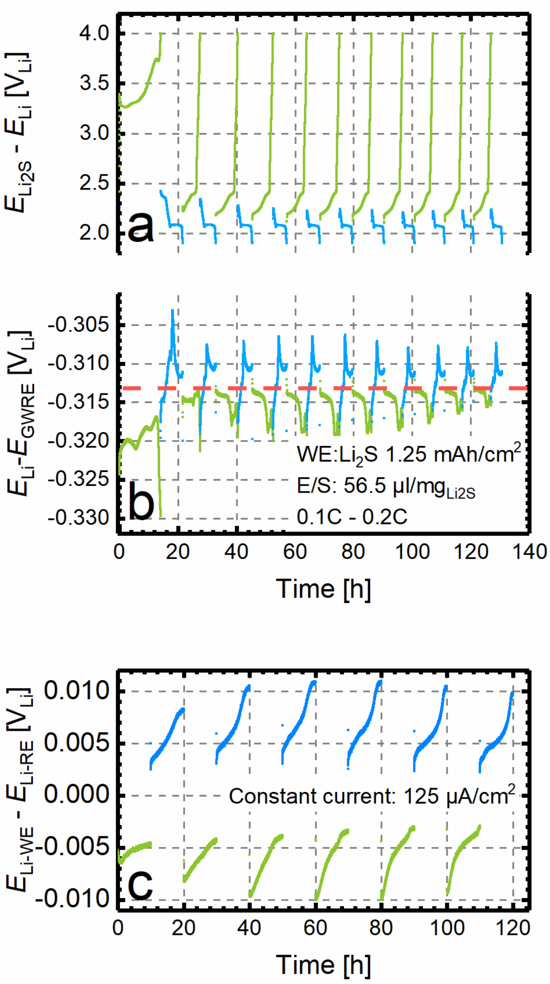

Figure 1 Galvanostatic cycling of a three-electrode Swagelok® T-cell consisting of Li_2S//Li and GWRE, where the cell was cycled at 0.1C during 1st charging and at 0.2C upon subsequent charging and discharging. The loading of Li_2S and electrolyte/sulfur ratio (E/S) are given in Fig.1b. 60 µl electrolyte consists of 1 M LiTFSI and 0.1 M $LiNO_3$ dissolved in DOL:DME(1:1, v:v) were added to the cell. (a) Voltage profile of Li_2S working electrode vs. Li metal counter electrode, where the line in green stands for charging (oxidation) of Li_2S electrode and the line in blue for discharging (reduction). (b) Voltage profile of Li counter electrode vs. GWRE, where the line in green represents lithium plating (reduction), line in blue corresponds to lithium stripping (oxidation) and the pink dash line marked the apparent center of potential oscillation. (c) Voltage profile of the Li working electrode vs. Li reference electrode in a three-electrode Swagelok® T-cell consisting of Li//Li and Li reference electrode, where the cell was cycled with a constant current of 125 µA/cm^2 to mimic the 0.1C current in Fig. 1b.

The suitability of GWRE in collecting proper EIS measurement in the Li-S system

The suitability of GWRE for an accurate EIS measurement in Lithium ion Batteries has already been validated, where the half-cell EIS obtained through GWRE was compared with the half of a full-cell impedance obtained in a symmetric cell at the relevant frequencies (100 kHz–0.1 Hz).[22]

A similar approach is adopted to examine the suitability of GWRE in the Li-S system. In order to acquire a rational and less error-prone impedance spectra, the symmetric cell setup is carefully designed.

Redox pair selection for EIS measurement: A defined redox reaction is a prerequisite for EIS analysis. However, it has been difficult to extract a well-defined polysulfide redox pair for EIS measurement, as the polysulfides are believed to disproportionate easily to other species in electrolyte solution. Nevertheless, we believe only several polysulfides are prevailing in a certain electrolyte system, such as S_4^{2-} in DOL:DME, S_8^{2-},S_6^{2-} and S_3^{-} radical in high donor solvents.[8,28,29] Using operando UV-Vis spectroscopy (in transmission mode), we have observed that S_8 is reduced to S_4^{2-} at the 1st discharge plateau, which is further reduced to S_3^{2-} in the transition phase between the two discharge plateaus (at ~2.2 V_{Li}).

Based on these observations, we believe the S_8/S_4^{2-} to be an apparent redox pair at the first discharge plateau, where little/no other polysulfides are detected, as shown in equation:[30]

$$S_8 + 4e^- \leftrightarrow (S_8^{4-}) \leftrightarrow 2S_4^{2-} \quad (2)$$

Therefore we nominally prepared a catholyte solution consisting of 5 mM S_8 and 10 mM "Li_2S_4" as redox pair for EIS measurement. The discussion of other long-chain polysulfides (e.g. Li_2S_8) not being prevailing in DOL:DME-based electrolyte was performed in our previous work[30]. Briefly, we show that the as-prepared "Li_2S_8" is less stable in DOL:DME-based electrolyte and disproportionate to "Li_2S_4" and elemental S_8 (Eq. 3).

- $$S_8^{2-} \leftrightarrow S_4^{2-} + \frac{1}{2}S_8 \quad (3)$$

This argument is supported by the result of UV-Vis spectroscopy in Fig.2a, where the absorption spectrum of experimentally prepared 1 mM "Li_2S_8" (marked as black solid line) is almost identical as the spectra summation/addition of experimentally prepared 1 mM "Li_2S_4" and 0.5 mM S_8 (marked as yellow dash line).

On top of the selection of redox pair, linearization of the system is also a necessity for a reliable EIS measurement. In reality, a quasi-linear condition can be achieved when for example a sufficiently small potential perturbation is applied to the system.[1] We marked the open circuit potential (~2.35 V_{Li}) of this redox pair (10 mM "Li_2S_4" & 5 mM S_8) on the discharge voltage profile in Fig. 2b. We notice that a potential perturbation of ~20 mV at the first discharge plateau will not drive a significant S_4^{2-} reduction on the WE, as higher overpotential is required to reduce S_4^{2-} (~2.2 $V_{Li,}$) compared to the reduction of S_8 (~2.4 V_{Li}).[30]

Therefore, the redox reaction during EIS measurement (~2.35±0.02 V_{Li}) is predominantly S_8 reduction and S_4^{2-} oxidation (Eq. 1).

Separation of working electrode (WE) EIS and counter electrode (CE) EIS via GWRE: Here, we assembled a symmetric three electrode Swagelok® T-cell with GWRE, where the electrodes (Vulcan carbon/Al) are separated by two glass fiber separator soaked with the catholyte solution (5 mM S_8 + 10 mM "Li_2S_4"). Fig. 3c shows the EIS of WE obtained via GWRE (blue line) is almost identical as the EIS of CE (red line) in the frequency range of ~65 kHz–0.1 Hz. To note, despite certain impedance distortions can be observed above 65 kHz (not shown), the impedance information at that frequencies is less relevant for our measurement. If we multiply the WE-EIS by a factor of two, the obtained EIS (yellow circle) superimposes on the measured full-cell EIS (black line). The understanding of these impedance spectra will be discussed extensively in the following section. Overall, the half-cell EIS obtained via GWRE delivers equivalent information as the full-cell EIS from a symmetric cell. In other word, the GWRE can be applied in the Li-S system to obtain the half-cell impedance in real-time.

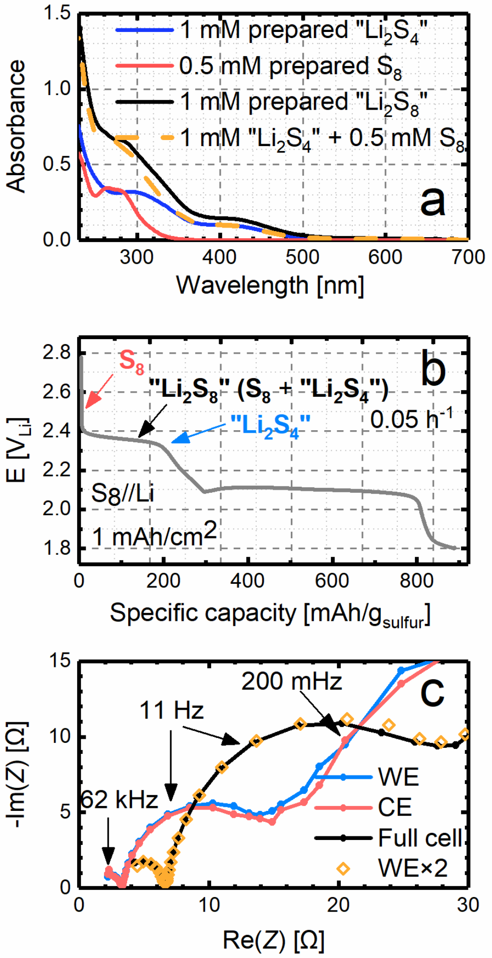

Figure 2 (a) UV-Vis spectra of 1 mM “Li_2S_4” (solid blue line), 0.5 mM S_8 (solid pink line) and 1 mM “Li_2S_8” (solid black line) in 1 M LiTFSI dissolved in DOL:DME (1:1, v:v), measured in an air-tight 1 mm thick cuvette at room temperature; The yellow dash line represents the mathematical spectra addition of the measured 1 mM “Li_2S_4” and 0.5 mM S_8. (b) The open circuit potential of prepared S_8 and polysulfides in DOL:DME (1:1, v:v) with 1 M LiTFSI and 0.1 M $LiNO_3$ which are marked in a typical discharge voltage profile of a S_8//Li cell in a DOL:DME-based electrolyte. (c) The impedance spectra measured in a symmetric Swagelok® T-Cell consisting of Vulcan carbon//Vulcan carbon and GWRE soaked in 60µl catholyte solution of 5 mM S_8 and 10 mM “Li_2S_4”dissolved in DOL:DME (1:1, v:v) with 1 M LiTFSI and 0.1 M $LiNO_3$. The solid pink and blue line represent the measured working and counter electrode impedance via GWRE, respectively. The solid black line stands for the measured full cell impedance between WE and CE, while the yellow circle corresponds to the mathematical multiplication of WE impedance by a factor of 2.

Understanding the Li-S impedance spectra in symmetric cells — a validation of equivalent circuit components

Since the ex-situ setup has already shown a complex impedance behavior (Fig. 2c), the *in-situ* EIS in a Li-S battery is believed to be even more complicated and more dynamic, owning to the various redox reactions and perpetual dissolution and precipitation of active material. We therefore want to first understand the impedance spectra of a simple setup – a symmetric cell under defined and static condition – before we apply GWRE into a cycling Li-S battery.

In the following, we assembled symmetric coin cells with two thin Vulcan carbon electrodes and one glass fiber (~200 µm), which is filled with sufficient catholyte solution (150 µl 10 mM “Li_2S_4” and 5 mM S_8 dissolved in DOL:DME(1:1, v:v) with 1 M LiTFSI and 0.1 M $LiNO_3$).

Table 1 Fit parameters of the equivalent circuit in Figure 3a

Parameters	Value	Comments
$R_{\text{sep.}}$	2 Ω	
$2R_{\text{ct}}$	20 Ω	Assuming an BET area of 1000 cm^2 and an BET normalized R_{ct} for polysulfide redox of 10 kΩ•cm$^2_{\text{BET}}$[19]
½C_{dl}	0.25 -1 mF	Assuming an surface area of 1000 cm^2 and a double layer capacitance of 5-20 µF/cm$^2_{\text{BET}}$[5]
tau	~100 s	Time constant for Warburg diffusion, calculated using equation 3
$2R_{\text{w}}$	~57 Ω	Diffusion resistance for a geometric area of 1.76 cm^2 (⌀15 mm electrode), calculated using equation 4
n	4 e$^-$	Electron transferred for the redox reaction in equation 1.
D_{ox} / D_{red}	1×10^{-6} cm^2/s	Diffusion coefficient of polysulfides, roughly estimation based on the work of various research groups[19,28,31]
L	0.01 cm	Diffusion length – half of the separator thickness
$c^0_{ox/red}$	5/10 mM	Concentration of S_8 (5 mM) and S_4^{2-}(10 mM)

We selected Vulcan carbon (coated on Al) as electrode rather than glassy carbon[17,19] to simulate the practical electrodes with high surface carbon and thus to qualitatively capture the EIS feature of a realistic S-cathode. A thin electrode (~5 µm) is chosen to eliminate the additional pore resistance (ionic resistance within a (thicker) porous electrodes, used in transmission line mode). The Randles-like equivalent circuit (shown in Fig. 3a) is therefore allowed to describe this setup and we are able to simulate the impedance spectrum based on the cell configuration and some literature value (Table 1).

According to Eq. 3 and 4, one is able to estimate the parameters for Warburg element, such as time constant (tau) and diffusion resistance (R_w), where *ox, red* stand for oxidized and reduced species, respectively.

$$tau_{\mathrm{ox/red}} = \frac{L^2}{D_{\mathrm{ox/red}}} \tag{3}$$

$$R_w = R_{w,\mathrm{ox}} + R_{w,\mathrm{red}} = \left[\frac{RT}{n^2F^2}\right]\left[\frac{L}{AD_{\mathrm{ox}}c_{\mathrm{ox}}^0}\right] + \left[\frac{RT}{n^2F^2}\right]\left[\frac{L}{AD_{\mathrm{red}}c_{\mathrm{red}}^0}\right] \tag{4}$$

Fig. 3b displays mainly two features of the simulated spectrum, namely a semicircle (apex at 18 Hz) and one 45° line followed by a depressed semicircle (apex at 0.01 Hz). Based on the equivalent circuit, the semicircle (apex at 18 Hz) is ascribed as charge transfer resistance. whereas the 45° line followed by the depressed semicircle at low frequency (~0.01 Hz) is a characteristic feature for a Warburg diffusion with transmissive boundary.[18]

Unlike Talian et al.[19], we believe the redox pair (polysulfides) in our catholyte solution have comparable diffusion coefficients in DOL:DME-based electrolyte such as $2.6•10^{-6}$ cm^2/s for S_8[28] and $7.0•10^{-6}$ cm^2/s for "S_4^{2-}"(operando UV-Vis)). We thus assume the D_{ox} and the D_{red} are equal (shown in table 1) for the simplified simulation, resulting in only one transmissive Warburg behavior in the simulated EIS (Fig. 2b.)

The experiment data is present in Fig. 3c, where three "semicircles" at distinct frequencies can be observed. Prior to further interpretation, we first experimentally examined the linearity, stability of the obtained impedance spectra as well as validated them using Kramers-Kronig analysis, as shown in S1.

We denote the three "semicircle" as Z_1 (apex at 8.8 kHz), Z_2 (apex at 11 Hz) and Z_3 (apex at 15 mHz) in Fig. 3c. In the following, each semicircle will be briefly analyzed and correlated with a physical-chemical process.

Z_1 is ascribed as contact resistance (R_{cont}) at the current collector/cathode interface. The capacitance that involves in the 1st semicircle (Z_1), is roughly estimated to be C = $(2\pi•f(\mathrm{apex})•R)^{-1} \approx 2.3$ µF, which is only the half of capacitance on a single electrode (in Fig. 3a). Eventually, we estimated the capacitance of this fast process to be 2.6 µF/cm$^2_{\mathrm{geo}}$ (normalized to the geometric area of the electrode ≈1.75 cm^2), which is reasonably consistent with the electrochemical double-layer capacitance.[5] A fast process that takes places at a surface of 1.75 cm^2 match wells to the contact resistance at the current collector/cathode interface.

Z_2 is assigned to the charge transfer resistance (R_{ct}) with an apex frequency at ~11 Hz, which is quite comparable with our simulation in Fig. 3b. Similarly, the capacitance of this process is roughly estimated to be 0.65 mF and it gives an areal capacitance of 2.3

$\mu F/cm^2_{BET}$ (normalized to the BET surface of 567 cm^2), which is also in agreement with the electrochemical double-layer capacitance. We thus preliminarily ascribe this process to charge transfer resistance that occurs at the interface of electrode/electrolyte.

Z_3 is considered to be Warburg diffusion processes. We estimated the BET-surface normalized capacitance to be ~0.5 mF/cm^2_{BET}, which is two magnitude higher than the electrochemical double-layer capacitance. Hence, this process is unlikely a slow charge transfer process but a Warburg diffusion process, which also have comparable frequencies with the (based on our cell configuration) simulated EIS in Fig. 3b.

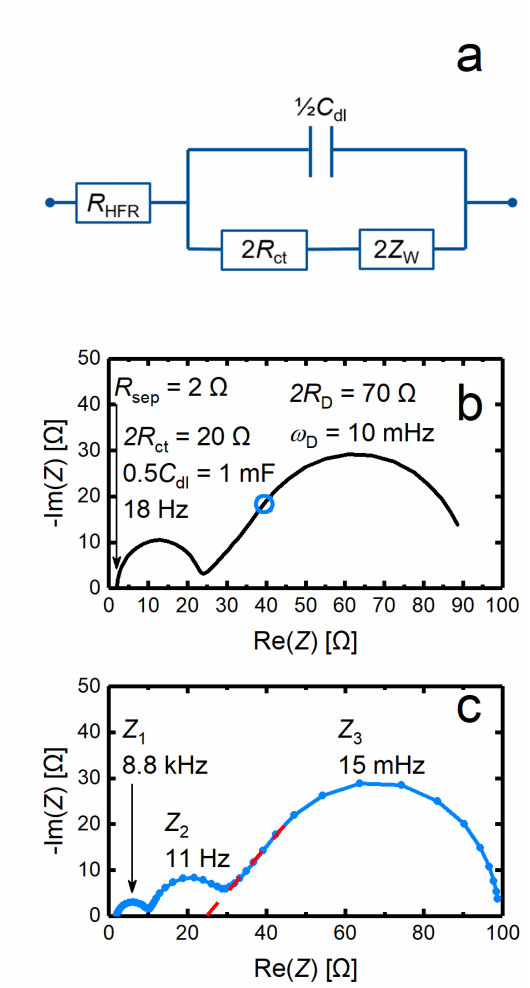

Figure 3 (a) a proposed Randles-like equivalent for an ideal symmetric cell setup. (b) Simulated impedance spectrum in a Nyquist plot based on the equivalent circuit in (a) and parameters from Table 1; (c) The measured impedance spectrum of a symmetric coin cell with Vulcan carbon (VC)//Vulcan carbon electrodes separated by one glass fiber separator, which is soaked with catholyte solution of 5 mM S_8 and 10 mM "Li_2S_4" in DOL:DME (1:1, v:v) with 1 M LiTFSI and 0.1 M $LiNO_3$. The crossing of the red dash line with x-abscissa is the value that is used for HFR correction in order to determine the phase angle of Warburg element (please refer to Fig. 5a). Potentiostatic impedance measurement with a perturbation of 20 mV were performed in the frequency range of 200 kHz to 1 mHz.

Validation the assignment for R_{cont} and R_{ct}

In the following, we vary various parameters in the symmetric cells, such as temperature, concentration of redox pair, separator thickness, and surface area of carbon substrate, to investigate how each “semicircle” responses to the individual parameter change.

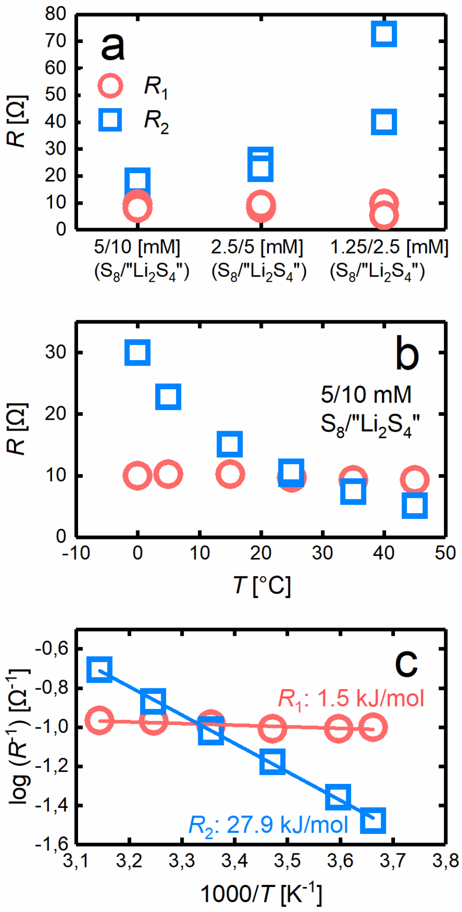

Figure 4 (a) The real resistance of Z_1 and Z_2 in symmetric coin cells with different concentration of redox pair at 25 °C, where two cells were measured for each concentration (b) The real resistance of Z_1 and Z_2 in symmetric coin cell with 5 mM S_8 and 10 mM “Li_2S_4” measured at different temperature. The R_1 and R_2 value were obtained by fitting the impedance with a Randles-like equivalent circuit. (c) Temperature-dependencies of R_1 and R_2 using the Arrhenius relation (equation 7).

First, we varied the concentration of redox pair in the symmetric cells and observe that R_1 (resistive part of Z_1) is independent of redox pair concentration (Fig. 4a), indicating a non-faradaic process. In contrast, R_2 (resistive part of Z_2) is negative correlated with the concentration of redox pair, that is, a lower concentration of redox pair leads to a larger R_2. This qualitative correlation fits well to the prediction of charge transfer resistance based on Eq. 5 and 6 for a Randles-like equivalent circuit.

$$R_{\mathrm{ct}} = \frac{RT}{nFI_0} \tag{5}$$

$$I_0 = nFAk^0[(C_{\mathrm{red}}^0)^p]^\alpha[(C_{\mathrm{ox}}^0)^q]^{1-\alpha} \tag{6}$$

with R being gas constant, T as for temperature, n is the number of electron transferred, F is the Faraday´s constant, k^0 as the rate constant at the equilibrium potential, C_{red}^0 and C_{ox}^0 are the bulk concentration of redox pairs, p and q are the stoichiometric factors for the reduced and oxidized species, respectively and α stands for the transfer coefficient.

Since S_8/"S_4^{2-}" is only an apparent redox pair, the exact composition of the catholyte solution remains unclear, so as n, p, q, k^0 and α. Hence, a quantitative correlation between R_{ct} and the nominally prepared concentration does not allow to be currently revealed.

Next, we probe the Temperature-dependency of Z_1 and Z_2 in the symmetric cells. As Fig. 4b clearly demonstrates, temperature has no influence on the R_1 but correlates with R_2 negatively. Although Eq. 5 shows that charge transfer resistance (R_{ct}) is positively correlated with T, the rate constant k^0 in Eq. 6 is negatively correlated with temperature through the Arrhenius relation r. Hence, the R_{ct} still demonstrates a negative correlation with temperature.

We evaluated the apparent activation energies of R_1 and R_2 using Arrhenius relation (equation 7).

$$\frac{1}{R_x} = A \times \exp(-\frac{E_a}{RT}) \qquad (7)$$

As shown in Fig. 4c, the activation energy for R_1 is determined to be 1.5 kJ/mol, which indicates Z_1 is a process related to the electric resistance (E_{a} = 0.84 kJ/mol[14]) rather than to the ionic conduction (E_{a} = 16 kJ/mol[6,14]) or charge transfer (E_{a} > 25 kJ/mol[6,14,32]).

Unlike it in LiBs, the activation energy for charge transfer process is difficult to determine in Li-S batteries owning to the undefined redox reactions at different temperature.[23,33] Nevertheless, the activation energy of R_2 is estimated to be 27.9 kJ/mol. Hence, the R_2 is believed to associate with charge transfer processes, albeit the undefined redox reactions.

In conclusion, R_1 is assigned as contact resistance at interface of electrode/current collector based on the estimated capacitance, temperature and redox pair concentration independency. On the other hand, R_2 is ascribed to the charge transfer resistance at the interface of electrode/electrolyte, owning to its capacitance, its dependency on temperature and redox pair concentration. To note, albeit the exact value of R_1, R_2 may vary when using different equivalent circuits fitting the EIS spectra, their dependencies on the temperature or redox-pair concentration would not significantly change on that account. A further validation for R_1 and R_2 is presented in supporting information, where the Vulcan carbon/Al electrode is replaced by a carbon paper electrode, which has a reduced carbon surface area and does not have an interface of Al current collector.

Validation the assignment for Warburg elements

We preliminarily assign the Z_3 as Warburg element based on the unrealistic "BET-normalized capacitance" and 45° line as a feature for ideal Warburg behavior (shown in Fig. 3b). In the following, we examine the response of Z_3 to the change of redox-pair concentration and the separator thickness.

The phase angle (Bode plot) for redox pair with three different concentrations are plotted in Fig. 5a, where the high-frequency resistances are corrected by taking the intersection of the red dash line with the x-axis as shown in Fig. 3c.

In the frequency region of 0.5 – 0.05 Hz in Fig. 5a, we clearly observe a phase angle plateau at ~45° for all three concentrations. The slight phase angle variation can be rationalized by 1) experimentally cell-to-cell variation and 2) the systematic error upon HFR determination, as discussed by Morasch et al.[4] Since the presence of a a phase angle plateau between 40° – 45° is only a weak evidence for Warburg diffusion behavior, we further inspect the concentration dependency of the time constant for this process (Z_3), as shown in Fig. 5b.

For a Warburg diffusion process, its time constant is only related to diffusion length (L) and the diffusion coefficient (D) as described in Eq. 3. The characteristic diffusion frequency (w_D, inverse of time constant) is marked exemplarily in Fig. 3b with the blue circle. It separates the diffusion into two regimes: 1) if $w \gg w_D$ (i.e., the 45 degree linear part of Warburg impedance), the species will not sense the boundary at $L = L_D$ (thickness of diffusion layer) and the system behaves effectively semi-infinite. 2) if $w \leq w_D$, the impedance response depends on whether the species are reflected (reflection boundary, showing a vertical 90° line) or extracted (absorbing/transmitting boundary, displaying a depressed semicircle).[18] Therefore, the time constant for Warburg diffusion is not affected by the concentration of diffusing species, so as the time constant for Z_3 as shown in Fig. 5b.

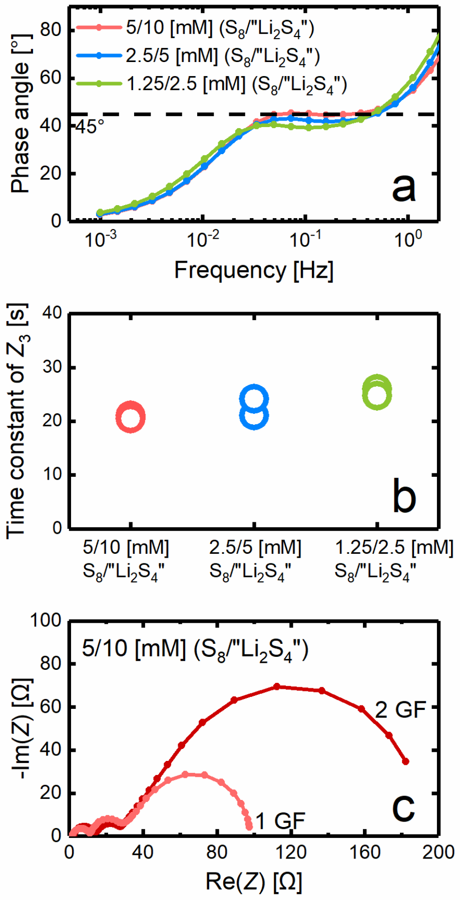

Figure 5 Impedance analysis of symmetric coin cells with various concentration of redox pairs. (a) HFR-corrected phase angle diagram showing a phase angle plateau around 45° (b) Plot of time constants (Z_3), which are obtained by fitting the Z_3 with a Warburg diffusion element (with absorbing boundary). (c) The impedance spectra of symmetric coin cells with 5 mM S_8 and 10 mM "Li_2S_4" separated either with one (pink curve) or two (dark red curve) glass fiber (GF) separators. All the measurements above were conducted at 25 °C.

As a final validation, we increased the diffusion length by doubling the separator thickness to examine the response of Z_3. As displayed in Fig. 5c, Z_1 as contact resistance and Z_2 as charge transfer resistance are not influenced by the change of diffusion length. However, Z_3 rises with the increased diffusion length. Fitting the impedance data with a randles-like equivalent circuit ($R + R_{\text{cont}}/Q_{\text{cont}} + (R_{\text{ct}}+W)/Q_{\text{ct}}$), we are able to obtain the relative increase of diffusion length either via the ratio of $\frac{R_3(2GF)}{R_3(1GF)} = \frac{166\ \Omega}{71.1\ \Omega} = 2.33$ or via the square root ratio of $\sqrt{\frac{\tau(2GF)}{\tau(1GF)}} = 2.39$. Moreover, the mixed diffusion coefficient of the redox pair (S_8/"Li_2S_4") can be estimated using equation 3, assuming the diffusion length (~100 μm) to be the half of glass fiber thickness. The mixed diffusion coefficient of polysulfides blends (S_8/"S_8^{4-}" or "$2S_4^{2-}$") is determined to be $4.7 \cdot 10^{-6}$ cm²/s ± 19%, where the 19% error originates from eight different cells with various concentration and separator thickness. This average diffusion coefficient obtained by impedance spectroscopy is in good agreement with the diffusion coefficients obtained via rotating ring disk electrode technique, such as $2.6 \bullet 10^{-6}$ cm^2/s ± 30%[28] and $7.0 \bullet 10^{-6}$ cm^2/s ± 30% (operando UV-Vis) for dissolved S_8 and "S_4^{2-}" in DOL:DME (1:1, v:v) with 1 M LiTFSI, respectively.

Equivalent circuit for the Li-S system

Fig. 6 display the proposed Randles-like equivalent circuit and an exemplary fits of the symmetric cell impedance spectra as well as the fit parameters. Clearly, this equivalent circuit with the listed nine fitting parameters provides quite a good fit to the impedance data (black circle) over the whole frequency range (100 kHz to 1 mHz).

From the fitting parameter we learned that R_{cont} has a value ≈ 4 $\Omega/cm^2_{\mathrm{geo}}$, which is close to the value proposed by Landesfeind et al.[5] in LiB system (~3 $\Omega/cm^2_{\mathrm{geo}}$) and not far from the value observed by Raccichini et al.[3] in a symmetric cell with industrial-scale produced electrodes (12–7 $\Omega/cm^2_{\mathrm{geo}}$). The origin of this contact resistance in Li-S system is rather complex and can be attributed to several possibilities, such as 1) an oxide layer on the current collector without involving S-species proposed by Raccichini et al.,[3] 2) an interlayer between current collector and electrode that involves S-species; 3) a coating with poor adhesion to the current collector and 4) a cell with insufficient compression[34]. Although several attempts have been performed in this study to understand the contact resistance in the Li-S system (see Fig. S4), a systematic and detailed investigation is still required to draw a firm conclusion in its origin.

The R_{ct} obtained in the symmetric cells varies from 4.5–19 $k\Omega/cm^2_{\mathrm{BET}}$ (25°C) depending on the redox pair concentration (1.25/2.5 mM to 5/10 mM S_8/"Li_2S_4"). These value are also in the same magnitude as it in Talian et al.[19] using glassy carbon as electrodes in symmetric cells. Considering the limited dissolution of S-species in electrolyte (S_8 dissolve < 10 mM and "Li_2S_4" dissolve < 40 mM in DOL:DME (1:1, v:v) with 1 M LiTFSI at 25 °C) and considering the large R_{ct} (4.5–19 $k\Omega/cm^2_{\mathrm{BET}}$ normalized by BET surface), it confirms the necessity of using high surface area carbon in Li-S batteries to reduce the total charge transfer resistance.

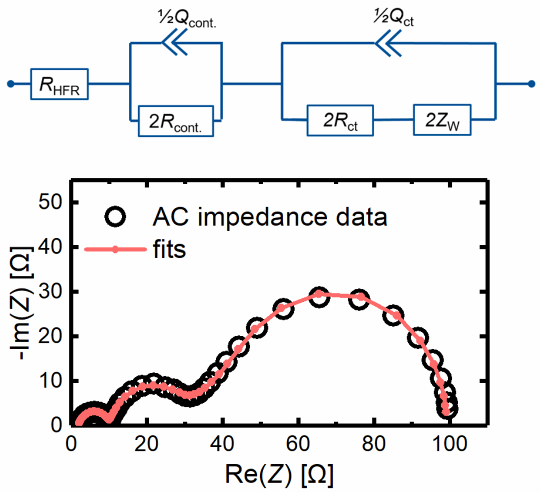

R_{HFR} = 2 Ω ± 18% $2R_{ct}$= 15.9 Ω ± 2%
$2R_{cont}$ = 8 Ω ± 5%
$0.5Q_{cont}$ = 1.64 • 10^{-5} F• $s^{(\alpha cont-1)}$ ± 16.5%
$0.5Q_{ct}$ = 1.51 ± • 10^{-3} F• $s^{(\alpha ct-1)}$ ± 6.8%
α_{cont} = 0.82 ± 2.5% α_{ct} = 0.88 ± 2.2%
$2R_{w}$ = 72 Ω ± 0.5% τ = 20.9 s ± 1.2%

Figure 6 (top panel) Randles-like equivalent circuit that is validated for symmetric coil cells of thin VC//VC electrodes soaked in catholyte solution. (bottom panel) The obtained impedance spectrum (black circle) of a symmetric coin cell with VC//VC electrodes separated by one glass fiber separator, which is soaked with catholyte solution of 5 mM S_8 and 10 mM "Li_2S_4" in DOL:DME (1:1, v:v) with 1 M LiTFSI and 0.1 M $LiNO_3$. The solid pink line represents the fitted impedance spectra using the fitting parameters listed underneath.

Testing procedures of *in-situ* impedance measurement in a three-electrode Li-S battery

In the following, we apply the gold wire reference electrode (GWRE) in a $Li_2S//LiC_6$ battery to deconvolute the cathode impedance spectra from the full-cell impedance spectra. In order to minimize the surface area asymmetry between the cathode and anode, and to avoid the highly dynamic chemical reaction at the surface of lithium metal, we use pre-formed graphite as anode that has a stable preformed SEI introduced by vinylene carbonate.[22,25]. In order to obtain SOC-resolved impedance in a cycling cell, we galvanostatically cycled the cell for 30 min (CC) with a c-rate of 0.1C, followed by a 20 min relaxation phase (OCV) and a further 20 min impedance measurement (EIS). This CC-OCV-EIS step is periodically repeated 20 times for each charge/discharge process. The raw voltage profile is shown in Fig. 7a, where an unconventional 1st charge process with a lower charging voltage manifests itself. In general, a much higher voltage is expected in the 1st charge in a $Li_2S//Li$ cell, while the lower charging plateau is only expected in the subsequent charging processes.[26,35] This phenomenon can be explained by the pre-formed stable SEI on the lithiated graphite, that would consume less of the formed polysulfides, so that polysulfides can be accumulated and in turn facilitate the oxidation of Li_2S by chemical reactions.[26,35] We therefore performed the same cycling procedure to a Li_2S//Li cell and a Li_2S//C_6 cell without pre-formed SEI, which is further discussed in Fig. S5.

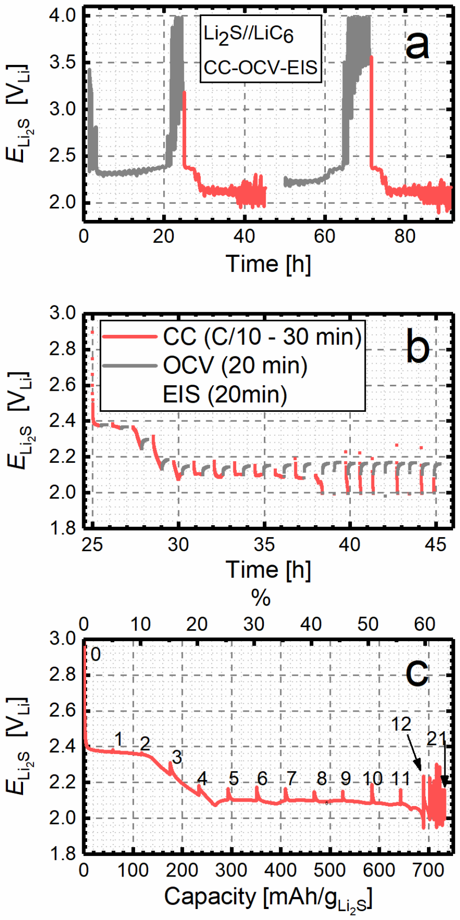

Figure 7 Galvanostatic cycling of a three-electrode Swagelok® T-cell consisting of Li_2S//LiC_6 and GWRE. The loading of Li_2S and LiC_6 are 1.44 mAh/cm^2 and 2.84 mAh/cm^2, respectively, where the LiC_6 electrode was pre-formed and 10% SOC pre-lithiated. 60 µl electrolyte composed of 1 M LiTFSI and 0.1 M $LiNO_3$ dissolved in DOL:DME(1:1, v:v) were added to the cell. The cycling protocol consists of 20 times repeated 30 min galvanostatic cycling at 0.1C followed by 20 min OCV and a 20 min impedance measurement for each charge/discharge process The voltage profile of the first two charge and discharge cycles is presented in (a), where the enlarged voltage profiles of the first discharge are demonstrated either with time (b) or with capacity/SOC (c).The numbers in (c) mark the positions where impedance measurements were conducted.

In this study, we take the discharge process to exemplarily demonstrate the applicability of GWRE in Li-S batteries. The voltage profile of 1st discharge process is plotted either with time (demonstrated in Fig. 7b) or with SOC (present in Fig. 7c), where two distinct discharge plateaus as well as a reasonable discharge capacity of ~700 mAh/g_{Li2S} are displayed.

Analysis of *in-situ* impedance spectra

Fig. 8a demonstrates the impedance spectra measured before and after the 1st charging process. In order to characterize the pristine Li_2S electrode, the very first impedance spectrum was collected 30 min direct after cell assembly, where a 45° line at high frequencies followed by a vertical line at low frequencies is shown. Unlike the 45° line presented for Warburg diffusion, this 45° line takes places at much higher frequencies (kHz) and is assigned to the transport process of electrolytes contained within porous electrodes (for non-faradaic processes with only double-layer capacitance induced current), as thoroughly discussed in the literature.[1–3,5,18]

One is able to obtain pore resistance (R_{pore}, ionic resistance inside the pores of porous electrode), by either extrapolating the low frequency branch to the x-axis ($Z_{El.}|_{(\omega_{low}\to 0)}$) via equation 8[2,5,14] or fitting the impedance result with equivalent circuit in transmission line mode (EC-TLM).[5]

$$R_{pore} = 3\left(\left(Z_{El.}|_{(\omega_{\text{low}}\to 0)}\right) - HFR\right) \approx 1\Omega \tag{8}$$

The apparent tortuosity (τ) of the pristine Li_2S electrode can be estimated through equation 9:

$$\tau = \frac{R_{pore}\cdot\varepsilon\cdot A\cdot\kappa}{d} \approx 2.4 \tag{9}$$

with ε being porosity (~60%), A as geometric area of electrode (~0.95 cm^2), κ as ionic conductivity of electrolyte (12.67 mS/cm at 25 °C) and d stands for the thickness of electrode (~30 μm). The MacMullin number of the pristine Li_2S electrode is estimated to be $N_M = \tau$ (tortuosity)/ε (porosity) ≈ 4. Both apparent tortuosity and MacMullin number of the Li_2S electrode are comparable with the respective parameters in the S-electrodes prepared by Raccichini et al.[3] and Oxis Energy Ltd.[3] Especially, the relative small MacMullin number of our electrodes can be rationalized by the uncompressed large Li_2S particles.

After the 1st charging process (100% SOC), the impedance spectrum (marked as 0 in Fig. 8a) clearly shows a semi-circle at high frequencies followed by a vertical line. As previously discussed, this semi-circle is assigned to the contact resistance, owing to the high frequencies (apex at 45 kHz, a fast process) and its geometric areal normalized capacitance (estimated to be ~2 $\mu F/cm^2_{\text{geometric}}$). The vertical line at low frequencies indicates the so-called blocking condition, i.e. R_{ct} becomes extremely large (ideally going to infinity).[5]

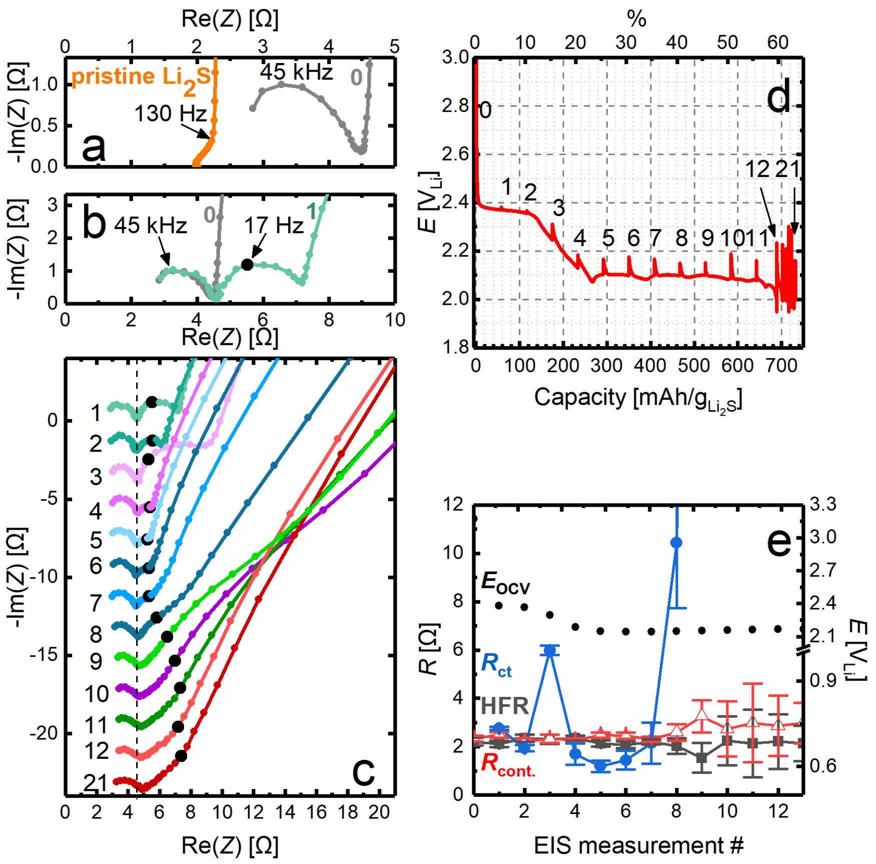

Figure 8 SOC-resolved impedance measurements of the three-electrode Swagelok® T-cell measured with GWRE from Fig. 7. Potentiostatic impedance measurements were conducted with a perturbation of 20 mV between 100 kHz and 0.01 Hz (~20 min acquisition time). (a) Nyquist plots of the Li_2S cathode prior to the 1st charging (pristine Li_2S electrode, line in orange) and after the 1st charging (line in grey, EIS-0). (b) Nyquist plots of the Li_2S cathode prior to the 1st discharge (= after the 1st charge, line in grey) and at 5% depth of discharge (line in light green, EIS-1). (c) SOC-resolved impedance spectra of a Li_2S cathode measured at the position marked in the voltage profile (d). The black dot in (b) and (c) labels the frequency of 17 Hz. (e) The evolution of HFR (grey), R_{cont} (red) and R_{ct} (blue) along with the equilibrium potential (black dot) ahead of the impedance measurements. The value of HFR, R_{cont}, R_{ct} are obtained semi-quantitatively by fitting the impedance spectra with a simple Randles-like equivalent circuit without Warburg elements as displayed in Fig. 6 (only in the frequency range of 100 kHz – 1 Hz).

Interestingly, the contact resistance (~2 Ω) is not present initially at the pristine electrode but continuously developed during the 1st charging, which suggests an S-species involved interlayer at current collector and electrode. Albeit we performed a XPS measurement on the surface of Al (Fig. S6), a more detailed investigation is required to understand its underlying formation mechanism

Fig. 8b displays the impedance spectrum of the first EIS during discharging (5% of theoretical capacity, marked as 1), where an additional semicircle at lower frequencies (with an apex at 17 Hz) is observed. The capacitance of this semicircle is estimated to be ~3 mF, which yields a BET surface normalized capacitance of 2.2 μF/cm$^2_{\mathrm{BET}}$. Comparing this with symmetric cell results (Fig. 3c), we noted several similarities, especially in frequencies and its capacitance, and therefore we ascribe this semicircle to charge transfer resistance in the cell.

The impedance at lower frequencies that comes after R_{ct} may be assigned to Warburg diffusion, which cannot be fully experimentally captured with a frequency limit of 10 mHz and therefore not discussed in the *in-situ* results.

All the relevant impedance spectra are presented in Fig. 8c and they are progressively shifted down by 2 Ω for clarity. To enable better comparison with first Impedance, 17 Hz frequency point is marked as a black dot in all the EISs.

We observe the contact resistance (1st semicircle) remains almost constant throughout the whole discharge process (only ~0.5 Ω increase from EIS-1 to EIS-21), suggesting this interlayer at current collector/electrode is potential and SOC independent and is not affected by the formed reaction intermediates upon cycling.

Compared to the contact resistance, the charge transfer resistance (R_{ct}, 2nd semicircle) is much more dynamic and varies at different SOC. Unfortunately, this dynamic R_{ct} variation does not allow easy interpretation, since R_{ct} is largely influenced by both the redox species and their concentration. However, we are able to better comprehend the variation of R_{ct} at different SOC with the information obtained in our previous study using operando UV-Vis spectroscopy (transmission mode)[30], which simultaneously provides information about both polysulfides species and their concentrations upon discharging.

Taking a closer look, the R_{ct} manifests itself immediately in the impedance spectrum once discharge initiates (5% depth of discharge, EIS-1 in Fig. 8b) and becomes smaller in the next measurement (EIS-2, at the end of 1st discharge plateau), which is followed by an increase in EIS-3. This oscillation that the R_{ct} (EIS-0 @ blocking condition) declines first (EIS-1&2) and then raises again (EIS-3), can be well rationalized by the variation of redox pair concentration using equation 5 and 6, if this relates to only one electrochemical reaction.

As evidenced by operando XAS[26] and XRD[36] techniques, only elemental sulfur is observed at the end of 1st charge (e.g. EIS-0), which leads to a huge R_{ct} in the absence of reduced part of the redox pair (i.e. $C^0_{\mathrm{red}} \rightarrow 0$). Once discharging initiates, elemental S_8 is apparently reduced to $^{2-}S_4^{2-}$ at the first discharge plateau (equation 2),[30] which will cause a decrease in R_{ct}. Upon further discharging till ~2.2 V_{Li} (middle of the transition of the two discharge plateau, operando UV-Vis), the concentration of the S_8 drops and approaches to zero (i.e. $C^0_{\mathrm{ox}} \rightarrow 0$) and consequently, an increase in R_{ct} will be expected.

After the 1st discharge plateau, we observe a similar R_{ct} oscillation from EIS-3 to EIS-12, as clearly shown by the blue line in Fig. 8e (evolution of impedance upon discharging). The formed S_4^{2-} is largely reduced to S_3^{2-} at ~2.2 V_{Li} (transition phase between the two discharge plateaus, equation 10), which will be further converted to a lower polysulfide species at ~2.1 V_{Li} (2nd discharge plateau, shown in non-stoichiometric equation 11):

$$S_4^{2-} + \frac{2}{3}e^- \rightarrow \frac{4}{3}S_3^{2-} \tag{10}$$

$$S_3^{2-} + ne^- \rightarrow mS_2^{2-}/S_1^{2-} \tag{11}$$

In principle, each electrochemical reaction shall be accompanied by one R_{ct} oscillation phenomenon owning to the relative concentration change of its redox pair, as it is shown for the 1st discharge plateau (from EIS 0-3). However, this may not be valid, if a disproportionation reaction is present that can modify the concentration of the redox pair. As proposed in the results of operando UV-Vis spectroscopy,[30] an additional fast disproportionation reaction (equation 12 in a non-stoichiometric form) can re-generate S_4^{2-} and moderates its concentration and consequently the R_{ct} oscillation phenomenon for the S_4^{2-} reduction step.

$$\mathrm{S}_3^{2-} \leftrightarrow \mathrm{pS}_4^{2-} + \mathrm{qS}_2^{2-}/S_1^{2-} \tag{12}$$

Moreover, the impedance spectra from EIS-9 to EIS 20 have to be carefully interpreted. Although the impedance spectra of EIS-9 to EIS 20 all have a ~45° line following the contact resistance semicircle, only EIS-12 and 20 can be interpreted as approaching blocking condition, where R_{ct} is so large that no more capacity can be extracted (Fig. 8d). Special attention has to be paid to the relative larger and less visible semicircle of R_{ct} in EIS-9, 10 and 11, which comes after the 45° line and superimposes with Warburg diffusion impedance. More specifically, the low frequency branch in EIS-9, 10, 11are less vertical and cross with each other, while the low frequency branch in EIS-12 and 20 are more vertical and almost in parallel to each other.

Comparing the impedance spectra of EIS-12 (blocking condition) and the impedance of pristine Li_2S electrode (Fig. 8a, blocking condition), a clear increase of pore resistance can be observed, which may be related to the inhomogeneous distribution of Li_2S after cycling. Exemplarily, the R_{pore} in EIS-12 is determined to be 5.5 Ω ± 91% by fitting the impedance spectra with EC-TLM. Accordingly, the apparent tortuosity can be roughly estimated via equation 9, which has a value of 13.2 ± 91% (assuming porosity, thickness, ionic conductivity are constant).

We chose a rather simple equivalent circuit (Randles-like EC in Fig. 6 without the part of Warburg diffusion) to semi-quantitatively fit the impedance data (100 kHz – ~1Hz) regardless the porous electrode, mainly because 1) the inhomogeneous and dynamic distribution of precipitates upon cycling and 2) a complicated diffusion process that simultaneously take place in both electrode and separator. The fitted parameters, such as HFR, R_{cont} and R_{ct} are plotted along with the measurements and summarized in Fig. 8e.

Evolution of R_{cont} in a Li-S battery over extended discharge/charge cycling

In order to understand how contact resistance evolves for a Li-S battery in the long-term, we assembled another three-electrode cell with GWRE and performed the EIS measurements only at the end of the discharge and charge process.

The discharge capacities and the coulombic efficiencies for the Li_2S//LiC_6 cell cycled at 0.2C are plotted over 21 cycles in Fig. 9a. Though, this cell setup with GWRE is not optimized for the long-term cycling of Li-S batteries, the delivered capacities and coulombic efficiencies shown in Fig. 9a are still acceptable and it are sufficient to demonstrate how the impedance evolves upon extended discharge/charge cycling.

The selected EISs are presented in Fig. 9b. Consistent with our observation in Fig. 8a, the contact resistance was absent in the pristine electrode (marked as green line) but slowly developed during the 1st charging process (line in light blue).

We noticed contact resistance (~10 Ω) here is larger compared to it in Fig. 8, which may be related to the cell-to-cell variance in the interlayer at current collector and electrode, as it can be easily influenced by the cycling conditions (electrode composition and drying temperature,[4] voltage,[5,34] temperature,[34] compression[34]). In addition, we also observe a growth (~4 Ω) of R_{cont} during the 1st discharge (marked as pink line in Fig. 9b), which eventually approaches to a “steady state” (line in dark blue, #21). This evolution of R_{cont} is clearly demonstrated in Fig. 9c and a similar trend of R_{cont} is also reported in LiB[5], despite the likely distinct compositions of the interlayers at electrode/current collector.[34]

More interestingly, we noticed that the R_{cont} measured at fully charged state (line in blue in Fig. 9c) is consistently smaller by 1-2 Ω than it at fully discharged state (line in red in Fig. 9c). We confirmed this phenomenon in other GWRE three-electrode cells (data not shown) and we believe this may relate to the different solubility of the charged/discharged products, which precipitate throughout the electrode as well as at the electrode/current collector interface.

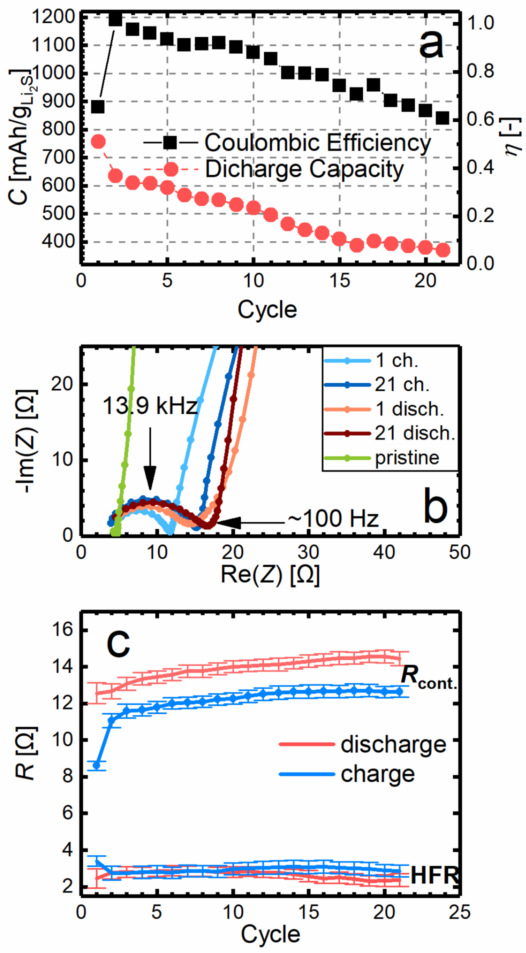

Fig. 9 Galvanostatic cycling of a three-electrode Swagelok® T-cell consisting of Li_2S//LiC_6 and GWRE with a cycling C-rate of 0.2C. The loading of Li_2S and LiC_6 are 0.95 mAh/cm^2 and 2.77 mAh/cm^2, respectively, where the LiC_6 electrode was pre-formed and 10% SOC pre-lithiated. Impedance measurements were performed at the end of charge and discharge. Potentiostatic impedance measurements were conducted with a perturbation of 20 mV between 100 kHz and 0.01 Hz.(a) Specific discharge capacity and coulombic efficiency versus cycle number. (b) Selected Li_2S cathode impedance spectra at the beginning and the end of the cycling. (c) The evolution of HFR, contact resistance along with cycling at both charged (blue) and discharge (red) states. The value of HFR and R_{cont} are obtained semi-quantitatively by fitting the data with a Randles-like equivalent circuit (HFR+R_{cont}/Q_{cont}, in the frequency range of 100 kHz-~100 Hz).

It is generally known that the discharged product Li_2S is isolating and insoluble in the DOL:DME-based electrolyte,[37] whereas the charged product S_8 have certain solubility (< 10 mM in DOL:DME(1:1, v:v) with 1 M LiTFSI), which can be beneficial in electronic conduction for the interlayer of cathode/current collector (i.e. less electronic contact resistance).

In closing, we compare the R_{cont} and R_{ct} in the Li-S system with them in the LiBs, as shown in Table 2.

Table 2 Comparison of contact resistance (R_{cont}) and charge transfer resistance (R_{ct}) in Li-S batteries and LiBs.

Cathode material	Li_2S/VC (2:1, w:w)	LNMO	LFP	Graphite
$R_{\mathrm{cont.}}$ ($\Omega \bullet cm^2_{geo}$)	2-15	>1-160 [5,34]	-	12[6]
R_{ct} @25 °C ($k\Omega \bullet cm^2{}_{BET}$)	>1.4	0.1 @10%SOC[5]	0.1[38]	$R_{\mathrm{ct}} + R_{\mathrm{SEI}}$ = 0.4[6]

Throughout the whole discharge process in Fig. 8, we identified the lowest R_{ct} (EIS-5, at the beginning of 2nd discharge plateau, 1400 $\Omega \bullet cm^2_{BET}$) in the Li_2S//LiC_6 cell, which is 10 times greater than it of LNMO cell (~100 $\Omega \bullet cm^2_{BET}$ at ~10% SOC). In other words, the exchange current density is allowed to be estimated using linearized Butler-Volmer equation (rearrangement of equation 5), as shown:

$$i_0 = \frac{RT}{FA_{\mathrm{BET}}R_{\mathrm{ct}}} \tag{13}$$

The highest exchange current density obtained in Fig. 8 is ~0.02 mA/cm^2_{BET}, which is consistent with it reported by Talian et al.[19](~0.0125 mA/cm^2) and is considerably lower compared to it in the Li-ion battery system, such as 0.02–0.3 mA/cm^2_{BET} for $LiNi_{0.5}Mn_{1.5}O_4$ (LNMO),[5,39] 0.17 mA/cm^2_{BET} for $LiFePO_4$ (LFP),[38] and 2.5 mA/cm^2_{BET} for graphite.[40] This high R_{ct} or low exchange current density of S-cathode 1) certify the necessity of using high surface conducting carbon in a Li-S battery and, 2) explains the limitation of the Li-S system in high rate cycling performance. A further improvement of Li-S batteries performance can be accomplished through the implementation of inexpensive high-surface catalyst to intrinsically modify the R_{ct} (kinetics) and/or accelerate the disproportionation reactions. A similar approach is successfully adopted in proton exchange membrane fuel cell using Pt nanoparticles to catalyze the hydrogen evolution and oxidation reaction.

Analogous to the R_{cont} in the high-voltage LNMO cathode, which is credited as the main reason for the increase of cathode impedance, the contact resistance R_{cont} in Li_2S/VC electrode also contributes significantly to the cathode EIS. Although the R_{cont} can be modulated via the compression/calendaring for the Li ion battery electrodes, the applying of high compression to S-electrodes has to be extremely cautious, considering the required diffusion of soluble active material in the porous electrodes. Nevertheless, a deeper and systematic investigation of R_{cont} is required to develop an effective strategy in eliminating R_{cont}.

Summary

In this study, we accommodate the gold wire micro-reference to Li-S batteries in order to separate the cathode impedance from the cell impedance in an operating Li-S battery. Prior to the analysis of *in-situ* EIS results, we first attempt to understand the impedance spectra of the Li-S system in a simple setup – a symmetric cell under defined and static conditions, such as redox pair and its concentration, electrode material, separator (diffusion length). We ascribe the high frequency (kHz), middle frequency (Hz) and low frequency impedance (mHz) to the contact resistance at the interface of electrode/current collector, the charge transfer resistance at the interface of electrode/electrolyte, and the Warburg diffusion resistance, respectively. We carefully validate the impedance assignments by examining their temperature and redox pair concentration dependencies as well as investigating their response 1) to different electrode substrates (e.g. carbon paper) and 2) to different diffusion length.

For the first time (to our knowledge), we are able to record the *in-situ* half-cell impedance in a Li-S battery. We take the discharge process to exemplarily demonstrate the applicability of GWRE in Li-S batteries. A contact resistance (R_{cont}) is evolved in the beginning of cycling and it approaches to a "steady state" in the subsequent discharge/charge cycles. Despite we observe a clear SOC-dependent charge transfer resistance (R_{ct}), it is difficult to interpret the *in-situ* EIS results on its own, since R_{ct} is largely influenced by both the species of redox pair and their concentrations. The interpretation of the R_{ct} in a discharging cell is therefore accomplished with the additional information (about polysulfide speciation and their concentration) provided by *operando* UV-Vis spectroscopy.

Considering the entanglement of the various redox and disproportionation reactions, dynamic precipitating of Li_2S and S_8, as well as the complex diffusion behavior, we chose rather a simple equivalent circuit (Randles-like) to semi-quantitatively fit the obtained *in-situ* EIS results. Both R_{cont} and R_{ct} contribute significantly to the S-cathode EIS. Especially, owning to the 10 times higher R_{ct} ($1.4\ \mathrm{k\Omega \bullet cm^2}_{\mathrm{BET}}$) compared to it with electrode materials in LiBs (e.g. LNMO; LFP, graphite), we certify the necessity of using high-surface area carbon in S-electrode.

We believe the *in-situ* half-cell impedance measurement using gold wire reference electrode will greatly contribute to the fundamental understanding of Li-S batteries and we emphasize the importance of developing a high-surface catalyst to improve the intrinsic kinetics for a high rate cycling performance of Li-S batteries.

Literature

1. Lasia Andrzej, *Electrochemical Impedance Spectroscopy and its Applications*, Springer-Verlag, New York, NY, (2004).

2. J. Landesfeind, J. Hattendorff, A. Ehrl, W. A. Wall, and H. A. Gasteiger, *J. Electrochem. Soc.*, **163**, A1373–A1387 (2016).

3. R. Raccichini, L. Furness, J. W. Dibden, J. R. Owen, and N. García-Araez, *J. Electrochem. Soc.*, **165**, A2741–A2749 (2018).

4. R. Morasch, J. Landesfeind, B. Suthar, and H. A. Gasteiger, *J. Electrochem. Soc.*, **165**, A3459–A3467 (2018).

5. J. Landesfeind, D. Pritzl, and H. A. Gasteiger, *J. Electrochem. Soc.*, **164**, A1773–A1783 (2017).

6. D. Pritzl, J. Landesfeind, H. A. Gasteiger, and S. Solchenbach, *J. Electrochem. Soc.*, **165**, A2145–A2153 (2018).

7. R. Tatara, P. Karayaylali, Y. Yu, Y. Zhang, L. Giordano, F. Maglia, R. Jung, J. P. Schmidt, I. Lund, and Y. Shao-horn, *J. Electrochem. Soc.*, **166**, A5090–A5098 (2019).

8. Q. He, Y. Gorlin, M. U. M. Patel, H. A. Gasteiger, and Y.-C. Lu, *J. Electrochem. Soc.*, **165**, A4027–A4033 (2018).

9. Y. Gorlin, A. Siebel, M. Piana, T. Huthwelker, H. Jha, G. Monsch, F. Kraus, H. A. Gasteiger, and M. Tromp, *J. Electrochem. Soc.*, **162**, A1146–A1155 (2015).

10. C. Barchasz, F. Molton, C. Duboc, J. C. Leprêtre, S. Patoux, and F. Alloin, *Anal. Chem.*, **84**, 3973–3980 (2012).

11. R. P. Martin, W. H. Doub, J. L. Roberts, and D. T. Sawyer, *Inorg. Chem.*, **12**, 1921–1925 (1973).

12. Z. Deng, Z. Zhang, Y. Lai, J. Liu, J. Li, and Y. Liu, *J. Electrochem. Soc.*, **160**, A553–A558 (2013).

13. N. A. Canas, K. Hirose, B. Pascucci, N. Wagner, K. A. Friedrich, and R. Hiesgen, *Electrochim. Acta*, **97**, 42–51 (2013).

14. N. Ogihara, S. Kawauchi, C. Okuda, Y. Itou, Y. Takeuchi, and Y. Ukyo, *J. Electrochem. Soc.*, **159**, A1034–A1039 (2012).

15. R. Petibon, C. P. Aiken, N. N. Sinha, J. C. Burns, H. Ye, C. M. Vanelzen, G. Jain, S. Trussler, and J. R. Dahn, *J. Electrochem. Soc.*, **160**, A117–A124 (2013).

16. J. Conder, C. Villevieille, S. Trabesinger, P. Novák, L. Gubler, and R. Bouchet, *Electrochim. Acta*, **244**, 61–68 (2017).

17. M. Adamič, S. D. Talian, A. R. Sinigoj, I. Humar, J. Moškon, and M. Gaberšček, *J. Electrochem. Soc.*, **166**, A5045–A5053 (2019).

18. V. F. Lvovich, *Impedance Spectroscopy: Applications to Electrochemical and Dielectric Phenomena*, John Wiley & Sons, Inc., Hoboken, NJ(2012).

19. S. D. Talian, J. Moskon, R. Dominko, M. Gaberscek, S. D. Talian, J. Moškon, R. Dominko, and M. Gaberšček, *Appl. Mater. Interfaces*, **9**, 29760–29770 (2017).

20. M. Ender and J. Illig, *J. Electrochem. Soc.*, **164**, A71–A79 (2017).

21. J. Costard, M. Ender, and M. Weiss, *J. Electrochem. Soc.*, **164**, A80–A87 (2017).

22. S. Solchenbach, D. Pritzl, E. Jia, Y. Kong, J. Landesfeind, and H. A. Gasteiger, *J. Electrochem. Soc.*, **163**, 2265–2272 (2016).

23. Y. V. Mikhaylik and J. R. Akridge, *J. Electrochem. Soc.*, **150**, A306–A311 (2003).

24. R. D. Rauh, F. S. Shuker, J. M. Marston, and S. B. Brummer, *J. Inorg. Nucl. Chem.*, **39**, 1761–1766 (1977).

25. A. T. S. Freiberg, A. Siebel, A. Berger, S. M. Webb, Y. Gorlin, M. Tromp, and H. A. Gasteiger, *J. Phys. Chem. C*, **122**, 5303–5316 (2018).

26. Y. Gorlin, M. U. M. Patel, A. Freiberg, Q. He, M. Piana, M. Tromp, and H. A. Gasteiger, *J. Electrochem. Soc.*, **163**, A930–A939 (2016).

27. G. Bieker, M. Winter, and P. Bieker, *Phys. Chem. Chem. Phys.*, **17**, 8670–8679 (2015).

28. Y.-C. Lu, Q. He, and H. A. Gasteiger, *J. Phys. Chem. C*, **118**, 5733–5741 (2014).

29. Q. Zou and Y.-C. Lu, *J. Phys. Chem. Lett.*, **7**, 1518–1525 (2016).

30. Q. He, A. T. S. Freiberg, M. U. M. Patel, S. Qian, and H. A. Gasteiger, *J. Electrochem. Soc.*, **168**, 080508 (2020).

31. F. Y. Fan, W. C. Carter, and Y.-M. Chiang, *Adv. Mater.*, **27**, 5203–5209 (2015).

32. T. R. Jow, S. A. Delp, J. L. Allen, J. Jones, and M. C. Smart, *J. Electrochem. Soc.*, **165**, 361–367 (2018).

33. A. Evans, M. I. Montenegro, and D. Pletcher, *Electrochem. commun.*, **3**, 514–518 (2001).

34. D. Pritzl, A. E. Bumberger, M. Wetjen, S. Solchenbach, H. A. Gasteiger, and J. Landesfeind, *J. Electrochem. Soc.*, **166**, A582–A590 (2019).

35. A. Berger, A. T. S. Freiberg, A. Siebel, R. Thomas, M. U. M. Patel, M. Tromp, H. A. Gasteiger, and Y. Gorlin, **165**, A1288–A1296 (2018).

36. S. Waluś, C. Barchasz, R. Bouchet, J.-C. Leprêtre, J.-F. Colin, J.-F. Martin, E. Elkaïm, C. Baehtz, and F. Alloin, *Adv. Energy Mater.*, **5**, 1500165 (2015).

37. M. Barghamadi, A. S. Best, A. I. Bhatt, A. F. Hollenkamp, M. Musameh, R. J. Rees, and T. Rüther, *Energy Environ. Sci.*, **7**, 3902–3920 (2014).

38. C. Heubner, M. Schneider, and A. Michaelis, *J. Power Sources*, **288**, 115–120 (2015).

39. M. Mohamedi, M. Makino, K. Dokko, T. Itoh, and I. Uchida, *Electrochim. Acta*, **48**, 79–84 (2002).

40. Y. Chang, J. Jong, and G. T. Fey, *J. Electrochem. Soc.*, **147**, 2033–2038 (2000).

Supplementary Information

In-situ Impedance Measurements for a Sulfur Cathode — an Application of Gold Micro-Reference Electrode in Li-S Batteries

Qi He#, Rafael Berk, Anna T.S. Freiberg, Daniel Pritzl, Sophie Solchenbach and Bharatkumar Suthar*

Technical University of Munich, Chair of Technical Electrochemistry, Lichtenbergstr. 4, D-85748, Garching, Germany

Email: #qi.he@tum.de; *bharat.k.suthar@iitb.ac.in;

Stability and linearity test of the Li-S system in a symmetric cell

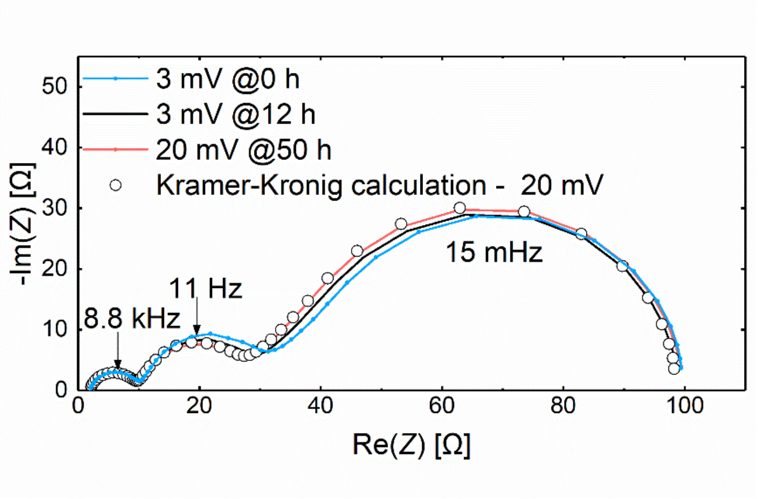

Fig. S1 The measured impedance spectra of a symmetric coin cell with Vulcan carbon (VC)//Vulcan carbon electrodes separated by one glass fiber separator, which is soaked with catholyte solution of 5 mM S_8 and 10 mM "Li_2S_4" in DOL:DME (1:1, v:v) with 1 M LiTFSI and 0.1 M $LiNO_3$. Potentiostatic impedance measurements were performed with a perturbation of 3 mV (line in blue and black) and 20 mV (line in red) in the frequency range of 200 kHz to 1 mHz. The black circuit represents the simulated impedance spectrum using Kramer-Kronig relation based on the EIS of 20 mV perturbation (line in red).

The impedance measurement of the Li-S system fulfills the requirement of linearity owning to the almost identical impedance spectra measured both with 3 mV and 20 mV perturbation. Unlike Talian et al.,[1] our system also shows a stability of the system over the course of 50 h (3000 min), which is also a pre-requisite for a reliable EIS measurement. The slight EIS shift in the beginning (0-12 h, blue line to the black line in Fig. S1) is probably caused by the time required for the temperature stabilization and a homogeneous wetting. Eventually, the impedance calculated from Kramer-Kronig relation (black circle) also fits well to the experimental results (red line).

Impedance spectrum of a symmetric coin cell with carbon paper as electrodes

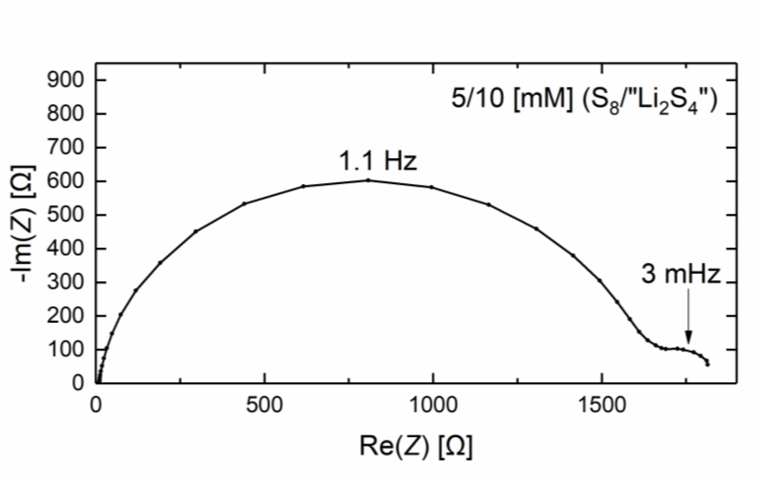

Fig. S2 the measured impedance spectrum of a symmetric coin cell with carbon paper//carbon paper electrodes separated by one glass fiber separator, which is soaked with catholyte solution of 5 mM S_8 and 10 mM "Li_2S_4" in DOL:DME (1:1, v:v) with 1 M LiTFSI and 0.1 M $LiNO_3$. Potentiostatic impedance measurements were performed with a perturbation of 20 mV in the frequency range of 200 kHz to 1 mHz.

We replaced the thin VC electrodes (~5 µm, 240 m^2/g_{VC}) by carbon paper electrodes (~110 µm, BET of 0.311 m^2/g) to explore the response of contact resistance and charge transfer resistance. As expected, we observe no semicircle (with an apex frequency of kHz), i.e. no contact resistance at the interlayer of electrode/Al current collector. Instead, a larger charge transfer resistance (~1600 Ω with an apex frequency of 1.1 Hz) and s small semicircle at 3 mHz can be observed. Similar as impedance obtained from a symmetric cell with glassy carbon electrodes,[1] the shape of Nyquist plot in Fig. S2 is quite distinct from it in the EIS of Vulcan carbon electrodes in Fig. 3c, without considering the contact resistance. This difference in the shape of Nyquist plot can be explained by the different magnitude of charge transfer resistance, which will be discussed in detail in Fig. S3.

Nevertheless, the measured charge transfer resistance (~850 Ω with apex frequency at 1.1 Hz) deviates from the calculated value (~180 Ω, 11 Hz) based on the actual BET area (23 cm^2) and 4200 Ω•cm^2 (BET surface normalized R_{ct} obtained from the Vulcan carbon electrode symmetric cell in Fig. 3c).This deviation is hypothesized to associate with 1) possible different carbon surface properties, which give rise to different surface-normalized capacitances for carbon paper (9 $\mu F/cm^2_{BET}$, obtained via fitting the data) and Vulcan carbon (~5.5 $\mu F/cm^2_{BET}$) and 2) thicker carbon paper electrode, which allows possible various redox and disproportionation reactions within the electrode before the polysulfides diffuse into the separator.

Dependency of Nyquist plots on the magnitude of R_{ct}

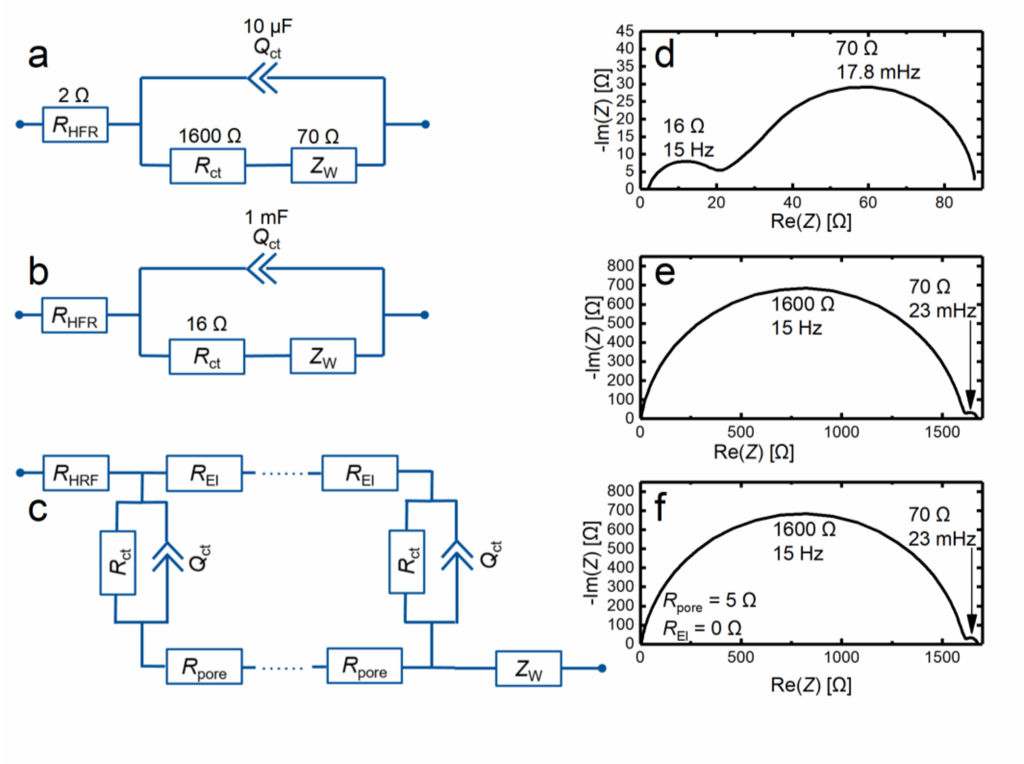

Fig. S3 Randles-like (a,b) and transmission line model (c) equivalent circuits to describe the EIS of symmetric cells with carbon paper electrodes. (d,e,f) Simulated EISs based on the corresponding equivalent circuits and the given parameters, where HFR (2 Ω), α_{ct} (0.9) Z_w (70 Ω)are constant for all the simulations and the contact resistance is here not considered.

Fig. 3a and 3b have same equivalent circuits but different carbon surface area, where Fig. S3a is assumed to have a 100 times larger surface compared to it in Fig. S3b and Fig. S3c, leading to various R_{ct} and Q_{ct} based on the equation 5 and 6 in main text. Consistent with our experimental results, Fig. S3a with a small R_{ct} and Q_{ct} (large surface, e.g. Vulcan carbon electrodes) displays an EIS (Fig. S3d) comparable to it as Fig. 3c in main text, where a clear 45° line can be seen for the Warburg element. In contrast, Fig. S3b with a larger R_{ct} and Q_{ct} (small surface, e.g. carbon paper electrodes) demonstrates a similar EIS shape (Fig. S3e) as it in Fig. S2, where no 45° line is observed, without even considering the complex diffusion behavior both in the carbon paper electrode (~110 µm) and glass fiber separator (~200 µm). Keeping in mind the porous and thick carbon paper electrodes, we also simulated an EIS (Fig. S3f) using transmission line model (Fig. S3c) with a realistic R_{pore} of 5 Ω (obtained in literature in LiB[2]) and we observe no significant difference in the Nyquist plot shape compared to it in Fig. S3e.

Contact Resistance in blocking condition

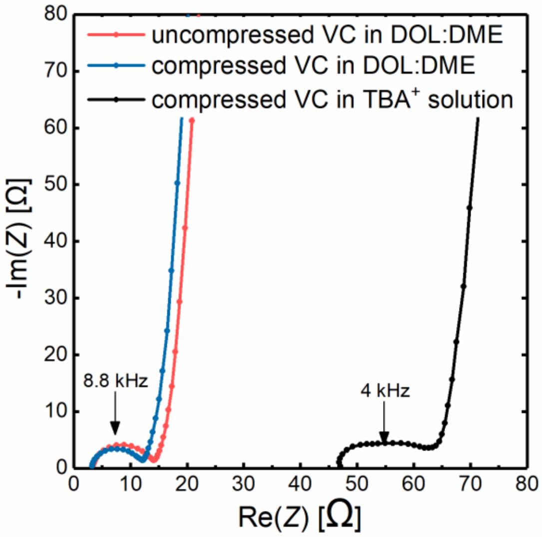

Fig. S4 Impedance spectra of a symmetric coin cell with Vulcan carbon (VC)//Vulcan carbon electrodes separated by one glass fiber separator, which is soaked with pure electrolyte solution of 1 M LiTFSI and 0.1 M $LiNO_3$ dissolved in DOL:DME (1:1, v:v) and/or with 10 mM TBATFSI in EC:EMC (3:7 wt.%).

The contact resistance can still be observed in the DOL:DME-based electrolyte (without redox pair, 12.67 mS/cm) and in the TBA-containing electrolyte (297μS/cm), regardless whether the VC electrodes were compressed or not.

The origin of this contact resistance may relate to the high PVDF content (~25wt. %) in the VC electrodes, which differs from the complex formation mechanism of contact resistance in the cycling Li-S cells (Fig. 8 and 9 in main text).

Dependency of Li_2S 1st charging plateau on the anode materials

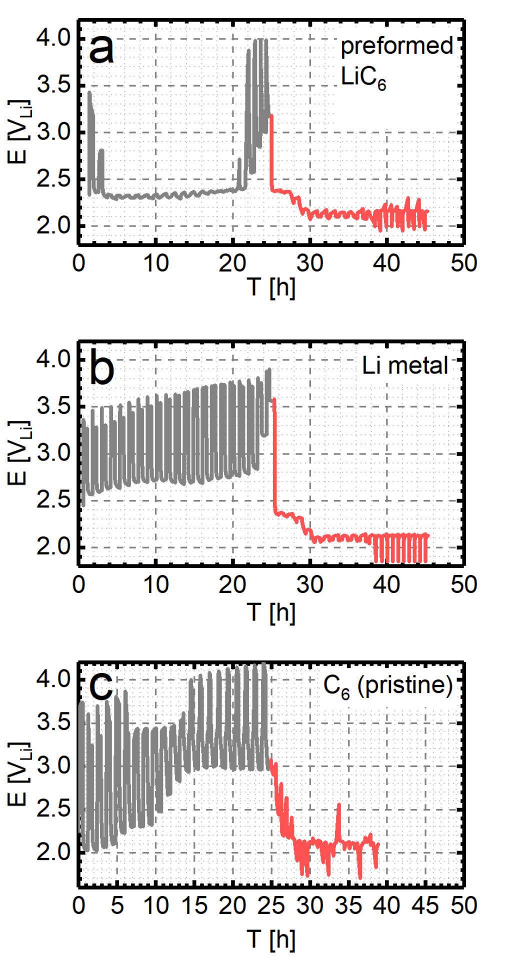

Fig. S5 Galvanostatic cycling of three-electrode Swagelok T-cells consisting of Li_2S and various anode material. 60 µl electrolyte composed of 1 M LiTFSI and 0.1 M $LiNO_3$ dissolved in DOL:DME(1:1, v:v) were added to the cell. The cycling protocol comprises of 20 times repeated 30 min galvanostatic cycling at 0.1C followed by 20 min OCV and a 20 min impedance measurement. (a) LiC_6 anode (2.84 mAh/cm^2) was pre-formed and 10% SOC pre-lithiated. (b) Lithium metal as anode (c) pristine graphite anode (4 mAh/cm^2). The loading of Li_2S cathode is 1.44, ~2.4 and ~3 mAh/cm^2 for (a), (b) and (c) respectively.

As described in the main text, the 1st charging process of Li_2S electrode is strongly dependent on whether anode possess a stable SEI. In Fig. S5a, the formed polysulfides during 1st charging are less consumed on the preformed graphite electrode, resulting in an accumulation of polysulfides that in turn facile the chemically reaction with Li_2S and thus helps lowering the 1st charging plateau.[3,4] In contrast, neither the lithium metal anode in Fig. S5b nor the pristine graphite electrode in Fig. S5c have a stable SEI, leading to a large consumption of polysulfides on the anode and a higher 1st charging plateau.

X-ray photoelectron spectroscopy of Al soaked in various solutions

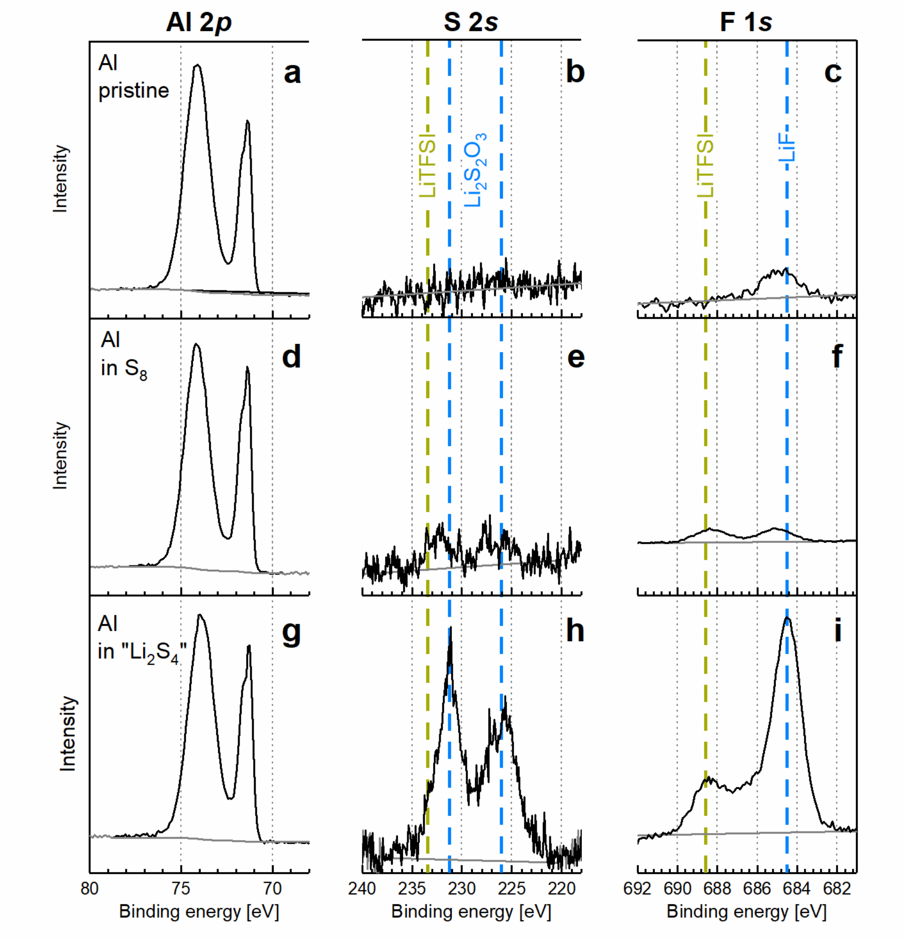

Fig. S6 X-ray photoelectron spectra of (a,b,c) pristine Al current collector and Al current collector previously soaked either in 5 mM S_8 (e,f,g) or 20 mM “Li_2S_4” (g,h,i) dissolved in DOL:DME(1:1, v:v) with 1 M LiTFSI and 0.1 $LiNO_3$ over one week and washed with a pure DOL:DME(1:1) solution in glovebox.

To understand how contact resistance evolves in a cycling Li-S battery such as in Fig. 8 and 9 in main text, we placed Al current collector in S_8 or polysulfide containing solution and performed XPS measurements.

As Fig. S6 h, i show, the Al current collector previously soaked in a polysulfide solution have a much clearer signal for $Li_2S_2O_3$ and LiF compared to it in pristine Al (Fig. S6b, c) and that soaked with dissolved S_8 (Fig. S6e, f). The formed solid LiF and $Li_2S_2O_3$ may be associated with the impeded electric conduction at the electrode/current collector interface, i.e. increased contact resistance. Nevertheless, a systematic and detailed investigation in contact resistance in Li-S batteries is required to understand its complex formation mechanism.

Literature

1. S. D. Talian, J. Moskon, R. Dominko, M. Gaberscek, S. D. Talian, J. Moškon, R. Dominko, and M. Gaberšček, *Appl. Mater. Interfaces*, **9**, 29760–29770 (2017).

2. J. Landesfeind, D. Pritzl, and H. A. Gasteiger, *J. Electrochem. Soc.*, **164**, A1773–A1783 (2017).

3. Y. Gorlin, M. U. M. Patel, A. Freiberg, Q. He, M. Piana, M. Tromp, and H. A. Gasteiger, *J. Electrochem. Soc.*, **163**, A930–A939 (2016).

4. A. Berger, A. T. S. Freiberg, A. Siebel, R. Thomas, M. U. M. Patel, M. Tromp, H. A. Gasteiger, and Y. Gorlin, *J. Electrochem. Soc.,* **165**, A1288–A1296 (2018).

3.3 Mechanistic Understanding of the Li-S Charge Process using *Operando* X-Ray Absorption Spectroscopy

This section presents the article "Understanding the Charging Mechanism of Lithium-Sulfur Batteries Using Spatially Resolved *operando* X-Ray Absorption Spectroscopy",[104] which was published in March 2016 in the Journal of The Electrochemical Society. It is an open access article distributed under the terms of the Creative Commons Attribution 4.0 License. The main research work was done by Yelena Gorlin, who is also the first author of the paper. This work was presented by Yelena Gorlin at the 229th ECS Meeting in San Diego, California (May 29- June 2, 2016). The permanent web-link to the article is http://dx.doi.org/10.1149/2.0631606jes.

Apart from the discharge process that has been intensively researched in the previous sections, we here also investigate the charging mechanism of Li-S batteries. More specifically, the understanding of Li_2S charging mechanism is achieved by addressing the reaction intermediates produced 1) at the initial high voltage charging process (> 3.5 V_{Li}) and 2) at the subsequent charging process (with a voltage ~2.5 V_{Li}) in the second cycle.

Operando XANES measurement are performed to monitor both amorphous and crystalline S_8 and Li_2S as well as the polysulfide species that are present in the electrolyte upon charging. Excellent electrochemical performance of the spectroelectrochemical cell and well-characterized reference XAS spectra have been achieved prior to these *operando* XAS experiments. In addition, the spatially resolved XAS results can prevent any misinterpretations that may be caused by the overlap of the signals from the separator and from the cathode region. Furthermore, the relative concentration change of the sum of all the S-species (S_8, Li_2S, and Li_2S_x) can be tracked using the edge height at 2487.3 eV, providing additional information about the evolution of solid Li_2S and of dissolved polysulfides upon charging in either the cathode or the separator.

Eventually, this study provides several relevant insights into the charging mechanism of a Li-S battery: (i) Merely S_8 is detected at the initial high voltage charging process, while polysulfides are the dominant species observed in the subsequent charging process. (ii) Li_2S can directly be electrochemically activated, indicated by the appearance of a potential peak during the extraction of the first 10 mAh/g_{Li_2S}. (iii) The chemical reaction between polysulfides and Li_2S is essential for the charging process, as it can chemically active Li_2S, leading to a much lower charging potential.

Author Contributions

Y.G. wrote the beamtime proposals. M.U.M.P. prepared the reference samples. Y.G., M.U.M.P., Q.H. and M.P. conducted the XAS measurements at Diamond Light Source in the UK. Y.G. M.U.M.P. and A.F. performed the XAS measurements at Stanford Synchrotron Radiation Lightsource in the US. M.T. discussed the XAS results. Y.G. and H.G. wrote the manuscript. All authors discussed the results and commented on the manuscript.

A930 *Journal of The Electrochemical Society*, **163** (6) A930-A939 (2016)

Understanding the Charging Mechanism of Lithium-Sulfur Batteries Using Spatially Resolved Operando X-Ray Absorption Spectroscopy

Yelena Gorlin,[a,*,z] Manu U. M. Patel,[a] Anna Freiberg,[a,*] Qi He,[a] Michele Piana,[a,] Moniek Tromp,[b] and Hubert A. Gasteiger[a,***]**

[a] *Chair of Technical Electrochemistry, Department of Chemistry and Catalysis Research Center, Technische Universität München, Garching, Germany*
[b] *Van't Hoff Institute for Molecular Sciences, University of Amsterdam, Amsterdam, Netherlands*

Replacement of conventional cars with battery electric vehicles (BEVs) offers an opportunity to significantly reduce future carbon dioxide emissions. One possible way to facilitate widespread acceptance of BEVs is to replace the lithium-ion batteries used in existing BEVs with a lithium-sulfur battery, which operates using a cheap and abundant raw material with a high specific energy density. These significant theoretical advantages of lithium-sulfur batteries over the lithium-ion technology have generated a lot of interest in the system, but the development of practical prototypes, which could be successfully incorporated into BEVs, remains slow. To accelerate the development of improved lithium-sulfur batteries, our work focuses on the mechanistic understanding of the processes occurring inside the battery. In particular, we study the mechanism of the charging process and obtain spatially resolved information about both solution and solid phase intermediates in two locations of an operating Li_2S-Li battery: the cathode and the separator. These measurements were made possible through the combination of a spectro-electrochemical cell developed in our laboratory and synchrotron based *operando* X-ray absorption spectroscopy measurements. Using the generated data, we identify a charging mechanism in a standard DOL-DME based electrolyte, which is consistent with both the first and subsequent charging processes.

[DOI: 10.1149/2.0631606jes]

Manuscript submitted December 31, 2015; revised manuscript received February 29, 2016. Published March 9, 2016. This article is a version of Paper 258 from the San Diego, California, Meeting of the Society, May 29–June 2, 2016.

Lithium-sulfur (Li-S) batteries are an emerging battery technology that has the potential to meet the energy density and cost requirements of electric vehicles. Recently, several studies have identified that the attainment of areal capacities as high as 4–8 mAh/cm^2 while minimizing the electrolyte content are the key factors in meeting these requirements.[1–3] The only currently commercialized Li-S battery has a significantly lower areal capacity of 2.5 mAh/cm^2 and operates in the presence of excess electrolyte,[4] necessitating significant technological breakthroughs to facilitate the possible use of Li-S batteries in the transportation sector. One of the main barriers to achieving such breakthroughs is the lack of fundamental understanding of the mechanism behind the operation of Li-S batteries.[1,5,6] In particular, it is not yet clear how the mechanism of discharge differs from the charge mechanism,[5] and if these two processes might change upon an increase in active material loading or reduction in electrolyte volume.[1] Consequently, there is a pressing need for performing *operando* characterization of Li-S batteries under a variety of conditions to identify fundamental aspects of the charging and discharging processes.

One attractive but insufficiently explored system for a mechanistic characterization of Li-S batteries is the charging process of a Li_2S cathode, a possible alternative to the conventional S_8 cathode, with a potential to enable batteries with silicon or tin rather than lithium anodes.[7,8] Specifically, it has been recently reported that a Li-S battery, which is assembled in a discharged state using a Li_2S cathode, requires an application of a high overpotential in the very first charge, even though each subsequent charge can be performed at a lower potential.[9,10] Furthermore, several studies have shown that the exact value of the required overpotential during the first charge of Li_2S can be manipulated and reduced by varying the charging rate,[8,9,11] cathode morphology and structure,[9,11–15] and electrolyte composition.[9,16–20] The results of these recent studies, however, have not yet been incorporated into a general understanding of the charging process of Li-S batteries, and the intermediates of the initial charge of Li_2S have only been characterized using X-ray diffraction (XRD),[8,9] a technique that is capable of detecting crystalline solids, but cannot provide information about amorphous species. X-ray absorption spectroscopy (XAS) is an alternative *operando* characterization technique that is especially suited for the characterization of Li-S batteries, because it is capable of detecting solid S_8 and Li_2S as well as polysulfides dissolved in the electrolyte.[21,22] To date, *operando* XAS has only been applied to the study of Li-S batteries assembled in a charged state using S_8 cathodes,[21–25] and has not been used to identify intermediates during the initial charge of Li_2S. Since the initial charging process differs significantly from all the subsequent charges, XAS characterization of both the starting species and the intermediates associated with these charging processes has an opportunity to facilitate a significantly improved mechanistic understanding of the operation of Li-S batteries.

Motivated by advancing the mechanistic understanding of Li-S chemistry, we have performed XAS characterization of Li_2S-Li battery using a spectro-electrochemical cell designed in our laboratory,[21] which is capable of spatially resolved measurements. In the experiments, we obtain, for the first time, information about both solid and solution phase intermediates produced in two locations of the cell, the Li_2S cathode and the separator, and thus generate a unique set of spatially resolved data that is able to discriminate between the changes in the concentration of the species in the separator and the changes in the composition of the species in both locations of the cell. Using the observed trends in the X-ray absorption spectra, we identify that S_8 is forming in the DOL-DME based electrolyte throughout the entire charging process, propose a charging mechanism that is consistent with both the first and the second charge of the Li_2S-Li battery, and discuss how different experimental conditions can change the charging overpotential. Furthermore, we identify that oxidation of parts of Li_2S particle, which are not in direct contact with a conductive carbon support, requires a chemical step, and that during the second charge this chemical step is facilitated by the presence of a significant concentration of polysulfide intermediates. Our results demonstrate how spatially resolved spectroscopic measurements can aid in the development of a significantly enhanced fundamental understanding of an operating battery.

---

*Electrochemical Society Student Member.
**Electrochemical Society Member.
***Electrochemical Society Fellow.
[z] E-mail: yelena.gorlin@tum.de

Experimental

Electrochemical measurements.—Electrochemical measurements were performed in an *operando* cell developed in our laboratory[21] and in a standard T-cell made from Swagelok components. In all studies, the same electrolyte was used. It consisted of 1 M lithium perchlorate ($LiClO_4$, battery grade, 99.99% trace metal basis, Sigma-Aldrich) and 0.5 M lithium nitrate ($LiNO_3$, 99.99% trace metal basis, Sigma-Aldrich) dissolved in a mixture of 1,3-dioxolane (DOL, anhydrous, 99.8%, Sigma-Aldrich) and 1,2-dimethoxyethane (DME, anhydrous, 99.8%, Sigma-Aldrich) (1:1 vol:vol); in the following text, we will refer to the electrolyte simply as DOL-DME. $LiClO_4$ salt was used in our study instead of a more common bis(trifluoromethanesulfonyl) imide lithium (LiTFSI) salt, because it was important to avoid the signal of the sulfonyl group in the *operando* X-ray absorption spectra. Prior to use, all salts were dried under dynamic vacuum at 110°C for 48 h, using a glass oven (Büchi, Switzerland), while all solvents were dried over Sylobead MS 564C zeolites (3 Å, Grace Division) for a minimum of 24 h.

Li_2S/C electrodes were prepared using commercially available powder (99.98% trace metal basis, Sigma-Aldrich), which was used as received. Weighed amounts of Li_2S, Vulcan carbon (XC-72, Tanaka Kikinzoku Kogyo), and polyvinylidene fluoride (PVDF, HSV900, Kynar) were taken in an airtight container with a wt% ratio of 60:30:10 and mixed thoroughly using a planetary centrifugal vacuum mixer (Thinky, Japan). The obtained solid mixture was dispersed in 2.5 mL of N-Methyl-2-pyrrolidone (NMP, anhydrous, 99.5%, Sigma-Aldrich) in three sequential steps. After each addition of NMP, the contents were mixed until a total solid content of approximately 200 mg per milliliter of NMP was achieved. The ink was coated onto an 18 μm thick aluminum foil using a 250 μm gap Mayer rod. The ink preparation was performed under vacuum in the Thinky mixer, while the coating was done in an argon-filled glove box (MBraun; <1 ppm H_2O and <1 ppm O_2). Initially, the coating was dried overnight inside the glove box. Then, the electrodes were punched out either as disks with a diameter of 10 mm (for T-cells) or squares with 10 mm dimensions (for *operando* cells) and dried for an additional 8 h under a dynamic vacuum at 110°C, using a glass oven (Büchi, Switzerland). The obtained electrodes had Li_2S loading of 2.0 ± 0.2 mg/cm^2 and a thickness of approximately 90 μm.

The synthesized Li_2S/C composite electrode, a lithium metal foil (99.9% purity, 450 μm, Rockwood Lithium, USA), 260 μm glass fiber separator (Glass microfiber filter 691, VWR, Germany), and 60–80 μl of electrolyte ($\sim$40 $\mu l_{electrolyte}/mg_{Li_2S}$), were used to assemble electrochemical cells in an argon-filled glove box (MBraun; 1 ppm H_2O and <1 ppm O_2). Prior to cell assembly, the cell components of Swagelok T-cells and *operando* cells were dried in a vacuum oven at 70°C for several hours. The Swagelok cells and the *operando* cells were assembled with two or one glass fiber separators, respectively. After assembly, electrochemical cells were connected to a potentiostat (Bio-Logic SAS, France), which was used to record an electrochemical impedance spectrum (EIS) and the open circuit voltage (OCV). The open circuit voltage (OCV) period between the cell assembly and the beginning of the charge was typically 1–4 h. All charges and discharges of the cathode were performed galvanostatically at a C-rate of 0.1 h^{-1} or 0.2 h^{-1} (based on a theoretical capacity of 1165 mAh/g_{Li_2S}). Specifically, the first charge was performed at a C-rate of 0.1 h^{-1} to a cutoff voltage of 4.0 V vs. the lithium metal anode, while the subsequent discharge and charge were performed at a rate of 0.2 h^{-1} to a cutoff voltage of 1.5 V and 3.0 V vs. the lithium metal anode, respectively. To determine how the initial potential during the first charge varied with the prescribed current, two additional experiments were performed using charging rates of 0.05 h^{-1} (1.49 mAh/cm^2) or 0.5 h^{-1} (0.09 mAh/cm^2).

Operando sulfur K-edge XAS measurements.—Sulfur K-edge XAS measurements were performed at the 14-3 beamline of the Stanford Radiation Synchrotron Laboratory (SSRL, SLAC National Laboratory, Menlo Park, USA) and at I18 beamline of the Diamond Light Source (DLS, Didcot, UK). The experimental conditions, which offered the best chance for avoiding radiation damage of the intermediate species forming in the electrolyte of the battery, were identified at the I18 beamline of the DLS, while the spatially resolved *operando* data presented in this paper were obtained at the SSRL. Beamline 14-3 at SSRL is an intermediate X-ray regime (2–5 keV) beamline with a Kirkpatrick-Baez (KB) mirror system, which offers a microfocus capability. During the experiments, the beam was focused to 20 μm in one direction and defocused to 400–500 μm in the other direction to simultaneously offer spatial resolution in the direction normal to the electrodes and maximize the signal to noise ratio. The *operando* cell was mounted in a small sample chamber filled with helium gas at ambient pressure, and an 8 μm Kapton foil metallized with 100 nm aluminum layer (Multek, USA) was used as an X-ray window. The exact position of the cell relative to the X-ray beam was controlled by a Newport sample stage with submicron accuracy. During the OCV period, a line scan, which monitored sulfur fluorescence signal, was used to identify the positions of the Li_2S electrode (sulfur containing region) and the separator (the region without any initial sulfur species).

Throughout the experiment, X-ray absorption spectra were recorded at the sulfur K-edge in fluorescence mode using a Vortex silicon drift detector (Hitachi) with Xspress3 pulse processing electronics (Quantum Detectors). The incoming X-ray beam was monochromatized using a Si(111) crystal, and its intensity (I_0) was measured using an ion chamber positioned near the exit of the beam. To avoid unnecessary irradiation of the sample, data acquisition was performed approximately every 130 mAh/g_{Li_2S} and consisted of an average of two spectra with each spectrum lasting 3 minutes and having a step size of 0.5 eV in the 2466–2483 eV region. To account for possible changes in the incoming X-ray beam, all collected X-ray absorption spectra were divided by I_0, yielding the raw absorption of the sulfur K-edge, in which the edge step provides a measure of the relative concentration of the sulfur species. These raw spectra were subsequently processed using the Athena software package to yield the normalized spectra with an edge-step of one.[26] The energy scale of all spectra was calibrated to a literature value of the maximum of the sulfur K-edge of 2472.0 eV.[27] Depending on whether the focus is on the changes in the concentration or the type of sulfur species, either the raw or the normalized spectra are presented.

XAS data analysis.—Three standards: S_8, Li_2S_n in DOL-DME, and Li_2S were used to perform analysis of X-ray absorption spectra using the same general approach as described previously.[21] Li_2S standard was prepared from a commercially available powder (99.98% trace metal basis, Sigma-Aldrich). To minimize the self-absorption experienced by the standard, the sample was both ball-milled to reduce the particle size of Li_2S and diluted with boron nitride to 0.5 wt%. S_8 standard was prepared from commercially available S_8 powders (99.998% trace metal basis, Sigma-Aldrich), which was grinded using mortar and pestle and diluted with boron nitride to 0.5 wt%. Li_2S_n (Li_2S_6 average composition) standard was a solution-based standard synthesized in a DOL-DME solvent using the same commercially available Li_2S and S_8 powders. More specifically, 11.5 mg of Li_2S was mixed 40.1 mg S_8 in 5 ml of DOL-DME solvent and stirred overnight. X-ray absorption near edge structure (XANES) spectra of the three references are presented in Fig. 1. The figure highlights the features, which are subsequently used to distinguish between the three types of sulfur species. S_8 standard has only one peak at 2472 eV and a distinct concave feature at 2475.5 eV. Li_2S has two peaks, with one peak centered at 2473 eV and the other at 2476 eV, and can be identified by a convex shape at 2475.5 eV. Li_2S_x standard has a spectrum that is similar to the spectrum of S_8, but with an additional smaller peak at 2470–2471 eV, which corresponds to a charged terminal sulfur atom found in all polysulfides.[28] Although, in theory, it may be possible to distinguish between various polysulfide species by comparing the ratio between the two features at 2470 eV and 2472 eV,[28] which correspond to terminal and internal sulfur atoms, such analysis is complicated by the fact that sulfur also has a feature

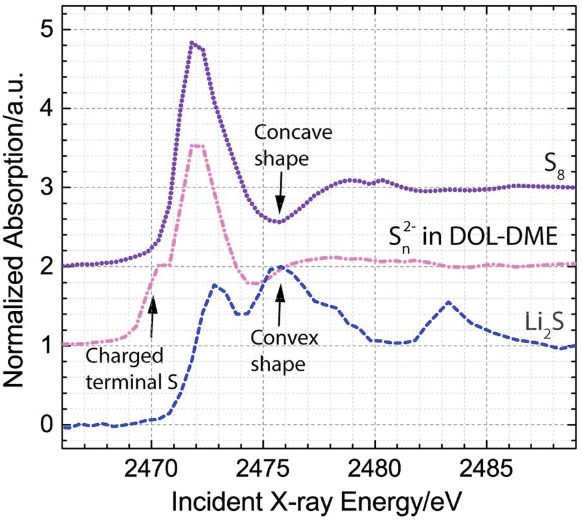

Figure 1. XANES spectra of three references: Li_2S (dashed line) and S_8 (dotted line) powders diluted to ~0.5 wt% in boron nitride and solution phase polysulfides (S_n^{2-}, average composition of Li_2S_6) dissolved in DOL-DME solvent (dash-dotted line).

corresponding to an internal atom at 2472 eV and by the possible effects of self-absorption, which cannot be avoided at sulfur concentrations above 30 mM.[29] Therefore, in our study, we will not perform quantitative principle component analyses, but will use the three discussed features of S_8, Li_2S, and S_n^{2-} to qualitatively analyze the obtained spectra.

Results and Discussion

Successful spatially resolved XAS measurements during the charging process of Li-S batteries require an *operando* battery cell that can achieve both a standard electrochemical performance and allow spectroscopic access to the electrodes and the separator. Consequently, prior to using our *operando* cell at the synchrotron facility, we had focused on the electrochemistry of the cell and confirmed that it could achieve the same electrochemical behavior as a standard T-cell design with a Li_2S cathode (~2 mg_{Li_2S}/cm^2), a lithium metal foil anode, and a glass fiber separator soaked with 80 μl of electrolyte (1 M $LiClO_4$ and 0.5 M $LiNO_3$ dissolved in a DOL-DME). In Fig. 2, we plot the galvanostatic charge and discharge curves in both the *operando* cell and a standard T-cell as a function of time (Fig. 2a) and specific capacity (Fig. 2b). In the experiments, the first charge is performed at a C-rate of 0.1 h^{-1}, while the subsequent discharge and second charge are performed at a rate of 0.2 h^{-1} (referring to the theoretical capacity of 1165 mAh/g_{Li_2S}). As seen in Fig. 2a, the electrochemical performance of the T-cell and the *operando* cell are nearly identical. Both cells reach close to 100% of the theoretical capacity during the first charge, then discharge to approximately 75% of the theoretical capacity, and finally, during the last charge, reach 55% of the theoretical capacity. Additionally, in agreement with literature,[8,9,12] the first charge in both cells requires a significantly higher potential than the second charge. To highlight this difference in the required potential and to visualize what fraction of the theoretical capacity was reached during the first and the second charging processes, the same two charge curves are plotted as a function of specific capacity in Fig. 2b, while the discharge curve is omitted for clarity. Fig. 2b clearly demonstrates that the *operando* cell is able to reproduce the expected galvanostatic charge curves of the Li_2S cathode and can therefore be combined with XAS measurements to identify the intermediates produced during the initial and subsequent charging processes.

After appropriately benchmarking the electrochemical performance of the *operando* cell, we confirmed its spectroscopic spatial resolution capabilities at a synchrotron facility. Fig. 3a compares the raw XANES spectra obtained in the cathode and the separator of the battery at the open circuit voltage (OCV) before starting the initial charge with the raw spectrum of the Li_2S reference. We have chosen to present the raw spectra rather than the spectra with a normalized edge-step of 1, in order to provide a measure of the relative concentration of the sulfur species in the two locations of the battery. Since the battery is resting at OCV, the cathode (a sum of active material and solution species trapped in the pores of the electrode) is expected to contain exclusively Li_2S, while the separator (solution species) is expected to not have any sulfur species, because Li_2S is not soluble in organic solvents such as DOL-DME.[30] Inspection of the spectra in Fig. 3 is consistent with these expectations, identifying the species inside the cathode as Li_2S and failing to detect any significant absorption at the sulfur K-edge in the separator. Our results are the first demonstration of XAS measurements with spatial resolution in a direction normal to the electrodes, enabling a spectral distinction between species located in either one of the electrodes versus species contained in the separator of the same cell. After the successful confirmation of the spatial resolution capabilities of the *operando* cell and identification of the initial species in the cathode and the separator region, the battery was cycled using the same conditions as in the benchmarking experiments, and two new XANES spectra were collected in both locations at an interval of about 130 mAh/g_{Li_2S}. The resulting galvanostatic curves are plotted as a function of time in Fig. 3b. The same charging curves are also replotted as a function of specific capacity and are presented with the associated *operando* XANES spectra in Figs. 4 and 6.

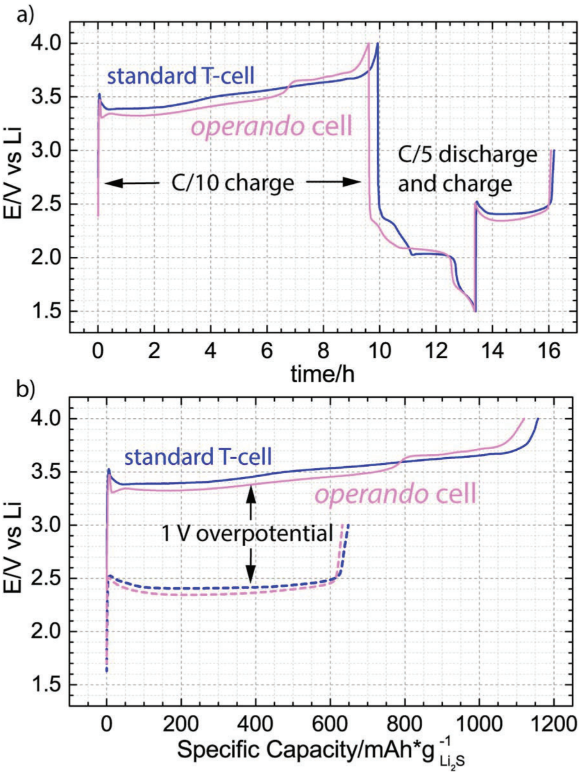

Figure 2. a) Benchmarking of the *operando* electrochemical cell against a standard T-cell made from swagelok components. The electrode loading was 2.0 ± 0.2 mg_{Li_2S}/cm^2 and 60–80 μL (~40 $\mu l_{electrolyte}/mg_{Li_2S}$), of DOL-DME electrolyte with 1 M $LiClO_4$ and 0.5 M $LiNO_3$ was added; metallic lithium foil was used as anode. b) Visualization of the difference in the charging potential between the first (solid lines) and the second (dashed lines) charges of Li_2S-Li cells.

Fig. 4a presents the initial charge of the Li_2S cathode, demonstrating that close to 100% of the theoretical capacity (1165 mAh/g_{Li_2S}) was achieved using a C-rate of 0.1 h^{-1} and that the initiation of the charging process required a short-term rise in the potential to a maximum

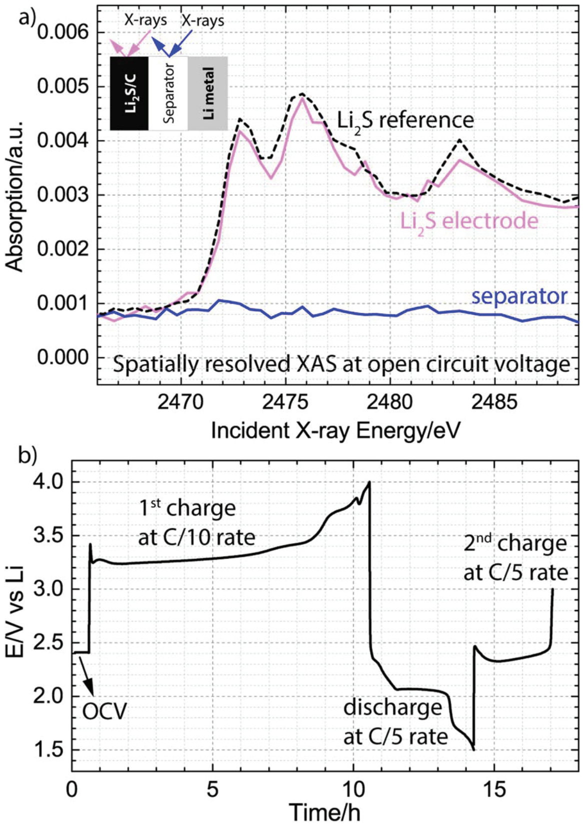

Figure 3. a) Validation of the spatially resolved X-ray absorption measurement capability during the open circuit voltage (OCV) period, demonstrating that the cathode consists only of Li_2S and that the separator does not have sulfur species. b) *Operando* electrochemistry in 1 M $LiClO_4$ and 0.5 M $LiNO_3$ dissolved in DOL-DME solvent showing 0.5 h OCV period, the 1st charge at a rate of 0.1 h^{-1} (0.23 mA/cm^2) as well as subsequent discharge and 2nd charge at a rate of 0.2 h^{-1} (0.46 mA/cm^2). The loading of Li_2S electrode was 2.0 mg/cm^2, and 80 μl of electrolyte was added to one glass fiber separator (∼260 μm thickness).

value of 3.4 V (Fig. 4a inset), which, in agreement with literature,[9,11] is dependent on the charging current. Additionally, the figure identifies the approximate location of 9 points (a-i), which correspond to a set of *operando* spectra collected either in the cathode or in the separator. Inspection of the normalized spectra obtained in the cathode (Fig. 4b), which are progressively shifted up by 0.5 a.u. for clarity, shows that at the very beginning of the charge, the cathode consists of only Li_2S, and that at the very end of the charge, the cathode consists of only S_8. Furthermore, while the spectra are continuously changing throughout the charge, no additional features appear in the 2470–2471 eV region, the signature region of the polysulfide intermediates.[28] The normalized spectra from the separator (Fig. 4c) further confirm that no detectable concentration of polysulfide intermediates is generated during the first charge. In particular, the spectra demonstrate that only one type of species, which correspond to a fully oxidized product, S_8, is found in the separator throughout the entire process (b-i). A normalized spectrum is not associated with the OCV period (point a), because after the assembly of the battery, we did not detect any species in the separator (Fig. 3a). To visualize more clearly how the spectra are developing throughout the charge, we plot the normalized intensity related to the Li_2S feature at 2475.3 eV and the normalized intensity of the polysulfide feature at 2470.3 eV for both the cathode and the separator in Fig. 4d. Although Li_2S was present only in the cathode, and polysulfide species were not detected in either location, all four sets of data are included to facilitate comparison and demonstrate the expected normalized intensity in the absence of the species. From Fig. 4d, it is seen that the normalized intensity of the cathode at 2475.3 eV decreases up until 1000 mAh/g_{Li_2S}, indicating a gradual conversion of Li_2S to S_8. After this point, no additional change is detected in the measured spot, despite the fact that the charging process proceeds, indicating that there is heterogeneity in the electrode or that some electrolyte oxidation is occurring.

To extract more information about the intermediates in the separator, Fig. 4e presents the raw XANES spectra, which directly probe the amount of species present, rather than providing information on the relative ratios of components as is the case for the normalized spectra presented above. From the plot, it is evident that the concentration of dissolved S_8 is changing throughout the charge. To visualize these changes, we plot the absorption intensity at incident energy of 2487.3 eV (i.e., the edge height) in the inset of the Fig. 4e. The inset demonstrates that formation of S_8 can be detected as early as after 10% of the charging process, and that the concentration of S_8 is increasing throughout the entire process. Our sensitivity to detecting S_8 in both the separator and the cathode is a significant improvement over previous *operando* studies based on XRD characterization, which could detect formation of S_8 only after 60% of the charging process,[8] or not at all.[9] Furthermore, our results demonstrate that during the first charge occurring at a significant overpotential, polysulfides do not exist in a detectable concentration, and that it is possible to extract the entire theoretical capacity by converting Li_2S to S_8.

To clarify what type of specific processes occur inside the battery based on DOL-DME electrolyte during the first charge, we need to consider how micro-meter sized insulating Li_2S particles could become electrochemically activated. It has been originally proposed that the first step to oxidation of Li_2S is a charge transfer step that leads to a lithium-deficient surface on the surface of large Li_2S particles.[9,12] This mechanism, however, does not provide a sufficient explanation for how an activation of an upper limit of 6% of the volume (10 nm outer layer of a particle with a diameter of 1000 nm, assuming that the whole outer surface of the particle is in contact with carbon) could lead to an extraction of the entire capacity. Therefore, a more likely mechanism involves a redox mediator that diffuses between the conductive carbon surface and the Li_2S particle and thus eliminates the need for direct contact between the two materials.[16] A recent study by Koh et al. has provided support for this mechanism by demonstrating that it was possible to charge Li_2S particles that were electronically completely isolated from the carbon electrode in a cell using a DME electrolyte.[31] The authors had proposed that the first charge of Li_2S did not occur through a direct electrochemical oxidation of Li_2S but rather through a combination of electrochemical and chemical reactions involving polysulfide impurities that lead to the generation of polysulfide redox mediators.[31] Although our spatially resolved XAS measurements do not detect polysulfides (sensitivity of XAS is on the order 100 ppm[32] or approximately 1 mM of dissolved sulfur (S_1 basis) in DOL-DME) and therefore, rule out polysulfide intermediates as sole redox mediators during the first charge occurring at a significant overpotential, they are consistent with either a combination of S_8 and a trace concentration of polysulfides or electrolyte oxidation fragments acting as such mediators.

To understand which of these two possibilities is occurring inside the battery, we need to consider the electrochemical and chemical reactions that can facilitate conversion of Li_2S to S_8 to an extent equating to close to a 100% theoretical capacity. The possible reaction pathway involving a combination of S_8 and a trace concentration of polysulfides is shown in Equations 1–3. In this proposed mechanism, the electrochemically generated $S_{8,solid}$ subsequently dissolves and diffuses toward a Li_2S particle. Then, $S_{8,solution}$ and Li_2S react chemically to produce S_n^{2-} in trace concentrations, and S_n^{2-} converts through a series of chain-growth/disproportionation reactions to a polysulfide species that can be electrochemically oxidized to solid S_8. The produced $S_{8,solid}$ can then dissolve and again react chemically with Li_2S. Consequently, during the first charge, parts of the micro-meter sized Li_2S particles which have interfacial contact with the conductive carbon support could become electrochemically activated (Equation 4), reflected by the occurrence of a peak potential (see inset of Fig. 4a) during the extraction of the first 10 mAh/g_{Li_2S} of the capacity

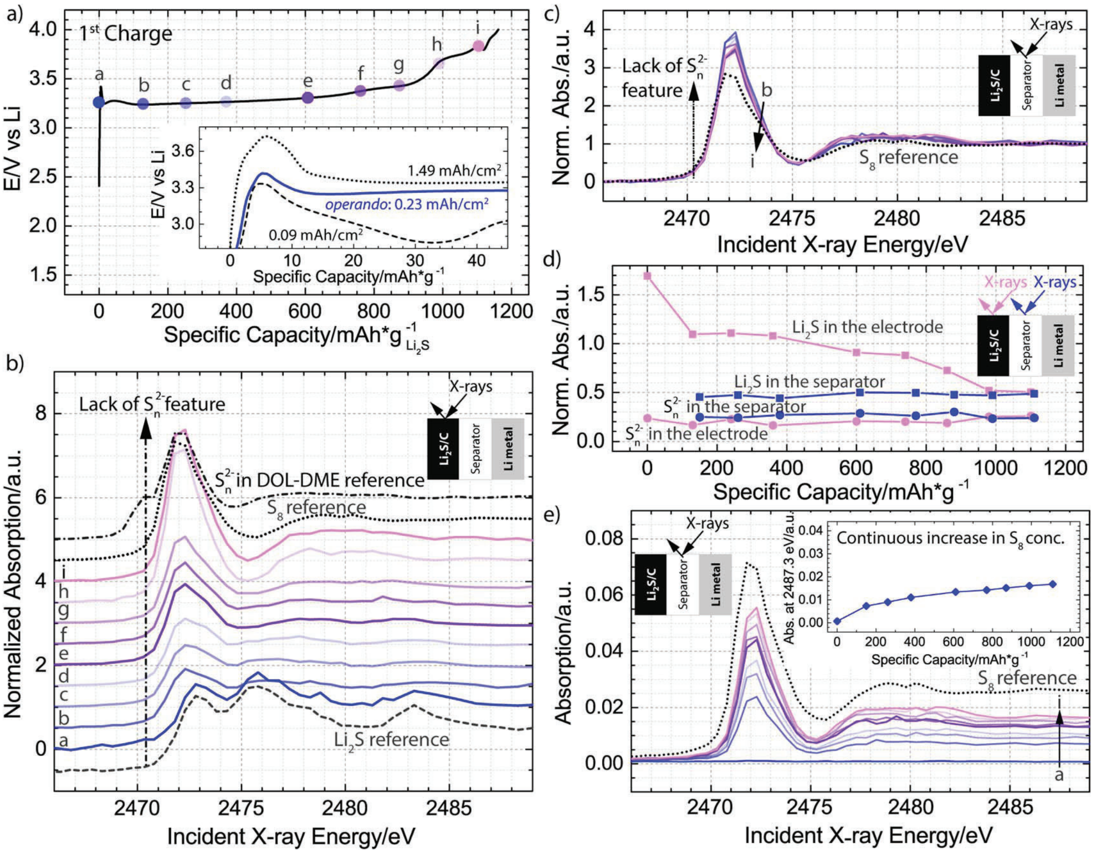

Figure 4. a) First charge in 1 M $LiClO_4$ and 0.5 M $LiNO_3$ dissolved in DOL-DME solvent plotted as a function of specific capacity normalized to the mass of Li_2S in the cathode with dots a-i indicating where spatially resolved X-ray absorption spectra were obtained; the inset shows the initial activation barrier for the charging process shown in the main plot as well as two additional processes performed at charging rates of 0.5 h^{-1} (1.49 mAh/cm^2) and 0.05 h^{-1} (0.09 mAh/cm^2). b), c) Normalized XANES spectra collected in the Li_2S cathode b) or the separator c); Li_2S, S_8, and polysulfide references are also plotted for comparison in b), while S_8 reference is plotted in c). d) Demonstration of the decrease in Li_2S component inside the electrode, without an associated increase in the S_n^{2-} component in the electrode structure; for comparison, equivalent trend lines are shown for the spectra obtained in the separator, which did not have the features of either Li_2S or S_n^{2-}. Li_2S (squares) is represented by the normalized intensity at 2475.3 eV, while S_n^{2-} (circles) is represented by the normalized intensity at 2470.3 eV. e) Raw XANES spectra collected in the separator of the battery; S_8 reference is plotted for comparison and the inset illustrates how the absorption intensity at incident energy of 2487.3 eV changes throughout the charging process.

(~1% of the theoretical capacity). At the same time, other parts of the micro-meter sized Li_2S particles could become oxidized through a series of chemical reactions (Equations 1–2), leading to production of polysulfides that can be electrochemically oxidized to S_8 (Equation 3), thus, enabling the extraction of the entire theoretical capacity. The fact that no polysulfides were detected by XAS is also consistent with this proposed mechanism, invoking only a trace concentration of polysulfides at any particular point of the charging process.

$$S_{8,solid} \rightleftharpoons S_{8,solution} \qquad [1]$$

$$\frac{n-1}{8} S_{8,solution} + \mathrm{Li_2S} \rightarrow S^{2-}_{n,trace} + 2Li^{+} \qquad [2]$$

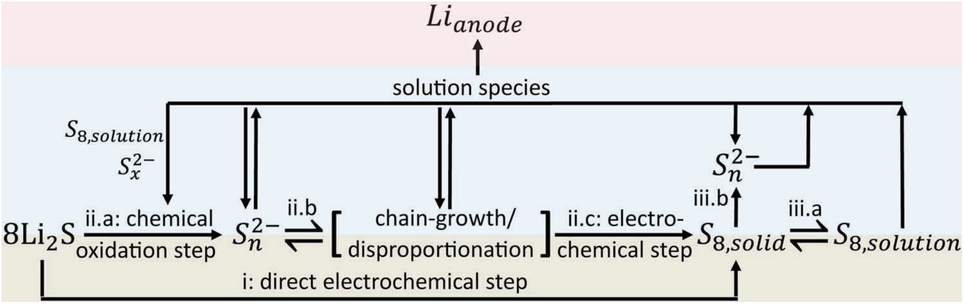

Figure 5. Schematic of the charging mechanism, consisting of either a direct electrochemical formation of $S_{8,solid}$ from Li_2S at the carbon/Li_2S interface (i), or a series of chemical steps (ii.a and ii.b) that eventually lead to the electrochemical oxidation of polysulfide species to $S_{8,solid}$ (ii.c). Once formed, $S_{8,solid}$ may dissolve in the electrolyte (iii.a) or react chemically with polysulfides to form a polysulfide species with a longer chain length (iii.b). Additionally, the schematic visualizes that during the charging process, a portion of the solution phase species ($S_{8,solution}$ or polysulfides) may diffuse to and react chemically with the lithium anode. With the exception of equilibrium between $S_{8,solid}$ and $S_{8,solution}$ species, none of the presented equations are balanced to simplify the illustration of the overall processes; for examples of balanced equations please see Equations 1–6 in the main text.

$$S^{2-}_{n,trace} \rightarrow \left[\frac{chain\text{-}growth}{disproportionation}\right] \rightarrow \frac{n}{8} S_{8,solid} + 2e^{-} \quad [3]$$

$$Li_2S \rightarrow \left[E_{peak} = 3.4\ V\ \right] \rightarrow \frac{1}{8} S_{8,solid} + 2Li^{+} + 2e^{-} \quad [4]$$

When considering the possibility of electrolyte facilitating oxidation of Li_2S, it is challenging to come up with a reaction pathway that is consistent with the observed electrochemistry. Unlike direct electrochemical oxidation of Li_2S, electrochemical oxidation of ethers or salts is not expected to depend on the current density and therefore, the short-term rise in the potential at the beginning of the charging process cannot be primarily attributed to electrolyte oxidation. Additionally, if only a small concentration of electrolyte oxidation products is generated during the extraction of the first 10 mAh/g_{Li_2S}, it is unclear how these species would get regenerated during the rest of the charging process, after they are consumed in a redox reaction that leads to oxidation of Li_2S. Alternatively, if the electrolyte species are electrochemically oxidized throughout the entire charging process, then the fact that electrolyte is present in excess in the battery would mean that this process can occur independently of subsequent oxidation of Li_2S, pointing to an unwanted additional side reaction, rather than a mediating process. In this scenario, it is unclear why the charging process would stop and not continue beyond the observed extracted capacity of 1160 mAh/g_{Li_2S}. Taking into account these considerations, we only consider a combination of S_8 and a trace amount of polysulfides as a viable reaction pathway that can lead to a complete conversion of Li_2S to S_8, but note that we cannot rule out that some electrolyte oxidation is also occurring during the charging process.

The discussed charging mechanism involving S_8 and polysulfides is portrayed schematically in Fig. 5. In addition to Equations 1–4, the figure includes three additional processes that are expected to occur inside the battery. In the first additional process, the solution species may diffuse to the anode and react chemically with Li metal. This process explains why it may be difficult to accumulate a considerable concentration of polysulfides during the first charge of Li_2S cathodes and is supported by recent results of Wang et al., who were able to first electrochemically activate Li_2S at 3.8 V and then complete the charging process at a significantly lower potential of 2.6 V in the presence of a ceramic barrier separating solution species from the lithium anode.[19] The other two additional processes correspond to chemical reactions that can occur in the event that a significant concentration of polysulfides is generated inside the battery. In addition to getting electrochemically oxidized at the electrode, these polysulfides can react chemically with solid Li_2S and S_8 and convert more of the total [S] concentration to polysulfides as shown by Equations 5 and 6.

$$Li_2S + \frac{n-1}{x-n} S^{2-}_{x} \rightarrow \frac{x-1}{x-n} S^{2-}_{n} + 2Li^{+} \quad [5]$$

$$\frac{n-x}{8} S_8 + S^{2-}_{x} \rightarrow S^{2-}_{n} \quad [6]$$

Having clarified the intermediates of the first charge and identified a possible charging pathway in the DOL-DME electrolyte, we now examine the details of the subsequent charge. The second charge began after 75% of the theoretical capacity was extracted during the discharge and reached 55% of the theoretical capacity (73% of the capacity reached during the discharge) at an overpotential that was significantly lower than the overpotential of the first charge. The process is shown in Fig. 6a together with the approximate location of 7 points (a-g), which are associated with a set of *operando* spectra collected in the cathode, and a set of 6 points (a-f), which are associated with a set of *operando* spectra collected in the separator. Because the charging process had ended rapidly, it was possible to collect a final spectrum only in the cathode but not in the separator. Inspection of the normalized spectra in Fig. 6b indicates that the initial spectrum in the cathode is already different from the spectrum of the first charging process, due to a polysulfide feature in the 2470–2471 eV region. Furthermore, the presence of the polysulfides in the electrolyte is confirmed by the normalized spectra collected in the separator in Fig. 6c, which contain a charged terminal sulfur feature throughout the entire charging process. The relative changes in the Li_2S and polysulfide components throughout the charge in both the electrode and the separator are visualized in Fig. 6d, while the components of the initial and final spectra of both the second and the first charge are compared in the Appendix. It is determined that the starting composition in the cathode of the second charge is consistent with presence of Li_2S and a polysulfide component, as well as what is likely a small amount of S_8, while, as discussed previously, the cathode of the first charge contains only Li_2S. Furthermore, the figure indicates that the species found in the cathode at the end of both the first and second charge can be completely described by S_8. Using the information about the sulfur species present in the cathode at the beginning and the end of the second charge, we can write the overall equation for the reaction process (Equation 7).

$$Li_2S + yS^{2-}_{x} + 2y\mathrm{Li}^{+} + \mathrm{m}S_8 \rightarrow [E < 2.5\ V]$$
$$\rightarrow \frac{(1+xy+8m)}{8} S_8 + 2(1+y)\,Li^{+} + 2(1+y)\,e^{-} \quad [7]$$

When the process shown in the Equation 7 is compared against the process shown in Equation 4, it becomes evident that the presence of polysulfides is important to lowering the charging potential during the second charge, as has been previously suggested in the literature.[9,19,33] When interpreted in the context of the mechanism in Fig. 5, the addition of polysulfides directly introduces a concentration of solution species that can undergo chain-growth and disproportionation reactions (ii.b) as well as diffuse to the electrode and either get electrochemically oxidized to S_8 (ii.c) or react chemically with Li_2S (ii.a) and S_8 (iii.b) to produce more polysulfides. The electrochemically formed S_8 can then regenerate polysulfide species by either dissolving into the electrolyte (iii.a) and subsequently reacting chemically with Li_2S (ii.a) or by reacting chemically with polysulfides (iii.b). This process can occur throughout the entire charging process until all of Li_2S is consumed. Consequently, the same charging mechanism shown in Fig. 5 is consistent with both the first and the second charge in the DOL-DME electrolyte.

It has been previously suggested by several research groups that a higher order polysulfide, such as S_6^{2-} or S_8^{2-}, and not S_8 is the initial oxidation product in the DOL-DME electrolyte.[9,19,22] In this pathway, lower order polysulfide (S_n^{2-}) could first be electrochemically oxidized to a higher order polysulfide, (i.e., S_8^{2-}, Equation 8), which could then react chemically with Li_2S and regenerate S_n^{2-}(Equation 9), until all the lower order polysulfides and Li_2S are converted to a higher order polysulfide. At this point, the second step of oxidation could occur at a higher potential, leading to electrochemical oxidation of a higher order polysulfide to S_8 (Equation 10).

$$S^{2-}_{n} \rightarrow \frac{n}{8} S^{2-}_{8} + \left(2 - \frac{n}{4}\right) e^{-} \quad [8]$$

$$Li_2S + \frac{n-1}{8-n} S^{2-}_{8} \rightarrow \frac{7}{8-n} S^{2-}_{n} + 2Li^{+} \quad [9]$$

$$S^{2-}_{8} \rightarrow S_{8,solid} + 2e^{-} \quad [10]$$

To determine whether S_8 or a higher order polysulfide is forming when polysulfides are electrochemically oxidized at a potential below 2.5 V during the second charge, we carefully examine the polysulfide feature. In the cathode this feature first increases in intensity, then remains constant for almost the entire charge, and decreases only in the last spectrum (Fig. 6d). Although these changes in the normalized intensity of the charged terminal sulfur in the polysulfide intermediate could be related to electrochemical and chemical processes occurring inside the battery, they can also be influenced by the diffusion of the polysulfides from the bulk electrolyte. In particular, at the end of both discharge and charge processes the concentration of polysulfides near the electrode surface would get smaller, as they would get rapidly

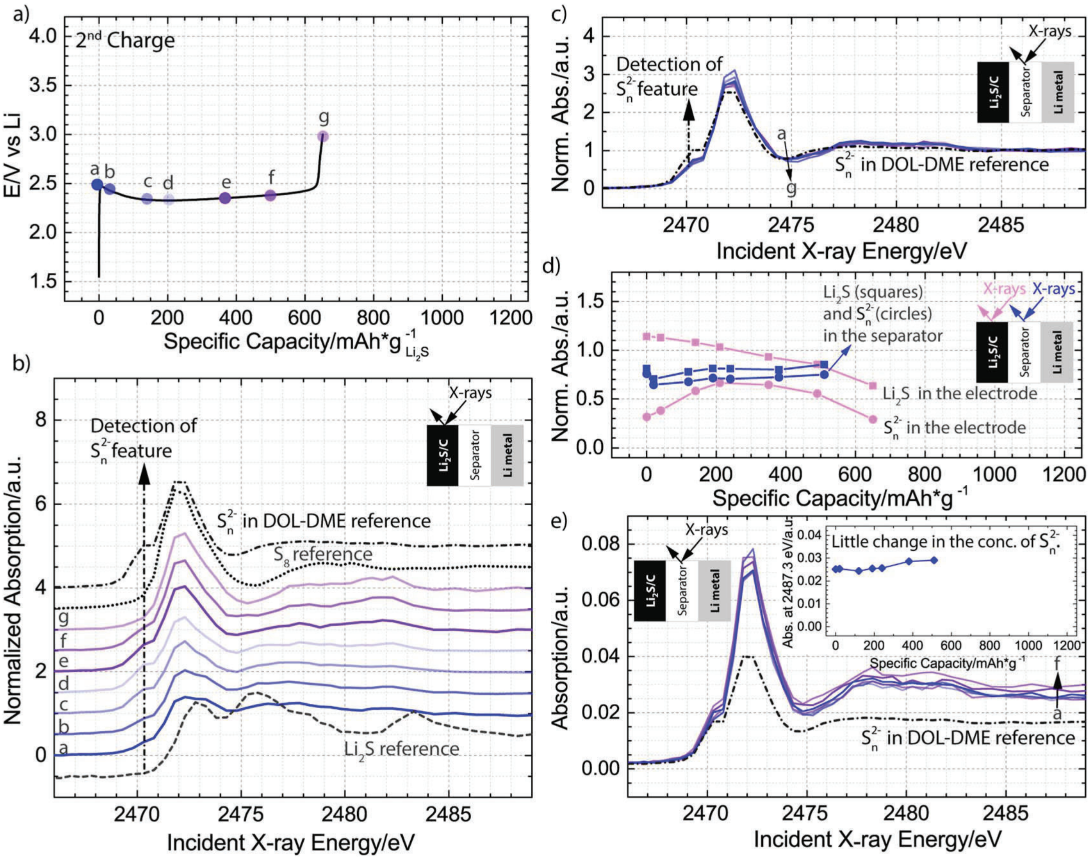

Figure 6. a) Second charge in 1 M $LiClO_4$ and 0.5 M $LiNO_3$ dissolved in DOL-DME solvent plotted as a function of specific capacity normalized to the mass of Li_2S in the cathode with dots a-f indicating where spatially resolved X-ray absorption spectra were obtained. b), c) Normalized XANES spectra collected in the Li_2S cathode b) or the separator c); Li_2S, S_8, and polysulfide references are also plotted for comparison in b), while the polysulfide reference is plotted in c). d) Demonstration of the decrease in Li_2S component inside the electrode, with an associated detection of polysulfide species in the electrode; for comparison, the same trend lines are shown for the spectra obtrained in the separator, in which no significant changes in the composition of the components occurred throughout the charge. The Li_2S fraction (squares) is represented by the normalized intensity at 2475.3 eV, while the polysulfide fraction (circles) is represented by the normalized intensity at 2470.3 eV. e) Raw XANES spectra collected in the separator of the battery; polysulfide reference is plotted for comparison, and the inset illustrates how the absorption intensity at incident energy of 2487.3 eV changes throughout the charging process.

reduced or oxidized. These rapid changes can explain both the initial rise in the polysulfide component in the cathode during the beginning of the charging process (the depleted polysulfides get replenished from the bulk of electrolyte) and the subsequent elimination of the polysulfide signal at the end of the process. Consequently, only the polysulfides in the separator (bulk electrolyte) could clarify whether a higher order polysulfide or S_8 is forming throughout the charge.

The separator is expected to be representative of the bulk concentration of solution based sulfur species in the battery, because the reported diffusion coefficients of polysulfides and sulfur range from $1.2 \cdot 10^{-5}$ to $2 \cdot 10^{-7}$ cm^2/s,[34–36] which corresponds to a diffusion time through the entire cathode and the separator (340 μm) of less than 1 h, even when considering the smallest reported diffusion coefficient in the calculation. To directly illustrate that the species in the separator are associated with electrochemical processes occurring in the cathode, Fig. 7 presents the discharge curve and the associated intermediates forming in the separator during the discharging process. The presented spectra are characterized both by changes in the composition of the intermediates and in their concentration. Specifically, it is seen that as the discharge transitions from a high to a low voltage plateau, the concentration of the solution based species (Fig. 7b) as well as the relative fraction of the charged terminal sulfur atoms (Fig. 7c) significantly increase. These changes correspond to reduction of $S_{8,solid}$ to polysulfides and to shortening of the polysulfide chain length. Consequently, our data confirm that characterization of the separator provides information about the solution phase products that are forming in the cathode, and indicate that if a higher order polysulfide and not S_8 was the main electrochemical oxidation product during the second charge, then its formation could be tracked by observing the changes in the separator species.

Considering formation of a higher order polysulfide, it is expected that this process would lead to a decrease in the relative ratio between the charged sulfur and internal sulfur atoms and/or a significant increase in the concentration of the solution based species. The decrease in the ratio of the two peaks would correspond to the formation of S_6^{2-} or S_8^{2-} from lower order polysulfides (reduction in the number of charged terminal sulfur atoms), while the change in the concentration of the solution based species would correspond to formation of polysulfides from solid Li_2S. Because the discharge process in between the first and second charge resulted in 75% conversion of the capacity stored in S_8 to Li_2S, the starting concentration of polysulfides can be estimated to correspond to approximately 30% of the total sulfur species. Consequently, the formation of a higher order polysulfide instead of solid S_8 should lead to a conversion of the remaining 70% of the species to S_6^{2-} or S_8^{2-} and a considerable increase in the concentration of the solution based species. Furthermore, the solubility of polysulfides is not expected to limit this process, as dissolution of the entire 2.0 mg of Li_2S in the added electrolyte (80 μl) could only lead to 0.07 M concentration of S_8^{2-} (0.09 M concentration of S_6^{2-}).

The already presented Fig. 6c rules out the gradual decrease in the peak ratios, demonstrating that the peaks are characterized by a small increase and not decrease in the ratio (the feature at 2472 eV decreases slightly, while the feature at 2470 eV does not change) between spectrum-b and spectrum-f. These small changes could only correspond to a light shortening and not lengthening of the polysulfide chain. To understand how the concentration of polysulfides changes throughout the charge, Fig. 6e compares the raw spectra, in which the edge jump is proportional to the concentration of sulfur atom in all of its possible forms (both $S_{8,\text{solution}}$ and polysulfides). From the figure, it is evident that the concentration increases only slightly throughout the charging process. As discussed previously, insufficient diffusion time cannot play a role in the lack of significant changes in the concentration, because the charging process lasted 3 h, while the time that was needed to diffuse through the electrode and the separator can be calculated to be less than one hour. Consequently, as illustrated in Fig. 8, our measurements are consistent with the charging pathway in which the main electrochemical product is a solid S_8 and not a solution based S_8^{2-} and indicate that the first and the second charging processes occur via the same mechanism shown in Figure 5.

We note that Yamin and co-workers have previously speculated about a similar type of charging mechanism.[34,37] More specifically, the authors had hypothesized that the anodic cyclic voltammetry (CV) features of various polysulfides dissolved in tetrahydrofuran (THF) solvent could only be explained, if all the polysulfides were to chemically convert to the same intermediate, which would then be electrochemically oxidized at the electrode surface.[34,37] They based their reasoning on the fact that the value of the slope of the peak anodic current versus the scan rate plotted on a log scale had a value of significantly lower than 0.5, while the potential at which the sole anodic peak occurred was independent of the used polysulfide chain length and concentration. Because S_8 is the most stable oxidation product, it was concluded by the authors that S_8 and not a polysulfide was the most likely electrochemical product.[34,38] Due to similarities in the cyclic voltammetry features of Li-S batteries based on THF[19,34,37] and DOL-DME[17,35,39] solvents, it is likely that Li-S batteries based on these solvents share the same mechanism of oxidation.

The developed understanding of the charging mechanism in the DOL-DME based electrolyte can be applied to the recent experimental reports that identify three main strategies of reducing the overpotential of the first charge: introduction of polysulfides into the electrolyte,[9,19,33] reduction in the charging rate,[9,16] and reduction in Li_2S particle size.[9,11,12] In the case of the introduction of polysulfides into the electrolyte, the charging mechanism has the possibility to occur via diffusion of the polysulfides to the electrode structure, if the added concentration of polysulfides is sufficient to sustain the charge at the prescribed rate without depleting the concentration of polysulfides to a trace level. Consequently, the process does not require pathway-(i) in Fig. 5, corresponding to an electrochemical activation of Li_2S, and can occur at a normal overpotential using pathway-(ii). In the case of the slower charging rate, $S_{8,\text{solid}}$, which is being produced electrochemically, has more time to dissolve into the DOL-DME electrolyte throughout the charging process (Fig. 5: iii.a) and react chemically

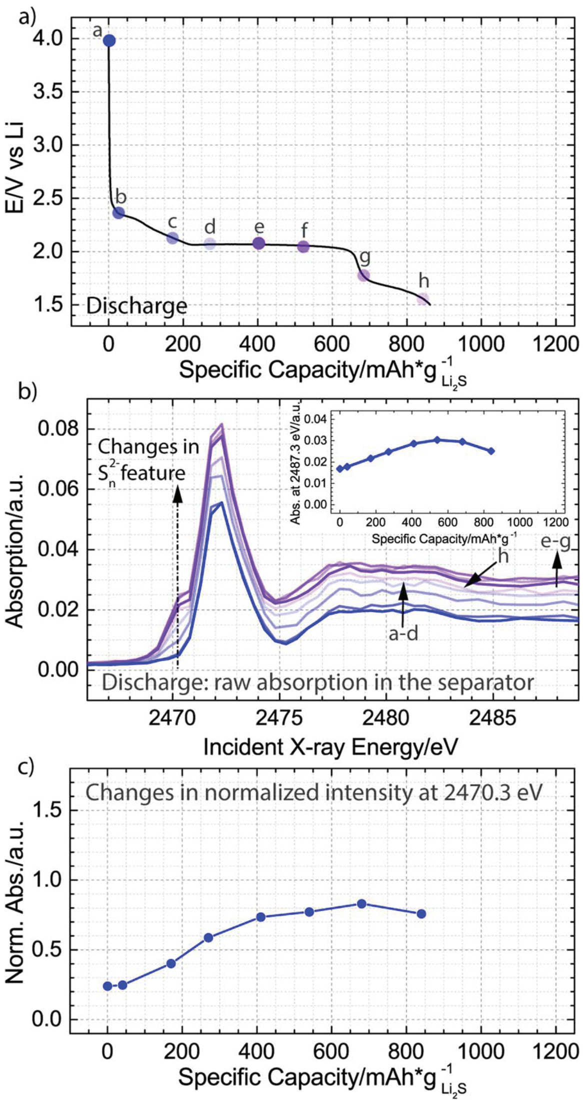

Figure 7. a) Discharge in 1 M $LiClO_4$ and 0.5 M $LiNO_3$ dissolved in DOL-DME solvent plotted as a function of specific capacity normalized to the mass of Li_2S in the cathode with dots a-h indicating where spatially resolved X-ray absorption spectra were obtained. b) Raw XANES spectra collected in the separator of the battery and corresponding to points a-g in panel (a); the inset illustrates how the absorption intensity at the incident energy of 2487.3 eV changes throughout the discharge. c) Analysis of the normalized XANES spectra, demonstrating an increase in the polysulfide feature at 2470.3 eV in the separator throughout the discharge. We note that in agreement with our previous work[21] and in contrast to recently published results by Wujcik et al.,[37] we do not detect a measurable concentration of radical species during the discharge in our ether based electrolyte.

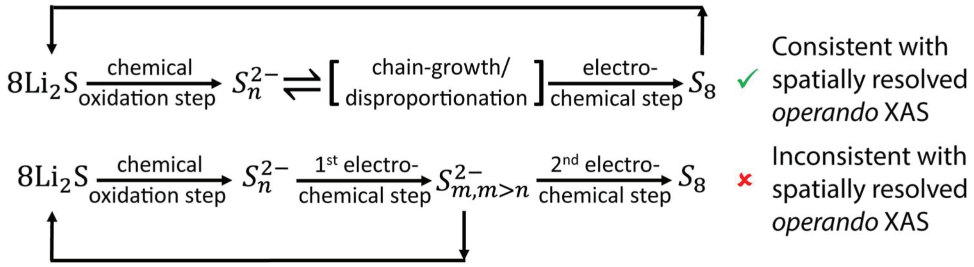

Figure 8. Schematic of two possible pathways to reach the final oxidation product, S_8. Electrochemical formation of a higher order polysulfide, S_m^{2-}, is found to be inconsistent with spatially resolved *operando* XAS measurements.

with Li_2S to produce polysulfides (Fig. 5: ii.a). As a result, if the charging rate is slow enough to generate a considerable concentration of the polysulfide species and the generated species are not lost to reactions with the lithium anode, then the first charge will be able to proceed at the same overpotential as the second charge. In the last strategy, which uses modified cathodes with smaller Li_2S particles, the smaller particle size leads to a significantly larger surface area of Li_2S, which facilitates the chemical reaction between S_8 and Li_2S (Fig. 5: ii.a). The increase in the chemical reaction promotes the charging pathway-(ii). The above analysis demonstrates how the effect of changes in experimental conditions, cathode structure, and electrolyte components can be understood from a mechanistic perspective and corroborates the charging mechanism proposed in our study. Future use of the identified mechanism will help inform rational design of novel cathodes and electrolytes and facilitate development of improved models of Li-S battery operation.

Conclusions

Our work highlights the advantages of spatially resolved XAS characterization, which can detect solution phase polysulfides and amorphous as well as crystalline solids, while also differentiating between the species forming in the electrode and the separator. Using this technique, we are able to obtain information about intermediates present in the cathode and the separator of an operating Li-S battery during the first and second charge of Li_2S and gain insight into the mechanism of Li_2S oxidation in the DOL-DME electrolyte solvent. Specifically, our results demonstrate that even though the first charging process, which occurs at a large overpotential, leads to the extraction of the entire theoretical capacity, corresponding to a complete conversion of Li_2S to S_8, no significant concentration of polysulfide intermediates can be detected throughout the process. Furthermore, analysis of the second charge, which occurs at a small overpotential, shows that the polysulfide species remain at a relatively constant concentration and composition, which is consistent with solid S_8 forming during the entire process. Finally, our results indicate that oxidation of Li_2S particles requires a chemical step, and that during the second charge, this chemical step is facilitated by the presence of a significant concentration of polysulfide intermediates. The identified pathways are expected to assist in reaching higher areal capacities in Li-S batteries by guiding both the development of models of Li-S battery operation and the design of improved cathode structures and electrolyte components.

Acknowledgments

The described XAS measurements were carried out at the Stanford Synchrotron Radiation Lightsource, a Directorate of SLAC National Accelerator Laboratory and an Office of Science User Facility operated for the U.S. Department of Energy Office of Science by Stanford University. Use of the Stanford Synchrotron Radiation Lightsource, SLAC National Accelerator Laboratory, is supported by the U.S. Department of Energy, Office of Science, Office of Basic Energy Sciences under Contract No. DE-AC02-76SF00515. The authors also thank Diamond Light Source, Didcot, UK for access to beamline I18 (SP 8734), K. Ignatyev and T. Geraki for support during the experiments at DLS, S. M. Webb and C. Roach for the support during the experiments at SLAC, as well as O. Gröger, A. Siebel, M. Wetjen, A. Berger, and A. Eberle for helpful discussions. Y. Gorlin gratefully acknowledges the support of the Alexander von Humboldt Postdoctoral Fellowship and Carl Friedrich von Siemens Fellowship Supplement. Portions of the research leading to these results have received funding from the German Ministry of Education and Research (BMBF) under agreement No. 03ET6045D.

Appendix

See Figure A1.

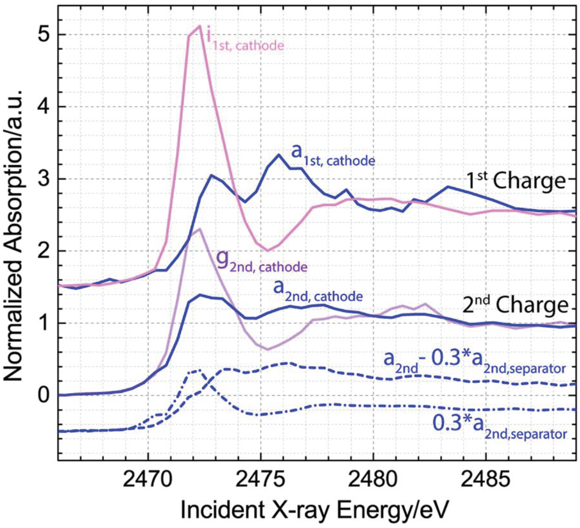

Figure A1. Demonstration of the initial and final XANES spectra in the cathode during the first and second charge. To visualize the components of the initial spectrum of the second charge, a fraction of the separator spectrum is subtracted from the cathode spectrum (after the end of discharge, the maximum possible concentration of solution based polysulfides is calculated to be ~ 30%, considering S_4^{2-} species) and both the separator fraction (dash-dotted line) and the resulting difference spectra (dashed line) are added to the plot.

References

1. D. Eroglu, K. R. Zavadil, and K. G. Gallagher, *J. Electrochem. Soc.*, **162**, A982 (2015).
2. O. Gröger, H. A. Gasteiger, and J.-P. Suchsland, *J. Electrochem. Soc.*, **162**, A2605 (2015).
3. M. Hagen, D. Hanselmann, K. Ahlbrecht, R. Maça, D. Gerber, and J. Tübke, *Adv. Energ. Mat.*, **5**, 1401986 (2015).
4. Y. V. Mikhaylik, I. Kovalev, R. Schock, K. Kumaresan, J. Xu, and J. Affinito, *ECS Trans.*, **25**, 23 (2010).
5. M. Wild, L. O'Neill, T. Zhang, R. Purkayastha, G. Minton, M. Marinescu, and G. J. Offer, *Energ. Environ. Sci.*, **8**, 3477 (2015).
6. P. G. Bruce, S. A. Freunberger, L. J. Hardwick, and J.-M. Tarascon, *Nat. Mater.*, **11**, 19 (2012).
7. J. Hassoun and B. Scrosati, *Angew. Chem.*, **49**, 2371 (2010).
8. H. Jha, I. Buchberger, X. Cui, S. Meini, and H. A. Gasteiger, *J. Electrochem. Soc.*, **162**, A1829 (2015).
9. Y. Yang, G. Zheng, S. Misra, J. Nelson, M. F. Toney, and Y. Cui, *J. Am. Chem. Soc.*, **134**, 15387 (2012).
10. Y. Yang, M. T. McDowell, A. Jackson, J. J. Cha, S. S. Hong, and Y. Cui, *Nano Lett.*, **10**, 1486 (2010).
11. K. Zhang, L. Wang, Z. Hu, F. Cheng, and J. Chen, *Sci. Rep.*, **4**, 6467 (2014).
12. K. Cai, M.-K. Song, E. J. Cairns, and Y. Zhang, *Nano Lett.*, **12**, 6474 (2012).
13. Y. Hwa, J. Zhao, and E. J. Cairns, *Nano Lett.*, **15**, 3479 (2015).
14. Z. Lin, C. Nan, Y. Ye, J. Guo, J. Zhu, and E. J. Cairns, *Nano Energy*, **9**, 408 (2014).
15. Y. Fu, Y.-S. Su, and A. Manthiram, *Adv. Energ. Mat.*, **4**, 1300655 (2014).
16. S. Meini, R. Elazari, A. Rosenman, A. Garsuch, and D. Aurbach, *J. Phys. Chem. Lett.*, **5**, 915 (2014).
17. F. Wu, J. T. Lee, N. Nitta, H. Kim, O. Borodin, and G. Yushin, *Adv. Mater.*, **27**, 101 (2015).
18. C. Zu, M. Klein, and A. Manthiram, *J. Phys. Chem. Lett.*, **5**, 3986 (2014).
19. L. Wang, Y. Wang, and Y. Xia, *Energ. Environ. Sci.*, **8**, 1551 (2015).
20. M. Cuisinier, C. Hart, M. Balasubramanian, A. Garsuch, and L. F. Nazar, *Adv. Energ. Mat.*, **5**, 1401801 (2015).
21. Y. Gorlin, A. Siebel, M. Piana, T. Huthwelker, H. Jha, G. Monsch, F. Kraus, H. A. Gasteiger, and M. Tromp, *J. Electrochem. Soc.*, **162**, A1146 (2015).
22. M. Cuisinier, P.-E. Cabelguen, S. Evers, G. He, M. Kolbeck, A. Garsuch, T. Bolin, M. Balasubramanian, and L. F. Nazar, *J. Phys. Chem. Lett.*, **4**, 3227 (2013).
23. M. U. M. Patel, I. Arčon, G. Aquilanti, L. Stievano, G. Mali, and R. Dominko, *ChemPhysChem*, **15**, 894 (2014).
24. R. Dominko, M. U. M. Patel, V. Lapornik, A. Vizintin, M. Koželj, N. N. Tušar, I. Arčon, L. Stievano, and G. Aquilanti, *J. Phys. Chem. C*, **119**, 19001 (2015).
25. M. A. Lowe, J. Gao, and H. D. Abruna, *RSC Adv.*, **4**, 18347 (2014).
26. B. Ravel and M. Newville, *J. Synchrotron Rad.*, **12**, 537 (2005).
27. J. M. Durand, J. Olivier-Fourcade, J. C. Jumas, M. Womes, C. M. Teodorescu, A. Elafif, J. M. Esteva, and R. C. Karnatak, *J. Phys. B: At., Mol. Opt. Phys.*, **29**, 5773 (1996).
28. T. A. Pascal, K. H. Wujcik, J. Velasco-Velez, C. Wu, A. A. Teran, M. Kapilashrami, J. Cabana, J. Guo, M. Salmeron, N. Balsara, and D. Prendergast, *J. Phys. Chem. Lett.*, **5**, 1547 (2014).

29. G. Almkvist, K. Boye, and I. Persson, *J. Synchrotron Rad.*, **17**, 683 (2010).
30. M. Barghamadi, A. S. Best, A. I. Bhatt, A. F. Hollenkamp, M. Musameh, R. J. Rees, and T. Ruther, *Energ. Environ. Sci.*, **7**, 3902 (2014).
31. J. Y. Koh, M.-S. Park, E. H. Kim, B. O. Jeong, S. Kim, K. J. Kim, J.-G. Kim, Y.-J. Kim, and Y. Jung, *J. Electrochem. Soc.*, **161**, A2133 (2014).
32. A. Manceau and K. L. Nagy, *Geochim. Cosmochim. Acta*, **99**, 206 (2012).
33. K. Han, J. Shen, C. M. Hayner, H. Ye, M. C. Kung, and H. H. Kung, *J. Power Sources*, **251**, 331 (2014).
34. H. Yamin, A. Gorenshtein, J. Penciner, Y. Sternberg, and E. Peled, *J. Electrochem. Soc.*, **135**, 1045 (1988).
35. Y.-C. Lu, Q. He, and H. A. Gasteiger, *J. Phys. Chem. C*, **118**, 5733 (2014).
36. F. Y. Fan, W. C. Carter, and Y.-M. Chiang, *Adv. Mater.*, **27**, 5203 (2015).
37. K. H. Wujcik, T. A. Pascal, C. D. Pemmaraju, D. Devaux, W. C. Stolte, N. P. Balsara, and D. Prendergast, *Adv. Energ. Mat.*, **5**, 1500285 (2015).
38. H. Yamin, J. Penciner, A. Gorenshtain, M. Elam, and E. Peled, *J. Power Sources*, **14**, 129 (1985).
39. L. Chen, Y. Liu, F. Zhang, C. Liu, and L. L. Shaw, *ACS Appl. Mater. Interfaces*, **7**, 25748 (2015).

4 Conclusions

This present thesis was aiming to better understand the fundamentals of the Li-S redox chemistry in aprotic electrolytes and thus to provide a foundation for the further development of Li-S batteries. Along with the gained insights into the Li-S mechanism, several novel experimental approaches were (further) developed for Li-S batteries, such as *operando* transmission UV-Vis spectroscopy, *in-situ* electrochemical impedance spectroscopy, and symmetric cell impedance.

In the first part of this thesis, we attempted to understand the relationship between the electrolyte solvent properties and the sulfur redox behavior, seeking to address the question of how the polysulfide speciation can be influenced by the use of different electrolyte systems. Hence, we systematically investigated the sulfur redox behavior and the polysulfide speciation in nine electrolyte solvents that cover a wide range of the three main physiochemical properties of electrolytes, viz. the dielectric constant (ε), the Gutmann donor number (DN) and the Gutmann acceptor number (AN). Various techniques were deployed, including cyclic voltammetry, the rotating ring disc electrode technique, UV-Vis spectroscopy, and galvanostatic cycling in a two-compartment cell, in which the anolyte and the catholyte are separated by an impermeable lithium ion conducting glass. As a result, we observed that the polysulfide speciation and the sulfur redox behavior are governed by the DN of the solvent, rather than by ε. We rationalized this with the classic hard soft acid base (HSAB) theory, suggesting for instance that soft acids (strongly solvated Li^+, e.g., Li^+ in high-DN solvents) prefer soft bases (e.g., long-chain polysulfides with more delocalized electrons) and vice-versa. This clearly demonstrated how the redox behavior of the sulfur species and the polysulfide speciation are mainly controlled by the interaction between a cation-complex with polysulfide anions via the HSAB theory — that is to say, the reaction pathway of lithium-sulfur batteries can be manipulated by the solvent donicity (DN) as well as by the type and the concentration of cations.

The second part of this thesis is devoted to the mechanistic understanding of the Li-S discharge process, which is separated into two steps, namely 1) the real-time identification of polysulfide intermediates in a DOL:DME-based Li-S battery using *operando* transmission UV-Vis spectroscopy and 2) the quantification of the important physical/chemical processes at the S-cathode during discharge via *in-situ* impedance spectroscopy. For this, we first developed an *operando* UV-Vis spectroelectrochemical cell, which provides a fairly comparable electrochemical performance compared to conventional battery cells and offers a rather high potential resolution. Next, we established a series of polysulfide reference spectra and systematically performed a peak assignment analysis, since the identification of a substance using UV-Vis spectroscopy hinges strongly on the comparison with reference spectra. Combining both the *operando* results and the *ex-situ* peak assignment based on reference spectra, we proposed a discharge mechanism that evolves S_8, S_4^{2-}, and a polysulfide species that has scarcely been reported in the literature. These are S_3^{2-} species, whose existence is validated by the *operando* UV-Vis results and by the rotating ring disc electrode measurements and they are dominantly present in the 2nd Li-S discharge plateau. Overall, this study elucidated the detailed reaction pathway leading from S_4^{2-} to Li_2S in a DOL:DME-based Li-S battery and presented an entirely novel *operando* UV-Vis spectroelectrochemical cell setup for any cell chemistry that involves chromophoric reaction intermediates or products.

Building on this work, a more quantitative approach was desired to quantify the contributions from possible physical/chemical processes upon discharge, seeking to identify the intrinsic cause for the poor rate capability and the limited capacity of Li-S batteries. For this, we employed *in-situ* electrochemical impedance spectroscopy in combination with a micro-reference electrode (the so-called gold wire reference electrode, GWRE) in the Li-S system, which allows a real-time separation of the S-cathode impedance from the overall cell impedance. In addition, since the interpretation of impedance spectra is not always straightforward, we recorded and analyzed reference impedance spectra from a well-designed symmetric cell setup, whereby the interpretation of these reference spectra was validated by a controlled variation of the experimental conditions. In this way, we were able to ascribe the complex and dynamic impedance spectra to their physic/chemical origins and thus could analyze them in a quantitative manner. This study provided the following new insights into the discharge process of Li-S batteries: (i) The aluminum current collector is corroded in the presence of polysulfides, leading to a contact resistance at the electrode/current collector interface. (ii) The much higher charge transfer resistance of the S-redox reactions on the carbon support can explain a) the necessity of having large amounts of conductive carbon in current sulfur-cathodes and, b) the poor rate capability of Li-S batteries despite the generally high content of conductive carbon material.

In the final part of this thesis, we investigated the charging process of a Li-S battery by characterizing the reaction intermediates produced at the different voltages. We deployed a novel *operando* cell design for the X-ray absorption spectroscopy, which can simultaneously provide a wealth of information on different S-species (including S_8, Li_2S_x, and Li_2S) and a high spatial resolution that allows to independently record spectra in the cathode electrode and in the separator region. By comparing the reaction intermediates produced at the high charging voltage in the first cycle with these produced at the low charging voltage of the second cycle, a rather detailed charging mechanism could be proposed. Emphasis was put on examining the chemical reaction between the dissolved polysulfides and the solid Li_2S that is required to facilitate the electrochemical oxidation of Li_2S, and thus to find ways to affect the charging potential of Li-S batteries.

In this PhD thesis, it was attempted to answer several fundamental questions about Li-S batteries and, to identify the intrinsic issues of the present Li-S batteries. In fact, we showed that the exchange current density of the sulfur-redox reactivities on a carbon support are, at most, 10% of these characteristic for the current Li-ion batteries materials, which raises the question, whether Li-S batteries will ultimately be able to compete with the most advanced Lithium-ion batteries. Therefore, the findings from this PhD thesis encourage future research work to focus on the development of high-surface area catalyst to increase the intrinsic exchange current density of the S-redox reactions, which would facilitate a faster and more complete conversion between S_8 and Li_2S, and hence open a path towards a higher rate capability. Further emphasis should be placed on the reduction of the weight of passive cell material in practical Li-S cells, e.g. having the excess amount of electrolyte and high carbon content in the cathode. Overall, we believe this work contributed to a better mechanistic understanding of Li-S batteries and that it was able to thus lay a foundation for a more accurate modelling/simulation and for the further development of Li-S batteries.

5 References

1. M. Winter, B. Barnett, and K. Xu, *Chem. Rev.*, **118**, 11433–11456 (2018).

2. M. S. Whittingham, *Chem. Rev.*, **114**, 11414–11443 (2014).

3. G. E. Blomgren, *J. Electrochem. Soc.*, **164**, A5019–A5025 (2017).

4. M. Winter, *Chem. Rev.*, **104**, 4245–4269 (2004).

5. D. R. Rolison, L. F. Nazar, and G. Editors, *Mater. Res. Soc. Bull.*, **36**, 486–493 (2011).

6. O. Gröger, H. A. Gasteiger, and J.-P. Suchsland, *J. Electrochem. Soc.*, **162**, A2605–A2622 (2015).

7. Regulation (EU) No 333/2014 of the European Parliament and of the Council of 11 March 2014 amending Regulation (EC) No 443/2009 to define the modalities for reaching the 2020 target to reduce CO2 emissions from new passenger cars, http://data.europa.eu/eli/reg/2014/333/oj, (2014).

8. R. Edenhofer, O., B. K. Pichs-Madruga, Y. Sokona, E. Farahani, S. Kadner, K. Seyboth, A. Adler, I. Baum, S. Brunner, P. Eickemeier, and T. Z. and J. C. M. (eds. . J. Savolainen, S. Schlömer, C. von Stechow, *IPCC-Summary for Policymakers. In: Climate Change 2014: Mitigation of Climate Change*, (2014).

9. D. Andre, S.-J. Kim, P. Lamp, S. F. Lux, F. Maglia, O. Paschos, and B. Stiaszny, *J. Mater. Chem. A*, **3**, 6709–6732 (2015).

10. D. Eroglu, K. R. Zavadil, and K. G. Gallagher, *J. Electrochem. Soc.*, **162**, A982–A990 (2015).

11. J. B. Goodenough and K.-S. Park, *J. Am. Chem. Soc.*, **135**, 1167–76 (2013).

12. X. Ji, K. T. Lee, and L. F. Nazar, *Nat. Mater.*, **8**, 500–506 (2009).

13. M. Wild, L. O'Neill, T. Zhang, R. Purkayastha, G. Minton, M. Marinescu, and G. J. Offer, *Energy Environ. Sci.*, **8**, 3477–3494 (2015).

14. G. Zhang, Z. Zhang, H. Peng, J. Huang, and Q. Zhang, *Small Methodes*, **1**, 1700134 (2017).

15. J. Muldoon and C. B. Bucur, Patent No. US20140234707A1 (2014).

16. H. Y. Ryu and H. J. Woo, Patent No. US20140162121A1 (2014).

17. B. Son, M. Jang, Y. M. Kim, and G. S. Park, Patent No. US20160190561A1 (2016).

18. K. J. Jeong, M. Y. Eom, C. H. Park, and W. D. Shin, Patent No. US20160268600A1 (2016).

19. A. Garsuch, K. Leitner, and T. J. Koplin, Patent No. US20120183854A1 (2012).

20. C. Barchasz, F. Molton, C. Duboc, J. C. Leprêtre, S. Patoux, and F. Alloin, *Anal. Chem.*, **84**, 3973–3980 (2012).

21. P. T. Cunningham, S. A. Johnson, and E. J. Cairns, *J. Electrochem. Soc.*, **119**, 1448–1450 (1972).

22. Q. Zou and Y.-C. Lu, *J. Phys. Chem. Lett.*, **7**, 1518–1525 (2016).

23. R. P. Martin, W. H. Doub, J. L. Roberts, and D. T. Sawyer, *Inorg. Chem.*, **12**, 1921–1925 (1973).

24. Y. Jung, S. Kim, B.-S. Kim, D.-H. Han, S.-M. Park, and J. Kwak, *Int. J. Electrochem. Sci.*, **3**, 566–577 (2008).

25. G. Bieker, J. Wellmann, M. Kolek, K. Jalkanen, M. Winter, and P. M. Bieker, *Phys. Chem. Chem. Phys.*, **19**, 11152–11162 (2017).

26. Q. Zou, Z. Liang, G. Du, C. Liu, E. Y. Li, Y. Lu, Q. Zou, Z. Liang, G. Du, C. Liu, E. Y. Li, and Y. Lu, *J. Am. Chem. Soc.*, **140**, 10740–10748 (2018).

27. Y. V. Mikhaylik and J. R. Akridge, *J. Electrochem. Soc.*, **151**, A1969–A1976 (2004).

28. Y. V. Mikhaylik and J. R. Akridge, *J. Electrochem. Soc.*, **150**, A306–A311 (2003).

29. A. Evans, M. I. Montenegro, and D. Pletcher, *Electrochem. commun.*, **3**, 514–518 (2001).

30. S. D. Talian, J. Moskon, R. Dominko, M. Gaberscek, S. D. Talian, J. Moškon, R. Dominko, and M. Gaberšček, *Appl. Mater. Interfaces*, **9**, 29760–29770 (2017).

31. Y. Gorlin, A. Siebel, M. Piana, T. Huthwelker, H. Jha, G. Monsch, F. Kraus, H. A. Gasteiger, and M. Tromp, *J. Electrochem. Soc.*, **162**, A1146–A1155 (2015).

32. T. Chivers and P. J. W. Elder, *Chem. Soc. Rev.*, **42**, 5996–6005 (2013).

33. M. Hagen, D. Hanselmann, K. Ahlbrecht, R. Maça, D. Gerber, and J. Tübke, *Adv. Energy Mater.*, **5**, 1401986 (2015).

34. G. Zhang, H.-J. Peng, C.-Z. Zhao, X. Chen, L.-D. Zhao, P. Li, J.-Q. Huang, and Q. Zhang, *Angew. Chemie Int. Ed.*, 1–6 (2018).

35. OXIS Energy Ltd., https://oxisenergy.com/technology/.

36. D. Aurbach, E. Pollak, R. Elazari, G. Salitra, C. S. Kelley, and J. Affinito, *J. Electrochem. Soc.*, **156**, A694–A702 (2009).

37. Y. V. Mikhaylik, I. Kovalev, R. Schock, K. Kumaresan, J. Xu, and J. Affinito, *ECS Trans.*, **25**, 23–34 (2010).

38. C. P. Grey and J. M. Tarascon, *Nat. Mater.*, **16**, 45–56 (2016).

39. X. Cheng, J. Huang, and Q. Zhang, *J. Electrochem. Soc.*, **165**, A6058–A6072 (2018).

40. X. Cheng, C. Yan, J. Huang, P. Li, L. Zhu, L. Zhao, Y. Zhang, W. Zhu, S.-T. Yang, and Q. Zhang, *Energy Storage Mater.*, **6**, 18–25 (2016).

41. M. Hagen, P. Fanz, and J. Tübke, *J. Power Sources*, **264**, 30–34 (2014).

42. S. S. Zhang, *Energies*, **5**, 5190–5197 (2012).

43. OXIS Energy Ltd., https://45uevg34gwlltnbsf2plyua1-wpengine.netdna-ssl.com/wp-content/uploads/2019/02/OXIS-Li-S-Ultra-Light-Cell-v4.1.pdf., (2019)

44. M. Marinescu, L. O. Neill, T. Zhang, G. J. Offer, S. Walus, and T. E. Wilson, *J. Electrochem. Soc.*, **165**, A6107–A6118 (2018).

45. F. T. Wagner, B. Lakshmanan, and M. F. Mathias, *J. Phys. Chem. Lett.*, **1**, 2204–2219 (2010).

46. Q. Pang, X. Liang, C. Y. Kwok, and L. F. Nazar, *Nat. Energy*, **1**, Article number 16132 (2016).

47. C. Qu, Y. Chen, X. Yang, H. Zhang, X. Li, and H. Zhang, *Nano Energy*, **39**, 262–272 (2017).

48. A. Jozwiuk, B. B. Berkes, T. Weiß, H. Sommer, J. Janek, and T. Brezesinski, *Energy Environ. Sci.*, **9**, 2603–2608 (2016).

49. M. Marinescu, T. Zhang, and G. J. Offer, *Phys. Chem. Chem. Phys.*, **18**, 584–593 (2015).

50. T. Cleaver, P. Kovacik, and M. Marinescu, *J. Electrochem. Soc.*, **165**, A6029–A6033 (2018).

51. H. Peng, J. Huang, X. Cheng, and Q. Zhang, *Adv. Energy Mater.*, **7**, 1700260 (2017).

52. Q. Pang, X. Liang, C. Y. Kwok, and L. F. Nazar, *J. Electrochem. Soc.*, **162**, A2567–A2576 (2015).

53. C. Lee, Q. Pang, S. Ha, L. Cheng, S. Han, K. R. Zavadil, K. G. Gallagher, L. F. Nazar, and M. Balasubramanian, *ACS Cent. Sci.*, **3**, 605–613 (2017).

54. K. Ueno, J. Park, A. Yamazaki, T. Mandai, N. Tachikawa, K. Dokko, and M. Watanabe, *J. Phys. Chem. C*, **117**, 20509–20516 (2013).

55. L. Suo, Y.-S. Hu, H. Li, M. Armand, and L. Chen, *Nat. Commun.*, **4**, Article number 1481 (2013).

56. X. Liu, J.-Q. Huang, Q. Zhang, and L. Mai, *Adv. Mater.*, **29**, 1601759 (2017).

57. B. Zhang, X. Qin, G. R. Li, and X. P. Gao, *Energy Environ. Sci.*, **3**, 1531–1537 (2010).

58. G. Zheng, Q. Zhang, J. J. Cha, Y. Yang, W. Li, Z. W. Seh, and Y. Cui, *Nano Lett.*, **13**, 1265–1270 (2013).

59. L. Yuan, H. Yuan, X. Qiu, L. Chen, and W. Zhu, *J. Power Sources*, **189**, 1141–1146 (2009).

60. M. Zhao, J. Huang, G. Tian, J. Nie, H. Peng, Q. Zhang, and F. Wei, *Nat. Commun.*, **5**, Article number 3410 (2014).

61. J. Song, M. L. Gordin, T. Xu, S. Chen, Z. Yu, H. Sohn, J. Lu, Y. Ren, Y. Duan, and D. Wang, *Angew. Chemie - Int. Ed.*, **54**, 4325–4329 (2015).

62. H. Wang, Y. Yang, Y. Liang, J. T. Robinson, Y. Li, and A. Jackson, *Nano Lett.*, **11**, 2644–2647 (2011).

63. Z. Wang, Y. Dong, H. Li, Z. Zhao, H. Bin Wu, C. Hao, S. Liu, J. Qiu, X. Wen, and D. Lou, *Nat. Commun.*, **5**, Article number 5002 (2014).

64. Q. Pang, D. Kundu, M. Cuisinier, and L. F. Nazar, *Nat. Commun.*, **5**, Article number 4759 (2014).

65. Z. W. Seh, W. Li, J. J. Cha, G. Zheng, Y. Yang, M. T. McDowell, P.-C. Hsu, and Y. Cui, *Nat Commun*, **4**, Article number 1331 (2013).

66. X. Liang, C. Y. Kwok, F. Lodi-marzano, Q. Pang, M. Cuisinier, H. Huang, C. J. Hart, D. Houtarde, K. Kaup, H. Sommer, T. Brezesinski, J. Janek, and L. F. Nazar, *Adv. Energy Mater.*, **6**, 1501636 (2016).

67. X. Liang and L. F. Nazar, *ACS Nano*, **10**, 4192–4198 (2016).

68. Z. W. Seh, J. H. Yu, W. Li, P. Hsu, H. Wang, Y. Sun, H. Yao, Q. Zhang, and Y. Cui, *Nat. Commun.*, **5**, Article number 5017 (2014).

69. M. Cuisinier, C. Hart, M. Balasubramanian, A. Garsuch, and L. F. Nazar, *Adv. Energy Mater.*, **5**, 1401801 (2015).

70. K. Xu, *Chem. Rev.*, **104**, 4303–4417 (2004).

71. J. Park, K. Ueno, N. Tachikawa, K. Dokko, and M. Watanabe, *J. Phys. Chem. C*, **117**, 20531–20541 (2013).

72. K. Ueno, J.-W. Park, A. Yamazaki, T. Mandai, N. Tachikawa, K. Dokko, and M. Watanabe, *J. Phys. Chem. C*, **117**, 20509–20516 (2013).

73. K. Dokko, N. Tachikawa, K. Yamauchi, M. Tsuchiya, a. Yamazaki, E. Takashima,

J.-W. Park, K. Ueno, S. Seki, N. Serizawa, and M. Watanabe, *J. Electrochem. Soc.*, **160**, A1304–A1310 (2013).

74. L. Cheng, L. A. Curtiss, K. R. Zavadil, A. A. Gewirth, Y. Shao, and K. G. Gallagher, *ACS Energy Lett.*, **1**, 503–509 (2016).

75. K. Ueno, J. Park, A. Yamazaki, T. Mandai, N. Tachikawa, K. Dokko, and M. Watanabe, *J. Phys. Chem. C*, **117**, 20509–20516 (2013).

76. M. Cuisinier, P.-E. Cabelguen, B. D. Adams, A. Garsuch, M. Balasubramanian, and L. F. Nazar, *Energy Environ. Sci.*, **7**, 2697–2705 (2014).

77. M. Agostini, Y. Aihara, T. Yamada, B. Scrosati, and J. Hassoun, *Solid State Ionics*, **244**, 48–51 (2013).

78. M. Nagao, A. Hayashi, and M. Tatsumisago, *Electrochim. Acta*, **56**, 6055–6059 (2011).

79. X. Judez, H. Zhang, C. Li, G. Eshetu, A. Gonz, M. Armand, and L. M. Rodriguez-Martinez, *J. Electrochem. Soc.*, **165**, A6008–A6016 (2018).

80. M. Barghamadi, A. S. Best, A. I. Bhatt, A. F. Hollenkamp, M. Musameh, R. J. Rees, and T. Rüther, *Energy Environ. Sci.*, **7**, 3902–3920 (2014).

81. W. Li, H. Yao, K. Yan, G. Zheng, Z. Liang, Y. Chiang, and Y. Cui, *Nat. Commun.*, **6**, Article number: 7436 (2015).

82. A. Rosenman, R. Elazari, G. Salitra, E. Markevich, D. Aurbach, and A. Garsuch, *J. Electrochem. Soc.*, **162**, A470–A473 (2015).

83. F. Wu, J. T. Lee, N. Nitta, H. Kim, O. Borodin, and G. Yushin, *Adv. Mater.*, **27**, 101–108 (2015).

84. Z. Lin, Z. Liu, W. Fu, N. J. Dudney, and C. Liang, *Adv. Funct. Mater.*, **23**, 1064–1069 (2012).

85. G. Ma, Z. Wen, M. Wu, C. Shen, Q. Wang, J. Jin, and X. Wu, *Chem. Commun.*, **50**, 14209–14212 (2014).

86. H. Jha, I. Buchberger, X. Cui, S. Meini, and H. A. Gasteiger, *J. Electrochem. Soc.*, **162**, A1829–A1835 (2015).

87. M. Wetjen, S. Solchenbach, H. A. Gasteiger, D. Pritzl, J. Hou, and V. Tileli, *J. Electrochem. Soc.*, **165**, A1503–A1514 (2018).

88. M. Wetjen, D. Pritzl, R. Jung, S. Solchenbach, R. Ghadimi, and H. A. Gasteiger, *J. Electrochem. Soc.*, **164**, A2840–A2852 (2017).

89. D. Lv, J. Zheng, Q. Li, X. Xie, S. Ferrara, Z. Nie, L. B. Mehdi, N. D. Browning, J. Zhang, G. L. Graff, J. Liu, and J. Xiao, *Adv. Energy Mater.*, **5**, 1402290 (2015).

90. G. Zhou, L. Li, C. Ma, and S. Wang, *Nano Energy*, **11**, 356–365 (2015).

91. Q. Sun, X. Fang, W. Weng, J. Deng, P. Chen, J. Ren, G. Guan, M. Wang, and H. Peng, *Angew. Chemie*, **127**, 10685–10690 (2015).

92. F. Y. Fan and Y. Chiang, *J. Electrochem. Soc.*, **164**, A917–A922 (2017).

93. K. Sun, A. K. Matarasso, R. M. Epler, X. Tong, D. Su, A. C. Marschilok, K. J. Takeuchi, E. S. Takeuchi, and H. Gan, *J. Electrochem. Soc.*, **165**, A416–A423 (2018).

94. H. Schneider, C. Gollub, T. Weiss, J. Kulisch, K. Leitner, R. Schmidt, M. M. Safont-Sempere, Y. Mikhaylik, T. Kelley, C. Scordilis-Kelley, M. Laramie, and H. Du, *J. Electrochem. Soc.*, **161**, A1399–A1406 (2014).

95. Y.-C. Lu, Q. He, and H. A. Gasteiger, *J. Phys. Chem. C*, **118**, 5733–5741 (2014).

96. S. Waluś, C. Barchasz, R. Bouchet, J.-C. Leprêtre, J.-F. Colin, J.-F. Martin, E. Elkaïm, C. Baehtz, and F. Alloin, *Adv. Energy Mater.*, **5**, 1500165 (2015).

97. R. Bonnaterre and G. Cauquis, *J. Chem. Soc. Chem. Commun.*, 293–294 (1972).

98. T. Fujinaga, T. Kuwamoto, S. Okazaki, and M. Hojo, *Bull. Chem. Soc. Jpn.*, **53**, 2851–2855 (1980).

99. T. Chivers and I. Drummond, *J. Chem. Soc. Dalt. Trans.*, 631–633 (1974).

100. S.-I. Tobishima, H. Yamamoto, and M. Matsuda, *Electrochim. Acta*, **42**, 1019–1029 (1997).

101. M. Cuisinier, P.-E. Cabelguen, S. Evers, G. He, M. Kolbeck, A. Garsuch, T. Bolin, M. Balasubramanian, and L. F. Nazar, *J. Phys. Chem. Lett.*, **4**, 3227–3232 (2013).

102. N. A. Cañas, D. N. Fronczek, N. Wagner, A. Latz, and K. A. Friedrich, *J. Phys. Chem. C*, **118**, 12106–12114 (2014).

103. Z. Li, Y. Zhou, Y. Wang, and Y. C. Lu, *Adv. Energy Mater.*, **9**, 1802207 (2018).

104. Y. Gorlin, M. U. M. Patel, A. Freiberg, Q. He, M. Piana, M. Tromp, and H. A. Gasteiger, *J. Electrochem. Soc.*, **163**, A930–A939 (2016).

105. M. U. M. Patel and R. Dominko, *ChemSusChem*, **7**, 2167–2175 (2014).

106. T. Poux, P. Novák, and S. Trabesinger, *J. Electrochem. Soc.*, **163**, A1139–A1145 (2016).

107. T. Zhang, M. Marinescu, S. Walus, P. Kovacik, and G. J. Offer, *J. Electrochem. Soc.*, **165**, A6001–A6004 (2018).

108. A. Vizintin, L. Chabanne, E. Tchernychova, I. Ar, L. Stievano, G. Aquilanti, M. Antonietti, T. Fellinger, and R. Dominko, **344**, 208–217 (2017).

109. Y. Yang, G. Zheng, S. Misra, J. Nelson, M. F. Toney, and Y. Cui, *J. Am. Chem. Soc.*, **134**, 15387–15394 (2012).

110. S. Meini, R. Elazari, A. Rosenman, A. Garsuch, and D. Aurbach, *J. Phys. Chem. Lett.*, **5**, 915–918 (2014).

111. K. Cai, M. Song, E. J. Cairns, and Y. Zhang, *Nano Lett.*, **12**, 6474–6479 (2012).

112. Y. Fu, Y. S. Su, and A. Manthiram, *Adv. Energy Mater.*, **4** (2014).

113. J. Conder, C. Marino, P. Novak, and C. Villevieille, *J. Mater. Chem. A*, **6**, 3304–3327 (2018).

114. B. D. A. Levin, M. J. Zachman, J. G. Werner, R. Sahore, K. X. Nguyen, Y. Han, B. Xie, L. Ma, L. A. Archer, E. P. Giannelis, U. Wiesner, L. F. Kourkoutis, and D. A. Muller, *Microsc. Microanal.*, **23**, 155–162 (2017).

115. C. Barchasz, J.-C. Leprêtre, F. Alloin, and S. Patoux, *J. Power Sources*, **199**, 322–330 (2012).

116. C. Barchasz, F. Molton, and C. Duboc, *Anal. Chem.*, **84**, 3973–3980 (2012).

117. S. Xin, L. Gu, N.-H. Zhao, Y.-X. Yin, L.-J. Zhou, Y.-G. Guo, and L.-J. Wan, *J. Am. Chem. Soc.*, **134**, 18510–3 (2012).

118. Y. Chen, H. Zhang, W. Xu, X. Yang, Y. Yu, X. Li, and H. Zhang, *Adv. Funct. Mater.*, **28**, Article number 1704987 (2018).

119. M. U. M. Patel, I. Arčon, G. Aquilanti, L. Stievano, G. Mali, and R. Dominko, *Chemphyschem*, **15**, 894–904 (2014).

120. N. A. Canas, K. Hirose, B. Pascucci, N. Wagner, K. A. Friedrich, and R. Hiesgen, *Electrochim. Acta*, **97**, 42–51 (2013).

121. J. Tan, D. Liu, X. Xu, and L. Mai, *Nanoscale*, **9**, 19001–19016 (2017).

122. A. T. S. Freiberg, A. Siebel, A. Berger, S. M. Webb, Y. Gorlin, M. Tromp, and H. A. Gasteiger, *J. Phys. Chem. C*, **122**, 5303–5316 (2018).

123. W. Zhu, A. Paolella, C.-S. Kim, D. Liu, Z. Feng, C. Gagnon, J. Trottier, A. Vijh, A. Guerfi, A. Mauger, C. M. Julien, M. Armand, and K. Zaghib, *Sustain. Energy Fuels*, **1**, 737–747 (2017).

124. J. Hannauer, J. Scheers, J. Fullenwarth, B. Fraisse, L. Stievano, and P. Johansson, *ChemPhysChem*, **16**, 2755–2759 (2015).

125. J. D. Mcbrayer, T. E. Beechem, B. R. Perdue, C. A. Apblett, and F. H. Garzon, *J. Electrochem. Soc.*, **165**, A876–A881 (2018).

126. A. J. Bard and L. R. Faulkner, *Electrochemical Methods Fundamentals and Applications*, 2nd ed., John Wiley & Sons, INC, New York, NY (2000).

127. K. J. Rountree, B. D. Mccarthy, E. S. Rountree, T. T. Eisenhart, and J. L. Dempsey, *J. Chem. Educ.*, **95**, 197–206 (2017).

128. J. Herranz, A. Garsuch, and H. A. Gasteiger, *J. Phys. Chem. C*, **116**, 19084–19094 (2012).

129. H. H. Perkampus, *UV-VIS spectroscopy and its applications*, Springer-Verlag, Berlin-Heiderberg (1992).

130. C. Hu, F. E. Muller-Karger, and R. G. Zepp, *Limnol. Oceanogr.*, **47**, 1261–1267 (2002).

131. B.-S. Kim and S.-M. Park, *J. Electrochem. Soc.*, **140**, 115–122 (1995).

132. V. F. Lvovich, *Impedance Spectroscopy: Applications to Electrochemical and Dielectric Phenomena*, John Wiley & Sons, Inc., Hoboken, NJ (2012).

133. S. Solchenbach, D. Pritzl, E. Jia, Y. Kong, J. Landesfeind, and H. A. Gasteiger, *J. Electrochem. Soc.*, **163**, 2265–2272 (2016).

134. M. Ender and J. Illig, *J. Electrochem. Soc.*, **164**, A71–A79 (2017).

135. J. Costard, M. Ender, and M. Weiss, *J. Electrochem. Soc.*, **164**, A80–A87 (2017).

136. T. A. Pascal, K. H. Wujcik, J. Velasco-Velez, C. Wu, A. a. Teran, M. Kapilashrami, J. Cabana, J. Guo, M. Salmeron, N. Balsara, and D. Prendergast, *J. Phys. Chem. Lett.*, **5**, 1547–1551 (2014).

137. A. T. S. Freiberg, A. Siebel, A. Berger, S. M. Webb, Y. Gorlin, M. Tromp, and H. A. Gasteiger, *J. Phys. Chem. C*, **122**, 5303–5316 (2018).

138. Q. He, Y. Gorlin, M. U. M. Patel, H. A. Gasteiger, and Y.-C. Lu, *J. Electrochem. Soc.*, **165**, A4027–A4033 (2018).

139. V. Gutmann, *Electrochim. Acta*, **21**, 661–670 (1976).

140. U. Mayer, V. Gutmann, and W. Gerger, *Monatshefte fuer Chemie*, **106**, 1235–1257 (1975).

141. R. Steudel and Y. Steudel, *Chem. - A Eur. J.*, **19**, 3162–3176 (2013).

142. R. D. Rauh, F. S. Shuker, J. M. Marston, and S. B. Brummer, *J. Inorg. Nucl. Chem.*, **39**, 1761–1766 (1977).

143. R. Bernhard, S. Meini, and H. A. Gasteiger, *J. Electrochem. Soc.*, **161**, A497–A505 (2014).

144. M. Metzger, B. Strehle, S. Solchenbach, and H. A. Gasteiger, *J. Electrochem. Soc.*, **163**, A798–A809 (2016).

145. H. Jha and H. A. Gasteiger, Patent No. DE102013005082A1 (2014).

146. S. S. Zhang, *J. Power Sources*, **231**, 153–162 (2013).

147. H. Yamin, A. Gorenshtein, J. Penciner, Y. Sternberg, and E. Peled, *J. Electrochem.*

Soc., **135**, 1045–1048 (1988).

148. R. Steudel and Y. Steudel, *Chem. -A Eur. J.*, **19**, 3162–3176 (2013).

149. T. A. Pascal, C. D. Pemmaraju, and D. Prendergast, *Phys. Chem. Chem. Phys.*, **17**, 7743–7753 (2015).

150. T. A. Pascal, K. H. Wujcik, J. Velasco-velez, C. Wu, A. A. Teran, M. Kapilashrami, J. Cabana, J. Guo, M. Salmeron, and N. Balsara, *J. Phys. Chem. Lett.*, **5**, 1547–1551 (2014).

151. J. Conder, R. Bouchet, S. Trabesinger, C. Marino, L. Gubler, and C. Villevieille, *Nat. Energy*, **2**, Article number 17069 (2017).

152. S. Zhang, K. Ueno, K. Dokko, and M. Watanabe, *Adv. Energy Mater.*, **5**, 1500117 (2015).

153. H. Wang, N. Sa, M. He, X. Liang, L. F. Nazar, M. Balasubramanian, K. G. Gallagher, and B. Key, *J. Phys. Chem. C*, **121**, 6011–6017 (2017).

154. A. Manthiram, Y. Fu, S. Chung, C. Zu, and Y. Su, *Chem. Rev.*, **114**, 11751–11787 (2014).

155. J. Paris and V. Plichon, *Electrochim. Acta*, **26**, 1823–1829 (1981).

156. N. Saqib, G. M. Ohlhausen, and J. M. Porter, *J. Power Sources*, **364**, 266–271 (2017).

157. D.-H. Han, B.-S. Kim, S.-J. Choi, Y. Jung, J. Kwak, and S.-M. Park, *J. Electrochem. Soc.*, **151**, E283–E290 (2004).

158. B.-S. Kim and S.-M. Park, *J. Electrochem. Soc.*, **140**, 115–122 (1993).

159. F. Gaillard and E. Levillain, *J. Electroanal. Chem.*, **398**, 77–87 (1995).

160. F. Gaillard, E. Levillain, and J. P. Lelieur, *J. Electroanal. Chem.*, **432**, 129–138 (1997).

161. P. Leghié, J. Lelieur, and E. Levillain, *Electrochem. commun.*, **4**, 628 (2002).

162. E. Levillain, F. Gaillard, P. Leghie, A. Demortier, and J. P. Lelieur, *J. Electroanal. Chem.*, **420**, 167–177 (1997).

163. H. Jha and H. A. Gasteiger, Patent No. 102013005082A1 (2014).

164. S.-H. Chung and A. Manthiram, *ACS Energy Lett.*, **2**, 1056–1061 (2017).

165. R. S. Assary, L. a. Curtiss, and J. S. Moore, *J. Phys. Chem. C*, **118**, 11545–11558 (2014).

166. Z. Feng, C. Kim, A. Vijh, M. Armand, K. H. Bevan, and K. Zaghib, *J. Power Sources*, **272**, 518–521 (2014).

167. M. Helen, M. A. Reddy, T. Diemant, U. Golla-Schindler, R. J. Behm, U. Kaiser, and M. Fichtner, *Sci. Rep.*, **5**, 12146 (2015).

168. T. A. Pascal, K. H. Wujcik, R. Wang, P. Balsara, and D. Prendergast, *Phys. Chem. Chem. Phys.*, **19**, 1441–1448 (2017).

169. Y.-C. Lu, Q. He, and H. A. Gasteiger, *J. Phys. Chem. C*, **118**, 5733–5741 (2014).

170. F. Y. Fan, W. C. Carter, and Y.-M. Chiang, *Adv. Mater.*, **27**, 5203–5209 (2015).

171. D. Aurbach, *Nonaqueous Electrochemistry*, Marcel Dekker, Inc., New York, NY (1999).

172. C. O. Laoire, S. Mukerjee, K. M. Abraham, E. J. Plichta, and M. A. Hendrickson, *J. Phys. Chem. C*, **114**, 9178–9186 (2010).

173. J. Landesfeind, D. Pritzl, and H. A. Gasteiger, *J. Electrochem. Soc.*, **164**, A1773–A1783 (2017).

174. D. Pritzl, J. Landesfeind, H. A. Gasteiger, and S. Solchenbach, *J. Electrochem. Soc.*, **165**, A2145–A2153 (2018).

175. R. Petibon, C. P. Aiken, N. N. Sinha, J. C. Burns, H. Ye, C. M. Vanelzen, G. Jain, S. Trussler, and J. R. Dahn, *J. Electrochem. Soc.*, **160**, A117–A123 (2013).

176. C. Heubner, M. Schneider, and A. Michaelis, *J. Power Sources*, **288**, 115–120 (2015).

177. Y. Chang, J. Jong, and G. T. Fey, *J. Electrochem. Soc.*, **147**, 2033–2038 (2000).

178. Lasia Andrzej, *Electrochemical Impedance Spectroscopy and its Applications*, Springer-Verlag, New York, NY (2014).

179. J. Landesfeind, J. Hattendorff, A. Ehrl, W. A. Wall, and H. A. Gasteiger, *J. Electrochem. Soc.*, **163**, A1373–A1387 (2016).

180. R. Raccichini, L. Furness, J. W. Dibden, J. R. Owen, and N. García-Araez, *J. Electrochem. Soc.*, **165**, A2741–A2749 (2018).

181. R. Morasch, J. Landesfeind, B. Suthar, and H. A. Gasteiger, *J. Electrochem. Soc.*, **165**, A3459–A3467 (2018).

182. R. Tatara, P. Karayaylali, Y. Yu, Y. Zhang, L. Giordano, F. Maglia, R. Jung, J. P. Schmidt, I. Lund, and Y. Shao-horn, *J. Electrochem. Soc.*, **166**, A5090–A5098 (2019).

183. Z. Deng, Z. Zhang, Y. Lai, J. Liu, J. Li, and Y. Liu, *J. Electrochem. Soc.*, **160**, A553–A558 (2013).

184. N. Ogihara, S. Kawauchi, C. Okuda, Y. Itou, Y. Takeuchi, and Y. Ukyo, *J. Electrochem. Soc.*, **159**, A1034–A1039 (2012).

185. R. Petibon, C. P. Aiken, N. N. Sinha, J. C. Burns, H. Ye, C. M. Vanelzen, G. Jain, S.

Trussler, and J. R. Dahn, *J. Electrochem. Soc.*, **160**, A117–A124 (2013).

186. J. Conder, C. Villevieille, S. Trabesinger, P. Novák, L. Gubler, and R. Bouchet, *Electrochim. Acta*, **244**, 61–68 (2017).

187. M. Adamič, S. D. Talian, A. R. Sinigoj, I. Humar, J. Moškon, and M. Gaberšček, *J. Electrochem. Soc.*, **166**, A5045–A5053 (2019).

188. G. Bieker, M. Winter, and P. Bieker, *Phys. Chem. Chem. Phys.*, **17**, 8670–8679 (2015).

189. T. R. Jow, S. A. Delp, J. L. Allen, J. Jones, and M. C. Smart, *J. Electrochem. Soc.*, **165**, 361–367 (2018).

190. D. Pritzl, A. E. Bumberger, M. Wetjen, S. Solchenbach, H. A. Gasteiger, and J. Landesfeind, *J. Electrochem. Soc.*, **166**, A582–A590 (2019).

191. A. Berger, A. T. S. Freiberg, A. Siebel, R. Thomas, M. U. M. Patel, M. Tromp, H. A. Gasteiger, and Y. Gorlin, **165**, A1288–A1296 (2018).

192. M. Mohamedi, M. Makino, K. Dokko, T. Itoh, and I. Uchida, *Electrochim. Acta*, **48**, 79–84 (2002).

Acknowledgements

First of all, I would like to express my deepest gratitude to my supervisor **Prof. Hubert Gasteiger**. Thank you for all the invaluable guidance and generous support throughout my whole PhD period. Like an artist in science, you have created a chef-d'oeuvre called TEC (Chair of Technical Electrochemical Chemistry), where the students are trusted and their potential are greatest possible unleashed. Thank you for sharing with us your commitment to science, honest and critical attitude, exceptional knowledge/experience as well as your great diligence.

I want to extend my sincerest gratitude to **Prof. Yi-Chun Lu**, who took me into the world of electrochemistry at 2013 and has accompanied and supervised me intensively in the beginning of my PhD. It was my honor being your first student and thank you for teaching me your outstanding knowledge and experience as well as trusting me unconditionally also at difficult period. Without your trust and encouragement, I would have not completed that many challenging Li-S projects.

Further I want to thank **Anna Freiberg** as the last S-related colleague at TEC, who has accompanied me during the middle and last period of my PhD. Thank you for all the inspirational discussion and precious time you put in reading my PhD thesis and manuscripts as well as your endless energy in organizing our lab.

Next thanks go to **Dr. Bharatkumar Suthar**, with whom I learnt most the impedance knowledge. I also enjoyed our conversation about all the non-electrochemistry stuff, such as religion, politics, history, literature. Thanks for sharing your thought about the fundamental question in life/human etc., which enriched me in other dimensions.

I also want to thank **Dr. Manu U.M. Patel**, who supported me in developing the *operando* UV-Vis electrochemical cell and thank you for all the scientific discussions.

In addition, I appreciate having **Dr. Morten Wetjen** as one of my colleague, who supported me and showed me his profession in his great communication skills. Besides, I thank **Benjamin Strehle** for his support and discussions during my PhD period.

Many thanks also go to **Veronika Pichler** and **Dr. Michele Piana** for their great enthusiasm in organizing TEC in every aspects and many TEC events/activities.

I also thank my former students, **Lennart Reuter**, **Rafael Berk**, **Simon Qian** and **Philip Rapp** for their scientific contributions.

Moreover, I appreciate **Dr. Yelena Gorlin** and **Dr. Juan Herranz** for their supervision. I am also grateful for the support of **Dr. Daniel Pritzl** and **Dr. Sophie Solchenbach** to the Li-S impedance project. In addition, I am thankful for the delightful office experience with **Fabian Linsenmann**, **Tanja Zünd** plus **Robert Morasch**.

In addition, I also thank **Dr. Anna Eberle**, **Dr. Johannes Landesfeind**, **Dr. Uta Schwenke**, **Johannes Sicklinger**, **Anne Berger**, **Burak Koyutürk** and all **other TEC members** for the great working atmosphere as well as **Oliver Gröger** (Volkswagen AG) for your support.

I gratefully acknowledge the financial support from the Federal Ministry of Economic Affairs and Energy under the auspices of the LiMo project (funding number 03ET6045D),

In the end, I would like to conclude my acknowledgement by expressing my deepest gratitude to my parents, **He Guoqiang (贺国强)** and **Yuan Xiaoping (袁小平)** for their support in every direction and their understanding as well as to my friends for being patient with me and all the lovely moment that we shared together.

Scientific Contributions

Articles

Q. He, A. T. S. Freiberg, M. U. M. Patel, S. Qian and H. A. Gasteiger, "*Operando* Identification of Liquid Intermediates in Lithium–Sulfur Batteries via Transmission UV-Vis Spectroscopy", Journal of The Electrochemical Society, 167, 080508 (2020).

Q. He, Y. Gorlin, M. U. M. Patel, H. A. Gasteiger and Y. C. Lu, "Unraveling the Correlation between Solvent Properties and Sulfur Redox Behaviors in Lithium-Sulfur Batteries", Journal of The Electrochemical Society, 165(16), A4027–A4033 (2018).

Y. Gorlin, M. U. M. Patel, A. T. S. Freiberg, **Q. He**, M. Piana, M. Tromp and H. A. Gasteiger, "Understanding the Charging Mechanism of Lithium-Sulfur Batteries Using Spatially Resolved *Operando* X-Ray Absorption Spectroscopy", Journal of The Electrochemical Society, 163(6), A930–A939 (2016).

Y. C. Lu, **Q. He** and H. A. Gasteiger, "Probing the Lithium-Sulfur Redox Reactions: A Rotating-Ring Disk Electrode Study", Journal of Physical Chemistry, 118 (11), 5733-5741 (2014).

Article in Preparation

Q. He, R. Berk, A. T. S. Freiberg, D. Pritzl, S. Solchenbach and B. K. Suthar, "*In-situ* Impedance Measurements for Sulfur Cathode – an Application of Gold Micro-Reference Electrode in Li-S Batteries", manuscript in preparation.

Oral Presentations

<u>Q. He</u>, B. K. Suthar, R. Berk, D. Pritzl, A. T. S. Freiberg and H. A. Gasteiger, "*In-situ* Impedance Spectroscopy of a Sulfur-Cathode in Li-S Batteries", 7th Workshop "Lithium-Sulfur Batteries", Dresden, Germany (2018).

<u>Q. He</u>, M. U. M. Patel, A. T. S. Freiberg and H. A. Gasteiger, "Characterization of Reaction Intermediates in Lithium-Sulfur Batteries via *Operando* Transmittance UV/Vis Spectroscopy", 6th Workshop "Lithium-Sulfur Batteries", Dresden, Germany (2017).

<u>Q. He</u>, H. A. Gasteiger, Y. Gorlin, M. U. M. Patel and Y. C. Lu, "A Systematic Study of the Correlation between Solvent Properties and Sulfur Redox Behaviors in Li-S Batteries", 232nd ECS Meeting, National Harbor, Maryland, USA (2017).

Q. He, <u>Y. C. Lu</u>, Y. Gorlin and H. A. Gasteiger, "Influence of Solvent on Lithium-Sulfur Redox Reactions: A Rotating Ring-Disk Electrode Study", 227th ECS Meeting, Chicago, USA (2015).

Poster Presentations

Q. He, M. U. M. Patel, M. Wetjen, Y. Gorlin and H. A. Gasteiger, "Influence of Different Electrolyte Solvents on the Li_2S Activation Processes in Li_2S //Li and Li_2S//Si Batteries", 5th workshop "Lithium-Sulfur-Batteries" Dresden, Germany (2016).

Q. He, Y. Gorlin, M. U. M Patel, A. Berger and H. A Gasteiger, "Regulating the Potential for Li_2S Activation by Selection of Electrolyte in Lithium Sulfur Batteries", 6th MSE Kolloquium, Munich, Germany (2016).

Q. He, Y. C. Lu, Y. Gorlin, M. U. M. Patel and H. A. Gasteiger, "Differentiating the Role of the Dielectric Constant and the Donor Number of Solvents for Li-S redox reactions", 4th workshop "Lithium-Sulfur-Batteries", Dresden, Germany (2015).

Q. He, Y. C. Lu, J. Herranz and H. A. Gasteiger, "Impact of Low Dielectric Constant Electrolytes on Li-S Battery Behavior", 3rd Workshop "Lithium-Sulfur-Batteries", Dresden, Germany (2014).

Y. C. Lu, **Q. He** and H. A. Gasteiger, "Probing the Lithium-Sulfur Redox Reactions via Rotating-Ring Disk Electrode", 17th IMLB, Como, Italy (2014).